Coordination and regulation of bystander memory T cells

Nicholas Joseph Maurice

A dissertation

submitted in partial fulfillment of the

requirements for the degree of

Doctor of Philosophy

University of Washington

2021

Reading Committee:

Martin Prlic, Chair

Marc A. Gavin

Kevin B. Urdahl

Program Authorized to Offer Degree:

Molecular and Cellular Biology

University of Washington

Abstract

Coordination and regulation of bystander memory T cells

Nicholas Joseph Maurice

Chair of the Supervisory Committee:
Martin Prlic, Ph.D.
Departments of Immunology and Global Health

Memory T cells (T_{mem}) are best understood as highly specific killers, using their T cell receptor (TCR) to identify and rapidly eliminate infected or transformed cells. Although T_{mem} are best understood through the lens of TCR-mediated activation, it is not the lynchpin of their function. T_{mem} can also respond to pro-inflammatory cytokines in the absence of activating TCR signals, termed bystander activation. Although this phenomenon was described over 20 years ago, it was thought to be of little biologic significance until it was shown that bystander activated T_{mem} could kill using TCR-independent mechanisms. These killing programs were best understood during systemic and/or chronic inflammation, leading many to classify bystander-mediated killing as an “immunologic accident” resulting from astoundingly high levels of inflammation. The full gamut of circumstances in which bystander activation can occur, as well as the signals governing it, remain unclear. Here we address basic questions in bystander T cell biology: 1) in what biological contexts does bystander activation occur, 2) how can limited inflammation beget

bystander activation, 3) what fate changes accompany bystander activation, and 4) do mechanisms that attenuate/control bystander activation exist?

Using both clinical vaccine samples and mouse models, we demonstrate that bystander activation is not a niche phenomenon but can also arise during dose- and anatomically-restricted inflammation. This hinges on CXCR3-mediated recruitment of T_{mem} to sites of early immune activation, at where they become bystander activated by pro-inflammatory cytokines and contribute to localized target killing. While induction of cytotoxicity is the best-known consequence of bystander activation, we demonstrate that other fates, like tissue retention, can be elicited by inflammation alone. Using a multi-omics approach, we demonstrate that homeostatic cytokine networks exist in healthy human placental tissues, which sufficiently bystander activate T_{mem} without precipitating cytotoxicity and tissue pathology. We show this to result from cooperation between anti-inflammatory cytokines and metabolites, which restrain bystander-mediated cytotoxicity without forfeiting other activation-induced programs of tissue retention and surveillance. Together, we show that bystander activation is an intentional program oft used to maximally leverage T_{mem} in the absence of TCR agonism and identify mechanisms to better wield or restrain this population therapeutically.

TABLE OF CONTENTS

LIST OF FIGURES

LIST OF TABLES

ACKNOWLEDGEMENTS

More important than this work are the people who supported me throughout the years. Though this list is exhaustive, it is by no means complete.

First, thank you to Martin Prlic, my Ph.D. advisor, for assembling a wonderful network of colleagues: (post-doctoral fellows and staff scientists) Jami Erickson, Florian Mair, Marie Frutoso, Caitlin DeJong, Laura Reichert-Spuhler, (graduate students) Andrew Konecny, Veronica Davé, Brianna Traxinger, Chloe Slichter, Julia Berkson, (clinical fellow) Stephen McCartney, (master's student) Sven Hagen, (technicians) Alexis Taber, Hayley Roozen, Kristin Weakley, Hannah Miller, Sarah Roepke, and (lab manager) Paula Walsh. Paula, it is hard to believe ten years ago we were technicians in the HVTN. It has been a joy watching you and your family (Chris, Poppy, and a soon-to-be son) grow over the years. Thank you for always having time to lend an ear and (mercifully) keeping me in line whenever I tried wearing socks and sandals in the lab. Jami and Florian, your arrivals mark a point where science became fun again—thank you for keeping me humble with your cutting (but loving) sass and for proving that good science does not come at the expense of fun (or coffee breaks). Jami, I could not have had a better friend in the lab. Lastly, Alexis, thank you for your abundance of patience as I learned to mentor you—and conversely, thank you for teaching me how to mentor (as well as use Gen Z slang). You will make a great physician scientist, no cap.

I am thankful for the camaraderie and support of current and former colleagues in Jenny Lund's lab (especially Jessica Swarts, Jessica Graham, Tisha Graham, Crystal Huynh, and Tanvi Arkatkar), Justin Taylor's Lab (especially Holly Steach and Jessica Schembri), and the HVTN (especially Antje Heit, Julie Williams, Terri Stewart, Greg Mize, Lamar Fleming, and Kimberly Smythe). Antje, thank you for being a true friend. I am forever grateful for the time spent with you and your family (Frank, Henrik, and Alan). I treasure all our times hiking, kayaking, surfing, and skiing (while singing "*Schifoan*"). Mit meinem ganzen Herzen, ich betrachte dich als Familie und werde dich sehr vermissen—alles Lieb.

I would like to acknowledge my thesis committee: Hilary Gammill, Daniel Campbell, Kevin Urdahl, W. Conrad Liles, and Marc Gavin, the Molecular and Cellular Biology Program: Nina Salama, Celeste Berg, Richard Gardner, Katie Peichel, Maia Low, and Andrea Brocato, as well as the

many collaborators that have graciously provided their technical and intellectual assistance: Raj “Swati” Shree, Lee Nelson, Evan Newell, Laura Islas, Lucas Sullivan, Anna Vigil, Michael Gerner, and Jason Krawic. A special thank you to Thuy Dao and Laura Yates for their outstanding administrative support and meticulousness when it comes to federal paperwork. Thank you to my previous mentors, (Fred Hutch) Stephen de Rosa, Julie McElrath, (Seattle Pacific University) Benjamin McFarland, Derek Wood, Charlotte Pratt, Tim Nelson, (Woodinville High School) Prudence Hockley, and Nancy “Babs” Herrigel-Babienko. Hockley and Babs, I wish you were still living. You were invested in me at a time when I so desperately needed it. Thank you for relentlessly challenging my complacency and changing my trajectory in life—I miss you both dearly.

I would like to thank Jeff Babienko, the Northshore Scholarship Foundation, and all those who supported the Dr. Nancy Herrigel-Babienko Memorial Scholarship. Being associated with Dr. Bab’s legacy is the highest honor. I would like to extend my deepest thanks to Hilda Raz for the permission to use her poem, *Diction*, in the opening comments of my thesis. The inclusion of this is not only to highlight the metaphorical “language” of immunity, but to recognize Prudence and Nancy for this poem was annually used for in-class analysis exercises. I would also like to thank Leslie and Pete Higgins and the ARCS Foundation (especially Meredith Wisti and Kitti Lyle) for their generous support through the ARCS Fellowship, as well as acknowledge my federal support from the NCATS TL1 program, the NIH F31 Ruth L. Kirschstein Predoctoral Individual National Research Service Award, and the NCI F99/K00 Predoctoral to Postdoctoral Fellow Transition Award.

I owe a significant portion of my growth as a community-centered scientist to those in the Seattle Vaccine Trials Unit and COVID-19 Prevention Network. A tremendous thank you to all, especially, Ro Yoon, James Lilly, Kim Louis, Stephaun Wallace, and the entire Community Advisory Board. You inspire me and put why I do this work in perspective.

There are many friends from graduate school, college, home, and abroad that I would like to thank; but any list would likely be incomplete: Thank you to my friends here at UW, Laura Gabrovsek, Ethan Ahler, Alec Wilkens, Kristen Mittelsteadt, Rachel Dam, Austin Gabel, Zak Yaffe, and Stephanie Varela; to those from Seattle Pacific, Brianne Hagerty, Erin Dunnington, Natalie Flath, Melissa Moran-Hodge, Anja Thompson, and Meghan Klein; to those from my youth: Douglas Wagoner, Reggie Arnold, and Rosie Sturgeon; those from abroad: Djamila Haramustek

and Johanna Geiger; and those from my time in Seattle, Lise Ferguson, Cait Lawson, Daniel Vandiver, Matthew Stokes, Eric Johnson, Kayle Walls, Becca Roy, Stefanie Shank, Yooree Chae, Tricia Turton, and Jennifer Hamann. Life is so much fuller and vivid with you in it.

Lastly, I am so lucky to have my family—despite our various and often, extreme differences. Thank you to my big brother, Stephen James, who in the past 32 years has somehow managed to be both my greatest nemesis and closest advocate—our relationship may ebb and flow, but I know we will always have each other's backs. Thank you to my parents, Gail and Stephen. Mom, thank you for raising me in an environment of creativity—some of my fondest memories are of you opening your art history books and showing me parallels between my LEGO buildings and architecture from around the world, helping me draw when I was far less coordinated, watching you construct stained glass pieces, or sitting on the kitchen countertop as you baked. Dad, thank you for bringing the many cats and dogs into our family over the years despite mom's protests. Lastly, thank you to my grandparents, John and Kathleen, better known as Pop-Pop and Tuffers. Thank you for demonstrating that one can be diligent and hardworking without forfeiting one's passion for artistry, creativity, sport, history, and culture. You have been such wonderful role models throughout my life. I love you all beyond words.

DEDICATION

To my parents, Gail and Stephen—in a world of chance and infinite possibilities, I am so lucky to call you my mom and dad.

Preface

List of abbreviations

γ_c	Common gamma chain (CD132/IL2RG)
ACK	Ammonium-chloride-potassium lysing buffer
ActA	Actin assembly-inducing protein
AdV	Adenovirus
AF	Alexa Fluor
Ag	Antigen
AHA	Acute hepatitis A
AhR	Aryl hydrocarbon receptor
APC	Allophycocyanin
APCs	Antigen-presenting cells
AViD	Aqua viability dye
B6	C57BL/6J mouse strain
BB	Brilliant blue fluor
BHI	Brain/Heart infusion media
BUV	Brilliant ultraviolet fluor
BV	Brilliant violet fluor
BViD	Blue viability dye
CB	Cord blood
cfu	Colony-forming units
CHX	Cycloheximide
CMV	Cytomegalovirus
CS	Cesarean section
CsA	Cyclosporin A
CTLA-4	Cytotoxic T-lymphocyte associated protein 4 (CD152)
CXCR3	CXC motif chemokine receptor 3
CXCR3L	CXCR3 ligands (CXCL9, CXCL10, and/or CXCL11)
Cy	Cyanine dye
CyTOF	Cytometry by time of flight
DAPI	4′,6-diamidino-2-phenylindole
DMSO	Dimethyl sulfoxide
Dz	Dazzle fluor
e	eFluor

EBV	Epstein-Barr virus
FACS	Fluorescence-activated cell sorting
FACSWash	Flow cytometry wash buffer
FBS	Fetal bovine serum
FITC	Fluorescein isothiocyanate
fPLAC	Fetal side of the placenta
gB	HSV-2 glycoprotein B
GFP	Green fluorescent protein
gp33	LCMV glycoprotein 33
GzmB	Granzyme B
HAV	Hepatitis A virus
HBV	Hepatitis B virus
HCV	Hepatitis C virus
HIV	Human immunodeficiency virus
HLA	Human leukocyte antigen
HSV-1	Herpes simplex virus 1
HSV-2	Herpes simplex virus 2
HVTN	HIV Vaccine Trials Network
IAV	Influenza A virus
IF	Immunofluorescence
IFN	Interferon
IFNγ	γ-interferon
IgG	Immunoglobulin G
IL	Interleukin
i.m.	Intramuscular
i.v.	Intravenous
IVB	Intervillous blood
KYN	L-Kynurenine
LC-MS	Liquid chromatography–mass spectrometry
LCMV	Lymphocytic choriomeningitis virus
LN	Lymph node
LN_2	Liquid nitrogen
LLO	Listeriolysin O
LM	*Listeria monocytogenes*

LPS	Lipopolysaccharide
Mφ	Macrophage
MACS	Magnet-activated cell sorting
MAIT cell	Mucosal associated invariant T cell
MB	Maternal blood
MedFI	Median fluorescence intensity
MeOH	Methanol
MFI	Maternal-fetal interface
MHC	Major histocompatibility complex
MMM	Marginal zone metallophilic macrophage
mPLAC	Maternal side of the placenta
MR1	MHC-related 1
MVA	Modified vaccinia Ankara
Nφ	Neutrophil
NFAT	Nuclear factor of activated T cells
NIRViD	Near-IR viability dye
NK cell(s)	Natural killer cell(s)
NKT cell(s)	Invariant natural killer T cells
NKG2DL	NKG2D ligands
OCT	Optimal cutting temperature compound
OVA	Ovalbumin
PBMC	Peripheral blood mononuclear cell
PBS	Phosphate-buffered saline
PD-1	Programmed death 1 (CD279)
PE	Phycoerythrin
PFA	Paraformaldehyde
pfu	Plaque forming units
RA	Rheumatoid arthritis
RBC	Red blood cell
RP	Splenic red pulp
RT	Room temperature
SA	Streptavidin
SAC	Seattle-area cohort
scRNAseq	Single-cell RNA sequencing

SD	Standard deviation
SPF	Specific pathogen free
TBS	Tris-buffered saline
TCF1	T cell factor 1
T_{CM}	T central memory
TCR	T cell receptor
T_{EM}	T effector memory
T_{EMRA}	T effector memory CD45RA–re-expressing
TLR	Toll-like receptor
TME	Tumor microenvironment
T_{mem}	Memory T cell
TNFα	Tumor necrosis factor alpha
TOX	Thymocyte selection-associated high mobility group box protein
T_{RM}	Resident memory T cell
Trp	L-Tryptophan
UMAP	Uniform manifold approximation projection
VSV	Vesicular stomatitis virus
VZV	Varicella zoster virus
WP	Splenic white pulp
WT	Wildtype
YFV	Yellow fever virus

Chapter 1. Introduction

Portions of this chapter are adapted from the following work with permission from Copyright© The American Association of Immunologists, *Journal of Immunology*:

Maurice NJ, Taber AK, Prlic M. The Ugly Duckling Turned to Swan: A Change in Perception of Bystander-Activated Memory CD8 T Cells. *J Immunol.* 2021 Feb 1;206(3) 455-462. DOI: 10.4049/jimmunol.2000937

1.1 Opening comments: on language and immunity

"God is in the details," I tell the kids in the public school at Milligan, Nebraska. They wonder what I mean. I tell them to look out the window at the spring fields the mud coming up just to the knee of the small pig in the far pasture. They tell me it's not a knee but a hock and I hadn't ought to say things I know nothing about. I say the light on the mud is pure chalcedony. They say the mud killed two cows over the weekend. I tell them the pig is alive and the spring trees are standing in a green haze. They tell me school is out in a week and they have to plant. The grain elevator at the end of Main Street stretches out her blue arms. The kids say chutes.

Hilda Raz, *Diction*

To command and leverage immune cells as a therapeutic, we must first understand their language. The language of T cells, the cytotoxic arm of our adaptive immune system, is largely understood through T cell receptor (TCR)-mediated communication. Each T cell will express a TCR, which detects non-self peptide antigens (Ag) in the context of self-encoded major histocompatibility complex (MHC) molecules, ultimately serving as the message which the T cell can integrate. The presence of an Ag on MHC which can bind TCR with sufficient affinity announces to this T cell that something is amiss (infection or transformation), calling it to arms. But while TCR and Ag are the T-cell equivalent to words, it is by no means a universal language. Ancient recombinases drive a molecular-level collapse of the Tower of Babel, rearranging TCR gene segments to beget an unfathomable diversity of TCR clones that will each be responsive to a unique Ag. Though this allows our immune system to recognize and respond to the full gamut of pathogens, it also means our T cells that lack specificity during an infection (e.g., a flu-specific cell during an HIV infection), are "left out" of the current immunologic conversation due to their linguistic differences. Do we make an immunologic concession to have this specificity, generating one-trick ponies of T cells that can solely be roused to action when their TCR binds cognate Ag?

Within the confines of human language, we can impart the same message albeit with wildly different means. We can construct sentences with the same meaning with unalike diction or convey a message by tone alone. But what of T cells—are they simply confined to the components of TCR and cognate Ag? Despite the role of Ag as an alarm, much punchier ways to biologically communicate danger to T cells exist, like inflammation. Pro-inflammatory cytokines can be sensed by and subsequently lead to the activation of T cells. In memory T cells (T_{mem}) (i.e., those that have undergone priming and contraction), inflammation-mediated activation, termed "bystander activation," parallels that of TCR: cellular proliferation, cytokine production, and direct target killing. This has largely been described in the context of chronic and/or systemic inflammation, leading some to disregard bystander activation as an immunologic accident arising from a din of pro-inflammatory alarms (with subsequent limited biological relevance). But the prospect of a common tongue across T cells warrants investigation, especially as this could be therapeutically harnessed to command T_{mem} irrespective of their TCR specificity. Therefore, the goal of this work is to understand the inflammation-mediated language of T cells, specifically the full range of circumstances in which it is employed and the mechanistic components dictating this language's structure.

1.2 Bystander activation: a non-conventional path to T_{mem} activation

A hallmark feature of adaptive immunity is the development of immunologic memory. $CD8^+$ T_{mem} respond rapidly upon TCR reencounter with cognate Ag by acquiring effector function and initiating cell division (1). Bystander activation of $CD8^+$ T_{mem} is driven by pro-inflammatory cytokines such as type I interferons (IFNs), interleukin (IL)-12, IL-15, and IL-18 and occurs in the absence of agonist TCR signals. This has been demonstrated in mouse models using TCR-transgenic T cells as well as with polyclonal $CD8^+$ T_{mem} using Nur77-GFP reporter mice. Briefly, GFP expression is transiently increased in T cells of these reporter mice after the cells receive a TCR signal, including those mediated by very weak agonists (2). Bystander-activated $CD8^+$ T_{mem} did not show increased GFP expression, demonstrating that bystander activation occurs independently of (measurable) agonist TCR signals (3). Thus, bystander activation of $CD8^+$ T_{mem} is a distinct phenomenon from TCR cross-reactivity, which can occur even in unrelated infections but is still TCR-mediated (4). The direct functional outcome of TCR-mediated versus bystander-mediated T_{mem} activation appears remarkably similar and can in both instances include T cell proliferation (5), cytokine expression (6-10), and direct target cytolysis (3, 11-13). The Ag-specific T cell response is stringently regulated and requires two signals (TCR + co-stimulation)

to allow for the initial activation of a naive T cell, and even a third signal (such as type I IFN or IL-12) for a $CD8^+$ T cell to acquire effector function (14). Furthermore, the duration of effector function is inherently limited, as T cells acquire expression of inhibitory proteins during the effector stage including expression of PD-1 and CTLA-4 (15). Prolonged activation of T cells leads to T cell exhaustion (also referred to as T cell dysfunction), which is characterized by a TCR signaling–dependent loss of the ability to proliferate or produce effector molecules, such as γ-interferon (IFNγ), in response to stimuli (16).

Given that numerous regulatory mechanisms are in place to tightly control the TCR-driven effector T cell response, it raises the question why T_{mem} are seemingly easily activated by inflammatory signals. One could argue that control mechanisms to regulate bystander activation of T_{mem} may not be critical if bystander activation only occurs in very rare and specific scenarios such as systemic viral infections, which is how bystander activation was initially discovered (5). Indeed, it had been proposed that bystander activation is not of major biological consequence (17). A lack of relevance could be possible if bystander activation of T_{mem} was a vestigial feature that stems from the gradual development of the adaptive immune system from the innate immune system (18). But further work is needed to understand the full scope of circumstances in which bystander activation is possible.

1.3 *Niche phenomenon of systemic infection or regular occurrence?* When and where T cell bystander activation occurs

The first indication that $CD8^+$ T_{mem} become activated during an infection even in the absence of Ag was made by Tough and colleagues (5) when they reported that a large fraction of $CD8^+$ T_{mem} proliferated in response to systemic infection with lymphocytic choriomeningitis virus, vaccinia virus, and vesicular stomatitis virus. Based on the large fraction of $CD8^+$ T_{mem} that proliferated, Tough et al. hypothesized that proliferation was driven by type I IFN rather than Ag. To test this hypothesis, they induced a type I IFN response by injecting mice with poly I:C and again observed that a substantial part of the T_{mem} population proliferated and referred to it as bystander proliferation. Importantly, bystander proliferation was much more limited compared with Ag-driven proliferation, as it appeared to only induce one round of cell division (5, 19). Whereas Ag-specific T cell expansion results in a substantial temporary increase of the T cell compartment during acute infections, bystander proliferation is seemingly providing little to no contribution to this increase in T cell numbers and also appears to have a negligible effect on the overall size of

the T_{mem} compartment (19). Studies by Welsh and colleagues (20, 21) suggested that bystander activation could even lead to a net loss of T_{mem} during heterologous infections. Although these initial observations of bystander activation focused primarily on proliferation, subsequent studies found that bystander-activated $CD8^+$ T_{mem} also gained effector function, including the ability to secrete IFNγ and express granzyme B (GzmB) (3, 7, 8, 22), which led to the shift in terminology from bystander proliferation to bystander activation. Importantly, bystander activation of $CD8^+$ T_{mem} that are not Ag specific has also been demonstrated during the course of systemic viral infections in human cohorts including primary human immunodeficiency virus (HIV) (23, 24), primary Epstein-Barr virus (EBV) (25), and (to varying degrees) during acute dengue virus infections (26-28). In these latter human studies, peptide/MHC tetramers were used to distinguish Ag-specific from bystander-activated T_{mem}. Of note, using human T cells specific for chronic viral infections such as cytomegalovirus (CMV) and EBV to assess bystander activation must be done carefully because it is challenging to distinguish between bystander activation and activation as a result of local viral reactivation. Though bystander activation has been most studied in the context of viral infections, there is evidence that other pathogens elicit inflammation sufficient for bystander activation. Both bacterial motifs (29-31) and systemic *Listeria monocytogenes* (3, 6-10, 32, 33) or *Yersinia pseudotuberculosis* (33) infections beget $CD8^+$ T_{mem} bystander activation.

1.3.1 Bystander activation of T_{mem} during chronic infections

Animal models demonstrate that chronic *Leishmania major* (12, 13) and *Borrelia burgdorferi* (34) infections result in prolonged bystander activation of $CD8^+$ T_{mem} at sites of infection. Similarly, bystander activation of $CD8^+$ T_{mem} was observed in patients infected with hepatitis B virus (HBV) (28, 35). Two recent reviews provide a more detailed overview of bystander activation in context of chronic infections (36, 37). Although bystander activation of T_{mem} is observed in settings of chronic inflammation, it is noteworthy that it is less clear how long the state of bystander activation can last for a $CD8^+$ T_{mem} on a single-cell level. To our knowledge, there are no studies that have addressed whether a $CD8^+$ T_{mem} can remain bystander activated for prolonged periods of time. Other possibilities include that bystander-activated $CD8^+$ T_{mem} could change expression of chemokine receptors and leave the site of inflammation, they could become nonresponsive to proinflammatory cytokines or have other regulatory mechanisms that would allow a return to steady state. Bystander-activated $CD8^+$ T_{mem} could also undergo apoptosis or related forms of programmed cell death. This has been observed in some mouse models of heterologous viral infections (20), in which chronic STAT1 signaling, mediated by type I IFNs (21) or IL-6 (38), drives bystander $CD8^+$ T_{mem} loss.

1.3.2 Bystander activation of T_{mem} in other settings

Although bystander activation has been predominantly studied in the context of various infections, evidence of bystander activation of $CD8^+$ T_{mem} has been observed in rheumatoid arthritis (RA) (39) and celiac disease (40). A recent study by Simoni and colleagues revealed the presence of bystander $CD8^+$ T_{mem}, including influenza A virus (IAV)-, CMV-, and EBV-specific T cells, in human solid tumors. It is still unclear if these $CD8^+$ T_{mem} are merely bystanders in the sense that they are not tumor-specific, or if they are actually bystander activated and secrete IFNγ or other effector molecules (41). These studies demonstrate that bystander $CD8^+$ T_{mem} must be considered in localized (i.e., tissue) microenvironments. Nevertheless, the full gamut of circumstances in which these bystander $CD8^+$ T_{mem} can become activated as well as their biological relevance remains less clear.

1.4 *A universal language?* Bystander activation across T cell subsets

In contrast to T_{mem} cells, there is no evidence that naïve T cells undergo bystander activation. Instead, naïve $CD8^+$ T cells become briefly activated in context of a systemic viral infection or *L. monocytogenes* infection, but may undergo apoptosis without a subsequent TCR signal (21, 42). Type I IFN was the first signal identified as sufficient to induce bystander proliferation of T_{mem}, but it can also lead to bystander activation (22). In addition to type I IFN, at least two of the following cytokines in combination are sufficient to trigger bystander activation: IL-12, IL-15, IL-18 (6-8, 31, 43-45), or TLR2 signaling (34) (Figure 1.1A–C). Freeman and colleagues (43) tested over 43 murine cytokines in over 1800 different cytokine combinations to induce TCR-independent IFNγ production in a rather heroic effort of identifying additional cytokine combinations that can elicit or diminish bystander activation of $CD8^+$ T_{mem}. The resulting data were complex and highlighted the importance of defining the cytokine composition of an inflammatory environment to understand why a T_{mem} cell did or did not acquire a bystander-activated phenotype.

Measuring IFNγ secretion and GzmB expression is certainly useful to assess bystander activation, but it is important to consider that other functional properties, cell fate, etc. may change as well, but these potential changes have not been extensively investigated to date. Similarly, how proinflammatory signals affect different T_{mem} subsets is poorly understood. Although this work is focused on bystander activation of $CD8^+$ T_{mem}, other T cell subsets, like $CD4^+$ T_{mem} (46)

and mucosal-associated invariant T cells (47, 48) can become bystander activated. Proinflammatory cytokines also activate invariant NKT cells (49, 50) and γδ T cells (51) in the absence of cognate Ag. The notion that cytokine signals may elicit different functional programs is particularly relevant for $CD4^+$ T_{mem} given their functional breadth (46). Importantly, bystander activation is not necessarily homogenous within or across $CD8^+$ T_{mem} subsets. The phenotype of a $CD8^+$ T_{mem} is shaped by its initial Ag-driven encounter(52), variable expression of cytokine receptors across T_{mem} subsets, which is further affected by previous Ag experience (53), and T cell responses to proinflammatory cytokines such as IL-12 can also vary by biologic sex (54).

$CD8^+$ T cells with a memory phenotype are not necessarily generated by previous exposure to Ag. Virtual $CD8^+$ T_{mem} cells acquire a memory phenotype because of homeostatic proliferation (55). Virtual $CD8^+$ T_{mem} cells also become bystander activated during heterologous infection in an IL-15–dependent manner (32), suggesting that bystander effector programs are not exclusive to $CD8^+$ T_{mem} that have been expanded by Ag. White and colleagues provided intriguing evidence that a virtual memory T cell–like population also exists in humans and accumulates with age (32). Given the age-associated increase of memory T cells in humans over time (32), determining how different T_{mem} subsets contribute to and affect immune responses in the elderly in a TCR-independent manner is of great clinical interest. Together, these studies highlight that most $CD8^+$ T_{mem} subsets are capable of becoming bystander activated and that this is in part dictated by cytokine receptor expression levels and may be further shaped by the tissue microenvironment.

1.5 The functional consequences of bystander activation in $CD8^+$ T_{mem}

1.5.1 Consequences of IFNγ secretion for the early immune response

In general, IFNγ has been shown to activate microbicidal effector programs in macrophages and other Ag-presenting cells (APCs), including production of reactive oxygen species (ROS), increased phagocytosis, and upregulation of Ag presentation/costimulatory molecules to generate Ag-specific T cell responses (9, 56, 57) and is thus a central cytokine of the host's immune response. Mouse model studies with *L. monocytogenes* have been leveraged to dissect the importance of direct and indirect IFNγ effects. IFNγ responses are critical to coordinate primary immune responses against *L. monocytogenes* (58). During the innate phase of *L. monocytogenes* infection, IFNγ–deficient mice suffer from a markedly higher splenic *L. monocytogenes* burden; however, the adoptive transfer of a wild-type bystander $CD8^+$

T_{mem} population dramatically lowers *L. monocytogenes* burden at this timepoint (7). This phenomenon is a result of IFNγ, derived from transferred bystander $CD8^+$ T_{mem} that became activated, orchestrating effector responses in nearby APCs (9) (Figure 1.1B, D). IFNγ signaling leads to an increase in phagocytosis and production of reactive oxygen species by APCs (9), which can directly limit *L. monocytogenes* replication (59-61). APCs also increase Ag presentation and expression of costimulatory molecules (9), which are critical signals for priming Ag-specific T cells. Ge and colleagues (56) recently reported that the early burst of IFNγ production by bystander $CD8^+$ T_{RM} recruited neutrophils, which, in turn, limited *S. aureus* growth during the first 3 d of bacterial pneumonia. Of note, $CD8^+$ T cell–derived IFNγ that is available in the first 24 h of an infection can restrict Ag-specific effector CD8 T cell differentiation in a paracrine manner resulting in an altered effector to memory balance (62). Furthermore, IFNγ could also act in an autocrine manner on $CD8^+$ T_{mem} (Figure 1.1D). Together, this suggests that IFNγ derived from bystander-activated $CD8^+$ T_{mem} interacts upstream and downstream of the innate immune system to control early pathogen replication.

1.5.2 GzmB-mediated killing without cognate Ag.

GzmB codelivery with perforin to a target cell results in its apoptotic death, but this cytotoxic payload poses risk to nearby cells (63). Ag-specific $CD8^+$ T cells secrete GzmB at the immunosynapse formed by their TCRs and cognate Ag/MHC class I on targets, minimizing the chance of GzmB uptake by unintended targets (63, 64). So how can GzmB-expressing bystander $CD8^+$ T_{mem} kill or identify target cells in the absence of cognate Ag? This remained unclear until it was shown that bystander-activated $CD8^+$ T_{mem} can identify and kill target cells in an NKG2D-dependent manner (Figure 1.1C, E) (3). The immunoreceptor NKG2D engages a suite of stress-induced NKG2D ligands (NKG2DLs), which serve as generalized signals of infection, stress, or transformation (65-67). NKG2D is used by NK cells to survey for and eliminate NKG2DL-expressing cells. In vivo blockade of NKG2D-NKG2DL interactions led to increased bacterial loads early after infection even in the absence of NK cells, indicating that bystander-activated $CD8^+$ T_{mem} are needed to eliminate *L. monocytogenes*–infected APCs expressing NKG2DLs (3). Numerous studies have documented the benefit of effector responses by bystander-activated $CD8^+$ T_{mem} in multiple animal models of infection, including *L. monocytogenes* (3, 7, 32, 33), *Y. pseudotuberculosis* (33), *S. aureus* pneumonia (56), murine gammaherpesvirus 4 (68), and IAV (69, 70). Together, these studies suggest that the role of bystander-activated $CD8^+$ T_{mem} during an acute infection is to help minimize pathogen spreading. Given the timing of how bystander activation appears to resolve when the Ag-specific T cell response takes over, it seems that this

mechanism could help minimize the risk that the pathogen outruns host immunity before the Ag-specific adaptive immune response kicks in.

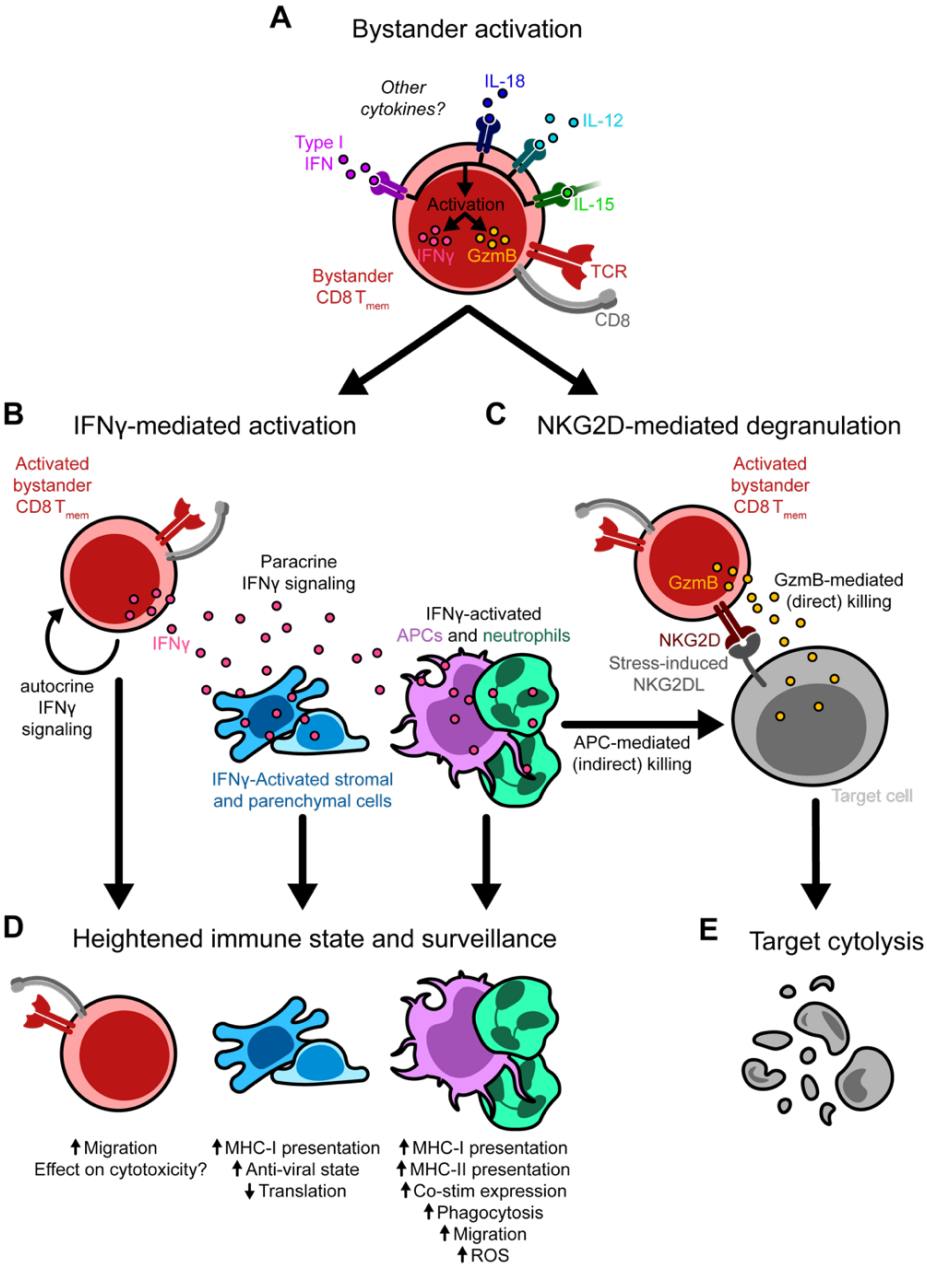

Figure 1.1 Effector functions of bystander-activated CD8$^+$ T$_{mem}$.

A Proinflammatory cytokines, including type I IFN or combinations of IL-12, IL-15, and/or IL-18, activate CD8$^+$ T$_{mem}$ to become bystander activated and express IFNγ and/or GzmB. **B** IFNγ could signal in an autocrine and paracrine manner. Both nonimmune cells (such as stromal and parenchymal cells) and leukocytes (e.g., CD8$^+$ T cells, APCs, and neutrophils) can be activated by IFNγ. **C** Engagement of NKG2D on bystander-activated CD8$^+$ T$_{mem}$ with stress-induced NKG2DLs on targets coordinates the delivery of cytotoxic GzmB granules to target cells. **D** IFNγ secretion has pleiotropic effects, which result in a heightened immune state. **E** Direct NKG2D-mediated and indirect IFNγ-mediated responses ultimately converge to result in target cell death.

1.6 Host consequences of CD8$^+$ T_{mem} bystander activation

1.6.1 Bystander-mediated pathology during prolonged inflammation

Although NKG2D-dependent killing can help control early pathogen spread during an acute infection, this mechanism was subsequently identified to cause immunopathology in context of chronic infections (12, 13) as well as human acute hepatitis A virus (AHA) (11) During AHA, both hepatitis A virus (HAV)-infected and -uninfected hepatocytes upregulate NKG2DLs (11). Bystander-activated CD8$^+$ T_{mem} maintain high NKG2D expression, especially in the presence of IL-15, and can target NKG2DL-expressing hepatocytes, whereas TCR stimulation downregulates NKG2D expression in HAV Ag–specific T cells (11). Bystander-mediated killing of NKG2DL-expressing cells in vitro strongly correlated with measures of liver damage in AHA patients, highlighting the probable role of bystander-activated CD8$^+$ T_{mem} in off-target damage (11). However, it is unclear whether these innate-like killing mechanisms, although capable of off-target damage, contribute to HAV clearance. During chronic cutaneous leishmaniasis, bystander CD8$^+$ T_{mem} are recruited to infected tissues, express GzmB, but fail to upregulate IFNγ (13). Stromal cells within *L. major*–infected ears uniformly upregulated NKG2DLs, which rendered them susceptible to NKG2D-mediated killing (12, 13). NK cell depletion did not alter pathology, whereas CD8$^+$ T cell depletion and/or NKG2D blockade dramatically reduced tissue pathology (12, 13). The notion that bystander-activated CD8$^+$ T_{mem} use NKG2D to kill target cells in a manner similar to NK cells somewhat blurs the adaptive-innate dichotomy, but NK cells and bystander-activated CD8$^+$ T_{mem} appear to have distinct roles because bystander-activated CD8$^+$ T_{mem} were the main driver of NKG2D-dependent pathology in context of chronic infection (13) and responsible for NKG2D-dependent early pathogen control following acute infection (3).

Similar to chronic infections, bystander-activated CD8$^+$ T_{mem} are also implicated in contributing to pathology in autoimmune diseases. The signals that drive bystander activation may be different in these scenarios. Pathologically high levels of IL-15 are found in affected tissues from patients with celiac disease (40, 71) and RA (72, 73), among other autoimmune disorders [reviewed by Jabri and Abadie (74)]. This IL-15 exposure dually enhances the direct cytotoxicity of bystander-activated CD8$^+$ T_{mem} by upregulating GzmB (75) as well as the NKG2D immunoreceptor (76), which is needed to eliminate NKG2DL-expressing targets. During high IL-15 exposure, the enhanced cytotoxic potential of bystander-activated CD8$^+$ T_{mem}, paired with aberrant expression of NKG2DL in affected tissues, biases for bystander-mediated cytopathies in celiac disease (40)

and RA (39). Although bystander-activated $CD8^+$ T_{mem} can kill NKG2DL-expressing targets and propagate autoimmune damage when exposed to pathologically high levels of inflammation, these proinflammatory cues must be maintained to sustain bystander activation. Withdrawal of bystander-activating cytokines can abrogate the cytolytic potential of bystander-activated $CD8^+$ T_{mem} in vitro (77), highlighting the critical role for IL-15 in this context.

1.6.2 Bystander $CD8^+$ T_{mem} and the tumor microenvironment.

Tumor micro-environments (TMEs) with a lymphocyte infiltrate are also a type of chronically inflamed tissue. Bystander $CD8^+$ T_{mem} infiltrate the TME, in which they can even outnumber tumor-specific T cells and may be distinguished from tumor Ag–specific cells via low CD39 expression (41, 78-80). Although murine tumor Ag–specific T cells within the TME are typically refractory to stimulation with cognate Ag and cannot be rescued by PD-1 blockade, bystander $CD8^+$ T_{mem} within the tumor maintain responsiveness, spared by their lack of tumor Ag specificity (81).

NKG2D-mediated killing by NK cells and IFNγ secretion by either tumor Ag–specific T cells and NK cells can contribute to solid tumor clearance (82, 83). Because bystander-activated $CD8^+$ T_{mem} can also employ these mechanisms, they could play a role in antitumor immunity. Indeed, recent mouse model studies demonstrate that bystander $CD8^+$ T_{mem} can contribute to tumor clearance once appropriately activated. Intratumoral injection of the cognate peptide Ag for bystander $CD8^+$ T_{mem} can elicit IFNγ production and limit tumor growth in vivo (84). Other studies demonstrate that bystander-activated $CD8^+$ T_{mem} can kill tumor cells in an Ag-independent manner in vitro (85-87). Bystander $CD8^+$ virtual T_{mem} become activated and upregulate GzmB upon exposure to tumor cells pretreated with chemotherapeutics that target DNA replication (88) and directly killed MHC class I–deficient targets in a GzmB-dependent manner in vitro (88). Of note, there is strong evidence that recognition of self-Ag/MHC is still required for bystander activation (89). Whether self-Ag/MHC is only required for activation or also to sustain effector function remains to be determined, but is particularly relevant for understanding the antitumor potential of bystander-activated T cells. Although the ability to leverage bystander-activated $CD8^+$ T_{mem} as a therapeutic modality may hinge on the subset and history of these cells (90), these data highlight the potential therapeutic promise of activated bystander $CD8^+$ T_{mem}. Furthermore, this underscores the importance of understanding the yet to be identified cues that permit and regulate bystander-mediated effector functions.

1.7 Open questions concerning $CD8^+$ T_{mem} bystander activation

It has been nearly 25 years since the language of inflammation was discovered as a mediator of $CD8^+$ T_{mem} function (5). But there is a significant outstanding question: is this phenomenon of bystander activation a bona fide biologic program or an immunologic accident? Answering this is challenging due to the ranging consequences of bystander activation for host (being neutral, beneficial, or detrimental in a context-dependent manner) and the contexts in which it has been studied (36, 37, 55). Bystander activation has been most described during profound inflammation (that is systemic and/or chronic). Here, the pro-inflammatory cues are so abundant that often peripheral $CD8^+$ T_{mem} become bystander activated, which is not reflective of most infections in which inflammation is acute and remains localized. This raises multiple questions: is bystander activation even possible when inflammation is limited (either in dose and/or anatomic location)? Untangling this will provide better insight into the biologic rationale of bystander activation, should it be conserved even in limited inflammation, as well as identify the circumstances in which bystander activation could augment host health.

Though the purpose of bystander activation remains unclear, recent discoveries have dispelled the notion that bystander activation is without consequence. Indeed, bystander-activated $CD8^+$ T_{mem} can kill in indirect and direct manners. Curiously, the direct method of killing predicates close contact between bystander-activated $CD8^+$ T_{mem} and target cells, so that NKG2D–NKG2DL engagement can occur (3, 11, 13). Does this happen by passively (i.e., by chance encounter of NKG2DL-expressing cells or activating bystander $CD8^+$ T_{mem} near targets) or are there active mechanisms to draw bystander-activated $CD8^+$ T_{mem} to their prey? While the former could explain the off-target bystander-mediated pathologies observed during profound inflammation, the latter could suggest a yet-appreciated role of bystander-activated $CD8^+$ T_{mem}.

There is a degree of similarity in the outcomes of TCR-activated and bystander-activated $CD8^+$ T_{mem}; yet it is thus far limited to proliferation and cytotoxicity. But TCR engagement is responsible for other T cell fates, contingent on the frequency of TCR engagement and/or other cell extrinsic signals. These include T cell exhaustion (from chronic TCR agonism) (81) or tissue residence (from receptors upregulated after TCR engagement) (91, 92). Can other T_{mem} fates be dictated by inflammation sans TCR agonism? To our knowledge, there is little information regarding the phenotypic and fate consequences of bystander activation.

Despite the many unknowns of bystander activation, there is evidence that many—if not most—subpopulations of $CD8^+$ T_{mem} are capable of bystander activation. Thus, this population is lucrative to wield therapeutically to enhance immune responses to pathogen or tumor. But bystander-activated $CD8^+$ T_{mem} are a double-edged sword. The same effector functions that can be leveraged to clear pathogen are those which cause cytopathies when left unchecked (36). Although inflammation is the common denominator to bystander activation, it is less clear if there are programs that can keep bystander-activated $CD8^+$ T_{mem} in check. Is bystander activation terminated by cessation of inflammation alone, or do other regulatory mechanisms exist? Understanding these regulatory pathways are critical, as they could be used to blunt bystander-mediated autoimmune pathologies, or conversely inhibited to enhance target killing in tumor or infection.

The goals of this dissertation are to address these questions, specifically: 1) when and where bystander activation occurs during acute, localized infections, 2) how bystander-mediated killing is spatially coordinated, 3) if non-cytotoxic cell programs are also elicited by bystander activation, 4) how tissue microenvironments shape bystander activation, and 5) do programs exist which attenuate bystander-activated $CD8^+$ T_{mem} functions.

Chapter 2. CXCR3 enables recruitment and site-specific bystander activation of CD8$^+$ T_{mem}

Maurice NJ, McElrath MJ, Andersen-Nissen E, Frahm N, Prlic M. CXCR3 enables recruitment and site-specific bystander activation of memory CD8$^+$ T cells. *Nat Commun.* 2019 Nov 1;10(1):4987. DOI: 10.1038/s41467-019-12980-2

Maurice NJ, Taber AK, Prlic M. The Ugly Duckling Turned to Swan: A Change in Perception of Bystander-Activated Memory CD8 T Cells. *J Immunol.* 2021 Feb 1;206(3) 455-462. DOI: 10.4049/jimmunol.2000937

Bystander activation of memory T cells occurs in the absence of cognate antigen during infections that elicit strong systemic inflammatory responses, which subsequently affect host immune responses. Here we report that memory T cell bystander activation is not limited to induction by systemic inflammation. We initially observe potential T cell bystander activation in a cohort of human vaccine recipients. Using a mouse model system, we then find that CD8$^+$ T_{mem} are specifically recruited to sites with APCs in a CXCR3-dependent manner. In addition, CXCR3 is also necessary for T cell clustering around APCs and T cell bystander activation, which temporospatially overlaps with the subsequent antigen-specific T cell response. Our data thus suggest that bystander activation is part of the initial localized immune response and is mediated by a site-specific recruitment process of memory T cells.

2.1 Background

The main purpose of memory T cells is to rapidly respond when antigen (Ag) is re-encountered, however memory T cells can also be activated in an inflammation-dependent, but Ag-independent manner (3, 5, 7, 9-11, 22, 25, 32). This phenomenon is referred to as bystander activation and has been reported in the context of acute and chronic infections in the mouse model system (34) as well as in humans, including chronic HCV infection (93), acute and chronic HIV infection (23, 94) , acute EBV infection (25), and acute HAV infection (11). Given that memory T cell bystander activation has been reported in context of these infections that are either systemic in nature or have systemic inflammatory effects, memory T cells seemingly become bystander-activated in a passive manner by responding to systemically available inflammatory cues.

Once bystander-activated, $CD8^+$ T_{mem} acquire an effector T cell-like phenotype, including expression of GzmB (3, 22, 25) , and IFNγ (7, 9, 10). The biological significance of acquiring cytotoxic effector function in the absence of cognate Ag was long unclear, until it was shown that bystander-activated $CD8^+$ T_{mem} are capable of direct cytolysis of target cells (3, 11, 13). Direct target cell killing depends on NKG2D (expressed on memory T cells)—NKG2D ligand (a family of stress-induced proteins) interactions, which was first demonstrated in a mouse model system (3) and more recently also shown using human T cells (11). Importantly, this innate-like recognition of target cells does not appear to be nearly as efficient as T cell receptor (TCR)-mediated target cell killing (3) but the consequences for the host are still significant given the large number of memory T cells and their ability to produce other effector molecules such as IFNγ (3, 7, 34, 36, 95). Bystander activation of T cells can be beneficial to the host as these cells contribute to early pathogen clearance (3, 7, 32). However, bystander-activated T cells have also been shown to drive pathogenesis in the context of chronic infections (12, 13, 34). Thus, bystander-activated T cells appear to be a double-edged sword with benefits for the host when activation is brief (early pathogen control during acute infection) and detrimental when activation is persistent (tissue damage during chronic infections). This includes IL-15-driven differentiation of T cells into an NK-like cell type during Celiac disease (40).

There is a key role for IL-12, IL-15, and IL-18 in activating memory T cells and a central role for IFNγ in orchestrating the subsequent immune response (9). Given the systemic nature of most infections studied so far, the existence of signals that could potentially recruit memory T cells to more localized sites of inflammation have not been investigated. Interestingly, recent data suggested that bystander activation may also occur when inflammation is localized, such as the tumor microenvironment with a T cell infiltrate consisting of tumor-specific and nonspecific T cells (41). The mechanisms that would allow bystander activation of memory T cells in such a scenario and the biological consequences of bystander activation are unclear.

Bystander activation of $CD8^+$ T_{mem} occurs in the presence of systemic inflammation, presumably because memory T cells are exposed to available inflammatory cytokines. Using samples from a human vaccine trial we find evidence that suggests bystander activation of $CD8^+$ T_{mem} may also occur shortly after vaccination. We use a mouse model to follow-up on this observation in an effort to determine whether and how bystander activation of $CD8^+$ T_{mem} can occur in the context of spatially localized inflammation. We demonstrate that bystander activation during localized inflammation hinges on the ability of $CD8^+$ T_{mem} to rapidly migrate to sites of early immune

activation in a CXCR3-dependent manner. Thus, our data suggest that memory T cell bystander activation is not a passive event limited to scenarios where inflammatory cues are widely available as shown so far, but an active, migration-driven process. Importantly, at least some bystander-activated T cells remain located at these immune activation sites for days and temporally and spatially overlap with incoming Ag-specific T cells. We discuss the relevance of these bystander-activated T cells as the result of a localized and site-specific recruitment process for memory T cells for the subsequent host immune response.

2.2 Results

2.2.1 Evidence of bystander activation following vaccination

We initially asked if we could detect any evidence of bystander activation of $CD8^+$ T_{mem} in a human cohort following immunization with a live-attenuated vaccine. We analyzed the activation profile of human immune cells isolated from peripheral blood mononuclear cells (PBMCs) immediately prior to and 3 days after intra-muscular (i.m.) immunization with a modified vaccinia Ankara (MVA) vector using samples of the HIV Vaccine Trial Network (HVTN) 908 clinical trial (Figure 2.1A, B) (96, 97). We found that memory ($CD45RO^+$) $CD8^+$ T cells displayed significantly increased median fluorescence intensities (MedFI) for GzmB in MVA/HIV62 but not placebo recipients (Figure 2.1C, E). Importantly, $CD8^+$ T_{mem} (bulk or $GzmB^+$) did not show increased expression of markers indicative of recent TCR signaling, such as 4-1BB (98) or PD-1 (99) (Figure 2.1F–H). Similarly, mucosal-associated invariant T (MAIT) cells can also be bystander-activated (45, 100, 101) and showed a significant increase in CD69 expression, indicating that an i.m. administered vaccine may be sufficient to activate cells in an inflammation-dependent manner (Figure 2.1I). We next used a mouse model system to determine if bystander activation can occur as a result of localized inflammation.

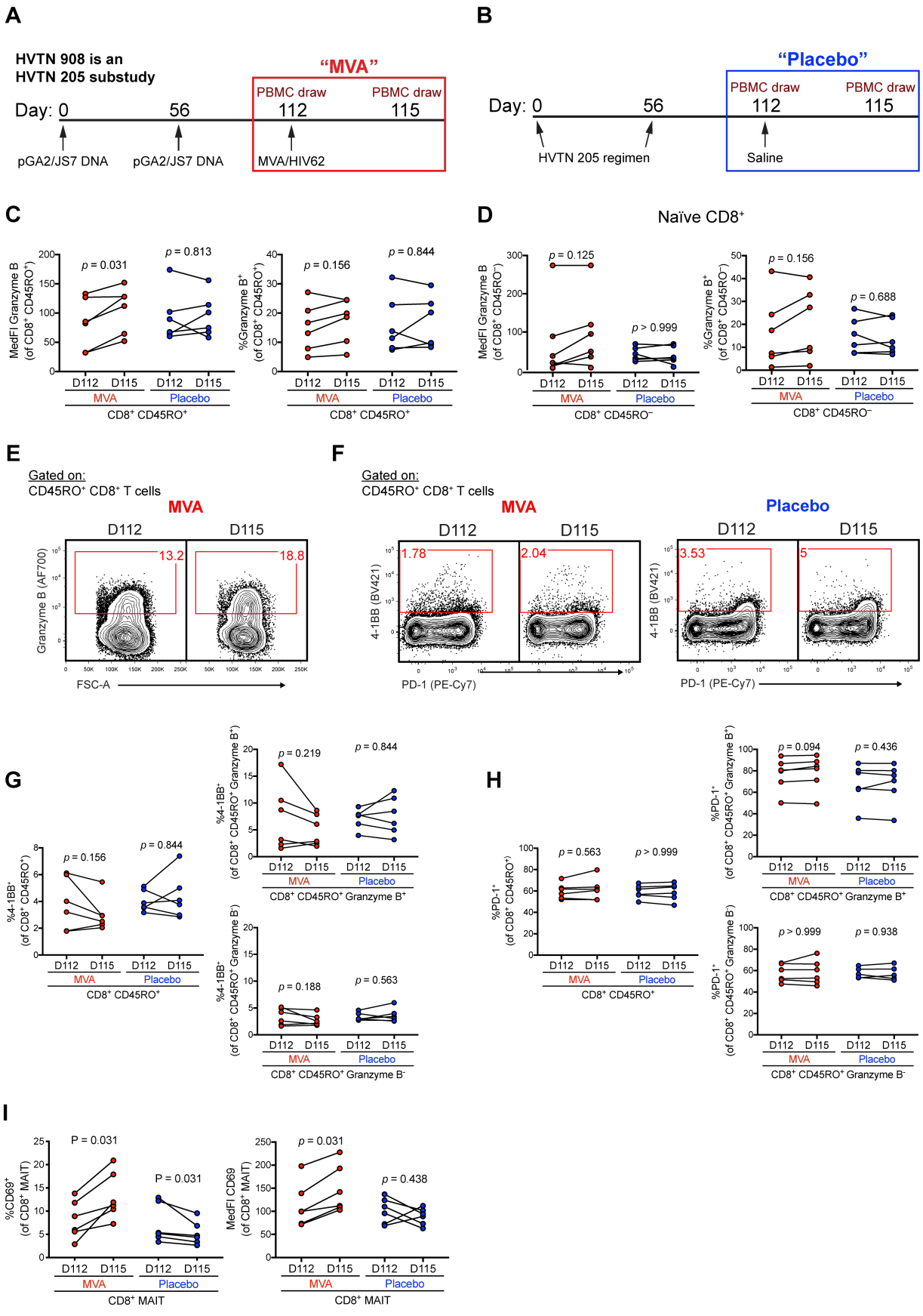
A
HVTN 908 is an
HVTN 205 substudy
"MVA"
PBMC draw
PBMC draw
Day: 0
56
112
115
pGA2/JS7 DNA
pGA2/JS7 DNA
MVA/HIV62
B
"Placebo"
PBMC draw
PBMC draw
Day: 0
56
112
115
HVTN 205 regimen
Saline
C
MedFI Granzyme B (of CD8+ CD45RO+)
p = 0.031
p = 0.813
%Granzyme B+ (of CD8+ CD45RO+)
p = 0.156
p = 0.844
D112 D115 D112 D115
MVA Placebo
CD8+ CD45RO+
D
Naïve CD8+
MedFI Granzyme B (of CD8+ CD45RO−)
p = 0.125
p > 0.999
%Granzyme B+ (of CD8+ CD45RO−)
p = 0.156
p = 0.688
CD8+ CD45RO−
E
Gated on:
CD45RO+ CD8+ T cells
MVA
D112
D115
Granzyme B (AF700)
13.2
18.8
FSC-A
F
Gated on:
CD45RO+ CD8+ T cells
MVA
Placebo
D112
D115
4-1BB (BV421)
1.78
2.04
3.53
5
PD-1 (PE-Cy7)
G
%4-1BB+ (of CD8+ CD45RO+)
p = 0.156
p = 0.844
CD8+ CD45RO+
%4-1BB+ (of CD8+ CD45RO+ Granzyme B+)
p = 0.219
p = 0.844
CD8+ CD45RO+ Granzyme B+
%4-1BB+ (of CD8+ CD45RO+ Granzyme B-)
p = 0.188
p = 0.563
CD8+ CD45RO+ Granzyme B-
H
%PD-1+ (of CD8+ CD45RO+)
p = 0.563
p > 0.999
CD8+ CD45RO+
%PD-1+ (of CD8+ CD45RO+ Granzyme B+)
p = 0.094
p = 0.436
CD8+ CD45RO+ Granzyme B+
%PD-1+ (of CD8+ CD45RO+ Granzyme B-)
p > 0.999
p = 0.938
CD8+ CD45RO+ Granzyme B-
I
%CD69+ (of CD8+ MAIT)
P = 0.031
P = 0.031
CD8+ MAIT
MedFI CD69 (of CD8+ MAIT)
p = 0.031
p = 0.438
CD8+ MAIT

Figure 2.1 Evidence for bystander activation of human CD8$^+$ T$_{mem}$ following vaccination

A, **B** Immunization schematics for HVTN 908 "Early Immune Responses to Vaccination," a substudy to HVTN 205 (see Methods). **A** In HVTN 908, some participants of the HVTN 205 trial received a boost with an MVA vector (day 112). We interrogated PBMC samples collected immediately prior to the MVA boost or saline placebo (day 112) and on day 3 post MVA-immunization (day 115) to determine if we could detect any CD8$^+$ T$_{mem}$ with a phenotype indicative of bystander-activation. **B** The HVTN 908 clinical trial design included a cohort receiving saline instead of the MVA vector and PBMCs from this placebo cohort were included in our sample analysis (we were blinded until flow cytometry data were acquired and analyzed). The samples from this placebo cohort served as an important control for potential batch effects between day 112 and day 115 samples to ensure that we could distinguish differences in biology from differences that may be technical in nature (for example, differences that could be introduced in sample processing, etc.). **C-I** Flow cytometric phenotyping of PBMC subsets in HVTN 908. **C** Granzyme B expression (median fluorescence intensity (MedFI) and frequency) in CD45RO$^+$ CD8$^+$ T cells (i.e., CD8$^+$ T$_{mem}$). **D** Granzyme B MedFI and frequency in CD45RO$^-$ CD8$^+$ T cells (i.e., naïve CD8$^+$ T cells). **E** Representative granzyme B staining in CD45RO$^+$ CD8$^+$ T cells. **F** Representative staining of PD-1 (x-axis) and 4-1BB (y-axis) in CD45RO$^+$ CD8$^+$ T$_{mem}$. **G** 4-1BB or **H** PD-1 frequency of bulk, GzmB$^+$, and GzmB$^-$ CD45RO$^+$ CD8$^+$ T$_{mem}$. **I** Frequency and MedFI of CD69 in CD8$^+$ MAIT cells. In **C**, **D**, **G**, **I** each symbol represents one donor at one timepoint (n = 6 MVA vaccine recipients, n = 6 placebo recipients). Connected symbols are from the same donor; all samples were stained and analyzed at once. Indicated are statistical significances by Wilcoxon matched-pairs signed rank test. Staining panels and gating strategies are respectively provided in Table 2.1 and Figure 2.21.

2.2.2 Ag-nonspecific T cells cluster at sites of early immune activation

We wanted to visualize where and how early bystander activation occurs in spatial relation to activated APCs and Ag during the nascent stages of a localized immune response. To develop a traceable population of CD8$^+$ T$_{mem}$ with defined Ag-specificity, we adoptively transferred naive, congenically marked OT-I CD8$^+$ T cells, which express a TCR that recognizes the SIINFEKL peptide of chicken egg ovalbumin (OVA), into wild-type (WT) C57BL/6J recipients (Figure 2.2A). We subsequently infected recipient mice with OVA-expressing vesicular stomatitis virus (VSV-OVA). This acute infection provides cognate Ag and inflammatory cues to generate effector OT-I T cells, which then contracted into a stable pool of memory OT-I T cells 60 days post infection (referred to as OT-I memory mice) (102). As our main goal was to interrogate how T$_{mem}$ become activated in a localized manner, we tested several low-dose immunization strategies with *actA*$^-$ and wild-type (WT) *Listeria monocytogenes* (LM). OT-I T cells are not activated by any *Listeria*-derived Ags (3), thus any augmentation of OT-I T cell function would be due to inflammation-driven bystander effects (Figure 2.2B, Figure 2.4A). We immunized OT-I memory mice with 10^6 colony forming units (cfu) *actA*$^-$ LM to mimic the live-attenuated human MVA vaccine. However, within 24 h of immunization with *actA*$^-$ LM nearly all white pulps (WP) in the

spleen stained positive for LLO and were enriched for memory OT-I T cells (Figure 2.4B). A further titration in dose did not alleviate this problem, so this approach was not suitable to examine site-specific bystander activation of memory T cells. We next immunized mice with 1000 cfu of WT LM. This low challenge dose initially resulted in a very localized infection as infected APCs migrate to the periarteriolar lymphoid sheath inside the splenic WP within 6–12 hours (103-105) and was thus ideal to determine whether bystander activation only occurred passively with memory T cells close to infected/activated APCs or was the result of site-specific recruitment of memory T cells.

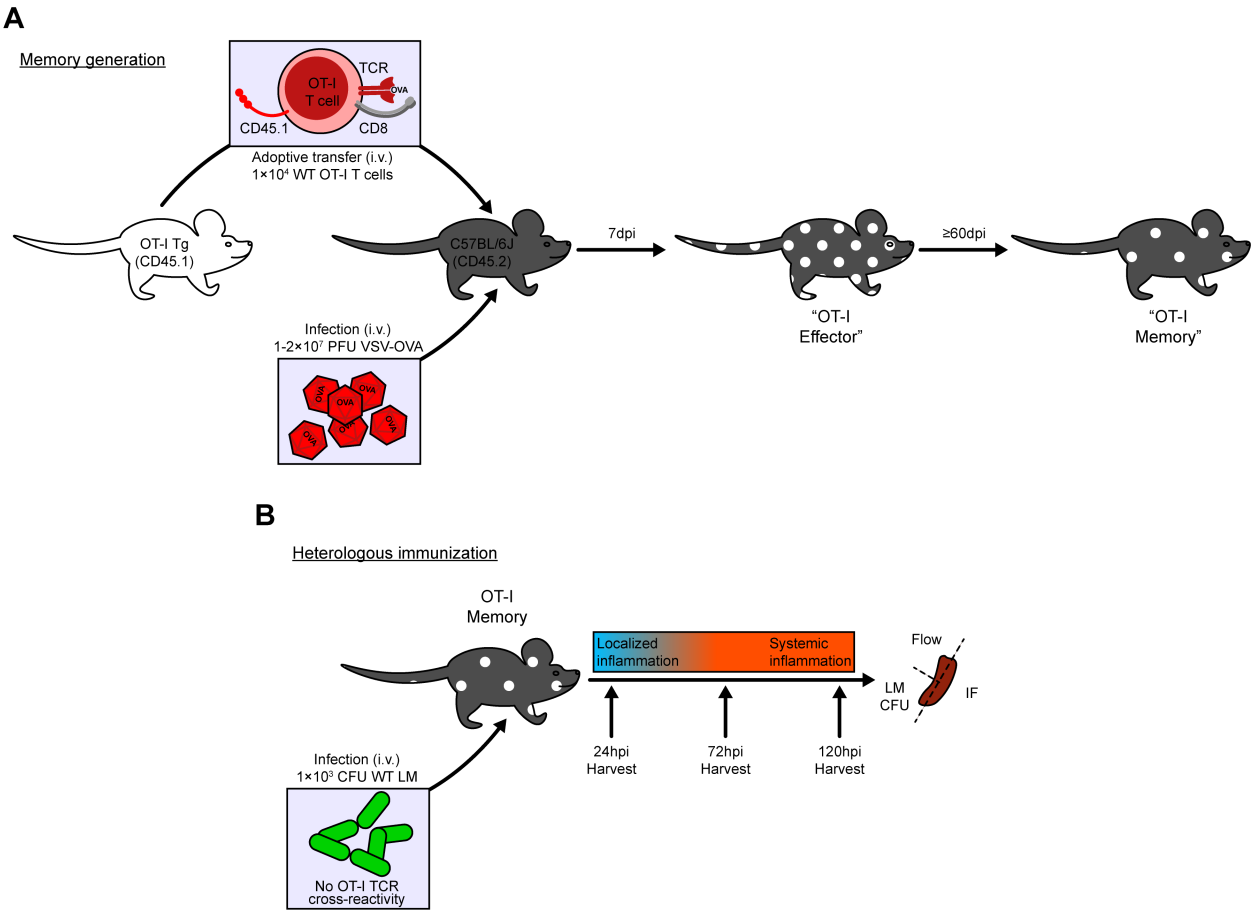

Figure 2.2 OT-I transgenic model of CD8⁺ T_{mem} bystander activation

A Schematic of OT-I T cell adoptive transfer and subsequent memory OT-I T cell generation via VSV-OVA infection. **B** Schematic of (bystander activating) WT LM immunization and subsequent tissue sampling.

We examined the distribution of splenic OT-I T cells in situ using immunofluorescence (IF) of whole-spleen sections (Figure 2.3A–F, Figure 2.4C, D). Using antibodies against CD45.1, Listeriolysin O (LLO), and CD169, we respectively stained for congenically marked OT-I cells, LM Ag, and marginal zone metallophilic macrophages (MMM). $CD169^+$ MMM border the splenic white pulp (WP), delineating areas of WP and red pulp (RP) (106). Immunization with WT LM led to foci of LM Ag in a limited number of WP in the spleen (Figure 2.3C, D) and OT-I T cells formed dense clusters bordering specifically at sites that stained positive for LM Ag. These OT-I T cells appeared to cluster in a manner strikingly similar to day 7 (Ag-specific) effector cells (Figure 2.3C–F). We employed a digital pathology software, HALO, to enumerate OT-I T cells within the splenic RP, WP (both as a whole or stratified by LM Ag staining) in an unsupervised manner (Figure 2.3G, H). Although WT LM immunization did not globally alter OT-I T cell density from that in unimmunized control animals (Figure 2.4C), the density of OT-I T cells was significantly increased in WP foci that stained for LM Ag versus those that were negative for LM Ag (Figure 2.3H). This suggests that the transient bystander activation of memory T cells (Figure 2.4E, F) early after immunization is not a consequence of being merely close to activated APCs, but instead T_{mem} appeared to actively migrate toward activated APCs. We next wanted to define how this may happen and discern migration from proliferation-driven effects.

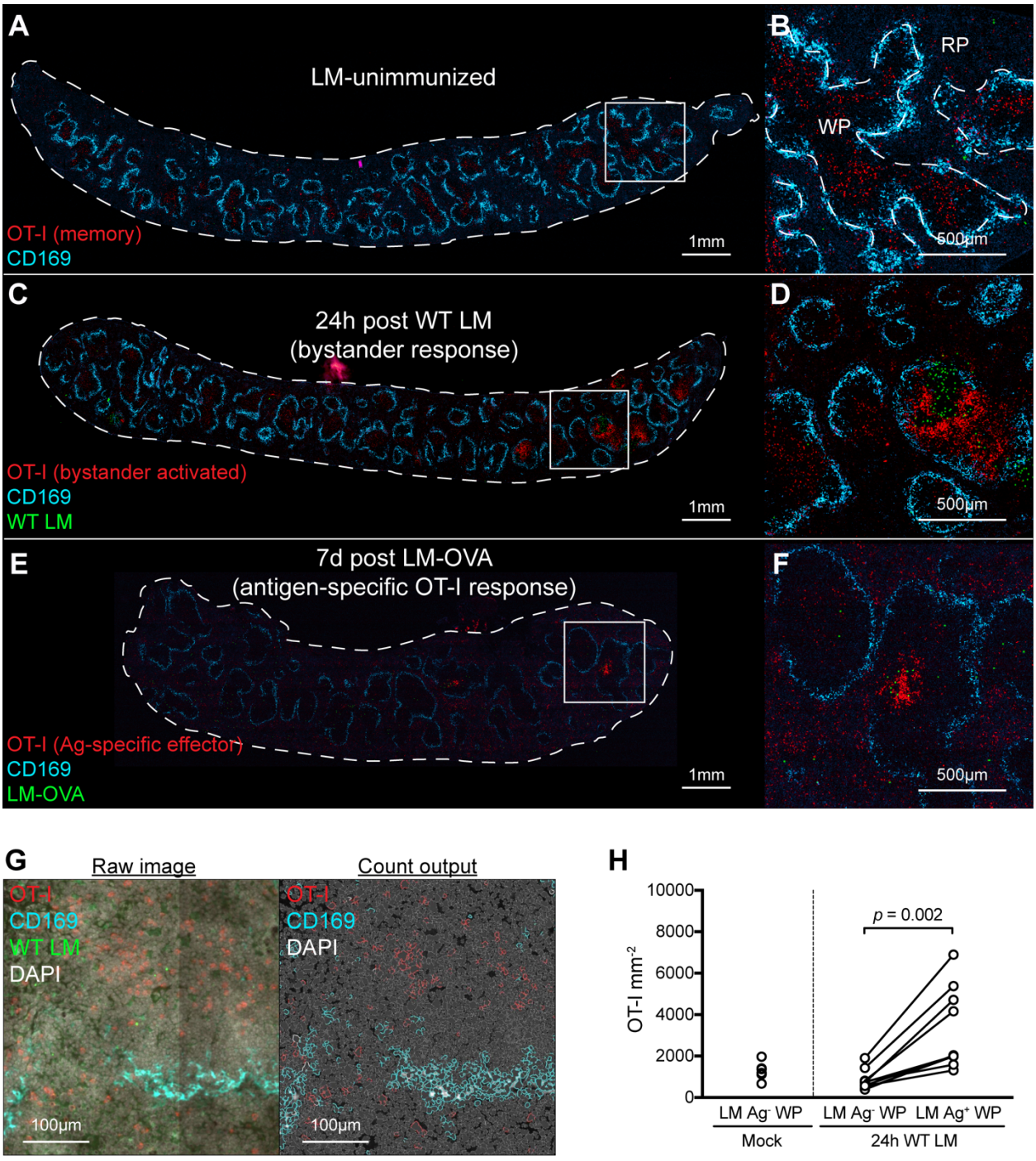

Figure 2.3 CD8⁺ T_{mem} densely cluster at sites of early immune activation

A–**F** Representative 8 μm, whole-spleen sections showing OT-I (red), marginal zone metallophilic macrophages (MMM) (cyan), and LM Ag (green). **A** Whole-spleen section and magnified selection **B** from LM-unimmunized OT-I memory mouse. **C** Whole-spleen section and magnified selection **D** from OT-I memory mouse 24 h post WT LM (bystander-activating) immunization. **E** Whole-spleen section and magnified selection **F** from animal 7 days post OT-I transfer and LM-OVA immunization, showing OT-I effector (Ag-specific) response. **G** Raw IF

images showing OT-I (red), MMM (cyan), LM Ag (green), and DAPI (gray), and cell identity outputs used for cell enumeration (OT-I, red; MMM, cyan; co-staining, white; nuclei, gray) from HALO digital pathology software. **H** Splenic OT-I T cell densities from WT LM Ag-positive and -negative WP as enumerated from HALO-analyzed IF images. In **A**–**F** image contrast of single-channel images was increased using Adobe Photoshop equally across all samples prior to layer compilation. Pixel size for LM Ag channels was doubled to increase visibility using Adobe Photoshop. **A**, **B** Is representative of $n = 6$ mice. **C**, **D** is representative of $n = 10$ mice. **E**, **F** is representative of $n = 3$ mice. In **H** each individual symbol (mock immunization) or connected symbol pair (24 h post WT LM immunization) represents one animal from 3 experiments ($n = 6$ mock-immunized, $n = 10$ WT LM-immunized). Indicated are statistical significances by Wilcoxon matched-pairs signed rank test.

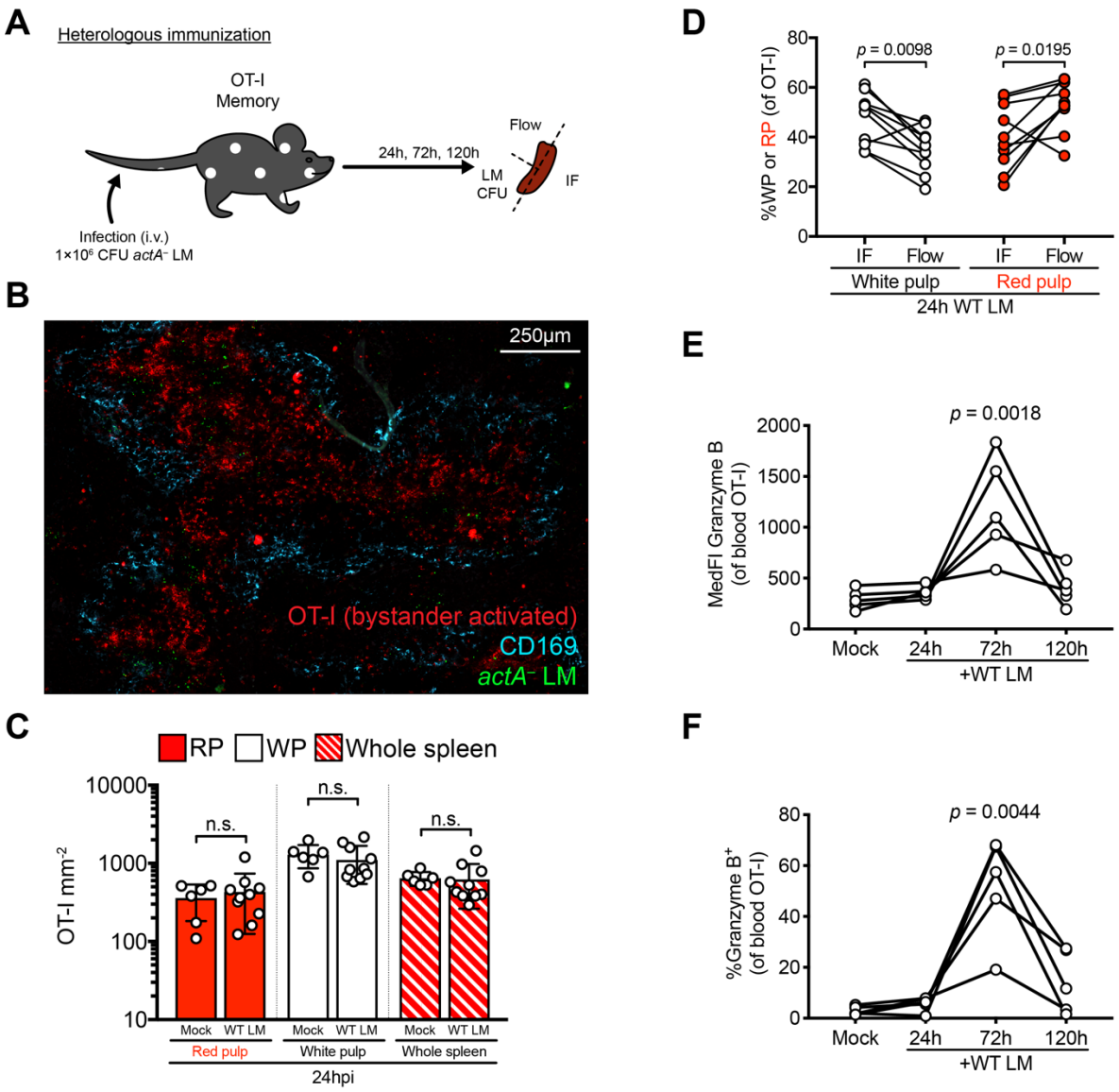

Figure 2.4 CD8⁺ T_{mem} clustering precedes systemic inflammation and bystander activation.

A Overview of *actA*⁻ LM immunization and tissue sampling. **B** Representative image of LM Ag and OT-I clustering at the splenic WP from *actA*⁻ LM-immunized mice 24 hours post infection. **C** OT-I densities within splenic compartments calculated from IF and HALO enumeration 24h post WT LM or mock immunization. **D** Frequency of WP and RP OT-I T cells detected by i.v. staining and flow cytometric analysis versus IF at 24h post WT LM infection. **E**–**F** GzmB (**E**) MedFI and (**F**) frequency in blood OT-I cells 24, 72, and 120 hours after WT LM immunization. **B** is representative of *n* = 3 spleens. In **C** each symbol represents one compartment from one mouse across 4 experiments (*n* = 10 WT LM immunized; *n* = 6 unimmunized), summaries shown are mean ± SD; indicated are statistical significances by Mann-Whitney test with α = 0.05. In **D** each connected symbol pair represents one compartment from one mouse across 3 experiments (*n* = 10). Indicated are statistical significances by Wilcoxon matched-pairs signed rank test. In **E** and **F** each symbol represents 2-5 animals concatenated from the same technical replicate (replicate

n = 5). Symbols are connected by matching replicate. Indicated are statistical significances with adjusted *p* values < 0.05 by Dunn's multiple comparison test against mock-immunized events.

2.2.3 Early bystander-activated CD8$^+$ T_{mem} clusters are Ki-67 negative

Using the same experimental setup, we next confirmed that OT-I T cells near splenic LM Ag foci were truly bystander-activated (i.e., GzmB$^+$) using IF. We simultaneously assayed for the expression of Ki-67, a marker indicative of cellular proliferation, to determine whether the increased density of OT-I T cells resulted from OT-I replication. Within 24 h of WT LM immunization, clustering OT-I T cells predominantly contained cytotoxic molecules and were thus bystander-activated (Figure 2.5A–E). Despite this, clustering OT-I T cells did not show Ki-67 staining (Figure 2.5A, B), suggesting OT-I T cell enrichment results from recruitment. OT-I T cells from LM-uninfected animals displayed minimal GzmB staining (Figure 2.6A, B). We again employed HALO digital pathology software to enumerate Ki-67$^+$ and granzyme B$^+$ OT-I T cells within WP that stained positive or negative for LM Ag (Figure 2.5C). The density of Ki-67$^+$ OT-I T cells remained unchanged between LM Ag-positive and -negative WPs (Figure 2.5F); but the density of GzmB$^+$ cells was highly elevated within WP containing detectable LM Ag (Figure 2.5D), with approximately half of the memory OT-I T cells expressing GzmB within these foci (Figure 2.5E). Thus, bystander-activated cells capable of killing are most enriched at sites in close proximity to activated APCs and Ag early after immunization. To ensure that this phenomenon is not limited to TCR transgenic memory T cells, we next sought to determine whether endogenous CD8$^+$ T_{mem} are also initially bystander-activated in a locally restricted manner.

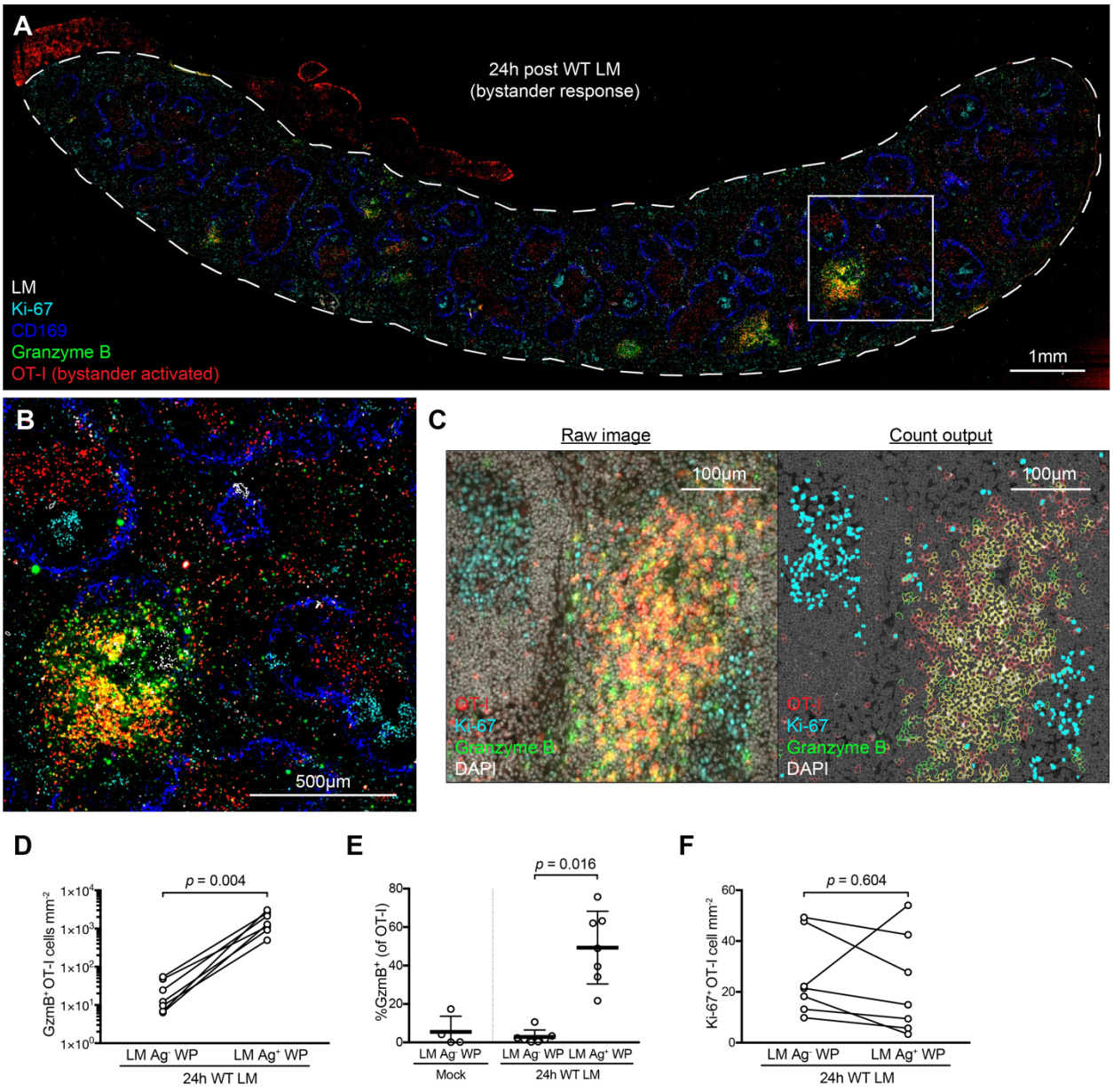

Figure 2.5 Bystander-activated OT-I T cells form clusters without proliferating.

A, **B** Representative image of spleen 24 h post WT LM immunization from serially-sectioned 8μm slides stained for LM (white), CD169$^+$ MMM (blue), OT-I T cells (red), GzmB (green), and Ki-67 (cyan). **C** Raw IF images showing OT-I T cells (red), Ki-67 (cyan), GzmB (green), and DAPI (grey), and cell identity outputs used for cell enumeration (OT-I T cells, red; GzmB, green; OT-I and GzmB co-staining, yellow; Ki-67$^+$ nuclei, cyan; Ki-67$^-$ nuclei, grey) from HALO digital pathology software. **D**–**F** Enumeration of cell densities and frequencies from HALO-analyzed images. **D** Density of GzmB$^+$ OT-I T cells amongst splenic WP stained for the absence (LM Ag$^-$) or presence (LM Ag$^+$) of WT LM 24 h after immunization. **E** Frequency of GzmB expression in OT-I T cells within WP from unimmunized animals (Mock) and WP from animals 24 h post WT LM immunization (24 h WT LM), stratified by the presence of LM Ag. **F** Density of Ki-67$^+$ OT-I T cells amongst splenic WP absent or containing LM Ag 24 h after WT LM immunization. In **A**, **B** image is representative of $n = 7$ spleens. Contrast was increased and tissue orientation was modified in

Adobe Photoshop to overlay serially sectioned slides. LM Ag staining was outlined to increase visibility using “find edges” in ImageJ; after, all channels were merged using ImageJ. In **D**–**F** each symbol (mock immunization) or connected symbol pair (24 h post WT LM immunization) represents one animal from three experiments ($n = 4$ mock-immunized, $n = 7$ WT LM-immunized). Indicated are statistical significances by Wilcoxon matched-pairs signed rank test.

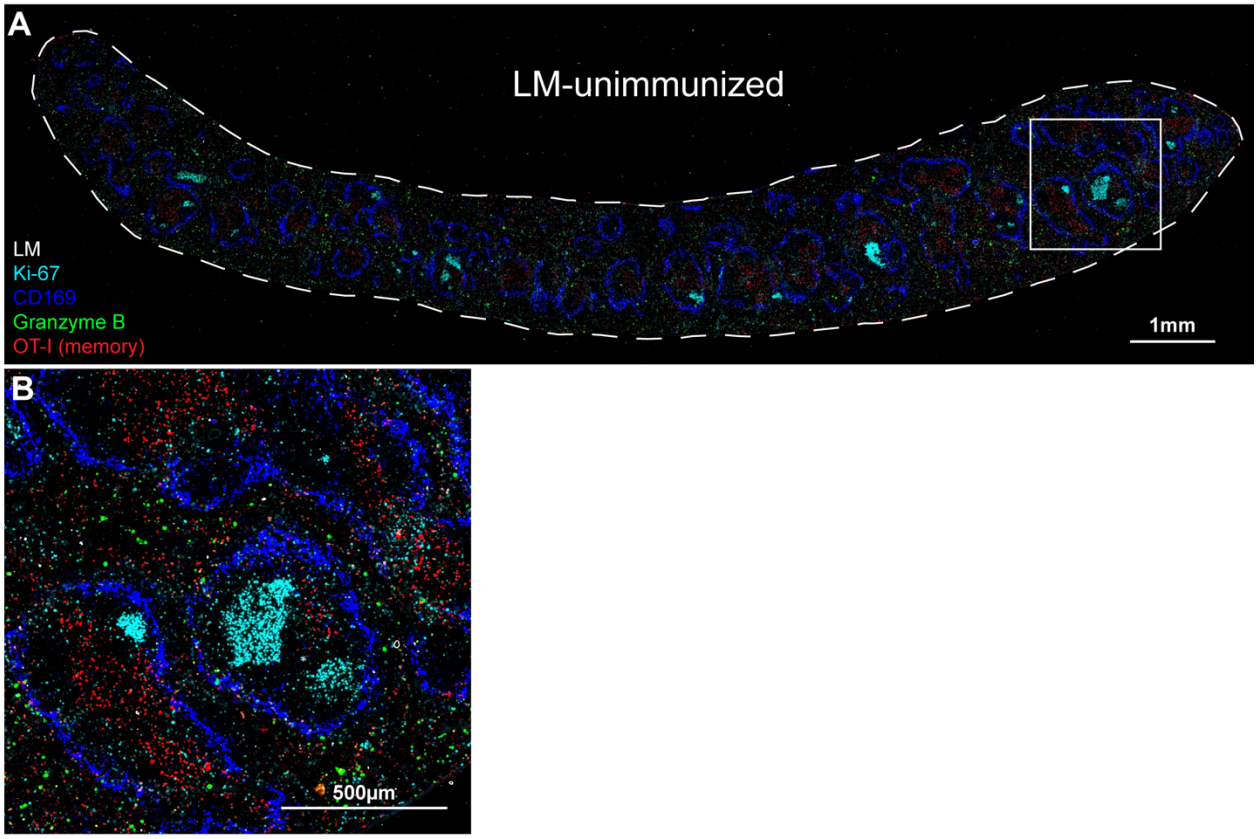

Figure 2.6 Ki-67 and GzmB staining in spleens from LM-unimmunized OT-I memory mice

A, **B** Representative image of LM-unimmunized spleen from serially sectioned 8µm slides stained for geographic markers: LM (white) and MMM (blue); and OT-I phenotyping: OT-I (red), GzmB (green), and Ki-67 (cyan). In **A**, **B** image contrast was increased at an equal level as in Fig. 2.6 and tissue orientation was modified in Adobe Photoshop to overlay serially sectioned slides. All channels were merged and LM staining was outlined using “find edges” to increase visibility using ImageJ. Image is representative of ($n = 4$).

2.2.4 Bystander activation of endogenous CD8$^+$ T$_{mem}$

As bystander activation occurred in the WP of the spleen, we employed intravenous (i.v.) labeling of CD8β to distinguish OT-I and endogenous CD8$^+$ T cells located in the splenic WP vs. RP by flow cytometric analysis (Figure 2.7A) (107, 108). In vivo i.v. labeling of CD8β resulted in uniform

staining of cells in circulation and limited staining of cells within lymphoid structures (i.e., lymph node (LN) and splenic WP); as the RP of the spleen is circulatory in nature, we identified CD8β$^+$ splenocytes as those within the RP using both IF and flow cytometry (Figure 2.7B, C). From our flow cytometric analyses, we interrogated the expression of effector molecules, GzmB and IFNγ, in OT-I and bulk endogenous CD8$^+$ T_{mem} from the splenic RP and WP (Figure 2.7D, E). Mirroring our IF data, we observed that 24 h after WT LM immunization, a greater frequency of bystander-activated (i.e., GzmB$^+$) OT-I T cells were detected in the WP versus the RP (Figure 2.7E). This bias for bystander-activated OT-I T cells within the WP was present at later time points but peaked 72 h post immunization (Figure 2.7E, Figure 2.8A). In contrast, the GzmB response of bulk endogenous CD8$^+$ T cells did not mount until 120 h post immunization, likely reflecting the Ag-specific immune response to WT LM (Figure 2.7E, Figure 2.8A). Transient IFNγ production was observed in WP OT-I T cells 24 h post immunization, coinciding with initial OT-I T cell clustering (Figure 2.7E, Figure 2.8B). In concurrence with our IF data, Ki-67 expression was not increased in WP or RP OT-I T cells until later timepoints (Figure 2.8C, D). To ensure that the bystander responses were not a feature unique to transgenic OT-I T cells, we measured GzmB and IFNγ responses in endogenous CD8$^+$ T_{mem}, which were identified via NKG2D expression (Figure 2.7F, G) (109). Much like OT-I T cells, endogenous CD8$^+$ T_{mem} had similar GzmB and IFNγ kinetics (Figure 2.7H, Figure 2.8A–C). The majority of IFNγ-producing cells within the WP 24 h post immunization, whether OT-I or endogenous CD8$^+$ T_{mem}, were predominantly GzmB$^+$ (Figure 2.7G). The magnitude of GzmB responses 24 h post immunization was directly correlated with the magnitude of the IFNγ responses in both endogenous CD8$^+$ and OT-I T_{mem} (Figure 2.7I). Furthermore, at 24 h post immunization, the magnitude of the IFNγ and GzmB responses in endogenous CD8$^+$ T_{mem} mirrored the response magnitudes in their OT-I counterparts (Figure 2.7J), which remained significant at 72 h post immunization, but not at 120 h post immunization (Figure 2.8E, F). We found that splenic IFNγ expression 24 h post immunization strongly correlated with splenic IL-12 levels (Figure 2.7K, L) and next used IF to determine the magnitude and site-specific manner of IFNγ production. In concordance with our flow cytometry data, IFNγ production was most pronounced in cell clusters surrounding LM Ag foci (Figure 2.7M). We leveraged IF staining NKG2D to identify the spatial orientation of endogenous CD8$^+$ T_{mem} and NK cells. Endogenous NKG2D$^+$ cells aggregate near LM Ag foci and upregulate GzmB (Figure 2.7N).

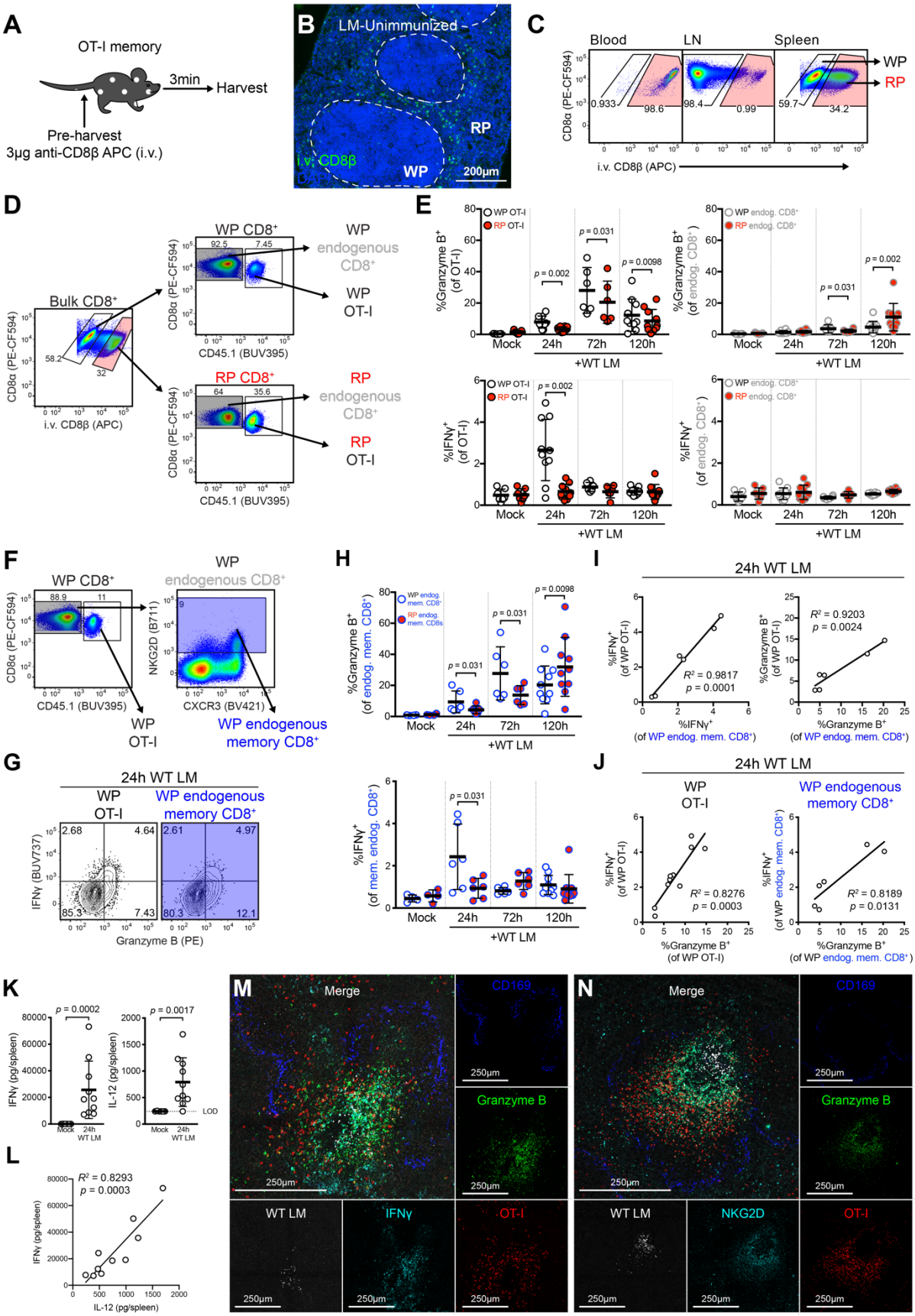
A
OT-I memory
3min
Harvest
Pre-harvest
3μg anti-CD8β APC (i.v.)
B
LM-Unimmunized
RP
WP
i.v. CD8β
DAPI
200μm
C
Blood
LN
Spleen
WP
RP
CD8α (PE-CF594)
i.v. CD8β (APC)
D
Bulk CD8⁺
WP CD8⁺
RP CD8⁺
WP endogenous CD8⁺
WP OT-I
RP endogenous CD8⁺
RP OT-I
CD45.1 (BUV395)
E
WP OT-I
RP OT-I
WP endog. CD8⁺
RP endog. CD8⁺
%Granzyme B⁺ (of OT-I)
%Granzyme B⁺ (of endog. CD8⁺)
%IFNγ⁺ (of OT-I)
%IFNγ⁺ (of endog. CD8⁺)
Mock
24h
72h
120h
+WT LM
F
WP CD8⁺
WP endogenous CD8⁺
NKG2D (B711)
CXCR3 (BV421)
WP OT-I
WP endogenous memory CD8⁺
G
24h WT LM
IFNγ (BUV737)
Granzyme B (PE)
H
WP endog. mem. CD8⁺
RP endog. mem. CD8s
%Granzyme B⁺ (of endog. mem. CD8⁺)
%IFNγ⁺ (of mem. endog. CD8⁺)
I
24h WT LM
%IFNγ⁺ (of WP OT-I)
%Granzyme B⁺ (of WP OT-I)
%IFNγ⁺ (of WP endog. mem. CD8⁺)
%Granzyme B⁺ (of WP endog. mem. CD8⁺)
J
24h WT LM
WP OT-I
WP endogenous memory CD8⁺
K
IFNγ (pg/spleen)
IL-12 (pg/spleen)
LOD
L
IFNγ (pg/spleen)
IL-12 (pg/spleen)
M
Merge
CD169
Granzyme B
WT LM
IFNγ
OT-I
N
Merge
CD169
Granzyme B
WT LM
NKG2D
OT-I

Figure 2.7 Endogenous $CD8^+$ T_{mem} are bystander activated in a localized manner

A Schematic for i.v. labeling of circulating $CD8^+$ cells. **B** Splenic IF for i.v.-labeled cells. **C** Representative flow staining of $CD8\alpha^+$ cells for i.v. CD8β from matched blood, lymph node (LN), and spleen. **D** Representative flow gating for red pulp (RP) and white pulp (WP) subsets within bulk endogenous $CD8^+$ T cells and OT-I T cells. **E** Frequencies of GzmB or IFNγ expressing OT-I or bulk endogenous $CD8^+$ T cells after WT LM immunization, subset by splenic compartment. **F** Representative flow gating for endogenous $CD8^+$ T_{mem} via NKG2D expression. **G** Representative flow plots demonstrating effector molecule production 24 h post immunization in OT-I (white) and endogenous $CD8^+$ T_{mem} (blue) from WP. **H** Frequency of $GzmB^+$ and $IFN\gamma^+$ endogenous $CD8^+$ T_{mem} within splenic RP and WP after immunization. **I**, **J** Comparison of (**I**) effector molecule expression between OT-I and endogenous $CD8^+$ T_{mem} or (**J**) GzmB expression versus IFNγ expression 24 h post immunization. **K** Luminex analysis of spleens 24 h after immunization for IFNγ (left) and IL-12p70 (right) and **L** comparison of IFNγ and IL-12p70 levels. **M**, **N** Representative IF from animals 24 h after immunization, overlaying two serial spleen sections stained for $CD169^+$ MMM (blue) and WT LM (white); and granzyme B (green), OT-I T cells (red), and (**M**) IFNγ or (**N**) NKG2D (cyan). In **E**, **H** each symbol represents one splenic tissue compartment from one mouse from three experiments ($n = 6$, 10, 7, and 10, respectively for mock, 24 h, 72 h, and 120 h samples). Indicated are statistical significances by Wilcoxon matched-pairs signed rank test. In **I**, **J**, each symbol represents one mouse from three experiments ($n = 6$ and 10). In **K**, **I**, each symbol represents one mouse from two experiments ($n = 6$ unimmunized and 10 immunized). Indicated in **K** are statistical significances by Mann–Whitney tests. Summaries shown in **E**, **H**, **K** are mean ± SD. Summaries shown in **I**, **J**, **L** are linear regressions, with indicated statistical significance of regression fits. **M**, **N** are representative of $n = 2$.

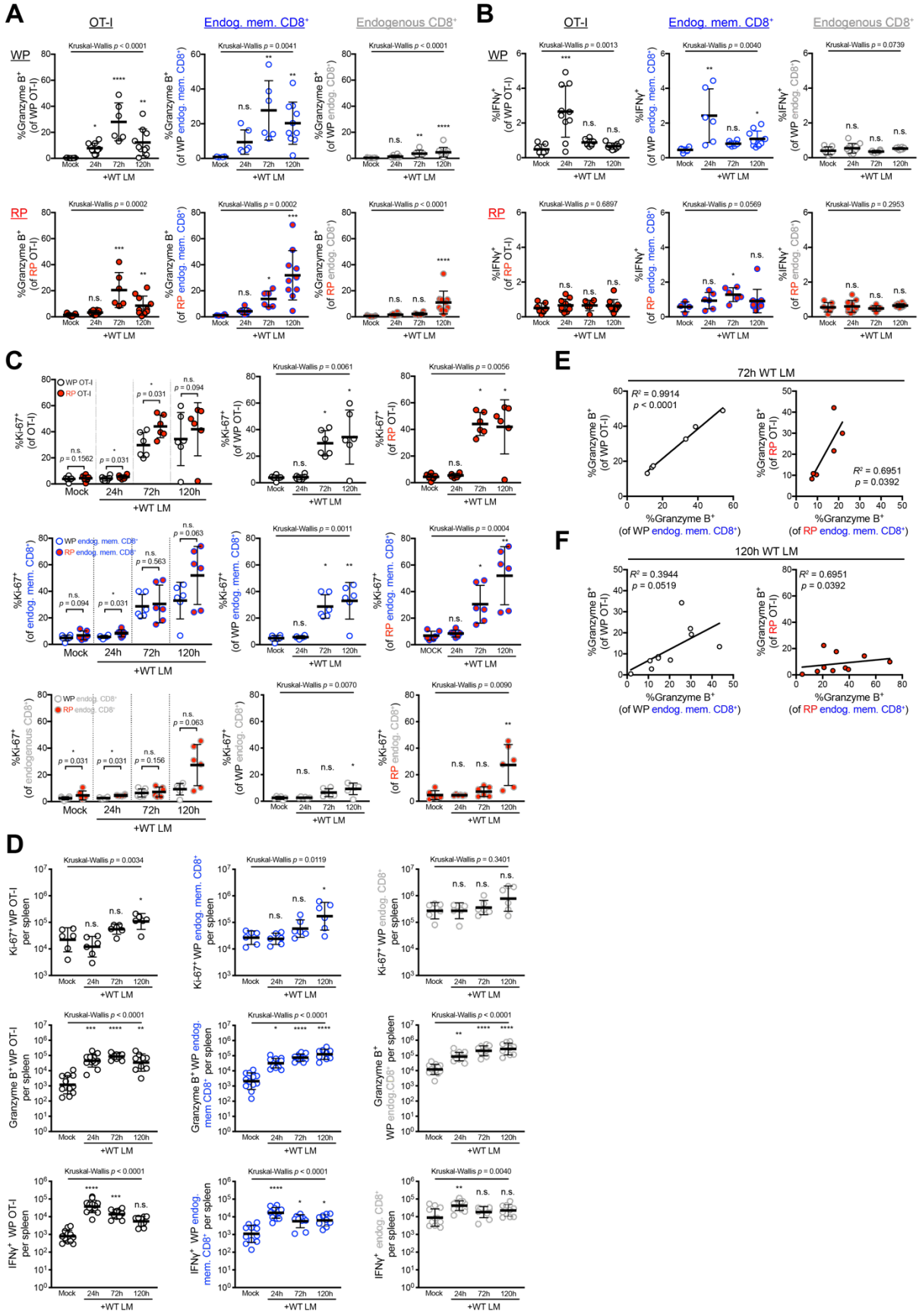
A
OT-I
Endog. mem. CD8+
Endogenous CD8+
WP
RP
%Granzyme B+ (of WP OT-I)
%Granzyme B+ (of WP endog. mem. CD8+)
%Granzyme B+ (of WP endog. CD8+)
%Granzyme B+ (of RP OT-I)
%Granzyme B+ (of RP endog. mem. CD8+)
%Granzyme B+ (of RP endog. CD8+)
Kruskal-Wallis p < 0.0001
Kruskal-Wallis p = 0.0041
Kruskal-Wallis p < 0.0001
Kruskal-Wallis p = 0.0002
Kruskal-Wallis p = 0.0002
Kruskal-Wallis p < 0.0001
B
OT-I
Endog. mem. CD8+
Endogenous CD8+
WP
RP
%IFNγ+ (of WP OT-I)
%IFNγ+ (of WP endog. mem. CD8+)
%IFNγ+ (of WP endog. CD8+)
%IFNγ+ (of RP OT-I)
%IFNγ+ (of RP endog. mem. CD8+)
%IFNγ+ (of RP endog. CD8+)
Kruskal-Wallis p = 0.0013
Kruskal-Wallis p = 0.0040
Kruskal-Wallis p = 0.0739
Kruskal-Wallis p = 0.6897
Kruskal-Wallis p = 0.0569
Kruskal-Wallis p = 0.2953
C
%Ki-67+ (of OT-I)
%Ki-67+ (of WP OT-I)
%Ki-67+ (of RP OT-I)
%Ki-67+ (of endog. mem. CD8+)
%Ki-67+ (of WP endog. mem. CD8+)
%Ki-67+ (of RP endog. mem. CD8+)
%Ki-67+ (of endogenous CD8+)
%Ki-67+ (of WP endog. CD8+)
%Ki-67+ (of RP endog. CD8+)
WP OT-I
RP OT-I
WP endog. mem. CD8+
RP endog. mem. CD8+
WP endog. CD8+
RP endog. CD8+
Kruskal-Wallis p = 0.0061
Kruskal-Wallis p = 0.0056
Kruskal-Wallis p = 0.0011
Kruskal-Wallis p = 0.0004
Kruskal-Wallis p = 0.0070
Kruskal-Wallis p = 0.0090
D
Ki-67+ WP OT-I per spleen
Ki-67+ WP endog. mem. CD8+ per spleen
Ki-67+ WP endog. CD8+ per spleen
Granzyme B+ WP OT-I per spleen
Granzyme B+ WP endog. mem CD8+ per spleen
Granzyme B+ WP endog.CD8+ per spleen
IFNγ+ WP OT-I per spleen
IFNγ+ WP endog. mem. CD8+ per spleen
IFNγ+ endog. CD8+ per spleen
Kruskal-Wallis p = 0.0034
Kruskal-Wallis p = 0.0119
Kruskal-Wallis p = 0.3401
Kruskal-Wallis p < 0.0001
Kruskal-Wallis p < 0.0001
Kruskal-Wallis p < 0.0001
Kruskal-Wallis p < 0.0001
Kruskal-Wallis p < 0.0001
Kruskal-Wallis p = 0.0040
E
72h WT LM
R² = 0.9914
p < 0.0001
R² = 0.6951
p = 0.0392
%Granzyme B+ (of WP endog. mem. CD8+)
%Granzyme B+ (of RP endog. mem. CD8+)
F
120h WT LM
R² = 0.3944
p = 0.0519
R² = 0.6951
p = 0.0392
%Granzyme B+ (of WP endog. mem. CD8+)
%Granzyme B+ (of RP endog. mem. CD8+)
Mock
24h
72h
120h
+WT LM

Figure 2.8 Temporal patterns of bystander activation are conserved in endogenous CD8$^+$ T_{mem}

A–**C** Frequencies of (**A**) GzmB$^+$, (**B**) IFNγ$^+$, or (**C**) Ki-67$^+$ OT-I T cells, endogenous CD8$^+$ T_{mem}, and bulk endogenous CD8$^+$ T cells within WP or RP during heterologous WT LM immunization. **D** Counts of GzmB$^+$, IFNγ$^+$, or Ki-67$^+$ OT-I T cells, endogenous CD8$^+$ T_{mem}, and bulk endogenous CD8$^+$ T cells from WPs during heterologous WT LM immunization. **E**, **F** Scatter plots comparing magnitude of WP or RP OT-I and endogenous memory CD8$^+$ T cell responses at (**E**) 72 hours or (**F**) 120 hours after WT LM immunization. In **A** and **B** each symbol represents one mouse from 3 experiments (n = 4 to 10 per condition per time point); summaries shown are mean ± SD and indicated are statistical significances by Kruskal-Wallis tests and Dunn's multiple comparisons test at * $p < 0.05$, ** $p < 0.01$, *** $p < 0.001$, **** $p < 0.0001$. In **C** each symbol represents one splenic compartment from one animal (left panels) or one animal (center and right panels) (n = 6 from 2 technical replicates). Summaries shown are mean ± SD. In left panels, indicated are statistical significances by Wilcoxon matched-pairs signed rank test. For center and right panels, indicated are statistical significances by Kruskal-Wallis tests and Dunn's multiple comparisons test against LM-unimmunized animals (mock) at * $p < 0.05$, ** $p < 0.01$, *** $p < 0.001$, **** $p < 0.0001$. In **D** each symbol represents one animal (n = 6 to 13 per time point, 2 to 5 technical replicates). Summaries shown are mean ± SD; indicated are statistical significances by Kruskal-Wallis tests and Dunn's multiple comparisons test at * $p < 0.05$, ** $p < 0.01$, *** $p < 0.001$, **** $p < 0.0001$. In **E** and **F** each symbol represents one mouse from 3 experiments (n = 6-10). Indicated are statistical significances by linear regression.

We next examined if CD69$^+$ CD103$^+$ CD8$^+$ T (resident memory phenotype) cells become similarly bystander-activated during WT LM immunization (Figure 2.9A, B). We observed an increase in CD69 expression by T cells as expected given that inflammatory signals are sufficient to induce CD69 expression. Importantly, the CD69$^+$ CD103$^+$ population only changed slightly in frequency and showed minimal expression of effector molecules compared with OT-I or endogenous CD8$^+$ T_{mem} (Figure 2.9C–G). These data suggest that bystander-activated cells at secondary lymphoid organs are primarily migratory and not resident in nature. To better understand how T_{mem} are recruited and activated in this site-specific manner we next wanted to characterize these cells more in depth.

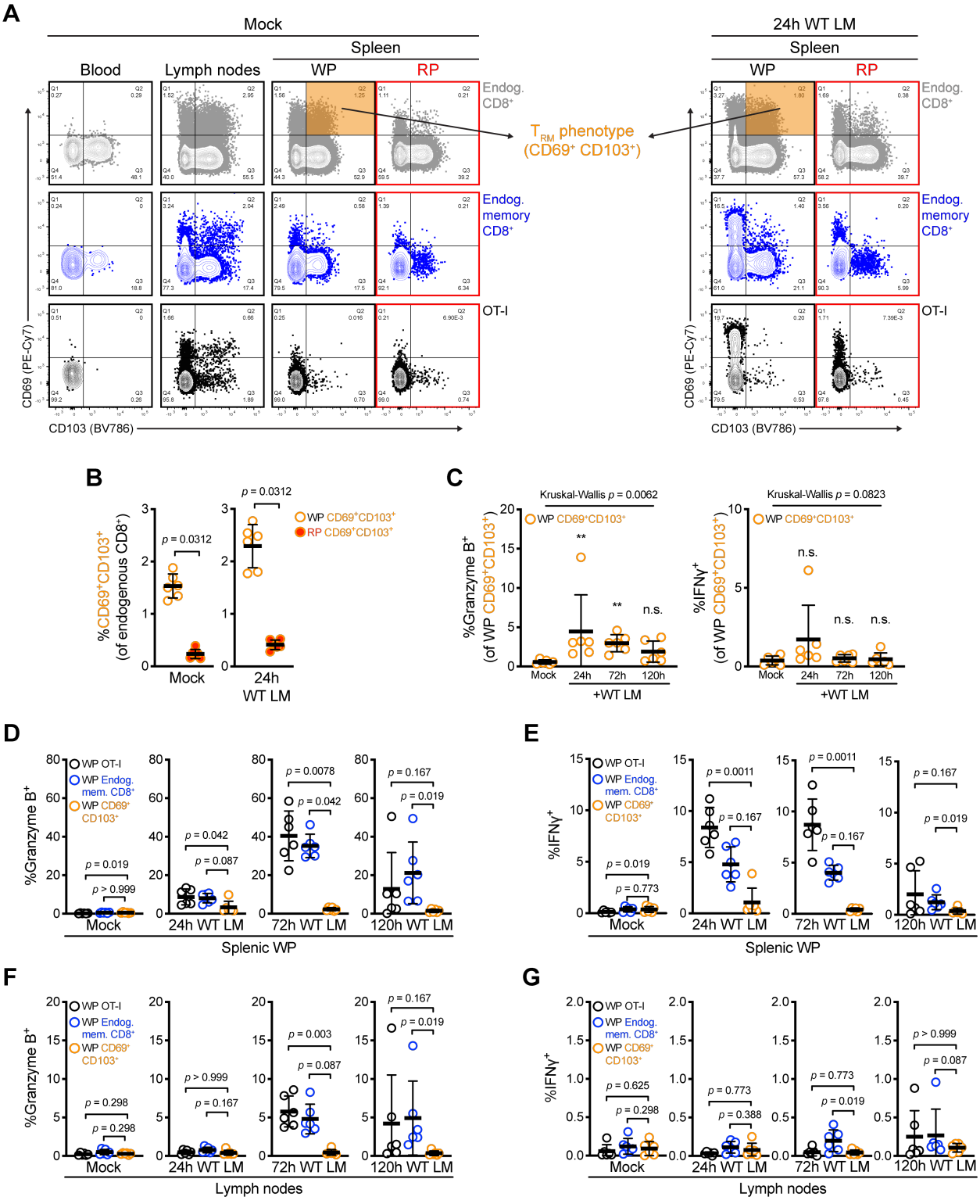

Figure 2.9 **T_{RM}-phenotype CD69$^+$ CD103$^+$ cells in spleen and LN are less responsive to in vivo bystander activation**

A Gating strategy demonstrating CD69 CD103 co-expression patterns in bulk endogenous $CD8^+$ T cells (grey), endogenous $CD8^+$ T_{mem} (blue), or OT-I T_{mem} (black) isolated from blood, LN, splenic WP, or circulatory splenic RP (red outline). Left panel set depicts an LM-unimmunized animal and right panel set depicts an animal 24 hours after WT LM immunization; T_{RM} phenotype cells (i.e., those that are $CD69^+CD103^+$) are highlighted in orange. **B** frequencies of WP (orange outline, white fill) and RP (orange outline, red fill) $CD69^+CD103^+$ endogenous $CD8^+$ cells. **C** Frequencies of $GzmB^+$ (left) or $IFN\gamma^+$ (right) in $CD69^+CD103^+$ endogenous $CD8^+$ T cells during WT LM immunization. **D**–**G** Comparison of (**D**, **F**) GzmB and (**E**, **G**) IFNγ expression between OT-I T_{mem} (black outline), endogenous $CD8^+$ T_{mem} (blue outline), and $CD69^+CD103^+$ endogenous $CD8^+$ T cells (orange outline) during LM immunization. Panels (**D**, **E**) represent cells from the splenic WP (the site of LM infection) and (**F**, **G**) represent LNs (a site typically spared from infection). In **B**–**G** summaries shown are mean ± SD; each symbol represents one cell population from one animal (n = 6 from 2 technical replicates). In **B**, indicated statistical significances were determined by Wilcoxon matched-pairs signed rank test. In **C**, indicated statistical significances were determined by Kruskal-Wallis tests and Dunn's multiple comparisons test at * $p < 0.05$, ** $p < 0.01$, *** $p < 0.001$, **** $p < 0.0001$. In **D**–**F** indicated statistical significances are adjusted p values determined by Dunn's multiple comparison tests.

2.2.5 Surface CXCR3 is decreased on bystander-activated T cells

As we observed bystander activation of OT-I and endogenous $CD8^+$ T_{mem} within the WP 24 h post immunization, we focused our following analyses solely on cells residing in the WP. We sought to determine whether bystander activation at this site is associated with other phenotypic changes. We compared the expression of phenotypic markers between populations of OT-I and endogenous $CD8^+$ T_{mem} sourced from LM-unimmunized and -immunized (24 h post immunization) animals (Figure 2.10A). We further subset WP OT-I and endogenous $CD8^+$ T_{mem} from LM-immunized animals by their bystander activation status (i.e., GzmB positivity) and included a reference population of endogenous naïve ($NKG2D^-$ $CD62L^+$ $CD127^+$) $CD8^+$ T cells as a baseline control for phenotypic changes (Figure 2.10B). An effector ($CD62L^-$ $CD127^-$) phenotype was enriched in bystander-activated OT-I and endogenous $CD8^+$ T_{mem} 24 h post immunization with WT LM (Figure 2.11A, B); but the presence of $CD62L^+$ $KLRG1^-$ cells within bystander-activated OT-I T cells suggests that the ability to become bystander-activated is not restricted to a specific memory phenotype (Figure 2.10C, Figure 2.11A, B). Most striking, however, were changes in staining profiles for CXCR3, a chemokine receptor needed to allow Ag-specific effector T cells to find infected target cells (110). In unimmunized animals, OT-I and endogenous $CD8^+$ T_{mem} uniformly express CXCR3 (Figure 2.10C, D), but within 24 h of WT LM immunization, bystander-activated OT-I and endogenous $CD8^+$ T_{mem} displayed a significant drop in numbers, frequency and MedFI for surface CXCR3 (Figure 2.10C, D, Figure 2.11C).

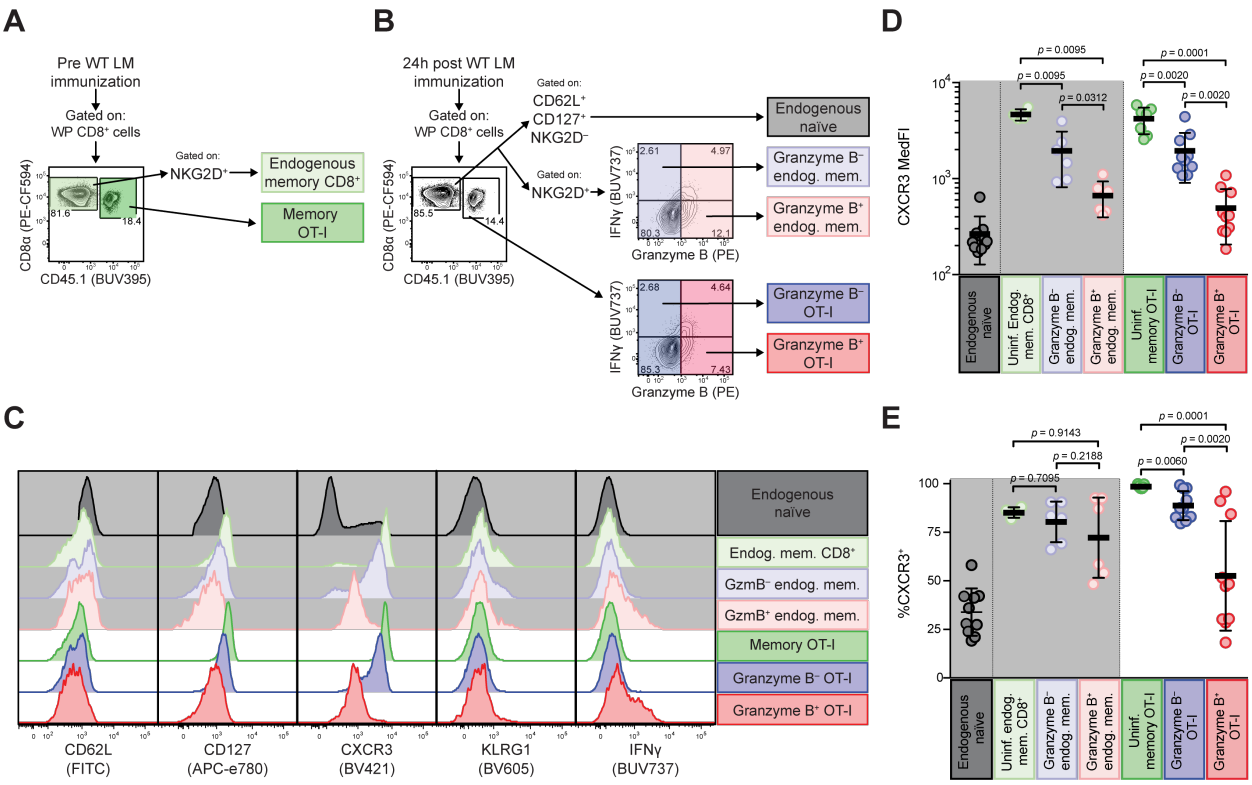

Figure 2.10 Bystander-activated CD8⁺ T_{mem} display decreased surface CXCR3

A, **B** Representative flow plots showing populations used for representative overlays in **C** and frequencies and median fluorescence intensity (MedFI) reported in **D** and **E**. **A** Representative gating for WP OT-I (green) endogenous CD8⁺ T_{mem} (light green) from unimmunized OT-I memory mice. **B** Representative flow plots from OT-I memory WP splenocytes 24 h post WT LM infection, showing gating of endogenous naïve CD8⁺ T cells (gray), GzmB⁺ (i.e., bystander-activated) and GzmB⁻ endogenous CD8⁺ T_{mem} (light red and light blue, respectively) and OT-I T cells (red and blue, respectively). **C** Histogram overlays of populations outlined in **A**, **B** for phenotypic and functional markers. Cells endogenous to hosts have a light gray background. **D**–**E** CXCR3 MedFI (**D**) and frequency (**E**) in CD8⁺ T cell subsets. **B** is from $n = 3$ animals concatenated into a single file. **C** is a representative plot from concatenated populations shown in **A**, **B**. In **D** and **E** a single point represents a subpopulation from each animal ($n = 6$ for endogenous T_{mem} and 10 for transgenic and endogenous naïve populations) from 3 experiments. Summary statistics shown are mean ± SD. Indicated are statistical significances by Wilcoxon matched-pairs signed rank test.

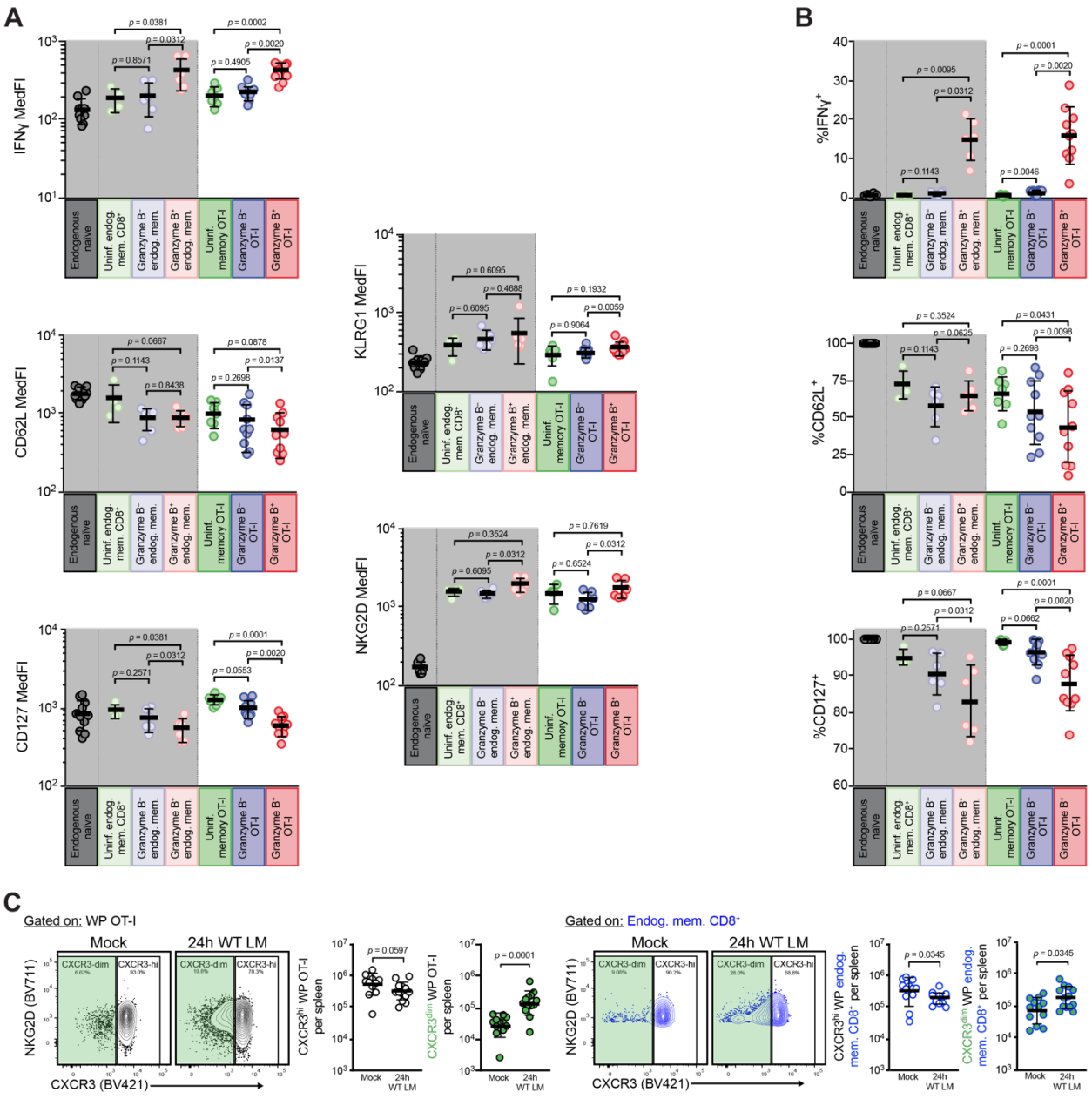

Figure 2.11 Bystander-activated CD8$^+$ T$_{mem}$ are phenotypically distinct.

A MedFI or **B** frequency of markers assessed by flow analysis in WP CD8$^+$ T cell populations. OT-I and endogenous CD8$^+$ T$_{mem}$ are from LM-unimmunized mice. Endogenous naïve, GzmB$^+$ (i.e., bystander-activated) and GzmB$^-$ (i.e., non-bystander activated) endogenous CD8$^+$ T$_{mem}$ and OT-I T$_{mem}$ are from mice 24 hours after WT LM immunization. Endogenous cell populations are shown in columns with grey backgrounds. **C** Identification and absolute number of CXCR3^{dim} (green fill) and CXCR3^{hi} (white fill) populations in WP OT-I (black outlines and flow plots) and WP endogenous CD8$^+$ T$_{mem}$ (blue outlines and flow plots). In **A**, **B** a single point represents a population from a single animal (n = 6–10), summaries shown are mean ± SD. Indicated are statistical significances by Wilcoxon matched pairs signed rank test. In **C** a single point represents a specific population from a single animal (n = 12-13 per condition from 5 technical replicates). Summaries shown are mean ± SD; indicated are statistical significances by Mann-Whitney tests.

As WT LM detection causes rapid secretion of CXCR3 ligands (CXCR3L), CXCL9 and CXCL10, by human PBMC (111) and CXCR3L engagement and signaling can lead to dimmed staining owing to receptor internalization (112), we next asked if this loss of surface CXCR3 expression we observed could be due to ligand engagement at sites of early immune activation. We isolated OT-I and endogenous CD8$^+$ T_{mem} and exposed them to recombinant CXCL9 and CXCL10 (Figure 2.12A, B). We observed a rapid, CXCL9 and CXCL10 dose-dependent decrease in CXCR3 expression on both OT-I and endogenous memory CD8$^+$ T_{mem} (Figure 2.12C, D, Figure 2.13A) and cycloheximide (CHX)-independent CXCR3 re-expression following ligand removal (Figure 2.13B–E). These data indicate that murine CXCR3 can be recycled to the cell surface following internalization, whereas human CXCR3 is restored via de novo protein synthesis (113). Finally, we wanted to define CXCL9 and CXCL10 expression in situ and stained serially sectioned slides for CD169 and LLO; CXCR3L (CXCL9 and CXCL10); and CD45.1 (for OT-I T cells) and CD11b. We found that WP OT-I T cells colocalized in areas staining for both CXCL9 and CXCL10 (Figure 2.14A, B, Figure 2.15). Thus, we next asked if CXCR3 is necessary for recruitment of T_{mem} to activated APCs and undergoing bystander activation.

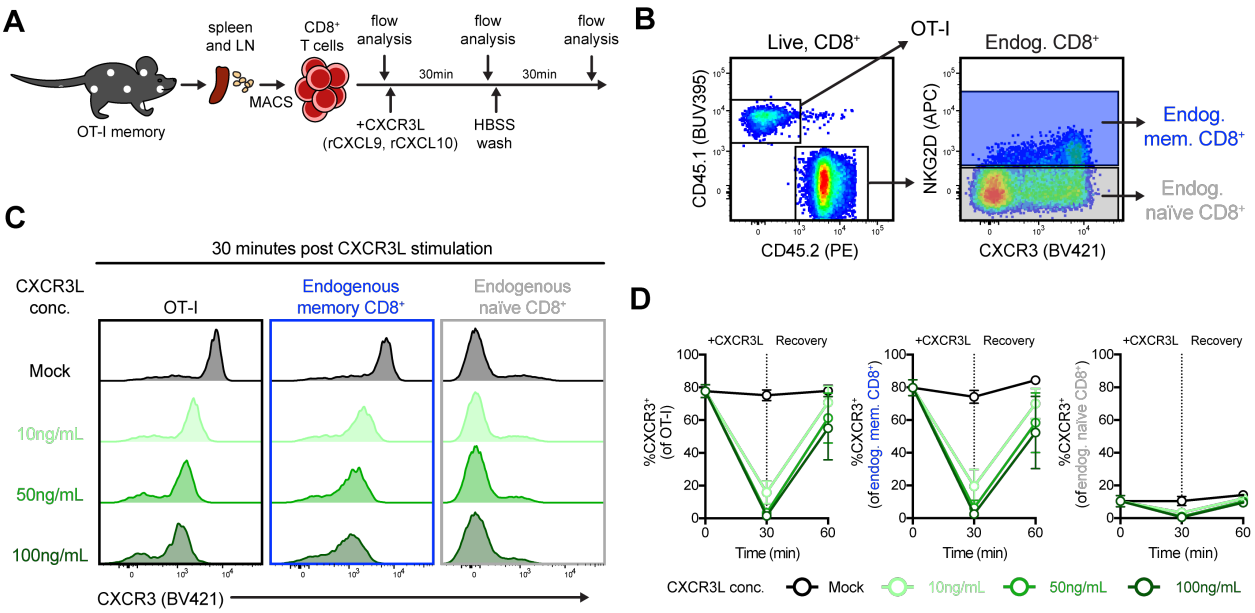

Figure 2.12 CXCR3L engagement leads to surface CXCR3 loss.

A Schematic for CD8$^+$ T cell isolation, CXCR3L stimulation, and longitudinal sampling for flow analysis. **B** Representative gating of OT-I T cells, NKG2D$^+$ endogenous CD8$^+$ T_{mem} (blue), and NKG2D$^-$ endogenous naïve CD8$^+$ T cells (gray). **C** Representative histograms depicting surface CXCR3 flow staining in OT-I T cells (black border), endogenous CD8$^+$ T_{mem} (blue border), and endogenous naïve CD8$^+$ T cells (gray border) after 30 min of mock (dark gray histogram) or CXCL9 plus CXCL10 (rCXCR3L) stimulation (10 ng/mL, light green; 50 ng/mL, medium green;

100 ng/mL, dark green per chemokine). **D** Frequencies of OT-I T cells (left), endogenous CD8$^+$ T_{mem} (center), and endogenous naïve CD8$^+$ T cells (right) expressing surface CXCR3 prior to rCXCR3L stimulation (0 min), after rCXCR3L stimulation (30 min), and 30 min after rCXCR3L removal (60 min). Symbols and line connectors are color-coded by rCXCR3L concentration as in **C**. **C** is a representative plot from one of two technical replicates. In **D** each symbol represents the mean (n = 2 at each timepoint) ± SD with lines connecting means from two technical replicates.

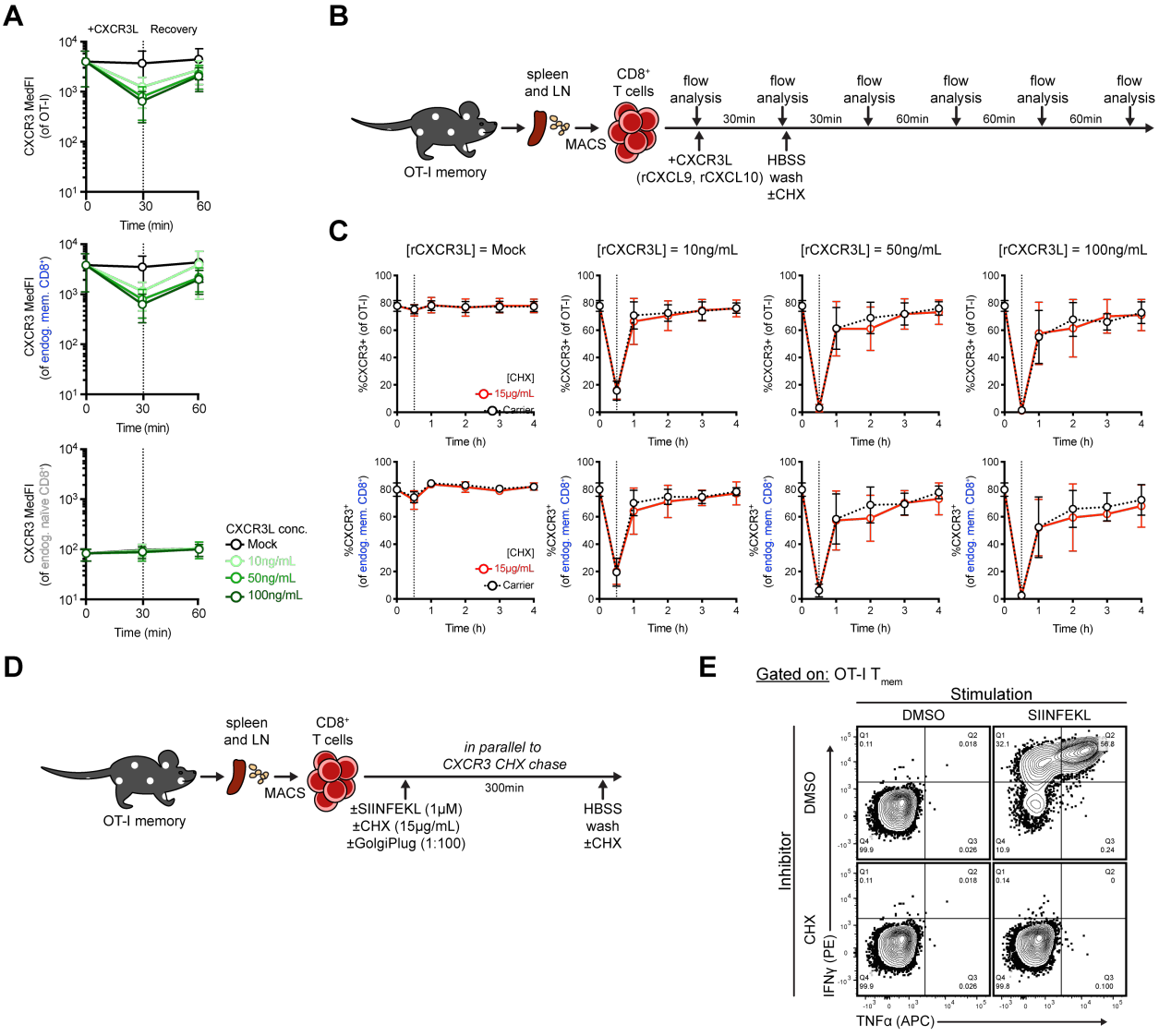

Figure 2.13 De novo protein synthesis is not responsible for CXCR3 restoration in mice

A CXCR3 MedFI in OT-I T cells (top), endogenous CD8$^+$ T_{mem} (middle), and endogenous naïve CD8$^+$ T cells (bottom) prior to rCXCR3L stimulation (0min), after rCXCR3L stimulation (30min), and 30 minutes after rCXCR3L removal (60min). Color indicates rCXCR3L concentration (mock, black; 10ng/mL, light green; 50ng/mL, medium green; 100ng/mL, dark green). **B** CHX chase assay to test if mouse CXCR3 is restored through *de novo* protein synthesis. **C** CXCR3 frequency in OT-I (top) or endogenous CD8$^+$ T_{mem} (bottom) during CHX (red, solid line) or carrier (black, dashed line) treatment. Vertical reference line signifies end of rCXCR3L stimulation and addition

of CHX-containing media. **D** Schematic of peptide stimulation assay to control for CHX performance. **E** Representative flow plot depicting OT-I T_{mem} production of effector cytokines via cognate Ag (SIINFEKL peptide) in the presence or absence of CHX.

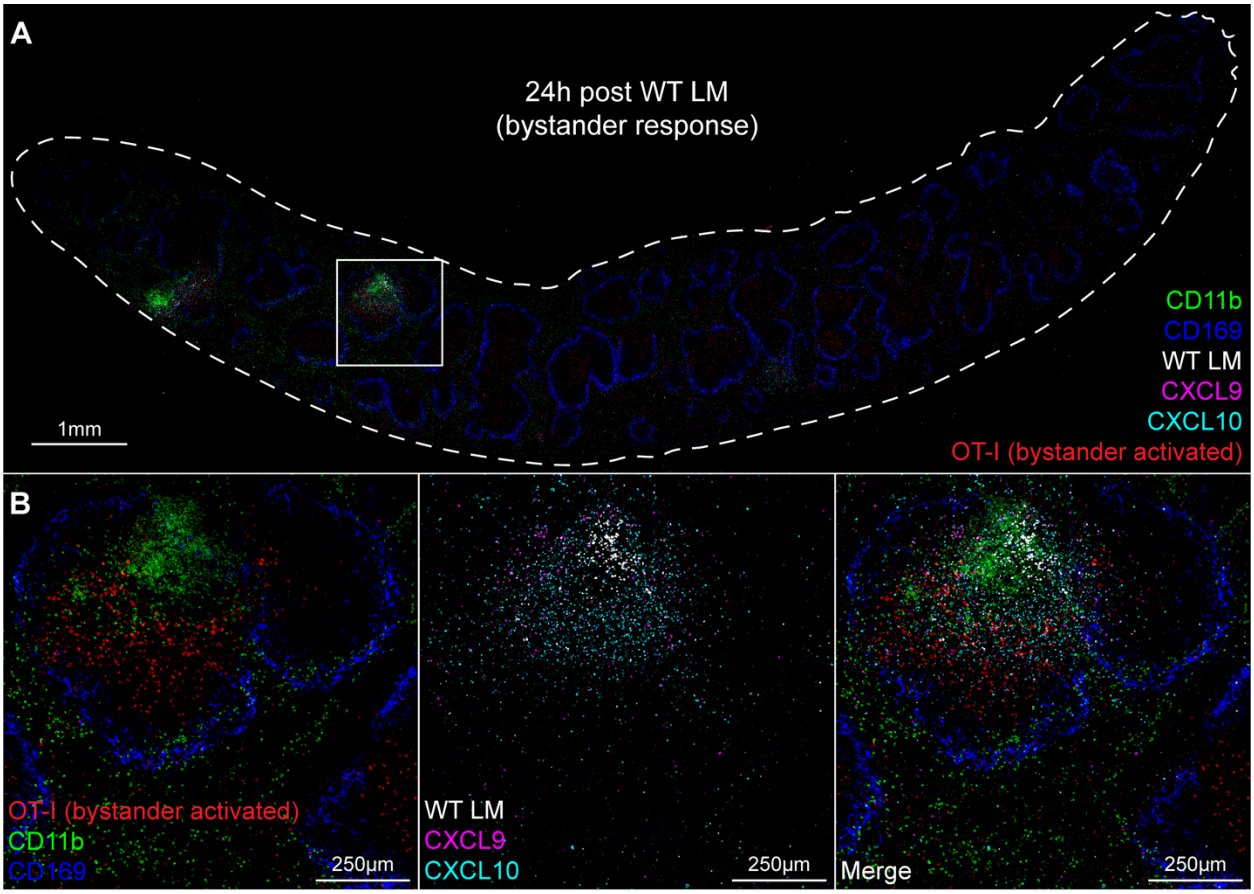

Figure 2.14 CXCR3L gradients emanate from foci of splenic LM infection

A, **B** Representative IF image of spleen from animal 24 h post WT LM immunization. The image is composed of three 8 μm serial sections stained for CD11b (green) and CD169$^+$ MMM (blue); OT-I T cells (red) and WT LM (white); and CXCL9 (magenta) and CXCL10 (cyan). **A**, **B** is representative of $n = 5$ animals from two technical replicates. Image orientation was modified in Adobe Photoshop to permit overlaying of serially sectioned slides. Contrast was equally increased amongst all individual images; after, punctate staining in LM, CXCL9, and CXCL10 images was outlined using ImageJ command “find edges” to enhance visibility prior to merging.

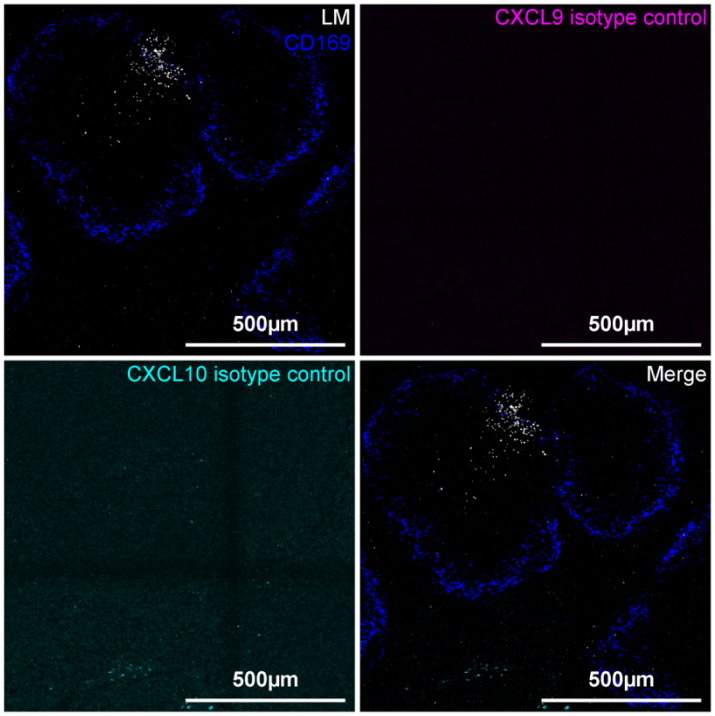

Figure 2.15 Isotype control staining for CXCR3L antibodies

Representative image depicting CXCL9 and CXCL10 IF isotype control staining in same foci from serial sections in Fig 2.15. Image is representative of *n* = 3 spleens and image processing was identical to that in Fig 2.15: Image orientation was modified in Adobe Photoshop to permit overlaying of serially-sectioned slides; contrast was equally increased amongst all individual images; CXCL9 and CXCL10 isotype control images were outlined using ImageJ command "find edges" prior to merging.

2.2.6 Localized bystander activation requires CXCR3

To determine whether recruitment of T_{mem} towards activated APCs is CXCR3-dependent, we generated memory mice using WT or *Cxcr3*$^{-/-}$ OT-I T cells (as described in Figure 2.2A) and immunized the mice with WT LM to induce bystander activation (Figure 2.16A). We interrogated the bystander responses in the WP of OT-I (either WT or *Cxcr3*$^{-/-}$) and endogenous CD8^{+} T_{mem} (which are all *Cxcr3*$^{+/+}$) (Figure 2.16B). After WT LM immunization, *Cxcr3*$^{-/-}$ OT-I T cells had limited IFNγ and GzmB expression in comparison with WT OT-I and endogenous CD8^{+} T_{mem} (from both WT or *Cxcr3*$^{-/-}$ OT-I T cell transfers) (Figure 2.16C). At 24 h post immunization, the frequency of IFNγ^{+} or GzmB^{+} *Cxcr3*$^{-/-}$ OT-I T cells was significantly less than endogenous CD8^{+} T_{mem} from the same animal (Figure 2.16D) or WT OT-I T cells from animals of the experimental control group (Figure 2.16E, F). Although there were pronounced CXCR3-

dependent differences in IFNγ and GzmB responses in OT-I T cells, the endogenous $CD8^+$ T_{mem} had IFNγ and GzmB responses of similar magnitude (Figure 2.16E, F). We utilized IF to determine whether clustering near LM Ag and target cells was perturbed by CXCR3-deficiency. *Cxcr3*$^{-/-}$ OT-I T_{mem} remained at a higher frequency (as % of $CD8^+$ T cells) than their WT counterparts during the memory stage but had a stable memory phenotype (Figure 2.17A). This is in agreement with a previous report illustrating that *Cxcr3*$^{-/-}$ $CD8^+$ T cells undergo limited contraction but maintain their ability to reactivate and exert cytotoxicity (114). Nevertheless, the splenic distribution of *Cxcr3*$^{-/-}$ and WT OT-I cells was of a similar pattern (Figure 2.16H, mock); this too, was reflected in uninfected WP foci 24 h after WT LM immunization. In contrast to the dense clusters that WT OT-I T cells form with other $GzmB^+$ cells around areas rich in LM Ag, *Cxcr3*$^{-/-}$ OT-I T cells remained largely $GzmB^-$ and on the periphery of clustering, $GzmB^+$ cells (Figure 2.16H, 24 h WT LM). Importantly, *Cxcr3*$^{-/-}$ OT-I T cells are not inherently defective in becoming bystander-activated as we observed GzmB expression at later time points when the infection had become systemic (Figure 2.16G). Similarly, *Cxcr3*$^{-/-}$ OT-I memory T cells express IFNγ following in vitro exposure to IL-12, IL-15, and IL-18 (Figure 2.16I–M, Figure 2.17B, C).

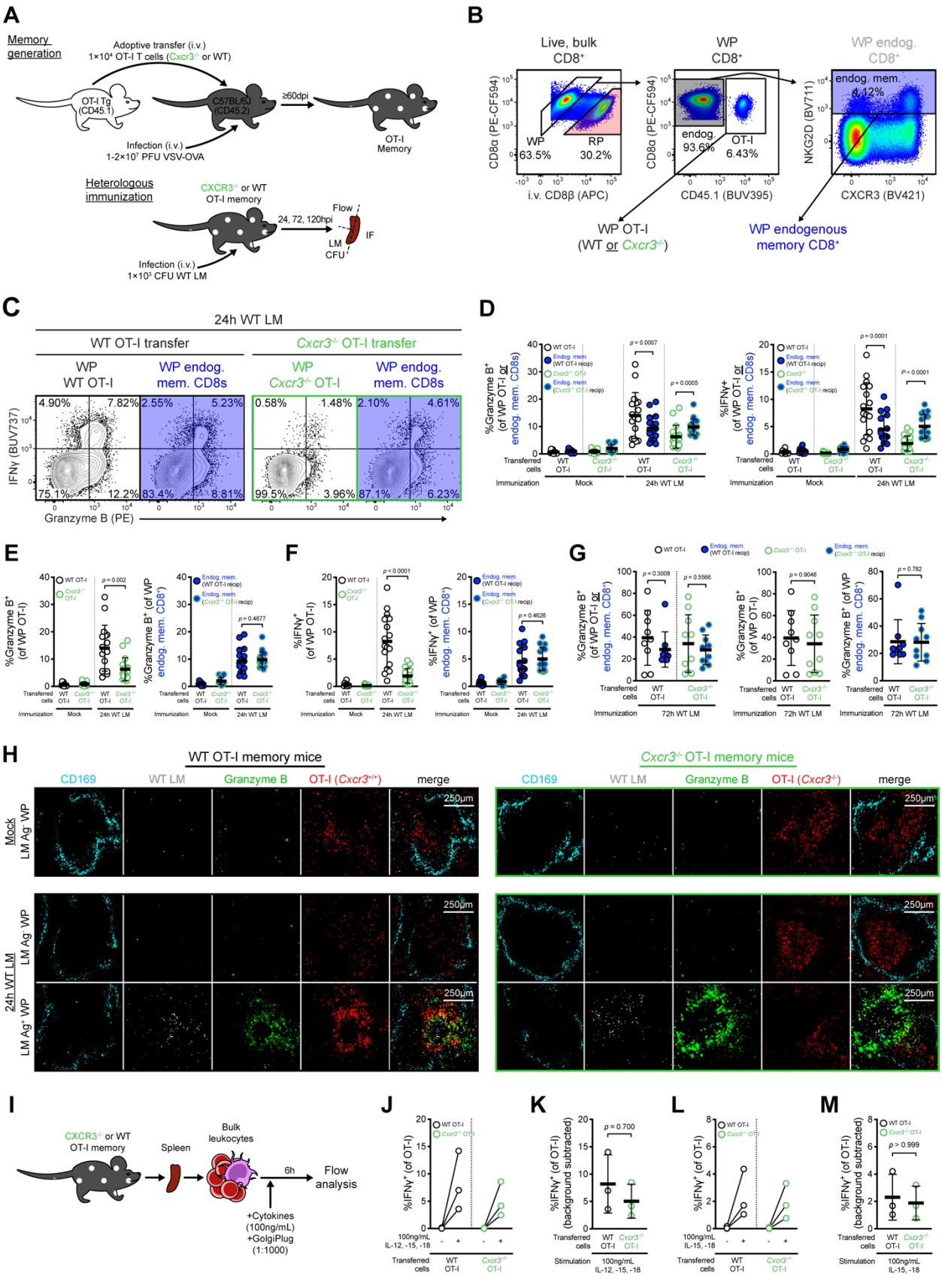
A
Memory generation
Adoptive transfer (i.v.)
1×10⁴ OT-I T cells (Cxcr3-/- or WT)
OT-I Tg (CD45.1)
C57BL/6J (CD45.2)
≥60dpi
OT-I Memory
Infection (i.v.)
1-2×10⁷ PFU VSV-OVA
Heterologous immunization
CXCR3-/- or WT OT-I memory
24, 72, 120hpi
Flow
IF
LM CFU
Infection (i.v.)
1×10⁵ CFU WT LM
B
Live, bulk CD8+
WP CD8+
WP endog. CD8+
CD8α (PE-CF594)
i.v. CD8β (APC)
WP 63.5%
RP 30.2%
endog. 93.6%
OT-I 6.43%
CD45.1 (BUV395)
endog. mem. 4.12%
NKG2D (BV711)
CXCR3 (BV421)
WP OT-I (WT or Cxcr3-/-)
WP endogenous memory CD8+
C
24h WT LM
WT OT-I transfer
Cxcr3-/- OT-I transfer
WP WT OT-I
WP endog. mem. CD8s
WP Cxcr3-/- OT-I
IFNγ (BUV737)
Granzyme B (PE)
4.90%
7.82%
2.55%
5.23%
75.1%
12.2%
83.4%
8.81%
0.58%
1.48%
2.10%
4.61%
99.5%
3.96%
87.1%
6.23%
D
%Granzyme B+ (of WP OT-I or endog. mem. CD8s)
%IFNγ+ (of WP OT-I or endog. mem. CD8s)
WT OT-I
Endog. mem. (WT OT-I recip)
Cxcr3-/- OT-I
Endog. mem. (Cxcr3-/- OT-I recip)
p = 0.0007
p = 0.0005
p = 0.0001
P < 0.0001
Transferred cells
Immunization
Mock
24h WT LM
E
%Granzyme B+ (of WP OT-I)
%Granzyme B+ (of WP endog. mem. CD8+)
p = 0.002
p = 0.4677
F
%IFNγ+ (of WP OT-I)
%IFNγ+ (of WP endog. mem. CD8+)
p < 0.0001
p = 0.4626
G
%Granzyme B+ (of WP OT-I or endog. mem. CD8+)
p = 0.3008
p = 0.5566
p = 0.9048
p = 0.782
72h WT LM
H
WT OT-I memory mice
Cxcr3-/- OT-I memory mice
CD169
WT LM
Granzyme B
OT-I (Cxcr3+/+)
OT-I (Cxcr3-/-)
merge
Mock
LM Ag- WP
24h WT LM
LM Ag+ WP
250μm
I
CXCR3-/- or WT OT-I memory
Spleen
Bulk leukocytes
6h
Flow analysis
+Cytokines (100ng/mL)
+GolgiPlug (1:1000)
J
%IFNγ+ (of OT-I)
100ng/mL IL-12, -15, -18
K
%IFNγ+ (of OT-I) (background subtracted)
p = 0.700
Stimulation
L
%IFNγ+ (of OT-I)
M
%IFNγ+ (of OT-I) (background subtracted)
p > 0.999

Figure 2.16 Localized bystander activation requires CXCR3-mediated chemotaxis

A Experimental overview. **B** Representative gating of WP OT-I and endogenous CD8$^+$ T_{mem}. In symbols for **C**–**G**, OT-I and endogenous CD8$^+$ T_{mem} are respectively filled white and blue; WT or *Cxcr3*$^{-/-}$ OT-I T cell recipients are, respectively, outlined in black and green. **C** Representative gating depicting IFNγ and GzmB expression 24 h post immunization. **D**–**F** Frequency of GzmB and IFNγ-expressing cell subsets 24 h after immunization. **G** Frequency of GzmB expression in OT-I and endogenous CD8$^+$ T_{mem} 72 h after immunization **H** Representative WP image from WT LM-unimmunized animals (mock, top row) and -immunized animals (24 h post immunization, bottom two rows). Slides were stained for geographic markers: LM Ag (white) and CD169$^+$ MMM (cyan); and phenotyping: OT-I (red) and GzmB (green). Image borders delineate OT-I genotype (WT, black; *Cxcr3*$^{-/-}$, green). In lower two rows, LM Ag-negative (top) and Ag-positive (bottom) foci are from the same LM-immunized animal. **I** Stimulation schematic of OT-I T_{mem} with bystander-activating cytokines. **J**, **L** Frequencies of IFNγ-expressing OT-I T cells after mock or cytokine stimulation. **K**, **M** Background-subtracted IFNγ$^+$ frequencies after cytokine stimulation of WT and *Cxcr3*$^{-/-}$ OT-I T_{mem}. In **D**–**G**, each symbol represents the transgenic or endogenous memory compartment of CD8$^+$ T cells per animal ($n = 9$ mock WT recipients, $n = 12$ mock *Cxcr3*$^{-/-}$ recipients, $n = 17$ 24-hour WT and *Cxcr3*$^{-/-}$ recipients, $n = 9$ and 10 72-hour WT and *Cxcr3*$^{-/-}$ recipients, respectively) across four to six technical replicates. Statistical significance is indicated (**D**, **G** left panel, and **E**, **F**, **G** center and right panels) and was assessed by Wilcoxon matched-pairs signed rank test and Mann–Whitney tests, respectively. In **H**, images are representative of $n = 3$ and 5 (unimmunized WT and *Cxcr3*$^{-/-}$ OT-I T cell recipients, respectively) and $n = 7$ and 8 (LM-immunized WT and *Cxcr3*$^{-/-}$ OT-I T cell recipients, respectively). In **J**–**M**, each symbol or connected pair represents one animal ($n = 3$) across three technical replicates. In **D**–**G**, **K**, **M**, summary statistics shown are mean ± SD; indicated are statistical significances by Mann–Whitney tests.

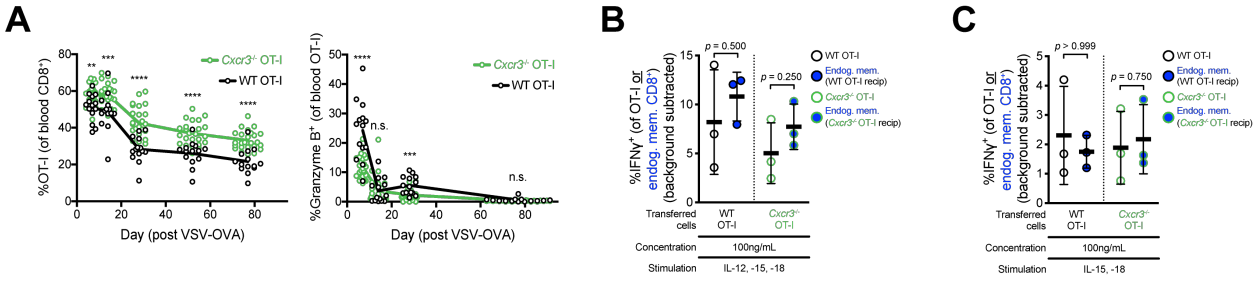

Figure 2.17 *Cxcr3*$^{-/-}$ OT-I T_{mem} are functionally intact despite altered contraction kinetics

A Frequency of WT (black) and *Cxcr3*$^{-/-}$ (green) OT-I T cells in the blood and the frequency of GzmB expression within circulating OT-I T cells. **B**–**C** Background-subtracted IFNγ expression levels in OT-I and endogenous CD8$^+$ T_{mem} 6 hours after stimulation with (**B**) 100ng/mL each of IL-12, -15, -18 or (**C**) 100ng/mL each of IL-15, -18. In **A** each symbol is representative of one animal, summaries shown are lines connecting means at each time point. $n = 14$ WT OT-I recipients; $n = 25$ *Cxcr3*$^{-/-}$ OT-I recipients. Indicated are statistical significances at *p < 0.05, **p < 0.01, *** < 0.001 comparing WT and *Cxcr3*$^{-/-}$ OT-I cells at the same time point by Mann-Whitney tests. In **B** and **C** each symbol is representative of a cell subset from a single animal ($n = 3$, three technical replicates); summaries shown are mean ± SD. Indicated statistical significances were calculated by Wilcoxon matched-pairs signed rank test.

Therefore, CXCR3 signaling mediates the chemoattraction of T_{mem} to areas with infected/activated APCs. Finally, CXCR3-mediated recruitment is also used by Ag-specific $CD8^+$ T cells to locate infected target cells (110). Given this overlap in recruitment mechanism, we hypothesized that bystander-activated $CD8^+$ T_{mem} can temporospatially overlap with Ag-specific $CD8^+$ T cells. Using adoptive transfers of P14 $CD8^+$ T cells (a TCR transgenic which recognizes lymphocytic choriomeningitis virus Ag, gp33), we interrogated how bystander-activated OT-I T cells were distributed in comparison with Ag-specific P14 T cells after LM-gp33 immunization (Figure 2.18A). Ag-specific P14 T cells were detectable in the spleen 96 h post immunization; however, P14 T cells formed discrete clusters that were not integrated with clusters of OT-I T cells, $GzmB^+$ endogenous cells, and LM Ag (Figure 2.18B).

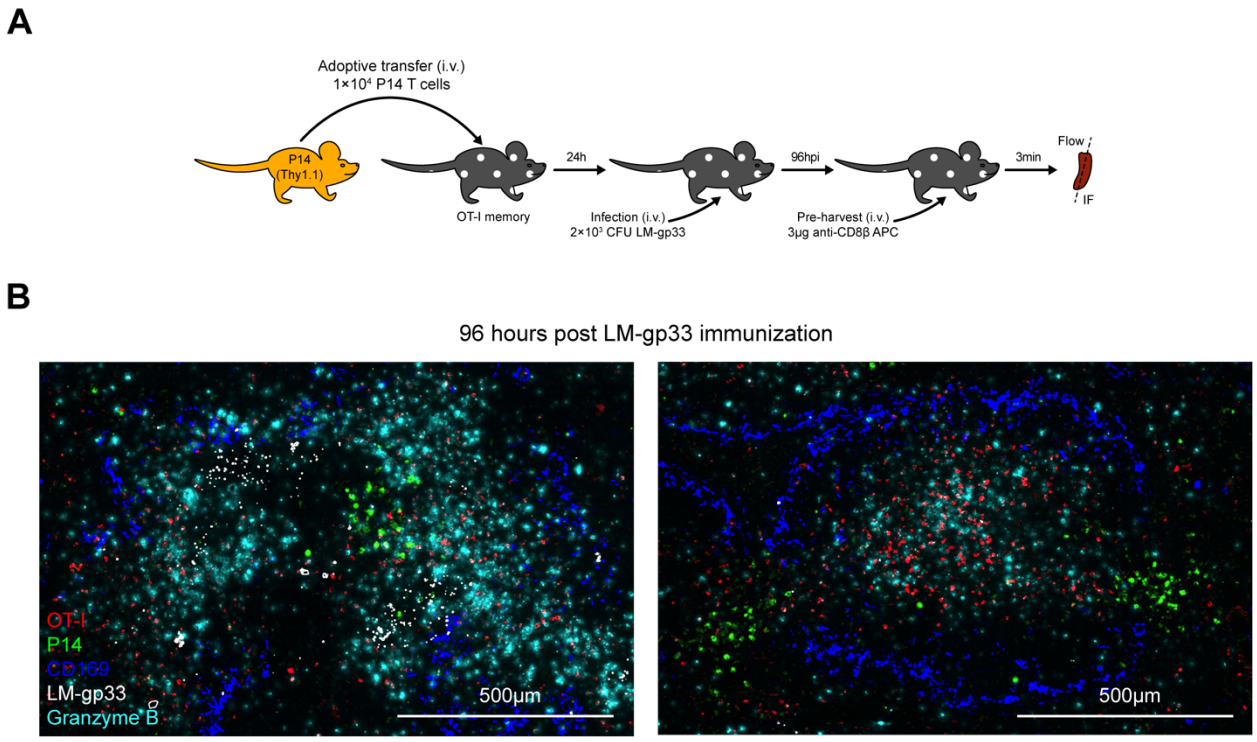

Figure 2.18 Bystander and *de novo* Ag-specific responses temporospatially overlap

A Schematic of adoptive transfer of naïve P14 TCR transgenic cells and subsequent LM-gp33 immunization (provides cognate Ag for P14 T cells, but bystander activates OT-I T_{mem}) and subsequent tissue sampling. **B** IF of splenic WP 96 hours after LM-gp33 immunization, with P14 T cells shown in green, OT-I T_{mem} in red, GzmB expression in cyan, CD169 in blue, and LM-gp33 in white. In **B** separate images are from different mice and representative of $n = 3$ animals. Image contrast was increased at an equal level and tissue orientation was modified in Adobe Photoshop to overlay serially-sectioned slides. All channels were merged and LM staining was outlined using "find edges" to increase visibility using ImageJ.

2.3 Discussion

Bystander activation of T_{mem} has been reported in the context of infections that are systemic in nature or have systemic inflammatory effects (36). In these instances, T_{mem} are exposed to systemic inflammatory cues and essentially become bystander-activated in a passive manner. We initially asked if bystander activation occurs when the inflammatory event is localized, specifically following delivery of an intra-muscular vaccine. Three days post vaccination, we observed phenotypic changes in the $CD8^+$ T cell compartment in vaccine recipients (but not in placebo recipients) that were consistent with bystander activation (Figure 2.1). Based on these data, we concluded that the i.m. vaccine either elicited a systemic inflammatory immune response strong enough to induce bystander activation or, alternatively, it could indicate that there was localized bystander activation in the draining lymph nodes followed by release of the bystander-activated T cells to the periphery. As we cannot experimentally test if human T_{mem} became bystander-activated in the lymph node draining the vaccination site, we used a mouse model to determine whether localized bystander activation could occur. We chose a low-dose LM mouse model of immunization in which activated APCs and inflammation are initially constrained to a limited number of white pulps in the spleen (Figure 2.3C). We found that OT-I T_{mem} were specifically recruited to and enriched at sites of early immune activation and bystander-activated in a highly localized yet still rapid manner (Figure 2.3, Figure 2.5). These data strongly suggested the existence of a mechanism that allowed active migration to the site of inflammation at a timepoint (24 h post immunization) that is typically considered to be dominated by the innate immune response (115). Previous reports also demonstrated early bystander-mediated activation of T_{mem}, but it is important to consider that these previous studies immunized/infected mice with high doses of attenuated *actA*$^-$ or WT LM, resulting in ubiquitous infection instead of localized infection (9, 10). These ubiquitous infection models have proven highly valuable to understand the inflammatory signals that activate T_{mem}, but they cannot determine whether bystander activation is merely a passive process. The strength of our low-dose WT LM infection model is that immune cell activation remains anatomically confined within the first 24 h of immunization. Furthermore, the early decrease of circulating OT-I and $CD8^+$ T cells 24 h after WT LM immunization mirrors the decrease of circulating human $CD8^+$ T cells after i.m. immunization with recombinant vectors (116).

Thorough characterization of the bystander-activated T cells revealed a decrease of CXCR3 expression levels specifically on $GzmB^+$ T cells indicating that these cells may have received a CXCR3-mediated signal leading to receptor internalization, which was supported by

colocalization of CXCR3L and OT-I T_{mem} in situ (Figure 2.10, Figure 2.12, Figure 2.14). Using *Cxcr3*$^{-/-}$ OT-I T cells, we found that CXCR3 was indeed necessary to recruit T_{mem}, which clustered tightly around these APCs (Figure 2.16) and became bystander-activated, including expression of GzmB and IFNγ (Figure 2.16). Importantly, since even the low-dose LM infection will spread over time and result in a systemic infection, we could examine if *Cxcr3*$^{-/-}$ OT-I T_{mem} became bystander-activated once the infection had become systemic. We found that *Cxcr3*$^{-/-}$ OT-I T_{mem} were bystander-activated at a later timepoint and thus ruled out that *Cxcr3*$^{-/-}$ T_{mem} have an inherent functional defect that rendered them incapable to become bystander-activated at all (Figure 2.16G, Figure 2.17B). Together, these data support a model where CXCR3-mediated signals drive T_{mem} to sites of inflammation to become bystander-activated.

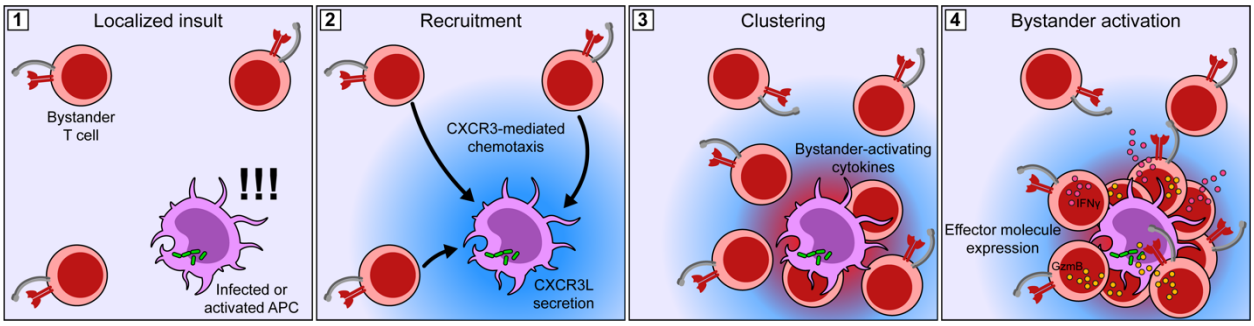

Figure 2.19 An updated model of active, localized CD8$^+$ T_{mem} bystander activation

Bystander activation during acute inflammation results from **1**) localized activation of APCs to **2**) secrete CXCR3Ls to recruit bystander CD8$^+$ T_{mem} to **3**) areas rich in bystander-activating cytokines, leading to **4**) localized bystander activation and bystander-mediated immune responses

Using a microscopy approach, a previous study showed that T_{mem} spatially orient themselves in areas prone to early immune activation within the lymph node, predisposing them to bystander activation and facilitating rapid responses (117). Using unsupervised digital pathology software analysis, our data demonstrate that in addition to this mechanism that predisposes T_{mem} to spatially encounter inflammation, T_{mem} also possess the ability to be recruited to sites of inflammation and participate in early immune responses (Figure 2.3, Figure 2.5). The subsequent immunological consequences of bystander activation are likely highly context-dependent and even the initial trigger for bystander activation can vary substantially (36). In our mouse model, we elicited a localized infection in animals that do not possess Ag-specific T_{mem}. Masopust et al. (118) exposed tissue-resident Ag-specific T cells to their cognate Ag and showed that this could also induce recruitment of bystander-activated T cells into the area where Ag was provided using

a different, IFNγ-dependent mechanism. Considering that bystander activation occurs in all these different experimental systems, we argue that bystander activation is not an immunological accident or vestigial feature of T_{mem}, but a well-orchestrated and conserved part of the immune response. We previously suggested that once bystander-activated, $CD8^+$ T_{mem} functionally resemble NK cells (3). Both are capable of killing targets upon engagement of innate immunoreceptors (specifically NKG2D); however, bystander-activated $CD8^+$ T_{mem} typically do not express innate inhibitory receptors that restrict killing (3). In addition, both migrate to sites of early immune activation and produce IFNγ, although NK cell migration appeared to be predominantly dependent on CCR5 (115). Thus, bystander-activated Ag-nonspecific $CD8^+$ T_{mem} can execute an NK-like program without being susceptible to inhibitory signals capable of disrupting NK-mediated killing/migration. An elegant study by Teixeiro and colleagues demonstrated that T_{mem} require tonic recognition of self (peptide/MHC) (beneath the threshold of TCR binding to cognate Ag/MHC) to become bystander-activated (89), indicating that the NK cells and bystander-activated T cells have complimentary rather than congruent surveillance functions despite the functional overlap. The goal is likely the same—curtail initial pathogen spread until the adaptive immune response is fully developed.

Finally, our data also provide a plausible explanation for why tumor nonspecific T_{mem} form part of the T cell infiltrate within solid tumors (41). Given that a tumor with a T cell infiltrate is by definition inflammatory and our data show that T_{mem} migrate to sites of inflammation, T_{mem} may be continually recruited in this context. Bystander-activated T cells do not see Ag in the tumor and should not become functionally exhausted, as exhaustion is a TCR-dependent process (119), which is also consistent with their recently reported phenotype in tumors (41). Bystander-activated T cells could potentially contribute to tumor clearance, either by NKG2D—NKG2D ligand mediated cytotoxicity or by IFNγ-mediated macrophage activation, which has been shown to lead to tumor cell clearance when NK cells were the source of IFNγ (82). However, these bystander-activated T cells may also occlude Ag-specific T cells, as both bystander-activated T cells and Ag-specific effector cells use CXCR3 to find target cells (110), thus competing for the same signals. Two recent studies demonstrate that the naive T cell response is highly sensitive to competition for Ag and even a minimal overlap in epitope-specificity by a T_{mem} population is sufficient to impair a primary T cell response (120, 121). Future studies will need to address if bystander-activated T cells are similarly effective at impairing primary T cell responses, particularly lower affinity responders (122), by limiting Ag availability. This is particularly relevant in the context of vaccination as we found that bystander-activated T cells still surrounded APCs

as the Ag-specific effector T cells developed and entered the area. Future studies will also need to examine if there is competition between Ag-specific effector T cells and bystander-activated T_{mem} and determine whether effector cells have other means to outcompete bystander-activated T_{mem} to access target cells or APCs. These interactions should also be considered for IL-15-based immunotherapies (123) that would activate Ag-specific and nonspecific T cells.

In summary, based on our data we propose that T_{mem}, a hallmark population of the adaptive immune system, play an active and critical role in the initiation of the early immune response even when inflammatory events are highly localized.

2.4 An updated understanding of localized bystander activation

Based on our findings, bystander activation can be elicited by even limited amounts of inflammation. While we show that the cytotoxic effector program is limited to the first few days of infection, it is still unclear if bystander activation durably alters $CD8^+$ T_{mem} in any way after inflammation resolves. Of note, we are the first to observe bystander activation after i.m. vaccination with viral vector-based vaccines. This contrasts with another study which examined bystander activation following yellow fever virus (YFV) and Dryvax vaccination (124). This study was unable to find evidence of bystander activation. However, the earliest time points examined were days 9 and 11 following Dryvax and YFV administration, respectively. YFV immunization results in transient viremia that can be measured between days 3 and 7 (124). Given that bystander activation of T_{mem} is transient and depends on the presence of inflammatory cues, the lack of bystander activation at time points past viremia is in line with our mouse models of acute infection, in which bystander activation is limited to the first few days of infection. Thus, earlier sampling in vaccine studies will be necessary to determine how widely bystander activation occurs in this context and its influence on the subsequent adaptive immune response.

Here we found non-specific T_{mem} recruitment to inflammation as an active method for localized bystander activation and bystander-mediated killing. While this could underly the phenomenon of vaccine-induced bystander activation in our sample set, follow-up studies from Linda Wakim's lab identified a passive pathway to localized bystander activation. Intranasal challenge with LPS or heat-killed or live bacteria revealed that T_{RM} located in the lung were bystander activated within 3 h of challenge (56). Together, this suggests two distinct pathways to localized bystander activation exist, one in which nearby T cells are passively bystander activated in situ Figure 2.20A, and

another where T cells are actively drawn towards bystander-activating cytokines Figure 2.20B. Further investigation will be necessary to determine if bystander activation differentially affects conventional (i.e., circulating) versus tissue resident CD8$^+$ T_{mem}.

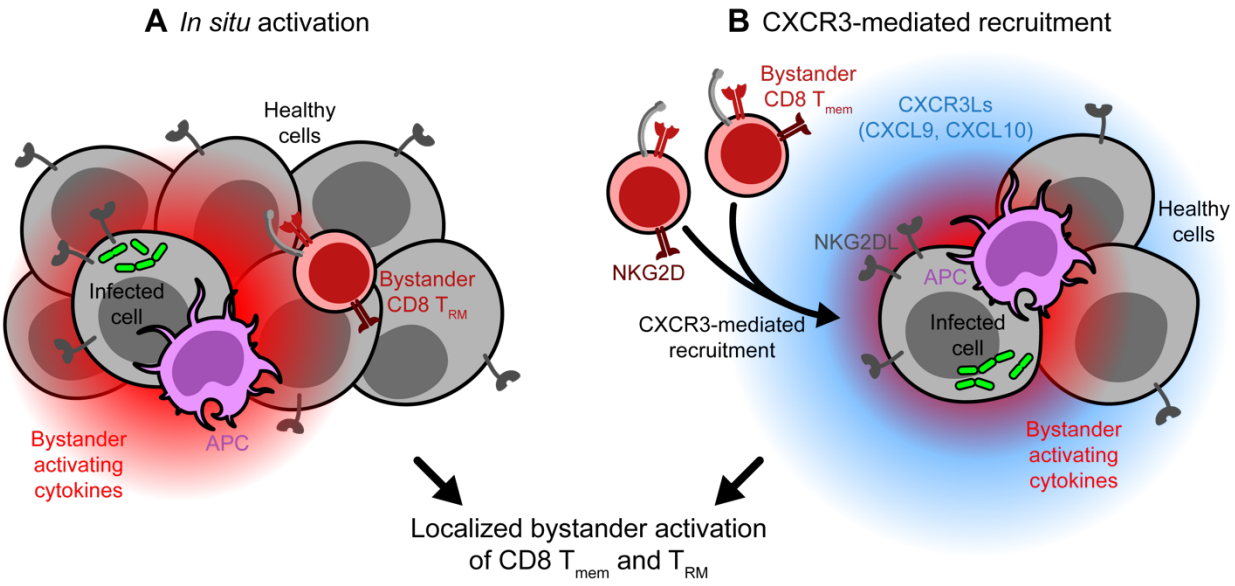

Figure 2.20 Passive and active pathways to localized bystander activation.

A Localized infection will lead to the generation of proinflammatory cytokines that can passively bystander activate CD8$^+$ T_{RM} in situ. **B** CXCR3 ligands (CXCR3L), including CXCL9 and CXCL10, are produced at sites of early immune activation. Circulating bystander CD8$^+$ T_{mem} are actively recruited in a CXCR3-dependent manner to these sites, in which they encounter bystander-activating cytokines. **A** and **B** both result in localized bystander activation and bystander-mediated effector responses.

2.5 Methods

2.5.1 Human clinical samples from HVTN 908

We acquired cryopreserved PBMC from participants enrolled in HVTN 908 (ClinicalTrials.gov NCT00908323), a parallel sub study of the HIV vaccine trial, HVTN 205 (ClinicalTrials.gov NCT00820846), in which volunteers were vaccinated with pGA2/JS7 DNA and MVA/HIV62 (96). All participants provided informed consent under HVTN protocols 908 and 205 under approval of HIV Vaccine Trials Network Institutional Review Boards. Our use of these human PBMC samples were approved by the HIV Vaccine Trials Network Institutional Review Boards and we conducted this study in compliance with all relevant ethical regulations. We specifically interrogated PBMC

at D112 (pre-immunization with MVA/HIV62) and D115 (3d post immunization with MVA/HIV62), collected under the HVTN 908 protocol. At D112, after PBMC draw, volunteers either received their first MVA/HIV62 boost or a saline placebo. Of these, we received PBMC from $n = 6$ MVA/HIV62 vaccinees and $n = 6$ saline placebo controls. Of note, vaccination regimen was blinded until completion of data acquisition and analysis.

2.5.2 Flow cytometric analysis of HVTN 908 samples

We thawed all D112 and D115 samples and immediately stained for markers outlined in Table 2.1. All stains occurred at room temperature (RT). We conducted viability staining in 1× phosphate-buffered saline (PBS) for 20 min. We simultaneously blocked nonspecific Fc and stained for tetramer for 1 h in 2% FBS-supplemented PBS (FACSWash). We then stained all other surface markers in FACSWash for 20 min. After, we fixed cells for 20 min in cytofix/cytoperm (BD Biosciences, San Diego, CA). Afterwards, we stained intracellular markers in 1× perm/wash buffer (BD Biosciences) for 30 min. We resuspended cells in FACSWash before acquiring events on a FACSymphony (BD Biosciences), which were later analyzed using FlowJo v9 and v10 (BD Biosciences). Gating strategies are depicted in Figure 2.21.

Table 2.1 Human bystander activation flow cytometry panel

Panel used for analyses in Figure 2.1; gating strategy in Figure 2.21

Antigen	Conjugate	Clone	Vendor	Dilution
Viability stain (in 1x PBS)				
LIVE/DEAD blue fixable viability dye (BViD)	UV450	N/A	Thermo Fisher Scientific	1:500
Tetramer stain (in FACSWash)				
GILGFVFTL (IAV $M1_{58-66}$) HLA-A*02 tetramer	PE	N/A	Fred Hutch	1:200
YVLDHLIVV (EBV $BRLF1_{190-198}$) HLA-A*02 tetramer	APC	N/A	Fred Hutch	1:200
Human TruStain FcX	N/A	N/A	BioLegend	1:20
Surface stain (in FACSWash)				
CD8	BUV395	RPA-T8	BD Biosciences	1:25
HLA-DR	BUV661	G46-6	BD Biosciences	1:50
CD69	BUV737	FN50	BD Biosciences	1:100
4-1BB (CD137)	BV421	4B4-1	BD Biosciences	1:25
CD45RA	BV510	HI100	BD Biosciences	1:80
CD161	BV605	HP-G310	BioLegend	3:50
CD4	BV711	OKT4	BioLegend	1:80
CD3	BV786	SK7	BD Biosciences	1:50
TCR Vα7.2	FITC	3C10	BioLegend	1:10
CD56	BB700	B159	BD Biosciences	1:50
CCR7 (CD197)	PE-CF594	150503	BD Biosciences	1:20
PD-1 (CD279)	PE-Cy7	EH12.1	BD Biosciences	1:50
CD45RO	APC-H7	UCHL1	BD Biosciences	1:25
Human TruStain FcX	N/A	N/A	BioLegend	1:20
BD Cytofix/Cytoperm fixation				
Intracellular stain (in 1x BD Perm/Wash)				
Granzyme B	AF700	GB11	BD Biosciences	1:80
Human TruStain FcX	N/A	N/A	BioLegend	1:20

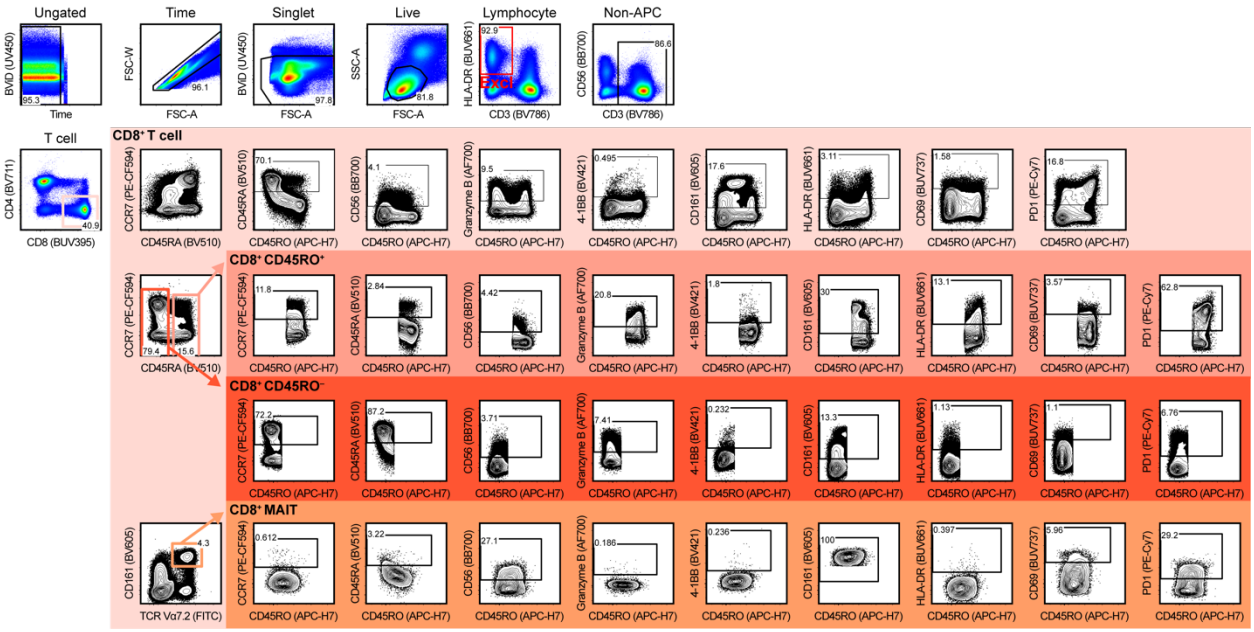

Figure 2.21 Flow cytometry gating strategy for HVTN 205/908 data.

Gating strategy for conventional and non-conventional $CD8^+$ T cell subsets is representative of that used in Figure 2.1; reagent list in Table 2.1

2.5.3 Mice

All mouse protocols in this study were approved by the Fred Hutchinson Cancer Research Center's Institutional Animal Care and Use Committee. All experimentation that we conducted in this study was in compliance with the ethical regulations outlined by the Institutional Animal Care and Use Committee. All mice were maintained in specific pathogen-free conditions. We purchased 6-week-old female C57BL/6 J mice from the Jackson Laboratory (Bar Harbor, ME). We maintained WT OT-I TCR transgenic mice on a CD45.1 background. Dr. Ross Kedl (University of Colorado, Denver) kindly provided *Cxcr3*$^{-/-}$ OT-I TCR transgenic mice on a CD45.1/CD45.2 background. Dr. Surojit Sarkar (Seattle Children's Research Institute) kindly provided LNs from P14 TCR transgenic mice on a Thy1.1 background. We collected submandibular blood in heparin from facial vein puncture immediately preceding euthanasia. After euthanasia, via CO_2 overdose and cervical dislocation, we collected spleens and axial, inguinal, and cervical LNs from mice and separated these tissues for analyses.

2.5.4 Viral and bacterial infections/immunizations

We used an OVA-expressing VSV construct. We used WT and *actA*$^{-}$ LM, as well as OVA- and gp33-expressing recombinants of these LM strains. We grew LM in BHI media (Thermo Fisher, Waltham, MA) to the log phase of growth (determined by OD_{600}). All pathogens were diluted in sterile 1× PBS for i.v. injection.

2.5.5 Adoptive transfers

We mechanically isolated lymphocytes from LN that were harvested from infection- and immunization-naive, 6- to 12-week-old female OT-I mice. To accomplish this, we mechanically passed tissue through a 70 μm cell strainer. We immediately enriched $CD8^+$ OT-I or P14 T cells using Miltenyi CD8 negative selection antibody cocktail and beads (Miltenyi Biotec, Germany), which we confirmed using flow cytometry. We diluted OT-I T cells in sterile 1× PBS and adoptively transferred 1×10^4 cells per C57BL/6 J recipient via i.v. injection. In order to visualize Ag-specific effector responses during LM infection, we immunized WT OT-I recipient mice with 2×10^3 CFU LM-OVA immediately after adoptive transfer. We sacrificed these mice 7 days post LM-OVA immunization. To develop OT-I memory mice, we infected OT-I recipient mice with 2×10^6 PFU VSV-OVA within 1 day after OT-I adoptive transfer. We surveyed OT-I expansion in peripheral blood at 7 days post immunization to confirm successful VSV-OVA infection. We aged mice ≥ 60 days until contraction of OT-I cells stabilized before conducting bystander-activating LM immunizations. To induce bystander activation in OT-I memory mice, we immunized animals with 1×10^6 CFU *actA*$^{-}$ LM or 1×10^3 CFU WT LM. We sacrificed mice 24, 72, and 120 h post immunization via CO_2 euthanasia.

2.5.6 In vivo CD8β labeling

As described (107, 108), we i.v. injected mice with 3 μg APC-conjugated anti-CD8β (eBioH35-17.2), which stains cells in circulation (including splenic RP), but not those in parenchymal tissues (including LN and splenic WP). After 3 min, we collected submandibular blood via facial vein puncture, euthanized mice, and harvested tissues. We immediately prepared single-cell suspensions of tissues used for flow cytometric analysis and stained with a distinct anti-CD8α antibody to delineate RP and WP $CD8^+$ T cells (alongside other antibodies for immunophenotyping). We confirmed in vivo CD8β labeling using IF. We stained acetone-fixed

8 µm spleen sections with biotinylated anti-APC (50 µg/mL, 1 h, RT, 5% mouse serum, 5% human serum in TBS). We then stained with streptavidin (SA)-Alexa fluor (AF)647 (20 µg/mL, 1 h, RT, 5% mouse serum, 5% human serum in TBS). We counterstained with DAPI (5 min, RT, PBS) and mounted slides in Prolong Gold (Thermo Fisher). We acquired images on an Aperio SlideScan FL (Leica Biosystems, Wetzlar, Germany), which were then processed in ImageJ (NIH, Bethesda, MD).

2.5.7 Ex vivo flow cytometric analysis of mouse tissues

We prepared single-cell suspensions of LN and spleen by mechanically passing tissue through a 70 µm cell strainer in complete RP10 media (RPMI 1640 supplemented with 10% FBS, 2 mM L-glutamine, 100 U/mL penicillin–streptomycin, 1 mM HEPES, 1 mM sodium pyruvate, 0.05 mM β-mercaptoethanol). To count cells, we stained suspension aliquots with trypan blue (Gibco) and counted using a TC20 Automated Cell Counter (Bio-Rad, Hercules, CA). We incubated blood with 1 mL and LN and spleen single-cell suspensions with an equal volume of ACK lysis buffer (Gibco) on ice for 20 min. We conducted all stains for flow cytometry on ice. We conducted viability staining in 1× PBS for 20 min. We stained surface markers in FACSWash + (1 × PBS supplemented with 2% FBS plus 0.2% sodium azide, and 2 mM EDTA) for 30 min. We fixed cells in cytofix/cytoperm (BD Biosciences) or eBioscience FOXP3 fixation/permeabilization buffer (Thermo Fisher) for 20 min. We then stained intracellular markers in 1× perm/wash buffer (BD Biosciences) or 1× eBioscience FOXP3 permeabilization buffer (Thermo Fisher) for 30 min. We resuspended cells in FACSWash + before acquiring events on an LSR II (BD Biosciences) or FACSSymphony (BD Biosciences), which were later analyzed using FlowJo v9 and v10 (BD Biosciences). Flow reagents, dilutions, and fixation/permeabilization methods are listed in Table 2.2 and Table 2.3. Gating strategy is depicted in Figure 2.22.

Table 2.2 Mouse general bystander activation flow cytometry panel

Panel used for analyses in Figure 2.4, Figure 2.7, Figure 2.8, Figure 2.10, Figure 2.11, Figure 2.16, Figure 2.17; gating strategy in Figure 2.22.

Antigen	Conjugate	Clone	Vendor	Dilution
i.v. stain				
CD8β	APC	eBioH35-17.2	Thermo Fisher Scientific	3µg per mouse
Viability stain (in 1x PBS)				
LIVE/DEAD aqua fixable viability dye (AViD)	V510	N/A	Thermo Fisher Scientific	1:500
Surface stain (in FACSWash+)				
CD45.1	BUV395	A20	BD Biosciences	1:200
CXCR3	BV421	CXCR3-173	BD Biosciences	1:100
KLRG1	BV605	2F1	BD Biosciences	1:200
NKG2D	BV711	CX5	BD Biosciences	1:200
CD62L	FITC	MEL-14	Thermo Fisher Scientific	1:300
CD8α	PE-CF594	53-6.7	BD Biosciences	1:300
CD127	APC-e780	A7R34	Thermo Fisher Scientific	1:100
CD16/32 (Fc block)	Purified	24.G2	BD Biosciences	1:300
BD Cytofix/Cytoperm fixation				
Intracellular stain (in 1x BD Perm/Wash)				
IFNγ	BUV737	XMG1.2	BD Biosciences	1:100
Granzyme B	PE	GB11	Thermo Fisher Scientific	1:100
Ki-67[a]	PE-Cy7	16A8	BioLegend	1:200
Granzyme A[a]	PE-Cy7	GzA-3G8.5	Thermo Fisher Scientific	1:100
CD16/32 (Fc block)	Purified	24.G2	BD Biosciences	1:300

[a]anti-Ki-67 or –Granzyme A were used alone (i.e., not in combination) in staining panel

Table 2.3 Mouse T_{RM} bystander activation flow cytometry panel

Panel used for analyses in Figure 2.9; gating examples for T_{RM} phenotype cells included in Figure 2.9 .

Antigen	Conjugate	Clone	Vendor	Dilution
i.v. stain				
CD8β	APC	eBioH35-17.2	Thermo Fisher Scientific	3µg per mouse
Viability stain (in 1x PBS)				
LIVE/DEAD aqua fixable viability dye (AViD)	V510	N/A	Thermo Fisher Scientific	1:500
Surface stain (in FACSWash+)				
CD45.1	BUV395	A20	BD Biosciences	1:200
CXCR3	BV421	CXCR3-173	BD Biosciences	1:100
PD-1	BV605	29F.1A12	BioLegend	1:150
NKG2D	BV711	CX5	BD Biosciences	1:200
CD103	BV786	M290	BD Biosciences	1:100
CD8α	PE-CF594	53-6.7	BD Biosciences	1:300
CD69	PE-Cy7	H1.2F3	Thermo Fisher Scientific	1:100
CD45.2	AF700	104	Thermo Fisher Scientific	1:300
CD16/32 (Fc block)	Purified	24.G2	BD Biosciences	1:300
Fixation in 1x eBioscience FOXP3 fixation/permeabilization buffer				
Intracellular stain (in 1x FOXP3 permeabilization buffer)				
IFNγ	BUV737	XMG1.2	BD Biosciences	1:100
Ki-67	AF488	11F6	BioLegend	1:200
Granzyme B	PE	GB11	Thermo Fisher Scientific	1:100
CD16/32 (Fc block)	Purified	24.G2	BD Biosciences	1:300

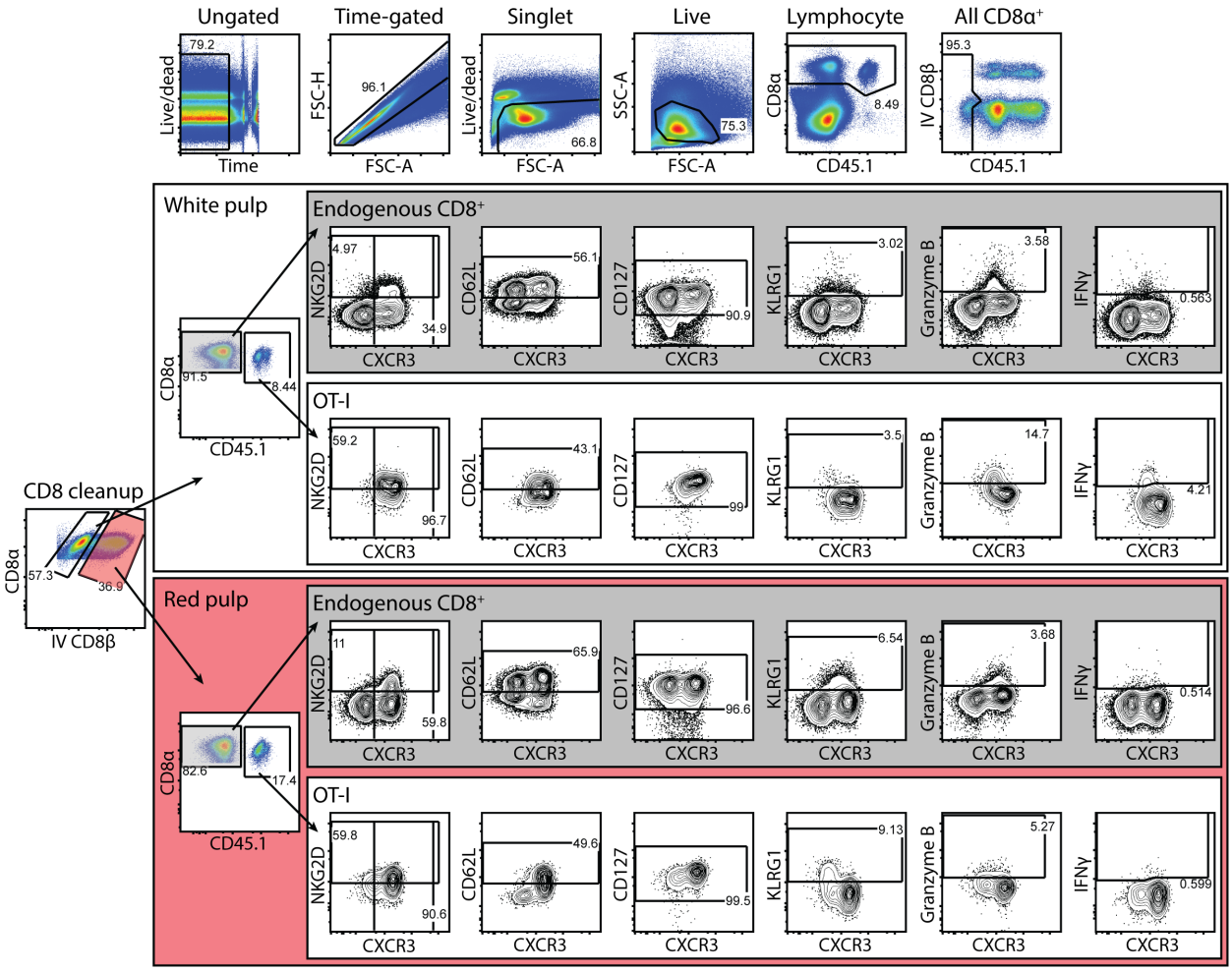

Figure 2.22 Flow cytometry gating strategy for mouse bystander CD8⁺ T_{mem} profiling

Gating strategy used for mouse samples in Figure 2.4, Figure 2.7, Figure 2.8, Figure 2.10, Figure 2.11, Figure 2.16, Figure 2.17; reagent list in Table 2.2.

2.5.8 In vitro CXCR3L stimulations and cycloheximide chase

We harvested spleen and LN from OT-I memory animals (Figure 2.2) and prepared single-cell suspensions. We immediately enriched CD8⁺ OT-I using Miltenyi CD8-negative selection antibody cocktail and beads (Miltenyi Biotec). After manually counting cells using trypan blue staining, we plated 0.5–2 million CD8⁺ T cells per well in a 96-well U-bottom tissue culture plate. We briefly treated cells with sterile dimethyl sulfoxide (DMSO) or 15 µg/mL cycloheximide (CHX) (Sigma Aldrich, St. Louis, MO) as described in Meiser et al. (113), before stimulating with recombinant mouse CXCL9 and CXCL10 (BioLegend, San Diego, CA) in combination at 10, 50, or 100 ng/mL in complete RP10. Media alone was used as a negative control. We cultured cells

in recombinant CXCR3L-containing media at 37 ºC 5% CO_2 for 30 min. Afterwards, we washed cells three times with 37 ºC 1× Hanks Balanced Salt Solution (Gibco) supplemented with DMSO or 15 µg/mL CHX (depending on treatment group). We then cultured cells in complete RP10 with DMSO or 15 µg/mL CHX and surveyed cells using flow cytometry at various timepoints. As a positive control, we stimulated $CD8^+$ T cells with 1 µM SIINFEKL peptide (Genemed Synthesis Inc., San Antonio, TX) in complete RP10 in the presence of 1:1000 Golgi plug (BD Biosciences) and DMSO or 15 µg/mL CHX. After 6 h of culture, we harvested cells and conducted flow staining for intracellular cytokines. We employed previously outlined flow cytometric staining protocols for mouse tissues (see ex vivo flow cytometric analysis of mouse tissues) to evaluate CXCR3 expression and cytokine production; flow reagents for CXCR3L and peptide stimulation assays are respectively listed in Table 2.4 and Table 2.5. Gating strategies are depicted in Figure 2.23.

Table 2.4 Mouse CXCR3L stimulation flow cytometry panel

Panel used for analyses in Figure 2.12 and Figure 2.13; corresponding gating example is depicted in Figure 2.23.

Antigen	Conjugate	Clone	Vendor	Dilution
LIVE/DEAD aqua fixable viability dye (AViD)	V510	N/A	Thermo Fisher Scientific	1:500
Surface stain (in FACSWash+)				
CD45.1	BUV395	A20	BD Biosciences	1:200
CXCR3	BV421	CXCR3-173	BD Biosciences	1:100
CD44	FITC	IM7	Thermo Fisher Scientific	1:300
CD45.2	PE	104	Thermo Fisher Scientific	1:300
CD8α	PE-CF594	53-6.7	BD Biosciences	1:300
NKG2D	APC	CX5	Thermo Fisher Scientific	1:100
CD16/32 (Fc block)	Purified	24.G2	BD Biosciences	1:300
CD45.2	AF700	104	Thermo Fisher Scientific	1:300
CD16/32 (Fc block)	Purified	24.G2	BD Biosciences	1:300
BD Cytofix/Cytoperm fixation				

Table 2.5 Mouse CHX intracellular cytokine staining flow cytometry panel

Panel used for analyses in Figure 2.13.

Antigen	Conjugate	Clone	Vendor	Dilution
Viability stain (in 1x PBS)				
LIVE/DEAD aqua fixable viability dye (AViD)	V510	N/A	Thermo Fisher Scientific	1:500
Surface stain (in FACSWash+)				
CD45.1	BUV395	A20	BD Biosciences	1:200
CXCR3	BV421	CXCR3-173	BD Biosciences	1:100
CD4	BV786	GK1.5	BD Biosciences	1:200
CD44	FITC	IM7	Thermo Fisher Scientific	1:300
CD8α	PE-CF594	53-6.7	BD Biosciences	1:300
CD45.2	AF700	104	Thermo Fisher Scientific	1:300
CD16/32 (Fc block)	Purified	24.G2	BD Biosciences	1:300
Fixation in 1x eBioscience FOXP3 fixation/permeabilization buffer				
Intracellular stain (in 1x FOXP3 permeabilization buffer)				
IFNγ	PE	XMG1.2	BD Biosciences	1:100
TNFα	AF647	MP6-XT22	BD Biosciences	1:100
CD16/32 (Fc block)	Purified	24.G2	BD Biosciences	1:300

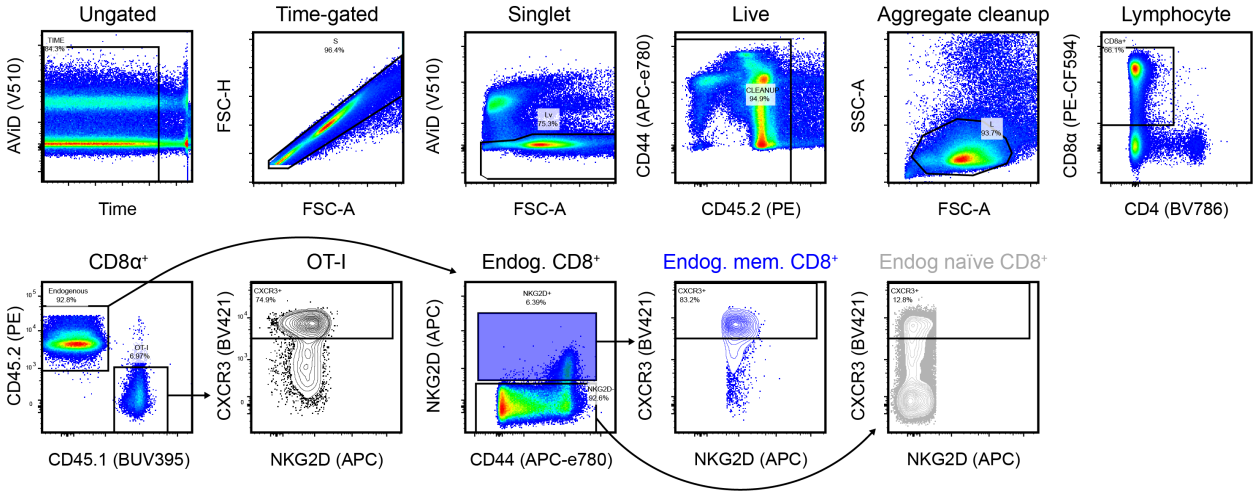

Figure 2.23 Flow cytometry gating strategy for in vitro CXCR3L stimulations

2.5.9 In vitro bystander-activating cytokine stimulations

We harvested spleen from memory WT and *Cxcr3*$^{-/-}$ OT-I animals and prepared single-cell suspensions (as earlier described in ex vivo flow cytometric analysis of mouse tissues). After erythrocyte lysis, bulk leukocytes were plated at ~ 1–2 million per well in a 96-well U-bottom tissue culture plate and stimulated with combinations of 100 ng/ml recombinant mouse IL-12p70, IL-15, and IL-18 (BioLegend) in the presence of 1:1000 Golgi plug. Media with 1:1000 Golgi plug, but without cytokines, was used as a negative control. We cultured cells for 6 h at 37 ºC 5% CO_2 before harvesting for intracellular cytokine staining. We conducted previously stated flow cytometry staining protocols using flow reagents listed in Table 2.6. Gating strategies are depicted in Figure 2.24.

Table 2.6 Flow cytometry panel for mouse bystander-activating cytokine stimulations.

Antigen	Conjugate	Clone	Vendor	Dilution
Viability stain (in 1x PBS)				
LIVE/DEAD aqua fixable viability dye (AViD)	V510	N/A	Thermo Fisher Scientific	1:500
Surface stain (in FACSWash+)				
CD45.1	FITC	A20	BD Biosciences	1:200
CXCR3	BV650	CXCR3-173	BD Biosciences	1:100
NKG2D	BV711	CX5	BD Biosciences	1:200
CD44	APC-e780	IM7	Thermo Fisher Scientific	1:300
CD8α	PE-CF594	53-6.7	BD Biosciences	1:300
CD16/32 (Fc block)	Purified	24.G2	BD Biosciences	1:300
Fixation in 1x eBioscience FOXP3 fixation/permeabilization buffer				
Intracellular stain (in 1x FOXP3 permeabilization buffer)				
IFNγ	e450	XMG1.2	Thermo Fisher Biosciences	1:100
Granzyme B	PE	GB11	Thermo Fisher Scientific	1:100
CD16/32 (Fc block)	Purified	24.G2	BD Biosciences	1:300

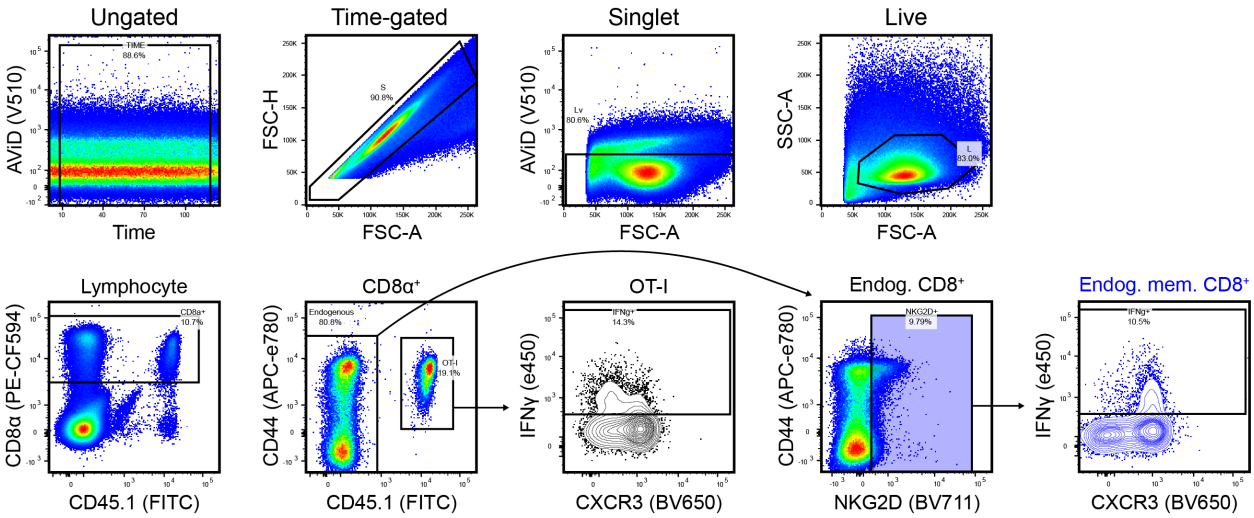

Figure 2.24 Flow cytometry gating strategy for in vitro bystander-activating cytokine stimulations

2.5.10 Immunofluorescence

For staining panels that exclude IFNγ, CXCL9, CXCL10, CD11b, or NKG2D, we immediately embedded unfixed tissues on edge in OCT (Sakura Finetek, Torrance, CA). We froze the tissues in the vapor phase of liquid nitrogen before storing the OCT blocks at −80 ºC. We cut 8 µm sections of tissues using a Leica CM1950 cryostat (Leica, Wetzlar, Germany), which were dried 18−72 h at RT before being stored at −80 ºC. For CD169, CD45.1, and LM Ag staining, we fixed slides in − 20 ºC acetone for 5 min and allowed slides to dry completely. For CD45.1, Ki-67, and granzyme B staining, we fixed slides in cytofix/cytoperm (BD Biosciences) for 5 min. We washed and rehydrated slides in PBS, blocked endogenous biotin (Vector Labs, Burlingame, CA), and incubated in staining buffer (1× TBS, 5% mouse serum, 5% human serum). All stains were conducted in staining buffer for 1 h at RT or overnight at 4 ºC; when staining for intracellular granzyme B and Ki-67, staining buffer was supplemented with 10% perm/wash (BD biosciences) to ensure cell permeabilization. For staining panels that include IFNγ, CXCL9, CXCL10, CD11b, or NKG2D, we fixed tissues overnight in 4ºC cytofix (BD Biosciences) diluted 1:4 in 1× PBS. We then dehydrated fixed tissues in 30% w/v sucrose in 1× PBS for 24 h. We similarly embedded, stored, sectioned, and blocked endogenous biotin in fixed and unfixed tissues. All stains on previously fixed tissues used 1× TBS + 0.3% Triton-X supplemented with 5% mouse serum and 5% human serum as staining buffer. We used 1× TBS + 0.3% Triton-X as a washing buffer. We conducted all stains for 2 h at RT or overnight at 4 ºC. Images were collected from an Aperio SlideScan FL or SP8 confocal microscope (Leica Biosystems) using × 20 objectives. IF reagents,

dilutions, and fixation/permeabilization methods are listed in Table 2.7, Table 2.8, Table 2.9, Table 2.10, Table 2.11, Table 2.12, Table 2.13.

Table 2.7 Mouse bystander OT-I T_{mem} location IF panel

Tissue type: unfixed				
Post-sectioning fixation: -20ºC acetone (5 minutes)				
Staining buffer: TBS + 5% human serum, 5% mouse serum				
Antigen	**Conjugate**	**Clone**	**Vendor**	**Dilution**
1º stain				
Mouse anti-mouse CD45.1	Biotin	A20	Thermo Fisher Scientific	1:50 (10µg/mL)
Rat anti-mouse CD169 (Siglec-1)	AF594	3D6.112	BioLegend	1:200 (2.5µg/mL)
2º stain				
Streptavidin	AF647	N/A	Thermo Fisher Scientific	1:100 (20µg/mL)
Rabbit anti-Listeria O Antiserum	N/A	N/A Polyclonal (Cat: 223021)	BD Biosciences	1:1,000-10,000[a]
3º stain				
Donkey anti-rabbit IgG	DyLight 488	Poly4064	BioLegend	1:100 (5µg/mL)
Nuclear counterstain				
DNA	DAPI	N/A	Thermo Fisher Scientific	1ng/mL

[a]Dilution range dependent on reagent lot

Table 2.8 Mouse bystander activation IF panel

Tissue type: unfixed				
Post-sectioning fixation: 1:4 BD Cytofix in 1x PBS (5 minutes)				
Staining buffer: 1x BD Perm/Wash in TBS + 5% human serum, 5% mouse serum				
Antigen	**Conjugate**	**Clone**	**Vendor**	**Dilution**
1º stain				
Mouse anti-mouse CD45.1	Biotin	A20	Thermo Fisher Scientific	1:50 (10µg/mL)
Rat anti-human/mouse Ki-67	N/A	11F6	BioLegend	1:200 (2.5µg/mL)
Goat anti-mouse Granzyme B	N/A	N/A Polyclonal (Cat: AF1865)	R&D Systems	1:100 (2µg/mL)
2º stain				
Streptavidin	AF594	N/A	BioLegend	1:100 (5µg/mL)
Chicken anti-rat IgG	AF647	N/A Polyclonal (Cat: A21472)	Thermo Fisher Scientific	1:100 (20µg/mL)
Donkey anti-goat IgG	AF488	N/A Polyclonal (Cat: A11055)	Thermo Fisher Scientific	1:100 (20µg/mL)
Nuclear counterstain				
DNA	DAPI	N/A	Thermo Fisher Scientific	1ng/mL

Table 2.9 Mouse splenic architecture IF panel

Tissue type: fixed (1:4 BD Cytofix in 1x PBS, overnight)				
Post-sectioning fixation: N/A				
Staining buffer: TBS + 0.3% Triton X + 5% human serum, 5% mouse serum				
Antigen	**Conjugate**	**Clone**	**Vendor**	**Dilution**
1º stain				
Rat IgG2b anti-mouse CD11b	N/A	M1/70	BioLegend	1:100 (5µg/mL)
Rat IgG1 anti-mouse CD169 (Siglec-1)	AF594	3D6.112	BioLegend	1:200 (2.5µg/mL)
Rabbit anti-Listeria O Antiserum	N/A	N/A Polyclonal (Cat: 223021)	BD Biosciences	1:1,000-10,000[a]
2º stain				
Mouse anti-rat IgG2b	AF647	MRG2b-85	BioLegend	1:100 (5µg/mL)
Donkey anti-rabbit IgG	DyLight 488	Poly4064	BioLegend	1:100 (5µg/mL)
Nuclear counterstain				
DNA	DAPI	N/A	Thermo Fisher Scientific	1ng/mL

[a]Dilution range dependent on reagent lot

Table 2.10 Mouse CXCR3L IF panel

Tissue type: fixed (1:4 BD Cytofix in 1x PBS, overnight)				
Post-sectioning fixation: N/A				
Staining buffer: TBS + 0.3% Triton X + 5% human serum, 5% mouse serum				
Antigen	**Conjugate**	**Clone**	**Vendor**	**Dilution**
1º stain				
Armenian hamster anti-mouse CXCL9	e660	MIG-2F5.5	Thermo Fisher Scientific	1:50 (4µg/mL)
Goat anti-mouse CXCL10	N/A	N/A Polyclonal (Cat: AF-466-NA)	R&D Systems	1:50 (4µg/mL)
2º stain				
Chicken anti-goat IgG	AF488	N/A Polyclonal (Cat: A21467)	Thermo Fisher Scientific	1:100 (20µg/mL)
Nuclear counterstain				
DNA	DAPI	N/A	Thermo Fisher Scientific	1ng/mL

Table 2.11 Mouse CXCR3L isotype control IF panel

Tissue type: fixed (1:4 BD Cytofix in 1x PBS, overnight)				
Post-sectioning fixation: N/A				
Staining buffer: TBS + 0.3% Triton X + 5% human serum, 5% mouse serum				
Antigen	**Conjugate**	**Clone**	**Vendor**	**Dilution**
1º stain				
Armenian hamster IgG control	eFluor 660	eBio299Arm	Thermo Fisher Scientific	1:50 (4µg/mL)
Goat IgG isotype control	N/A	N/A Polyclonal (Cat: 02-6202)	Thermo Fisher Scientific	1:1250 (4µg/mL)
2º stain				
Chicken anti-goat IgG	AF488	N/A Polyclonal (Cat: A21467)	Thermo Fisher Scientific	1:100 (20µg/mL)
Nuclear counterstain				
DNA	DAPI	N/A	Thermo Fisher Scientific	1ng/mL

Table 2.12 Mouse IFNγ bystander activation IF panel

Tissue type: fixed (1:4 BD Cytofix in 1x PBS, overnight)				
Post-sectioning fixation: N/A				
Staining buffer: TBS + 0.3% Triton X + 5% human serum, 5% mouse serum				
Antigen	**Conjugate**	**Clone**	**Vendor**	**Dilution**
1º stain				
Mouse anti-mouse CD45.1	Biotin	A20	Thermo Fisher Scientific	1:50 (10µg/mL)
Goat anti-mouse Granzyme B	N/A	N/A Polyclonal (Cat: AF1865)	R&D Systems	1:100 (2µg/mL)
Rat anti-mouse IFNγ	N/A	XMG1.2	Thermo Fisher Scientific	1:50 (4µg/mL)
2º stain				
Streptavidin	AF647	N/A	Thermo Fisher Scientific	1:100 (20µg/mL)
Chicken anti-goat IgG	AF488	N/A Polyclonal (Cat: A21467)	Thermo Fisher Scientific	1:100 (20µg/mL)
Chicken anti-rat IgG	AF594	N/A Polyclonal (Cat: A21471)	Thermo Fisher Scientific	1:100 (20µg/mL)
Nuclear counterstain				
DNA	DAPI	N/A	Thermo Fisher Scientific	1ng/mL

Table 2.13 Mouse NKG2D bystander activation IF panel

Tissue type: fixed (1:4 BD Cytofix in 1x PBS, overnight)				
Post-sectioning fixation: N/A				
Staining buffer: TBS + 0.3% Triton X + 5% human serum, 5% mouse serum				
Antigen	**Conjugate**	**Clone**	**Vendor**	**Dilution**
1º stain				
Mouse anti-mouse CD45.1	AF647	A20	BioLegend	1:50 (10µg/mL)
Goat anti-mouse Granzyme B	N/A	N/A Polyclonal (Cat: AF1865)	R&D Systems	1:100 (2µg/mL)
Rat anti-mouse NKG2D	Biotin	MI-6	Thermo Fisher Scientific	1:50 (10µg/mL)
2º stain				
Streptavidin	AF594	N/A	BioLegend	1:100 (5µg/mL)
Chicken anti-goat IgG	AF488	N/A Polyclonal (Cat: A21467)	Thermo Fisher Scientific	1:100 (20µg/mL)
Nuclear counterstain				
DNA	DAPI	N/A	Thermo Fisher Scientific	1ng/mL

2.6 Acknowledgements

We thank Jami R. Erickson for technical assistance in tissue harvesting; We thank Jami R. Erickson and Dietmar Zehn for critical review of the manuscript, Jessica L. Swarts and Julia D. Berkson for technical assistance in tissue harvesting, Veronica Davé for statistical advice, and Kimberly Smythe and Kimberly Melton for their input with IF assays and HALO analysis. We also thank Dr. Ross Kedl and Cody Rester (University of Colorado, Denver) and Dr. Surojit Sarkar (Seattle Children's Research Institute) for generously providing *Cxcr3*$^{-/-}$ OT-I mice and P14 cells, respectively. We thank the HVTN 205/908 study participants, and thank the HVTN 205/908 Protocol Teams, site staff and the NIAID HVTN for providing clinical specimens and data. N.J.M. is a Leslie and Pete Higgins Achievement Rewards for College Scientists Fellow and Dr. Nancy Herrigel-Babienko Memorial Scholar. This work was supported by NIH grants R01 AI 123323 to M.P. and TL1 TR002318 to N.J.M.

Chapter 3. Inflammatory signals are sufficient to elicit TOX expression in mouse and human CD8$^+$ T cells

Maurice NJ, Berner J, Taber AK, Zehn D, Prlic M. Inflammatory signals are sufficient to elicit TOX expression in mouse and human CD8$^+$ T cells. *JCI Insight.* 2021 Jul 8;6(13) e150744. DOI: 10.1172/jci.insight.150744

T cell receptor (TCR) stimulation leads to the expression of the transcription factor thymocyte selection–associated high-mobility group box (TOX). Prolonged TCR signaling, such as encountered during chronic infections or in tumors, leads to sustained TOX expression, which is required for the induction of a state of exhaustion or dysfunction. Although CD8$^+$ T_{mem} in mice typically do not express TOX at steady state, some human T_{mem} express TOX but appear fully functional. This seeming discrepancy between mouse and human T cells has led to the speculation that TOX is differentially regulated between these species, which could complicate the interpretation of preclinical mouse model studies. We report here that, similar to TCR-mediated signals, inflammatory cytokines which cause bystander activation are also sufficient to increase TOX expression in human and mouse T_{mem}. Thus, TOX expression is controlled by the environment, which provides an explanation for the different TOX expression patterns encountered in T cells isolated from specific pathogen–free laboratory mice versus humans. Finally, we report that TOX is not necessary for cytokine-driven expression of programmed cell death 1 (PD-1). Overall, our data highlight that the mechanisms regulating TOX expression are conserved across species and indicate that TOX expression reflects a T cell's activation state and does not necessarily correlate with T cell dysfunction.

3.1 Introduction

T cell exhaustion (i.e., dysfunction) is driven by chronic TCR stimulation with cognate Ag (125-127). It describes a differentiation state in which T cells have diminished capacity to respond to stimulatory inputs and limited effector capacity (126-128). The purpose of T cell exhaustion during chronic infections may be to limit tissue pathologies when pathogen cannot be immunologically eliminated (129, 130). Though exhaustion could be considered an immunologic concession during

chronic infection, it also occurs in tumors and causes an attenuated antitumor cytotoxic T cell response (131). Thus, mechanistically understanding and therapeutically overcoming T cell exhaustion has been a major goal of tumor immunotherapy. Chronic TCR stimulation elicits a program that leads to constitutively high expression of programmed cell death 1 (PD-1) (132). PD-1 is an inhibitory receptor that is expressed by activated and exhausted T cells and is often used as a biomarker to infer T cell functionality (133). When bound to its ligands, PD-1 negatively regulates T cell function (126). Therapeutic targeting of PD-1 with monoclonal antibodies, also referred to as immune checkpoint inhibitors, can reinvigorate a subset of these PD-1–expressing T cells (81, 126, 134, 135).

A set of recent studies demonstrated that the transcription factor thymocyte selection–associated high-mobility group box (TOX) protein drives or stabilizes this TCR-mediated T cell dysfunction and PD-1 upregulation (130, 136-140). When stably expressed, TOX drives Ag-specific T cell exhaustion in mouse models of chronic lymphocytic choriomeningitis virus (LCMV) infection, transplantable B16 melanoma, and inducible hepatocellular carcinoma (130, 136, 137). Further, putative tumor Ag–specific $CD8^+$ T cells isolated from primary human breast, ovarian, and skin cancer samples, as well as those specific for hepatitis C virus (HCV), mirror this phenotype, suggesting TOX dictates exhaustion programs in humans, too (130, 136, 137). Of note, TOX expression by HCV-specific T cells is reduced after treatment and clearance of the infection, but it is still detectable at higher levels than in T cells from HCV infections that spontaneously resolve and among T cells specific for influenza A virus (IAV) (130). Mechanistic insight is provided by targeted deletion of TOX in Ag-specific cytotoxic T cells, which diminishes PD-1 expression and restores functionality at the expense of cell survival (130, 136). Therefore, TOX concedes activation and effector function for exhaustion (i.e., PD-1 expression) and T cell survival during chronic TCR stimulation. In instances of brief TCR engagement, TOX is transiently induced to a level lower than that of exhausted T cells, but with limited known functional consequence (130, 136, 137).

Although the requirement for TOX has been well defined in the context of TCR-mediated dysfunction, there is nascent evidence that TOX expression by itself is not indicative of T cell exhaustion. Recent studies illustrated that TOX expression is detected in some functional $CD8^+$ cells, for instance, in $CD8^+$ effector memory (T_{EM}) and CD45RA-expressing T_{EM} (T_{EMRA}) subsets (141). $CD8^+$ T_{mem} cells specific for the latent viruses, CMV and EBV, had elevated TOX expression, compared with those specific for acute infections, which further suggests that TCR signals are critical in regulating TOX expression (141). In a second study, it was shown that a

fraction of the human T_{mem} population expresses *TOX* transcripts among other signature genes typically associated with T cell exhaustion (142). The observation that functional human T_{mem} cells express TOX also led to questions of whether TOX is functionally conserved between mouse and human T cells (143). Further complicating TOX and exhaustion, the murine tissue-resident T_{mem} (T_{RM}) cell transcriptome is characterized by the concomitant expression of transcripts encoding *Tox*, exhaustion markers, TCR signaling components, and cytotoxic molecules, well after initial priming events (144, 145). Although the role of TOX in these TOX-expressing populations with and without signs of T cell exhaustion is not fully understood, these data suggest that TOX expression by T_{mem} cells cannot be reliably used to extrapolate T cell function.

Although the role of TCR signals in initiating and maintaining PD-1 and TOX expression has been well established, relatively little remains known about non-TCR signals that could regulate their expression in T cells (146). We considered that cytokine-mediated stimuli could also affect TOX expression levels without promoting the induction of T cell exhaustion. First, proinflammatory cytokines, such as IL-15, can induce PD-1 without agonist TCR signals (146). Second, T_{RM} cells that are likely not detecting cognate Ag still upregulate PD-1 and other markers associated with exhaustion (144, 145, 147, 148), yet rely on IL-15 signaling for maintenance in some tissues (149, 150). Thus, inflammatory signals could provide an explanation for some of the seemingly disparate results of TOX expression and T cell function. Here, we show that proinflammatory cytokines were sufficient to induce TOX expression in the absence of agonist TCR signals in both mouse and human $CD8^+$ T_{mem} cells while concurrently inducing the expression of cytotoxic molecules (a phenomenon called bystander activation). Together, these data demonstrate that TOX expression per se does not indicate TCR-mediated dysfunction or even a recent TCR signals. We also demonstrate that PD-1 expression was still upregulated in TOX-deficient T cells, indicating that TOX was not necessary for PD-1 expression. Overall, our data reveal that TCR-independent mechanisms shape TOX and PD-1 expression heterogeneity in T_{mem} cells and indicate that they are conserved in both mouse and human T cells. Though these findings ultimately complicate the use of TOX exclusively as an exhaustion biomarker, they implicate TOX in inflammation-driven programs of T_{mem} cell activation.

3.2 Results

3.2.1 Cytokine stimulation induces TOX expression in mouse CD8$^+$ T_{mem}

The proinflammatory cytokines IL-12, IL-15, and IL-18 elicit IFNγ and GzmB expression in mouse and human CD8$^+$ T_{mem} in the absence of agonist TCR signals, a phenomenon commonly referred to a bystander activation (43, 44, 75). We first sought to determine if these cytokines could also induce TOX expression in a TCR-independent manner. To generate a well-defined population of CD8$^+$ T_{mem}, we transferred congenically marked OT-I CD8$^+$ T cells, which express a TCR specific for the SIINFEKL peptide of OVA, into WT C57BL/6J animals followed by infection with OVA-expressing vesicular stomatitis virus (VSV-OVA) (Figure 3.1A). We waited 60 days or longer before using these mice for subsequent experiments (referred to as VSV-OVA OT-I memory mice; Figure 3.1A). We isolated T cells from the spleens and lymph nodes (LNs) from VSV-OVA OT-I memory mice using negative-selection magnet-activated cell sorting (MACS) prior to ex vivo stimulation experiments (Figure 3.1A). This was done to ensure that cytokines act directly on T cells (151). As a negative control, we cultured bulk T cells in media alone (mock), and as a positive control, we stimulated T cells with anti-CD3/CD28 microbeads (Figure 3.1A). We used a combination of rIL-12, rIL-15, and rIL-18 (IL-12/15/18) to induce IFNγ and GzmB expression in a TCR-independent manner (Figure 3.1A). We found that IL-12/15/18 stimulation induced PD-1 expression in OT-I T_{mem}, but the increase in expression was markedly higher after TCR ligation (Figure 3.1B). PD-1 frequency and median fluorescence intensity (MedFI) in OT-I T_{mem} increased throughout the duration of IL-12/15/18 stimulation (Figure 3.1B). Similarly, TCR and IL-12/15/18 stimulation induced TOX upregulation in OT-I T_{mem} (Figure 3.1C). Next, we measured TCF1 expression, a transcription factor needed for T_{mem} self-renewal that is lost in terminally exhausted T_{mem} cells (152-155). Alongside increasing PD-1 and TOX levels, both TCR-mediated and IL-12/15/18–mediated stimulation led to significant loss of TCF1 expression in OT-I T_{mem} (Figure 3.1D). In sum, these data indicate that phenotypes often associated with exhaustion can be induced by TCR-independent, cytokine-mediated T_{mem} activation. Finally, we sought to determine whether stimulation similarly affected endogenous CD8$^+$ T_{mem} and CD8$^+$ naïve T ($T_{naïve}$) cells. IL-12/15/18 stimulation significantly increased TOX expression in endogenous CD8$^+$ T_{mem} but was not observed to the same degree in CD8$^+$ $T_{naïve}$ (Figure 3.2A, B). This CD8$^+$ T_{mem}–specific response is, too, reflected in IL-12/15/18–mediated upregulation of PD-1 (Figure 3.2C, D). This is likely, in some degree, due to the different propensities of T cell subsets (both major and memory) to become efficiently activated by cytokines (156) and differences in cytokine receptor expression

(particularly $T_{naïve}$, which require TCR-mediated activation to induce IL-12R and strongly increase IL-18R expression) (157, 158). Much akin to OT-I T_{mem}, TCR stimulation dramatically increased both TOX MedFI and PD-1 expression across endogenous subsets (Figure 3.2A–D), though the fold change in TOX staining intensity was most pronounced in $CD8^+$ T_{mem} (Figure 3.2A). Though IL-12/15/18 stimulation increased TOX MedFI in transgenic and endogenous $CD8^+$ T_{mem}, it was initially to a lower degree than that of TCR-stimulated cells (Figure 3.1C, Figure 3.2A). Because short-term TCR and IL-12/15/18 stimulation could dramatically augment TOX and PD-1 expression in $CD8^+$ T_{mem} from VSV-OVA OT-I memory mice, we next sought to test if the upregulation of TOX and PD-1 compromises functionality.

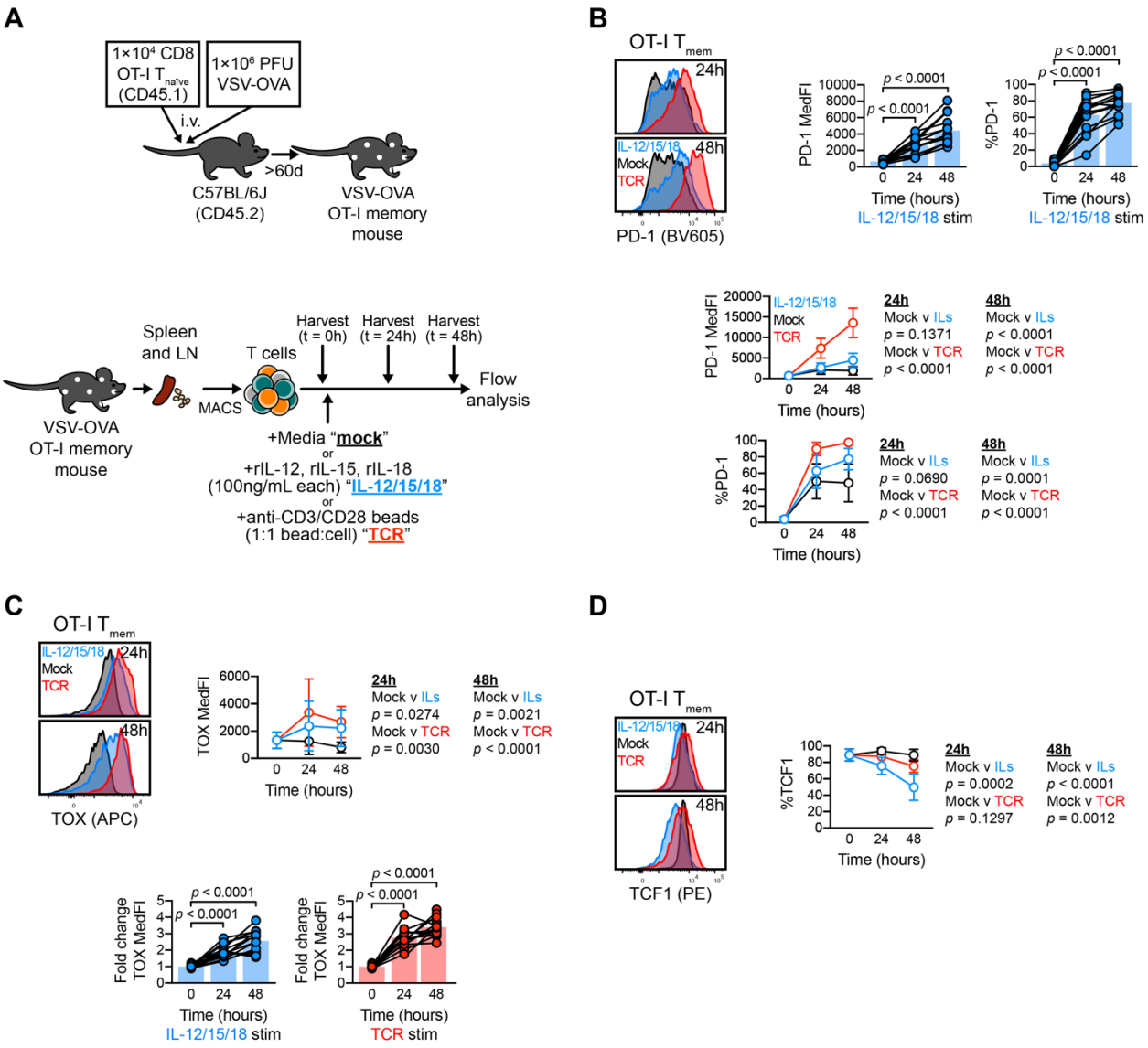

Figure 3.1 Cytokine stimulation induces TOX expression in transgenic mouse CD8⁺ T_{mem}

A Schematic of OT-I memory mouse generation and subsequent stimulation assays. OT-I $T_{naïve}$ cells were transferred and expanded with VSV-OVA, then aged to stable memory contraction; after, T cells were enriched from VSV-OVA expanded OT-I memory animals and stimulated with media alone (mock), IL-12, IL-15, and IL-18 in combination (IL-12/15/18; each at 100 ng/mL), or anti-CD3/CD28 microbeads (TCR) at an approximately 1:1 bead/cell ratio. **B**–**D** expression of (**B**) PD-1, (**C**) TOX, and (**D**) TCF1 within stimulated OT-I T_{mem} throughout experiment time course. TOX MedFI fold change in **C** was calculated against average TOX MedFI from mock stimulations in a subset-specific, batch-specific, and time point–specific manner. In **B** and **C**, bar chart symbols represent 1 animal at a unique time point/condition and are connected by animal identity, with bar indicating mean; the indicated statistical significances in **B** and **C** were calculated using paired *t* tests. In **B**–**D**, symbols in line plots comparing stimulation conditions represent the mean across all animals for a specific time point/condition ± SD; the indicated statistical significances were calculated using Mann-Whitney *U* tests. Results from $n = 14$ mice across 7 experiments are shown in **B** and **C**. Results from $n = 9$ mice across 2 experiments are shown in **D**.

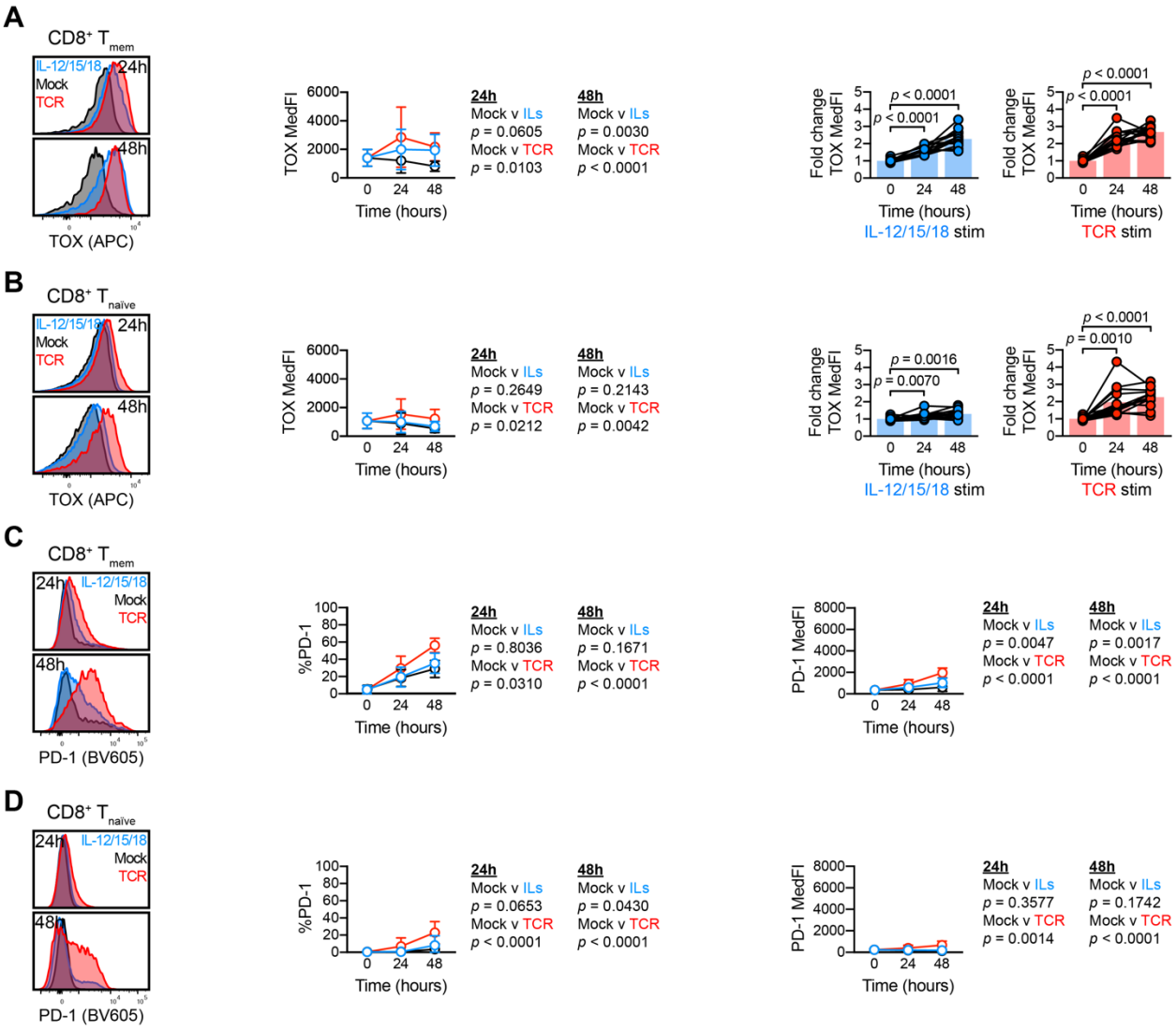

Figure 3.2 Cytokine stimulation induces TOX expression in endogenous mouse CD8$^+$ T$_{mem}$

A–**D** T cell stimulation responses after culture with media (mock), IL-12/15/18 (each at 100ng/mL,), or TCR agonist (1:1 bead to cell ratio). **A**–**B** Stimulation-induced changes of TOX expression in (**A**) endogenous CD8$^+$ T$_{mem}$ and (**B**) endogenous CD8$^+$ T$_{naïve}$ sourced from VSV-OVA OT-I memory mice. **C**–**D** Stimulation-induced changes of PD-1 expression in (**C**) endogenous CD8$^+$ T$_{mem}$ and (**D**) endogenous CD8$^+$ T$_{naïve}$ sourced from VSV-OVA OT-I memory mice. TOX MedFI fold changes in **A** and **B** were calculated against average TOX MedFI from mock stimulations in a subset-specific, batch-specific, and timepoint-specific manner. In **A**–**D**, symbols in line plots comparing stimulation conditions represent the mean across all animals for a specific timepoint/condition ± SD; the indicated statistical significances were calculated using Mann-Whitney tests. In **A** and **B**, bar chart symbols represent one animal at a unique timepoint/condition and are connected by animal identity, with bar indicating mean; the indicated statistical significances were calculated using paired *t* tests. All figures depict results from $n = 14$ mice across 7 experiments. All representative flow plots are sourced from the same animal.

3.2.2 Functional CD8$^+$ T_{mem} express TOX, PD-1, and effector proteins

We isolated T cells from VSV-OVA OT-I memory mice, as outlined in Figure 3.1A. We stimulated T cells in the presence of Golgi inhibitors (Figure 3.3A) and found that OT-I T_{mem} produced substantial amounts of IFNγ after IL-12/15/18 or TCR stimulation; yet IFNγ-expressing OT-I T_{mem} demonstrated higher TOX and PD-1 expression than those that failed to make IFNγ (Figure 3.3B, C). Similarly, OT-I T_{mem} that produced GzmB after stimulation also demonstrated increased TOX and PD-1 expression (Figure 3.4A, B). Together, these data indicate that TOX and PD-1 expression levels were elevated in activated, functional CD8$^+$ T_{mem} and suggest that TOX expression was also part of a cytokine-driven T cell activation program.

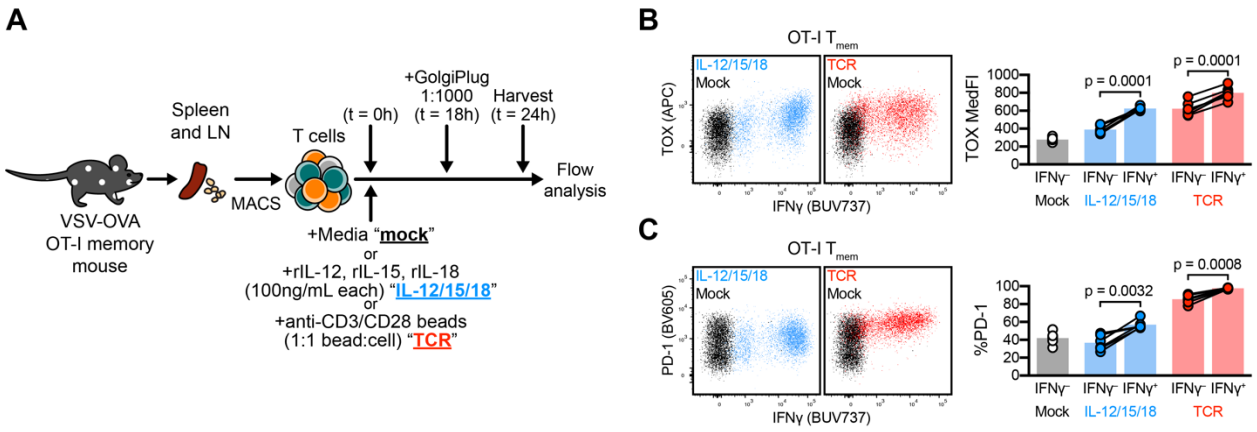

Figure 3.3 TOX and PD-1 expression occur in functional, IFNγ-expressing CD8$^+$ T_{mem}

ICS in tandem with TOX interrogation. **A** Experiment schematic, in which bulk T cells from VSV-OVA OT-I memory mice were stimulated (mock, black; IL-12/15/18, blue; TCR, red). Cells were treated with GolgiPlug 18 hours into stimulation and harvested for flow staining and analysis at 24 hours. **B** and **C** Expression of (**B**) TOX and (**C**) PD-1 in IFNγ$^+$ and IFNγ$^-$ OT-I T_{mem}. Representative plots depict cells from the same animal across different stimulation conditions. Symbols in **B** and **C** represent a T cell population within a unique animal with symbols connected by animal identity (n = 6 across 2 experiments). Bars represent mean and indicated statistical significances were calculated by paired t tests.

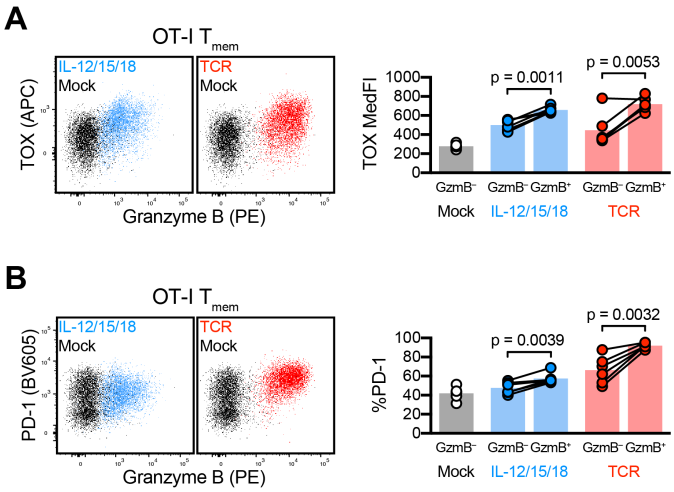

Figure 3.4 TOX and PD-1 expression occur in functional, GzmB-expressing CD8⁺ T_{mem}

T cells were isolated from VSV-OVA OT-I memory mice and stimulated (mock, black; IL-12/15/18, blue; TCR, red) for 24 hours (schematic shown in Fig. 3.3). **A**–**B** Expression of (**A**) TOX and (**B**) PD-1 within GzmB-positive and -negative OT-I T_{mem} after stimulation. Symbols in **A** and **B** represent a T cell population within a unique animal with symbols connected by animal identity (*n* = 6 across 2 experiments). Bars represent mean and indicated statistical significances were calculated by paired *t* tests.

3.2.3 Induction of TOX and PD-1 is heterogeneous in mouse CD8⁺ T_{mem}

To ensure that our data were not solely reliant on OT-I T cells, we also generated gBT-I memory mice using gBT-I TCR-transgenic cells (specific for an epitope of the herpes simplex virus 2 [HSV2] glycoprotein B [gB] protein) and a recombinant, gB epitope–expressing *Listeria monocytogenes* strain (*L. monocytogenes*–gB; Figure 3.6B). After stable contraction of TCR-transgenic T_{mem} (≥60 d), we conducted stimulation assays as previously outlined (Figure 3.1A). IL-12/15/18–mediated or TCR-mediated stimulation led to comparable TOX upregulation in OT-I and gBT-I T_{mem} (Figure 3.5A, B). Similarly, PD-1 expression was comparable in OT-I and gBT-I T_{mem} after stimulation (Figure 3.6C, D), with a concurrent loss of TCF1 expression (Figure 3.6E, F). We next asked if altering the nature of the priming infection could affect the ability to express TOX in response to cytokine-mediated activation at the memory stage. We adoptively transferred P14 transgenic T cells, a TCR-transgenic cell line specific for LCMV gp33, followed by infection with LCMV Armstrong or Docile (Figure 3.6G, H. These LCMV strains elicit acute and chronic infections, respectively (the latter causing T cell dysfunction). We then stimulated T cells (with the same culture setup as outlined in Figure 3.1A) from these P14 memory mice. P14 T_{mem} from LCMV Armstrong–infected mice readily upregulated PD-1 after TCR

or IL-12/15/18 stimulation (Figure 3.6I). The exhausted P14 T_{mem} from LCMV Docile–infected mice already uniformly expressed PD-1 prior to stimulation, but IL-12/15/18 or TCR stimulation further increased surface PD-1 expression (via increased MedFI; Figure 3.6J). P14 T_{mem} from LCMV Armstrong–infected mice increased TOX expression after TCR or IL-12/15/18 stimulation (Figure 3.5C). However, exhausted P14 T_{mem} from LCMV Docile–infected mice significantly increased TOX expression only after TCR stimulation (Figure 3.5D). Overall, P14 T_{mem} from LCMV Docile–infected mice showed a much more limited fold change in TOX MedFI compared with P14 T_{mem} from LCMV Armstrong–infected mice (Figure 3.5C vs. Figure 3.5D). Although differences between $CD8^+$ T_{mem} from mice with acute and chronic infections are expected, the differences between gBT-I and OT-I (~3- to 4-fold increase in TOX expression) compared with P14 (up to ~2-fold) need to be interpreted with caution because the gBT-I/OT-I and P14 experiments used different TOX antibody clones (REA473 and TXRX10, respectively). Overall, our data indicate that T_{mem} that were generated by different acute infections increased TOX expression in response to proinflammatory cytokines, suggesting that this was a broadly applicable mechanism of TOX induction in the T_{mem} compartment. We next sought to determine if PD-1 and TOX upregulation in response to stimulation was similarly recapitulated in human $CD8^+$ T cells.

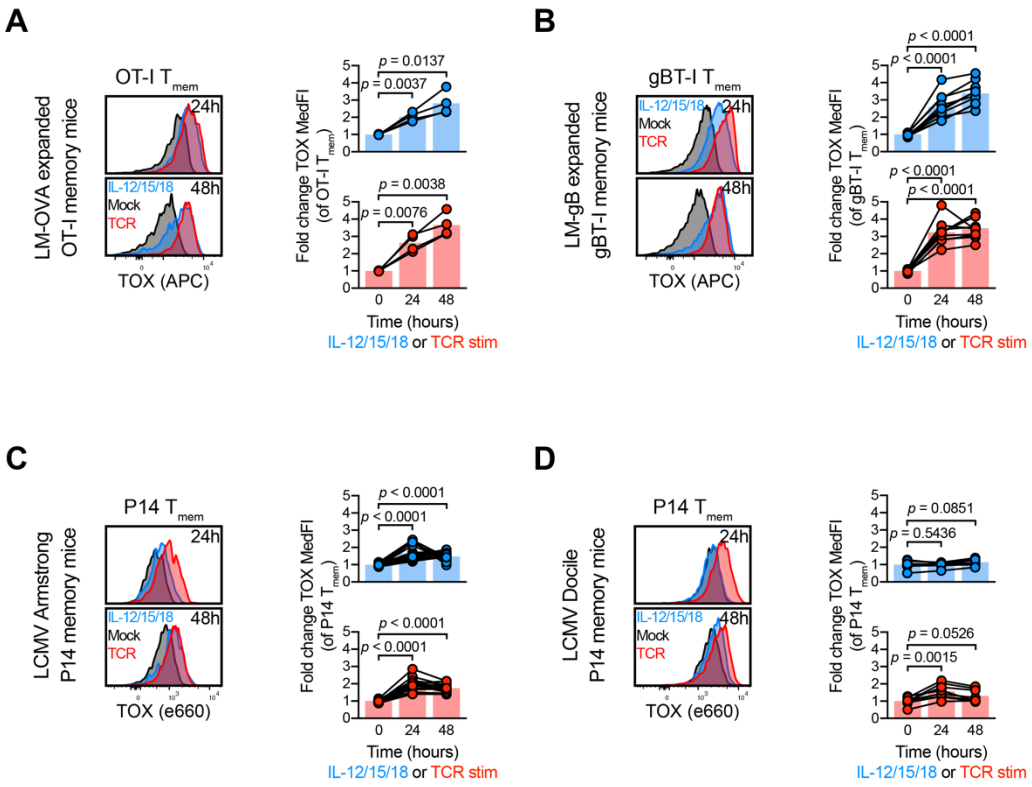

Figure 3.5 Cytokine-mediated TOX induction is limited in exhausted CD8⁺ T_{mem}

A and **B** Changes in TOX expression within *L. monocytogenes*–expanded TCR-transgenic T_{mem}: OT-I, specific for OVA Ag and gBT-I, specific for HSV2 gB Ag. MACS-enriched T cells from *L. monocytogenes*–expanded OT-I or gBT-I memory mice were stimulated with media alone (mock), recombinant IL-12, IL-15, and IL-18 in combination (IL-12/15/18; each at 100 ng/mL), or anti-CD3/CD28 microbeads (TCR) at an approximately 1:1 cell/bead ratio. **A** and **B** Representative TOX expression and TOX MedFI fold change during stimulation in *L. monocytogenes*–primed (**A**) OT-I and (**B**) gBT-I T_{mem}. **C** and **D** Changes in TOX expression within LCMV-specific TCR-transgenic P14 T cells expanded by acute (Armstrong) or chronic (Docile) LCMV infection. **C** and **D** Representative TOX expression and TOX MedFI fold change during stimulation in P14 T cells primed by (**C**) LCMV Armstrong and (**D**) LCMV Docile. TOX MedFI fold change was calculated against average TOX MedFI within mock stimulation in a batch-specific, time point–specific manner. We calculated indicated statistical significances using paired *t* tests. Each symbol represents a sample at a unique time point/condition, with bars delineating mean, which are connected by donor (n = 4 *L. monocytogenes*–OVA expanded OT-I memory mice across 2 experiments; n = 10 *L. monocytogenes*–gB expanded gBT-I memory mice across 2 experiments; n = 17 LCMV Armstrong-expanded P14 memory mice across 4 experiments; n = 8 LCMV Docile-expanded P14 memory mice across 2 experiments). Mouse identities are consistent between representative flow plots within the same generation/adoptive transfer condition.

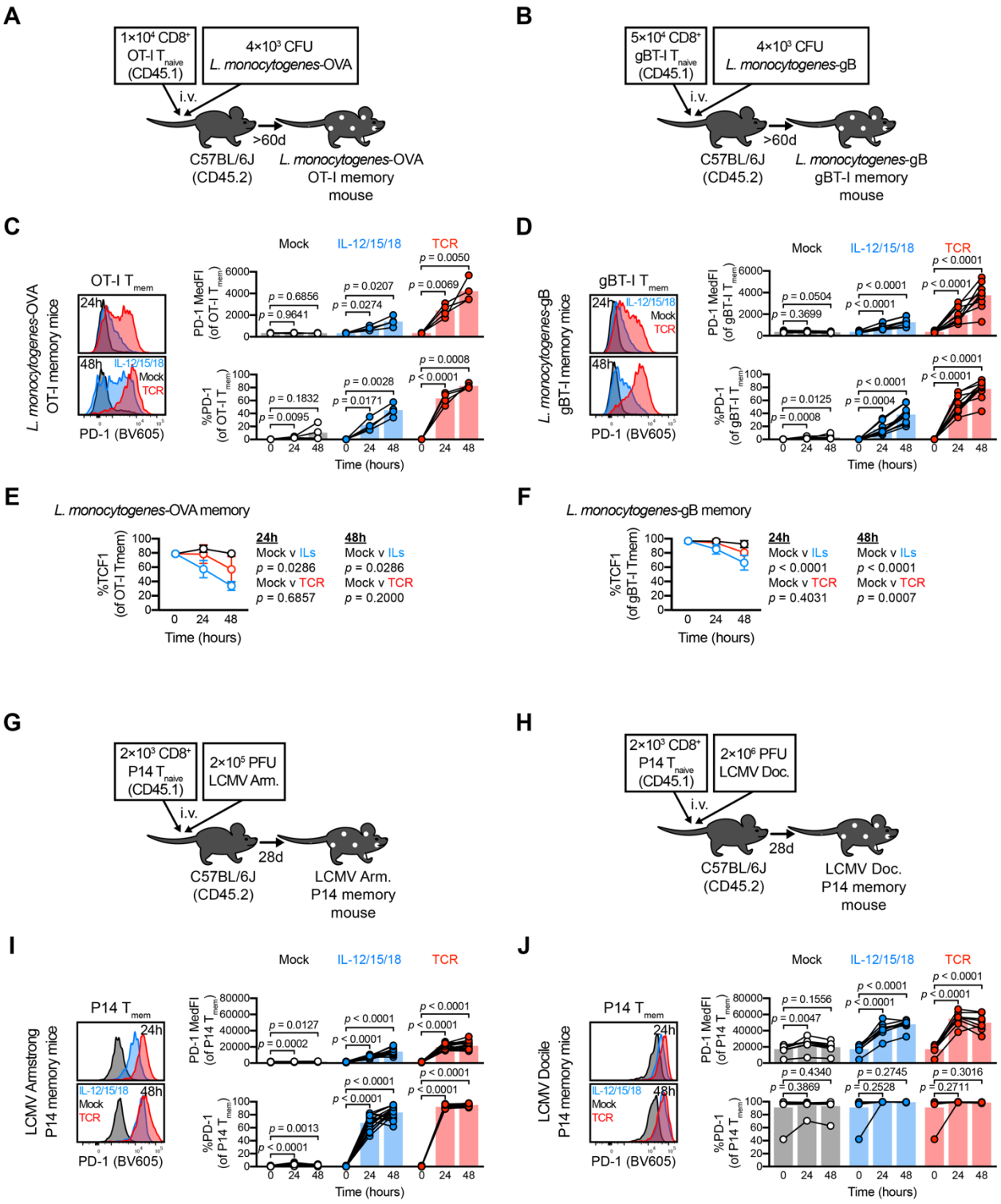

Figure 3.6 TOX induction varies across CD8⁺ T_{mem} elicited by different infections

A–**F** Changes in PD-1 and TCF1 expression within *L. monocytogenes*-expanded TCR transgenic T_{mem}. **A**–**B** Experiment schematic outlining the expansion of (**A**) OT-I (OVA-specific) and (**B**) gBT-I (gB-specific) transgenic T cells with *L. monocytogenes*-OVA and *L. monocytogenes*-gB,

respectively. MACS-enriched T cells from these memory mice were stimulated with media alone (mock), recombinant IL-12, -15, and -18 in combination (IL-12/15/18) (each at 100ng/mL), or antiCD3/CD28 microbeads (TCR) at a ~1:1 cell:bead ratio. **C**–**D** PD-1 MedFI and expression frequency within stimulated (**C**) OT-I T_{mem} or (**D**) gBT-I T_{mem}. **E–**F TCF1 expression within stimulated (**E**) OT-I and (**F**) gBT-I T_{mem}. **G**–**J** Changes in PD-1 expression within LCMV Armstrong- and Docile-expanded P14 T_{mem}. **G**–**H** Experiment schematic outlining the expansion of P14 transgenic T cells with (**G**) LCMV Armstrong (Arm.) or (**H**) LCMV Docile (Doc.), which respectively cause acute and chronic infection. **I**–**J** PD-1 MedFI and expression frequency within (**I**) LCMV Armstrong- and (**J**) Docile-expanded P14 T_{mem}. Symbols in **C**, **D**, **I**, **J** represent T cell populations from a single animal at a unique timepoint/condition and are connected by matched donor identities (when applicable), with bars depicting mean. Symbols in **E**, **F** represent mean values ± SD. Indicated statistical significances in **C**, **D**, **I**, **J** were calculated by paired *t* tests, and those in **E**, **F** were calculated using Mann-Whitney tests. Data in **A**–**F** depict n = 4 *L. monocytogenes*-OVA OT-I memory mice and n = 10 *L. monocytogenes*-gB gBT-I memory mice across 2 experiments. Data in **G** and **J** depict n = 17 LCMV Armstrong expanded P14 memory mice across 4 experiments and n = 8 LCMV Docile expanded P14 memory mice across 2 experiments.

3.2.4 Cytokine stimulation induces TOX and PD-1 in human $CD8^+$ T_{mem}

Using cryopreserved PBMCs from healthy, HIV-seronegative donors, we interrogated TOX and PD-1 expression by flow cytometry. We specifically gated $CD8^+$ T cells by a memory and naive binary, delineating $CD8^+$ T_{naive} as $CD45RO^-CCR7^+$, with remaining cells as $CD8^+$ T_{mem} (159) (Figure 3.7A), and interrogated basal TOX and PD-1 expression between these 2 subsets (Figure 3.7A). Because PD-1 expression is heterogeneous in humans (160, 161), we measured TOX MedFI across PD-1 low–, medium–, and high–expressing events. We found that $CD8^+$ T_{mem} with the highest PD-1 expression also demonstrated significantly elevated TOX MedFI (Figure 3.7B), mirroring correlations of TOX and PD-1 expression in our mouse model as well as human HCV infections (130). We next tested whether IL-12/15/18 stimulation increases PD-1 and TOX expression in T cell subsets and included mock and TCR stimulation conditions as negative and positive controls, respectively, but we also included stimulations using rIL-6, rIL-15, or rIL-12 and rIL-18 (Figure 3.7C). We chose these additional conditions because IL-6 activates $CD8^+$ T_{naive} (as evidenced by CD69 upregulation) and to discern individual activating contributions of each cytokine (Figure 3.8A). Across these conditions, IL-12/15/18–mediated and TCR-mediated stimulations led to the most prominent increase of TOX staining intensity and $PD\text{-}1^{hi}$ frequency in $CD8^+$ T_{mem} (Figure 3.7D, E). We measured TCF1 expression after mock, IL-12/15/18, and TCR stimulation. A decrease in TCF1 expression accompanied an increase in TOX and PD-1 expression after IL-12/15/18 or TCR stimulation (Figure 3.8B), akin to our mouse stimulation data. We further tested the degree of similarity between human and mouse T cells by measuring PD-1, TCF1, and TOX expression profiles in stimulated human $CD8^+$ T_{naive}. Like mouse $CD8^+$ T_{naive},

only TCR stimulation led to appreciable changes in TOX and PD-1 within human $CD8^+$ T_{naive} (Figure 3.7F and Figure 3.8C). Because IL-6 can activate $CD8^+$ T_{naive}, we used this condition to determine if PD-1 and TOX expression could occur in T_{naive} in the absence of a TCR signal. Despite inducing CD69 expression, we found that IL-6–mediated stimulation failed to increase TOX or PD-1 expression in $CD8^+$ T_{naive} (Figure 3.8D). Together, these data show that $CD8^+$ T_{mem} differentially expressed TOX, PD-1, and TCF1 at homeostasis and after both IL-12/15/18 and TCR stimulation. We next wanted to better define these changes across different T_{mem} subsets.

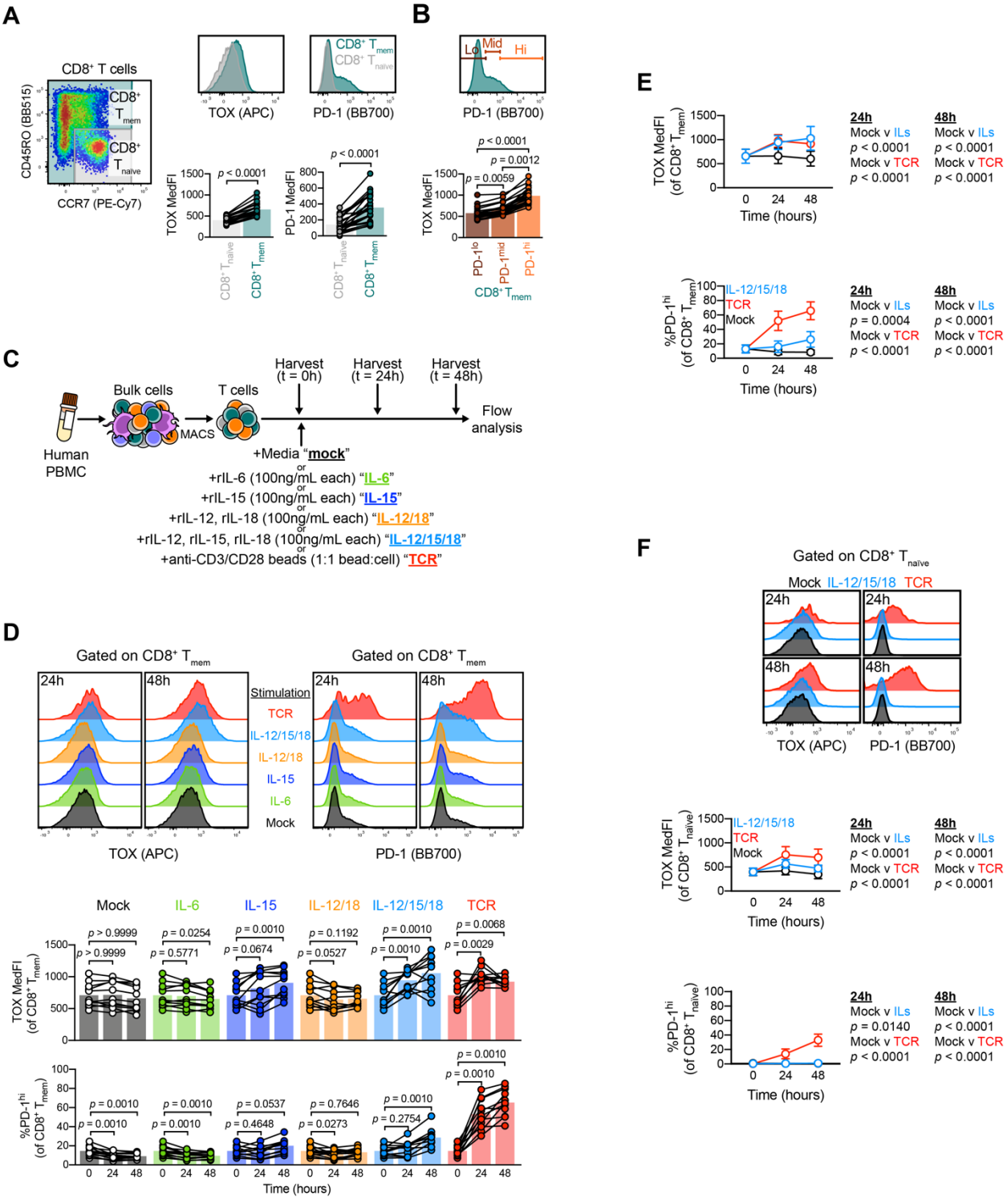

Figure 3.7 Inflammatory cytokines induce TOX and PD-1 expression in human CD8⁺ T_{mem}.

A Basal expression of TOX and PD-1 in CD8⁺ T_{mem} and T_{naive}. **B** TOX MedFI across PD-1 low–, medium–, and high–expressing CD8⁺ T_{mem}. (**C**) Schematic detailing T cell isolation from cryopreserved PBMCs and subsequent stimulation with recombinant IL-6, IL-15, IL-12/18, and IL-

12/15/18 (all at 100 ng/mL, each), or anti-CD3/CD28 microbeads (TCR, 1:1 bead/cell ratio) and subsequent flow interrogation. **D** TOX expression (MedFI) and PD-1^{hi} frequency in CD8^{+} T_{mem} throughout stimulation time course. **E** and **F** Comparison of TOX MedFI and PD-1^{hi} frequency in mock-, IL-12/15/18–, and TCR-stimulated (**E**) CD8^{+} T_{mem} and (**F**) CD8^{+} T_{naive}. In **A**, **B**, and **D**–**F**, we calculated indicated statistical significances by (**A** and **D**) Wilcoxon's matched-pairs signed-rank tests, (**B**) Friedman's test with Dunn's multiple comparisons tests, or (**E** and **F**) Mann-Whitney *U* tests. In **A** and **D**, each symbol represents a unique time point/treatment connected by donor with bars indicating mean (**A**, $n = 23$ across 4 experiments; **D**, $n = 11$ across 2 experiments). In **E** and **F**, each symbol represents the mean ± SD of the stimulation condition from $n = 23$ donors across 4 experiments. Representative plots from **A**, **D**, and **F** are sourced from the same donor.

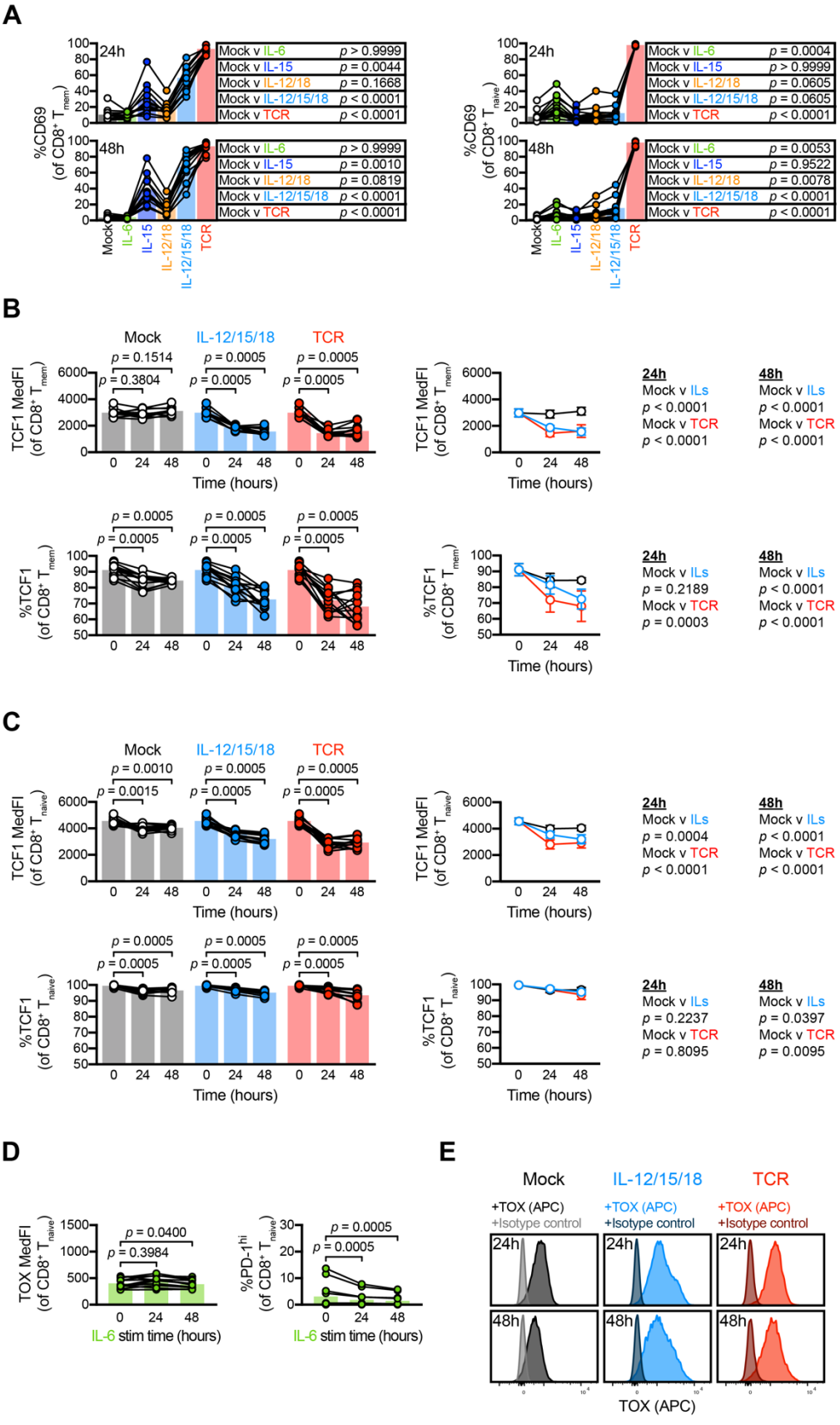
A
24h
48h
%CD69 (of CD8+ Tmem)
Mock v IL-6 p > 0.9999
Mock v IL-15 p = 0.0044
Mock v IL-12/18 p = 0.1668
Mock v IL-12/15/18 p < 0.0001
Mock v TCR p < 0.0001
Mock v IL-6 p > 0.9999
Mock v IL-15 p = 0.0010
Mock v IL-12/18 p = 0.0819
Mock v IL-12/15/18 p < 0.0001
Mock v TCR p < 0.0001
%CD69 (of CD8+ Tnaive)
Mock v IL-6 p = 0.0004
Mock v IL-15 p > 0.9999
Mock v IL-12/18 p = 0.0605
Mock v IL-12/15/18 p = 0.0605
Mock v TCR p < 0.0001
Mock v IL-6 p = 0.0053
Mock v IL-15 p = 0.9522
Mock v IL-12/18 p = 0.0078
Mock v IL-12/15/18 p < 0.0001
Mock v TCR p < 0.0001
Mock
IL-6
IL-15
IL-12/18
IL-12/15/18
TCR
B
Mock
IL-12/15/18
TCR
TCF1 MedFI (of CD8+ Tmem)
p = 0.1514
p = 0.3804
p = 0.0005
p = 0.0005
p = 0.0005
p = 0.0005
Time (hours)
24h
Mock v ILs p < 0.0001
Mock v TCR p < 0.0001
48h
Mock v ILs p < 0.0001
Mock v TCR p < 0.0001
%TCF1 (of CD8+ Tmem)
p = 0.0005
p = 0.0005
p = 0.0005
p = 0.0005
p = 0.0005
p = 0.0005
24h
Mock v ILs p = 0.2189
Mock v TCR p = 0.0003
48h
Mock v ILs p < 0.0001
Mock v TCR p < 0.0001
C
Mock
IL-12/15/18
TCR
TCF1 MedFI (of CD8+ Tnaive)
p = 0.0010
p = 0.0015
p = 0.0005
p = 0.0005
p = 0.0005
p = 0.0005
Time (hours)
24h
Mock v ILs p = 0.0004
Mock v TCR p < 0.0001
48h
Mock v ILs p < 0.0001
Mock v TCR p < 0.0001
%TCF1 (of CD8+ Tnaive)
p = 0.0005
p = 0.0005
p = 0.0005
p = 0.0005
p = 0.0005
p = 0.0005
24h
Mock v ILs p = 0.2237
Mock v TCR p = 0.8095
48h
Mock v ILs p = 0.0397
Mock v TCR p = 0.0095
D
TOX MedFI (of CD8+ Tnaive)
p = 0.0400
p = 0.3984
IL-6 stim time (hours)
%PD-1hi (of CD8+ Tnaive)
p = 0.0005
p = 0.0005
IL-6 stim time (hours)
E
Mock
IL-12/15/18
TCR
+TOX (APC)
+Isotype control
24h
48h
TOX (APC)

Figure 3.8 Inflammatory cytokines limit TCF1 expression in human CD8$^+$ T_{mem}.

A–**B** CD69 expression in stimulated CD8$^+$ T_{mem} (left) and CD8$^+$ T_{naive} (right) subsets. **B**–**C** TCF1 MedFI and expression frequency in (**B**) CD8$^+$ T_{mem} and (**C**) CD8$^+$ T_{naive} over stimulation time course. **D** TOX MedFI and PD-1^{hi} event frequencies in IL-6-stimulated CD8$^+$ T_{naive}. **E** TOX and isotype control staining in mock (left), IL-12/15/18 (center), and TCR (right) stimulated CD8$^+$ T_{mem}. Bar plot symbols in **A**–**D** depict a unique donor at a specific condition/timepoint, with symbols connected by donor identity and bars depicting mean; indicated statistical significances were calculated by **A** Friedman tests with Dunn's multiple comparisons tests or **B**–**D** Wilcoxon matched-pairs signed rank tests. Line plot symbols in **B** and **C** depict means ± SD across stimulation conditions with indicates statistical significances calculated by Mann-Whitney tests. **A** and **D** represent *n* = 11 donors across 2 experiments; **B** and **C** represent *n* = 12 donors across 2 experiments; **E** represents *n* = 3 donors.

3.2.5 Inflammation-induced PD-1 and TOX expression occurs in most but not all CD8$^+$ T_{mem}.

To test if inflammation-induced PD-1 and TOX expression differs across human CD8$^+$ T_{mem} subsets, we used CD45RO and CCR7 staining to further delineate central memory (T_{CM}; CD45RO$^+$ CCR7$^+$), T_{EM} (CD45RO$^+$ CCR7$^-$), and T_{EMRA} (CD45RO$^-$ CCR7$^-$) subsets (159, 162) (Figure 3.9A). When we measured TOX, PD-1, and TCF1 expression across these subsets, we noted that a substantial fraction of CD8$^+$ T_{EM} events were PD-1^{hi}, and both CD8$^+$ T_{EM} and T_{EMRA} cells expressed elevated levels and lower levels of TOX and TCF1, respectively, at homeostasis (Figure 3.9B). Although this observation is in line with the initial report demonstrating TOX heterogeneity in human CD8$^+$ T_{mem} subsets (141), it remained unknown if these CD8$^+$ T_{mem} subsets are equally capable of further TOX upregulation after stimulation. We observed that TOX, PD-1, and TCF1 expression kinetics in CD8$^+$ T_{CM} and T_{EM} largely resembled one another, with both IL-12/15/18 and TCR stimulation having increased the frequency of PD-1^{hi} events and TOX MedFI but having decreased TCF1 MedFI (Figure 3.9C). It is worth noting that although TCF1 MedFI in CD8$^+$ T_{CM} dropped profoundly after IL-12/15/18 or TCR stimulation, the loss in frequency of TCF1-expressing cells (as defined by subjective gating) was not as pronounced as what we observed in CD8$^+$ T_{EM} (Figure 3.10A). Although both IL-12/15/18–mediated and TCR-mediated stimulation were able to significantly increase the frequency of PD-1^{hi} events and lower TCF1 MedFI in CD8$^+$ T_{EMRA}, the degree of these changes was less pronounced than in CD8$^+$ T_{CM} or T_{EM} (Figure 3.9C). Moreover, CD8$^+$ T_{EMRA} did not significantly upregulate TOX expression after TCR stimulation. This, however, was not due to an inability to be stimulated because CD8$^+$ T_{EMRA} readily expressed the activation marker CD69 after cytokine-mediated or TCR-mediated

stimulation (Figure 3.10A). Finally, it is worth noting that when stimulated with IL-15 alone, CD8$^+$ T_{CM}, unlike CD8$^+$ T_{EM} and T_{EMRA}, failed to significantly express PD-1 (Figure 3.10B).

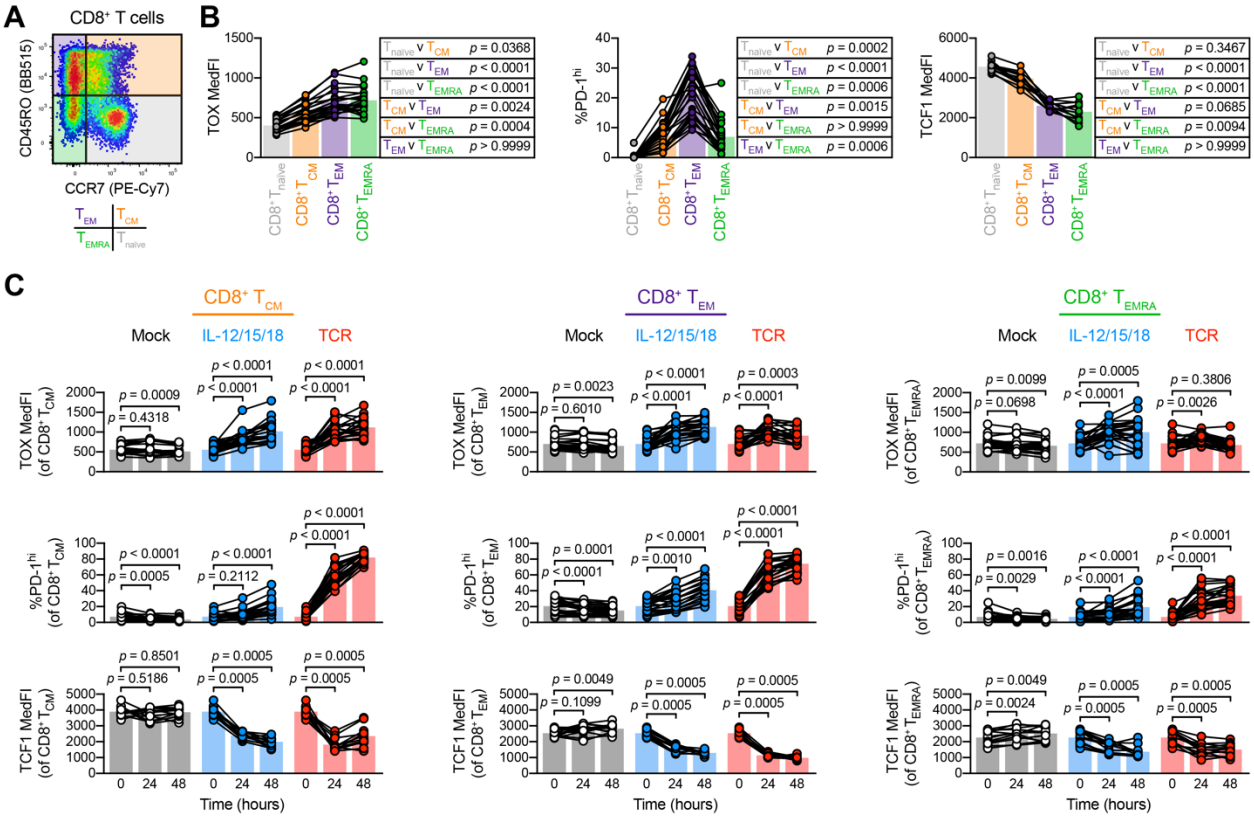

Figure 3.9 TOX and PD-1 upregulation are largely independent of T_{mem} subset.

Basal and stimulation-induced TOX and PD-1 expression in CD8$^+$ memory subsets. **A** Representative gating of CD8$^+$ T cells into T_{naive} (gray), T_{CM} (orange), T_{EM} (purple), and T_{EMRA} (green) subsets. **B** Basal expression levels (MedFI) of TOX and TCF1 and frequency of PD-1^{hi} cells across CD8$^+$ T cell memory subsets. **C** TOX MedFI, PD-1^{hi} frequency, and TCF1 MedFI after mock (black), IL-12/15/18 (each at 100 ng/mL, blue), or TCR (1:1 bead/cell ratio, red) stimulation in CD8$^+$ T_{CM} (left column), CD8$^+$ T_{EM} (center column), and CD8$^+$ T_{EMRA} (right column) cells. Symbols in **B** and **C** represent unique samples (by time point/condition/subset) and are connected by donor identity, with bars representing mean. We determined statistical significances in **B** and **C**, respectively, using Friedman's tests and Wilcoxon's matched-pairs signed-rank tests. **B** and **C** depict n = 23 donors across 4 experiments, except for TCF1 plots, which depict n = 12 donors across 2 experiments.

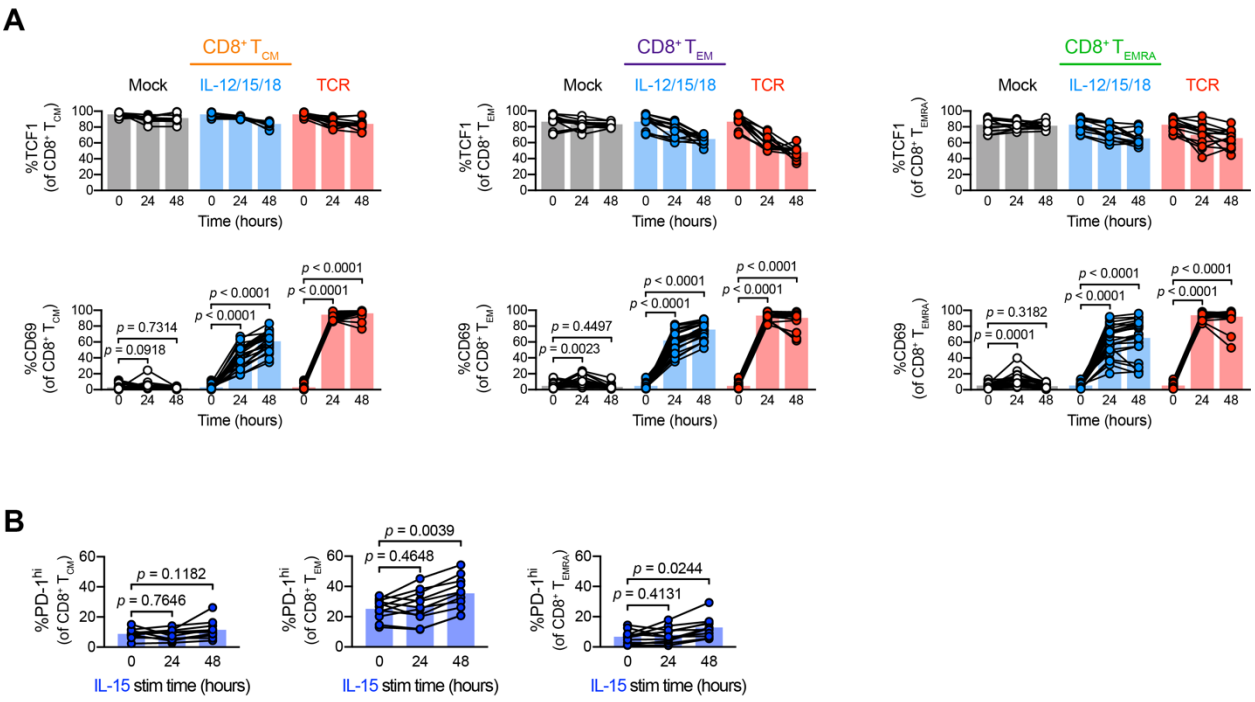

Figure 3.10 Inflammation-mediated phenotypic changes across CD8$^+$ T$_{mem}$ subsets.

A TCF1 (top row) and CD69 (bottom row) event frequency within CD8$^+$ T$_{mem}$ subsets after mock (black), IL-12/15/18 (blue), or TCR (red) stimulation. **B** PD-1^{hi} event frequency within CD8$^+$ T$_{mem}$ subsets after IL-15 stimulation. All cytokines were at 100ng/mL, each, in all stimulation conditions. In **A**–**B**, each symbol represents a cell population within a donor at a unique condition/timepoint, with symbols connected by donor identity and bar representing mean. All indicated statistical significances were calculated by Wilcoxon matched-pairs signed rank tests. Data in **A** depicts *n* = 12 (%TCF1) donors over 2 experiments and *n* = 23 donors (%CD69) over 4 experiments; **B** depicts *n* = 11 donors over 2 experiments.

We next interrogated T cells with defined TCR specificity, specifically IAV-specific CD8$^+$ T cells using HLA-A*02 tetramers loaded with the GILGFVFTL peptide (Figure 3.11A). We examined this CD8$^+$ T$_{mem}$ population because these cells were reported to not express appreciable levels of TOX at homeostasis, likely owing to their T$_{CM}$ phenotype (141). Within our sample set, IAV-specific CD8$^+$ T cells were predominantly T$_{CM}$ in half of the HLA-A*02 PBMC donors (Figure 3.11A). Nevertheless, all IAV-specific CD8$^+$ T cells were able to substantially upregulate TOX and PD-1 expression after IL-12/15/18 stimulation (Figure 3.11B), indicating that CD8$^+$ T$_{mem}$ with low levels of TOX and PD-1 at homeostasis can also contribute to TOX and PD-1 heterogeneity after recent activation. Alongside testing IAV-specific CD8$^+$ T cells, we also interrogated the effects of stimulation in mucosal associated invariant T (MAIT) cells. We selected this population because (a) MAIT cells are nonconventional T cells, recognizing bacterial metabolites as Ags presented on MHC-related 1 (MR1) (163); (b) inflammation is necessary for sustained MAIT cell effector

function (45, 48); and (c) MAIT cells are near-uniformly T_{EM} cells when defined by CD45RO and CCR7 (164). We identified MAIT cells using MR1 tetramers loaded with the 5-OP-RU metabolite (165), which largely fell into our T_{EM} gate (Figure 3.11C). Like IAV-specific $CD8^+$ T cells, IL-12/15/18 stimulation led to substantial TOX and PD-1 upregulation in MAIT cells (Figure 3.11D). Because inflammation is necessary for sustained MAIT cell effector function, we asked if MAIT cells are differentially capable of responding to other cytokine combinations. Alongside IL-12/15/18, IL-15 alone or IL-12 and IL-18 in unison could significantly increase both the frequency of PD-1^{hi} and TOX MedFI of MAIT cells, but not IAV-specific T cells (Figure 3.12A, B). Together, these data indicate that cytokine-driven activation programs were conserved across conventional and innate-like T cells.

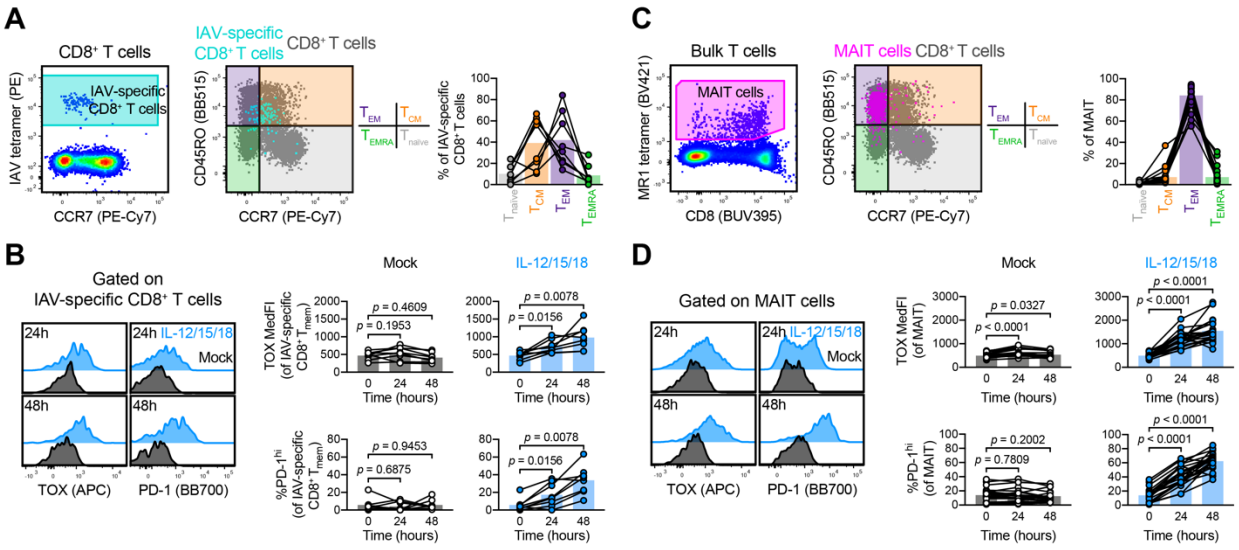

Figure 3.11 Inflammatory cytokines induce TOX and PD-1 expression in conventional and innate-like T cells.

TOX and PD-1 induction in IAV-specific $CD8^+$ T cells. **A** Gating and memory phenotyping of IAV-specific $CD8^+$ T cells. **B** Induction of TOX and PD-1 in IAV- specific $CD8^+$ T cells by mock (black) or IL-12/15/18 (each at 100 ng/mL, blue) stimulation. **C** and **D** TOX and PD-1 induction in MAIT cells. **C** Gating and memory phenotyping of MAIT cells. **D** Induction of TOX and PD-1 in MAIT cells by mock (black) or IL-12/15/18 (each at 100 ng/mL, blue) stimulation. Representative plots are sourced from the same donor. Symbols represent unique samples (by time point/condition/subset) and are connected by donor identity, with bars representing mean. We determined statistical significances in **B** and **D** using Wilcoxon's matched-pairs signed-rank tests. **A** and **B** depict n = 8 donors across 2 experiments; **C** and **D** depict n = 23 donors across 4 experiments.

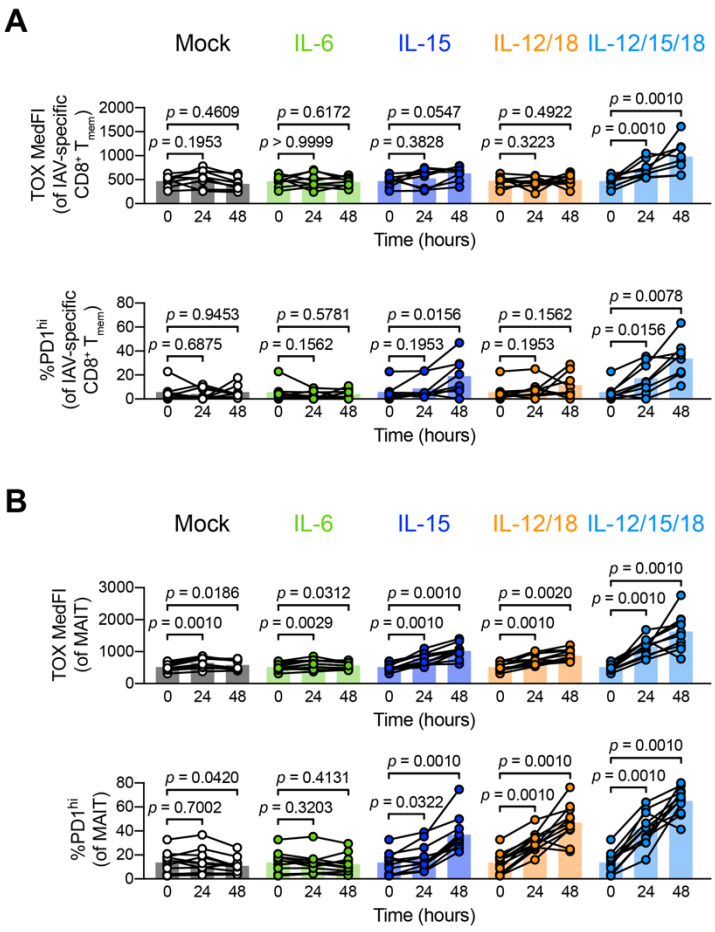

Figure 3.12 MAIT cells appear more sensitive to various cytokine combinations.

A–**B** TOX MedFI and frequency of PD-1^{hi} events in (**A**) IAV-specific CD8^{+} T cells and (**B**) MAIT cells after mock (black), IL-6 (green), IL-15 (dark blue), IL-12/18 (orange), or IL-12/15/18 (blue) stimulation (all cytokine concentrations 100/ng/mL, each). Data in **A** depicts *n* = 8 donors over 2 experiments; **B** depicts *n* = 11 donors over 2 experiments. All indicated statistical significances were calculated using Wilcoxon matched-pairs signed rank tests.

3.2.6 Cytokine stimulation-induced PD-1 expression is independent of TOX

Because PD-1 and TOX upregulation appeared tightly associated after cytokine-driven activation, we next asked if this association is mechanistic in nature. If TOX is necessary for PD-1 expression, then it would allow the use of surface-expressed PD-1 as a surrogate for intracellularly expressed TOX. TOX expression appears to drive PD-1 expression in a number of contexts because exhausted T_{mem} dramatically downregulate PD-1 after TOX deletion or knockdown (130, 136, 138, 139). Conversely, T cell transduction with TOX-encoding constructs leads to PD-1 upregulation (136-139). Although TOX controls PD-1 expression during exhaustion,

the role of TOX is less clear in activation. To dissect the function of TOX in stimulation-mediated PD-1 upregulation, we used WT and *Tox*$^{-/-}$ P14 T_{mem}. To generate these P14 T_{mem}, we adoptively transferred WT or KO P14 T cells into C57BL/6J hosts, which we subsequently infected with LCMV Armstrong to form a T_{mem} population (Figure 3.13). To determine if TOX deficiency alters stimulation-induced PD-1 upregulation, we cultured MACS-isolated T cells from WT and *Tox*$^{-/-}$ P14 memory mice (28 days after LCMV Armstrong infection) in the presence of mock, IL-12/15/18, or TCR stimulation (Figure 3.13). Both WT and *Tox*$^{-/-}$ P14 T_{mem} cells increased PD-1 expression after IL-12/15/18 or TCR stimulation (Figure 3.14A–C). Together these data indicate that TOX alone was not necessary for PD-1 upregulation in cytokine-stimulated $CD8^+$ T_{mem} and suggest other transcription factors were sufficient to drive PD-1 expression in the absence of TOX.

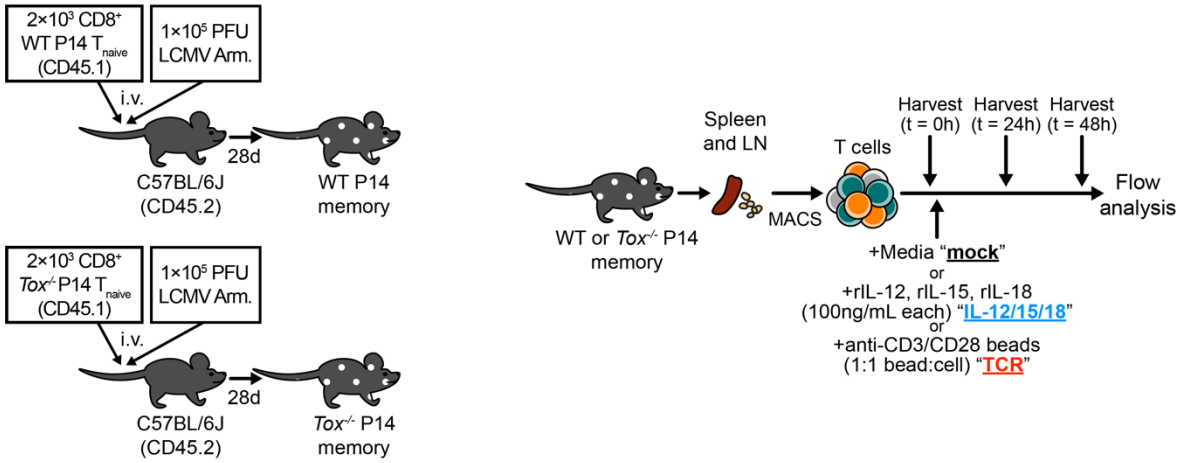

Figure 3.13 TOX-deficient P14 T_{mem} generation and stimulation overview

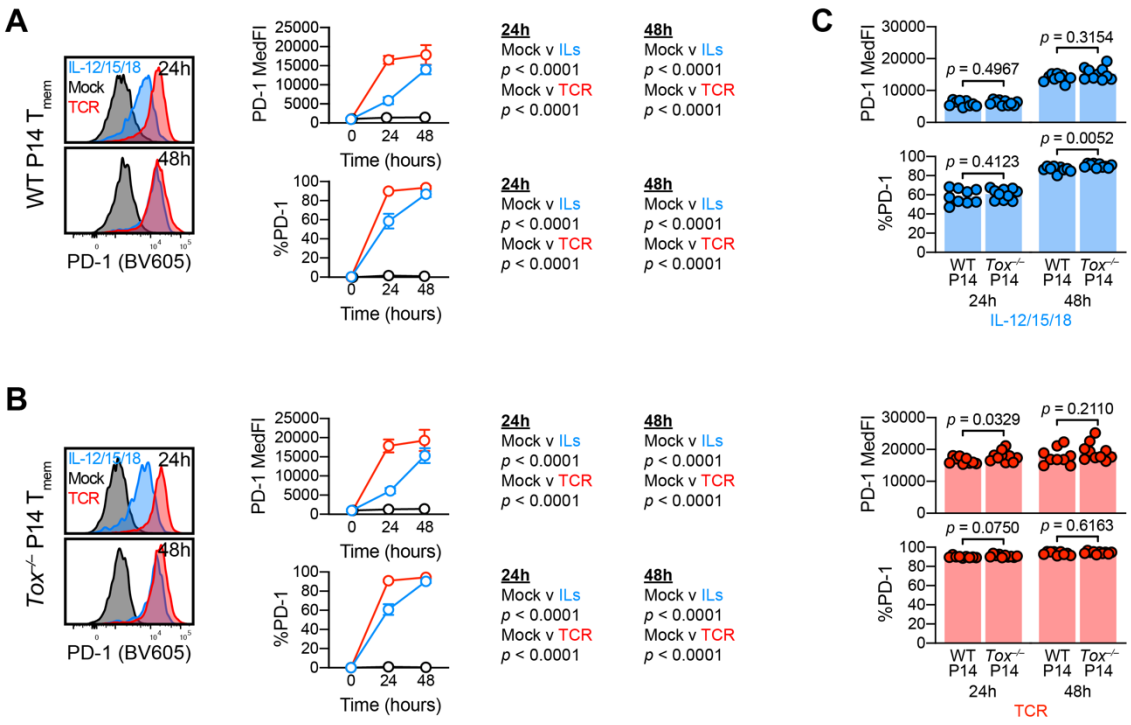

Figure 3.14 TOX deficiency does not abrogate stimulation-induced PD-1 expression

T cells were stimulated with media alone (mock), recombinant IL-12, IL-15, and IL-18 in combination (IL-12/15/18 or ILs; each at 100 ng/mL), or with anti-CD3/CD28 microbeads at an approximately 1:1 cell/bead ratio (TCR). **A** and **B** PD-1 MedFI and expression frequencies in (**A**) WT or (**B**) *Tox*$^{-/-}$ P14 T_{mem} over stimulation time course. **C** Comparison of PD-1 MedFI and expression frequencies between IL-12/15/18 (left) or TCR (right) stimulated WT and *Tox*$^{-/-}$ P14 T_{mem} cells. All indicated statistical significances were calculated using Mann-Whitney *U* tests. Symbols in **A** and **B** represent the mean ± SD from all animals at a specific time/condition; and symbols in **C** represent stimulated P14 T_{mem} populations within a single animal (n = 9 WT P14 recipients and n = 10 *Tox*$^{-/-}$ P14 recipient across 2 experiments).

3.2.7 Cytokine-induced PD-1 and TOX expression in mouse CD8^{+} T_{mem} is independent of calcineurin-mediated NFAT activation

Gene expression downstream of TCR ligation mechanistically hinges on the transcription factor, nuclear factor of activated T cells (NFAT). The calcium flux proceeding TCR engagement activates calcineurin, which subsequently activates NFAT, leading to its nuclear translocation and binding of partner transcription factors, ultimately leading to the expression of specific genes (166). In the contexts of transient or chronic TCR engagement, NFAT activation underlies the expression of PD-1 and TOX (136-139, 167, 168). Therefore, we asked if NFAT is also critical for PD-1 and TOX upregulation during inflammation-mediated activation. We conducted in vitro

stimulations with T cells from VSV-OVA OT-I memory mice in the presence of calcineurin inhibitors, cyclosporin A (CsA) and FK506 (0.1μg/mL and 1μg/mL, respectively) (169), or DMSO carrier (Figure 3.15A). In line with previous studies, we observed that the inhibition of calcineurin/NFAT impaired TCR-mediated induction of TOX and PD-1 (Figure 3.15B). Surprisingly, calcineurin/NFAT inhibition had failed to drastically reduce TOX or PD-1 levels in OT-I T_{mem} stimulated with IL-12/15/18 (Figure 3.15B). Due to this difference, we then asked if NFAT activation is of any consequence during inflammation-mediated activation of functionality. The activation (e.g., CD69 expression) and function (e.g., IFNγ and GzmB expression) of TCR-stimulated OT-I T_{mem} was completely attenuated by calcineurin/NFAT inhibition. Contrasting this, calcineurin/NFAT inhibition failed to drastically alter IL-12/15/18-mediated expression of CD69, IFNγ, or GzmB (Figure 3.15B). Together, these data show that despite the obvious parallels in TCR- and inflammation-activated $CD8^+$ T_{mem} phenotype and function, mechanistically distinct pathways underlie these seemingly congruent programs.

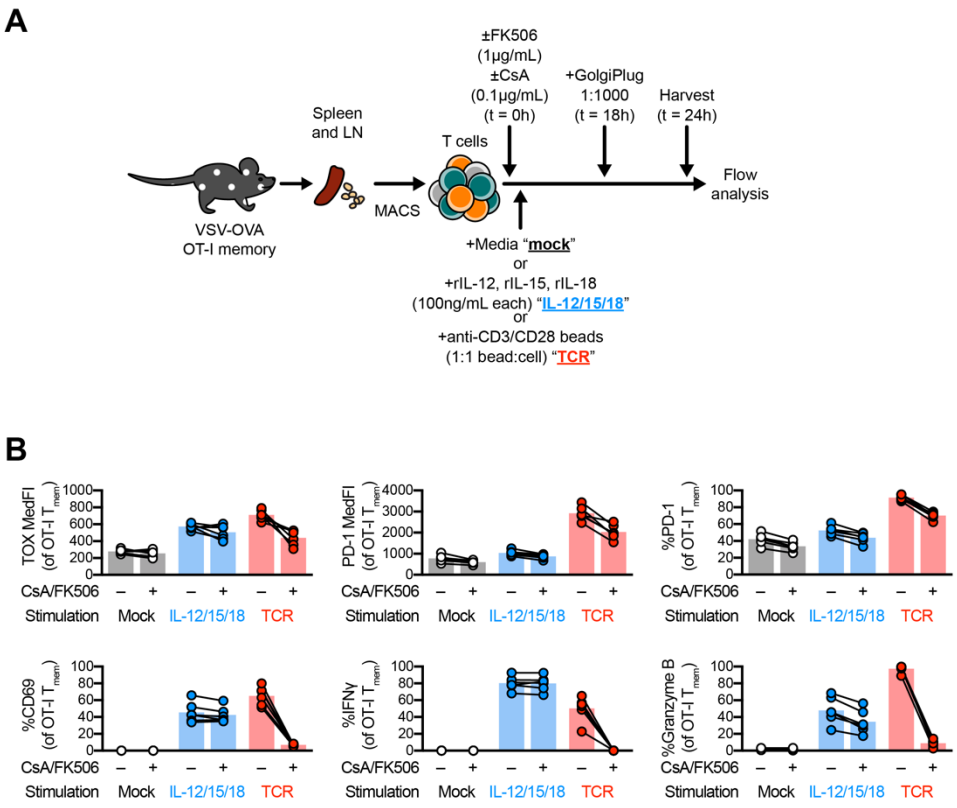

Figure 3.15 Bystander activation in mouse CD8⁺ T_{mem} is independent of calcineurin-mediated NFAT activation.

A Experiment schematic for T cell isolation and in vitro stimulation with media alone (mock), recombinant IL-12, IL-15, and IL-18 in combination (IL-12/15/18 or ILs; each at 100 ng/mL), or with anti-CD3/CD28 microbeads at an approximately 1:1 cell/bead ratio (TCR). Stimulations were conducted in the presence of calcineurin inhibitors, FK506 (1μg/mL) and cyclosporin A (CsA; 0.1μg/mL), or DMSO as a carrier control. GolgiPlug was added for the final 6 hours of culture to permit the intracellular accumulation of cytokines. **B** Expression of TOX and PD-1 (top row) and markers of activation or effector function (CD69, IFNγ, GzmB; bottom row) 24 hours after stimulation. **B** depicts T cells from *n* = 6 mice across 2 technical replicates, with points connected by mouse identity within the same stimulation condition. Bars represent mean values.

3.2.8 Bystander activation in human CD8⁺ T_{mem} is also calcineurin independent

Given the limitations of specific pathogen-free (SPF) mice and TCR transgenics, we next sought to test if inflammation-mediated effector functions are also calcineurin-independent in human, polyclonal CD8⁺ T_{mem}. This is of significant interest as inflammation-mediated bystander activation (i.e., the upregulation of IFNγ and GzmB) is likely of clinical importance (36, 37). We MACS-isolated bulk T cells from healthy PBMC donors and stimulated them in vitro with IL-12/15/18 or TCR agonists. We conducted this in the presence of CsA and FK506 or DMSO as a carrier control and interrogated cells with flow (Figure 3.16A). In congruence with our mouse experiments and

the body of literature (166, 170), we observed that TCR-mediated expression of IFNγ was impaired by calcineurin inhibition (Figure 3.16B). In contrast, GzmB expression was unaffected by CsA/FK506 treatment (Figure 3.16B). But it is worth noting that human $CD8^+$ T_{mem}, unlike those from mice, express GzmB at homeostasis (171). Like our mouse data, bystander activation of $CD8^+$ T_{mem} with IL-12/15/18 was unaffected by CsA/FK506-mediated calcineurin inhibition (Figure 3.16C). Given the parallels with TCR- and inflammation-mediated activation in $CD8^+$ T_{mem}, we asked to what degree do these programs overlap and interrogated the expression of TNFα and IL-2. While TCR-mediated stimulation could induce TNFα and IL-2 in human $CD8^+$ T_{mem} in a calcineurin-dependent manner (Figure 3.16B), stimulation with IL-12/15/18 failed to upregulate these molecules (Figure 3.16C). Thus, while there is significant overlap between TCR- and inflammation-mediated effector programs, they do not entirely mirror one another: TCR agonism gives rise to a greater breadth of functions in a calcineurin/NFAT-dependent manner.

T_{mem} subsets differ greatly in their response to TCR stimulation. T_{CM} upregulate IFNγ to a lesser degree after TCR ligation (162, 172). Therefore, we asked if IL-12/15/18–induced IFNγ expression similarly differed across $CD8^+$ T_{mem} subsets. We compared IFNγ and GzmB expression in IL-12/15/18–stimulated $CD8^+$ T cells subset by CD45RO and CCR7 expression (as in Figure 3.9A) and found that all T_{mem} subsets upregulated IFNγ in response to inflammation; but this was dominated by $CD8^+$ T_{EM} and T_{EMRA} (Figure 3.16D). Though one could argue this reflects different propensities to become bystander activated, T_{CM} predominantly upregulate CD69, a marker of activation, after IL-12/15/18 stimulation (Figure 3.10A). Together, this suggests that despite some of the differences between TCR- and inflammation-mediated T_{mem} activation, that the IFNγ responses to both stimuli are overlapping within specific T_{mem} subsets.

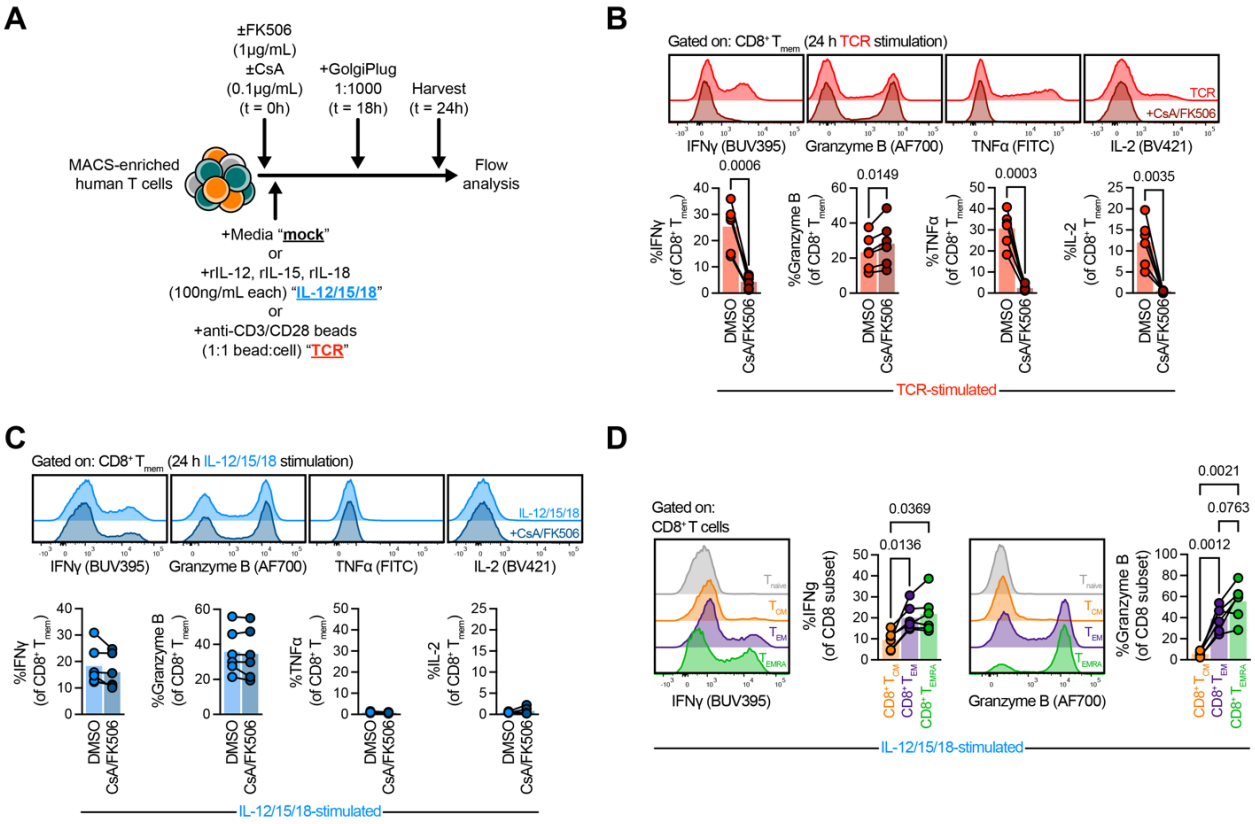

Figure 3.16 Bystander activation is calcineurin/NFAT independent in human CD8$^+$ T$_{mem}$ with subset-specific consequences.

A Experiment schematic for in vitro T cell stimulation with media alone (mock), recombinant IL-12, IL-15, and IL-18 in combination (IL-12/15/18 or ILs; each at 100 ng/mL), or with anti-CD3/CD28 microbeads at an approximately 1:1 cell/bead ratio (TCR). Stimulations were conducted in the presence of calcineurin inhibitors, FK506 (1μg/mL) and cyclosporin A (CsA; 0.1μg/mL), or DMSO as a carrier control. GolgiPlug was added for the final 6 hours of culture to permit the intracellular accumulation of cytokines. **B–D** Expression of effector molecules (IFNγ, GzmB, TNFα, and IL-2) in CD8$^+$ T$_{mem}$ 24 hours after stimulation with (**B**) TCR agonist or (**C–D**) IL-12/15/18. **B**, **C** Effects of CsA/FK506-mediated calcineurin inhibition on effector molecule expression. **D** IL-12/15/18-induced effector molecule expression across CD8$^+$ T$_{mem}$ subsets. In **B**–**D**, points represent cells from a unique donor (n = 6) connected by donor identity. Indicated are statistical significances where $p < 0.1$ by (**B**, **C**) paired t tests and (**D**) RM one-way ANOVA with Geisser-Greenhouse correction and Tukey's multiple comparisons test.

3.3 Discussion

TOX has been foremost studied in TCR-mediated exhaustion of mouse CD8$^+$ T cells in the context of tumor or chronic infection (130, 136, 137). A recent study reported TOX expression in functional circulating human CD8$^+$ T$_{mem}$, suggesting TOX expression does not necessarily dictate

dysfunction(141), which led to the speculation that TOX may have distinct roles across species, specifically mice and humans (143). Alternatively, TOX expression heterogeneity in humans may simply reflect the more complex environment that human T cells are exposed to in everyday life, which may not be readily appreciable in specific pathogen–free mice, such as routine inflammatory events in barrier tissues. Thus, we asked if proinflammatory cues could be sufficient to increase TOX expression and contribute to TOX heterogeneity. Although inflammation has been previously shown to enhance TCR-mediated TOX upregulation (in a VEGF-A–dependent manner that necessitates initial TCR signaling) (173), our findings are, to the best of our knowledge, the first to demonstrate TOX expression in the absence of agonist TCR signals. Transient IL-12/15/18 and TCR stimulation increased PD-1 and TOX expression in most $CD8^+$ T_{mem}. In mouse, dysfunctional P14 T_{mem} from LCMV Docile–infected mice still increased surface PD-1 expression after TCR stimulation, whereas IL-12/15/18 had little to no effect on TOX expression. Similarly, human T_{EMRA} cells showed limited to no increase in TOX expression after exposure to IL-12/15/18. The underlying mechanisms will require further investigation, but one could speculate that the cytokine stimulation was simply not potent enough to further enhance the already ongoing effector or activation program in these two T_{mem} subsets. The notion that not only TOX but also PD-1 expression can indicate an ongoing effector or activation program in $CD8^+$ T cells is important because PD-1 and (now also) TOX are used as biomarkers of T cell exhaustion (16, 174, 175). Of note, certain features of general activation programs of $CD8^+$ T_{mem} cells appear to be well conserved and have also been reported as transcriptomic overlap of tissue-resident, recently activated, and exhausted $CD8^+$ T cells (176). Although infection parameters and inflammatory events are well defined in mouse model studies, most human studies remain agnostic in regard to the infection and activation history of Ag-specific T cells. This in turn makes it difficult to correctly interpret the underlying reason for expression of PD-1 and TOX by human T cells.

Our data emphasize the need for conservative interpretation of TOX regarding activation and exhaustion and also caution against interpreting TOX expression purely through the lens of recent TCR-mediated activation. TOX expression is predictive of T cell exhaustion and unfavorable outcome in hepatocellular carcinoma animal models and clinical samples (177), in line with the paradigm of TOX-mediated, TCR-dependent T cell dysfunction. However, other studies have yielded contradictory data. Meta analyses of TOX expression in breast cancers reported TOX levels paradoxically correlating with increased immune cell function and favorable prognosis (178). This is perplexing, as in tumors, TOX expression is associated with T cell dysfunction (130,

136, 137). This discrepancy could be in part explained by TOX upregulation during activation, akin to what we observed during T cell activation in TCR-dependent and -independent stimulations. Thus, our data stress that all possible activation pathways of TOX and PD-1 induction must be considered before interpreting TOX as a biomarker of T cell dysfunction. A well-done human study (141) that interrogated TOX heterogeneity found elevated TOX in CMV-specific and EBV-specific $CD8^+$ T_{mem} and hypothesized that recent viral reactivation provide cognate Ag to facilitate TCR-mediated upregulation of TOX. This is certainly a plausible explanation, but our data highlight the need to also consider recent exposure to inflammation as a critical parameter affecting TOX expression. Conventional $CD8^+$ T_{EM} and T_{EMRA} (the predominant phenotype of CMV-specific and EBV-specific $CD8^+$ T cells) express elevated levels of TOX basally; T_{CM} (including IAV-specific $CD8^+$ T cells) and innate-like MAIT cells can, too, upregulate TOX expression after inflammation-mediated activation. Importantly, our data highlight that this mechanism of TOX expression was conserved across species, conventional $CD8^+$ T_{mem} subsets, and innate-like MAIT cells.

Because proinflammatory cytokines can concurrently induce TOX and PD-1 expression, these signals may drive TOX heterogeneity in other contexts. P14 T_{RM} show increased *Tox* expression at homeostasis, which is observed 90 days after priming with LCMV Armstrong (144). Because the acute infection is cleared well before this time point, it is unlikely that continued TCR signaling by cognate Ag drives this phenotype, despite elevated transcripts encoding mediators of TCR signaling (144). However, IL-15 is likely present within the tissue microenvironment. IL-15 is implicated in T_{RM} maintenance (149, 150), and transcriptional profiles indicative of IL-15/STAT5 signaling are detected in human T_{RM} (147, 148). Thus, IL-15 in tissue microenvironments may also contribute to TOX heterogeneity. Future work will be necessary to dissect the role of these inflammatory cues versus other signals that can shape T_{RM} phenotype, such as co-stimulation and tonic TCR signaling (145).

Previous studies have demonstrated that TOX ablation or knockdown leads to PD-1 downregulation in models of exhaustion (130, 136, 138, 139), and, conversely, introduction of TOX-expressing constructs enhances PD-1 expression (138, 139). Similarly, our data showed a close correlation in regards to TOX and PD-1 expression levels, but we found that PD-1 expression could be induced in stimulated $Tox^{-/-}$ P14 T_{mem}. Of note, these $Tox^{-/-}$ P14 T_{mem} lacked exon 5, which abrogates the ability to function as a transcription factor, but the truncated protein is still expressed and detected by the TOX antibody. Alfei et al. (130) previously showed that the early wave of effector cells formed from $Tox^{-/-}$ T_{naive} cells express significant levels of PD-1

independently of functional TOX. However, TOX is required for the expression of high levels of PD-1 at later stages, once the initial population of exhausted effector T cells are replaced by a proliferation competent TCF1 progenitor population (152). Together, these data suggest that the long-term expression of PD-1 requires TOX, but the activation-induced expression of PD-1 is TOX-independent. In the absence of TOX, PD-1 expression could be driven by TOX2, which can induce PD-1 expression in $CD8^+$ T cells (138, 139); however, it remains unclear if TOX2 is also upregulated by transient TCR-mediated or cytokine-mediated stimulation. Similarly, how different activating signals integrate to regulate TOX expression also requires further studies: although inflammatory cues increase TOX expression in T_{mem}, increased IL-12 signaling during the priming of T_{naive} has been shown to limit subsequent TOX expression at steady state (179-181).

Overall, our data suggest that the mechanisms that regulate TOX expression, both at homeostasis and after transient TCR or cytokine stimulation, were remarkably similar and quite possibly highly conserved between humans and mice. Our data further highlight the need to consider TOX and PD-1 expression as prominent indicators of ongoing activation and effector programs in T_{mem} instead of exclusive biomarkers of exhaustion.

3.4 *Hints of a regulatory program during bystander activation?*

Much to our surprise, bystander activation of $CD8^+$ T_{mem} parallels TCR-mediated activation in more ways than just cytotoxicity—we show that exposure to pro-inflammatory cytokines leads to the upregulation of TOX and PD-1 (Figure 3.17).

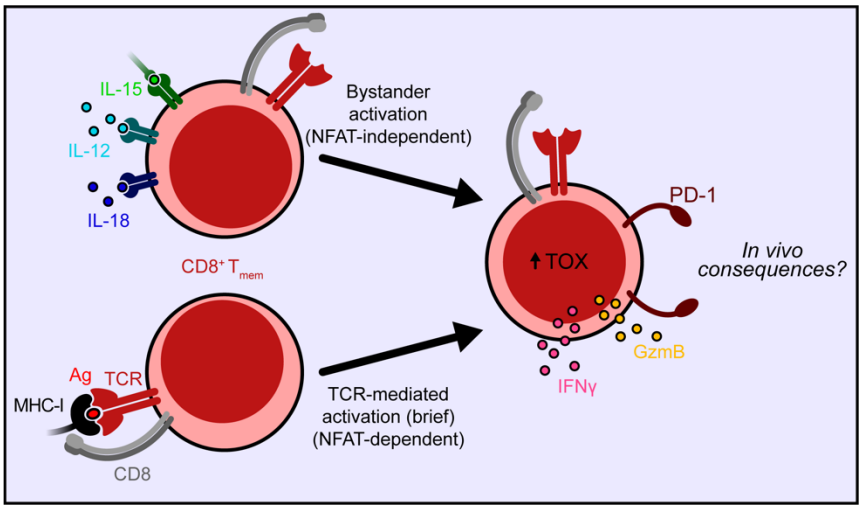

Figure 3.17 Bystander activation and TCR-mediated activation converge, eliciting effector functions as well as TOX and PD-1 upregulation.

Although the induction of TOX, PD-1, and effector molecules mechanistically differs between TCR- and inflammation-mediated activation, it is important to consider the role of PD-1 in these contexts. The upregulation of PD-1 after transient TCR stimulation during acute infection is believed to tune the $CD8^+$ T-cell response and limit TCR-mediated effector functions, as PD-1 blockade or knockout shifts subset distribution and is associated with tissue pathologies (182, 183). While this and other cell-intrinsic and -extrinsic mechanisms of T cell attenuation control TCR-mediated $CD8^+$ T-cell responses, it is less clear what controls the response of bystander-activated $CD8^+$ T_{mem}. While studies have suggested cessation of inflammation is responsible for terminating the effector program of bystander-activated $CD8^+$ T_{mem} (77), we previously observed that bystander responses change during *L. monocytogenes* infection despite persisting inflammation. Specifically, IFNγ expression in bystander-activated $CD8^+$ T_{mem} is limited to the first 24 h of infection; thereafter, bystander-activated $CD8^+$ T_{mem} largely express GzmB (6). While this may reflect a change in the inflammatory milieu, it is also possible that regulatory programs are at play. We observe an increase of PD-1 expression in bystander-activated $CD8^+$ T_{mem} as IFNγ expression wanes (Figure 3.18). Could this highlight a yet-appreciated regulatory programs which control bystander activation? Future work will be necessary, but these data point to new mechanisms that may allow us to better tune bystander-mediated effector responses.

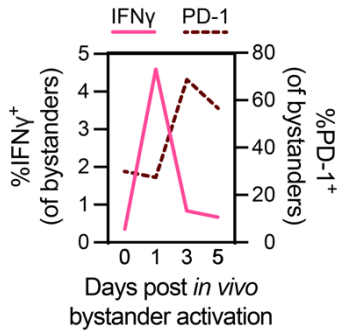

Figure 3.18 In vivo kinetics of IFNγ and PD-1 expression in bystander-activated $CD8^+$ T_{mem}

Ex vivo expression of IFNγ (pink, left axis) and PD-1 (maroon, right axis) in bystander-activated OT-I T_{mem} at the splenic white pulp during *L. monocytogenes* infection (Infection model and data from Chapter 2).

3.5 Methods

3.5.1 Mice

All animals were maintained in specific pathogen–free facilities and infected in modified pathogen–free facilities. Experimental groups were nonblinded; animals were randomly assigned to experimental groups; and no specific method was used to calculate sample sizes.

We purchased 6-week-old female C67BL/6J mice from The Jackson Laboratory; *Tox*$^{-/-}$ P14 mice (P14 *Tox*$^{tm1c(KOMP)Wtsi}$;*Mx*^{Cre};*Rosa26-STOP-eYFP*) were generated as previously described (130). WT and *Tox*$^{-/-}$ P14 mice, OT-I mice, and gBT-I mice were maintained on CD45.1 congenic backgrounds. We euthanized mice in accordance with institutional protocols and subsequently collected spleens and LNs for experimentation.

3.5.2 Development of memory mice

We prepared a single-cell suspension of LN cells that were harvested from female OT-I, P14, or gBT-I mice by mechanically passing LN tissue through a 70 to 100 μm strainer. To enrich transgenic T cells, we used MACS with a CD8 Negative Selection Kit (Miltenyi Biotec).

For OT-I memory mice, we adoptively transferred 1 × 10^4 OT-I T cells in sterile 1 × PBS i.v. per C57BL/6J recipient and subsequently infected recipients i.v. with 1 to 2 × 10^7 PFU VSV-OVA or 4 × 10^3 CFU OVA-expressing *L. monocytogenes* (*L. monocytogenes*–OVA). For gBT-I memory mice, we adoptively transferred 5 × 10^4 gBT-I T cells i.v. and subsequently infected recipient mice i.v. with or 4 × 10^3 CFU HSV2 gB–expressing *L. monocytogenes* (*L. monocytogenes*–gB). We allowed 60 days or longer to pass after initial VSV or *L. monocytogenes* infections before assaying tissues.

For P14 memory mice, we adoptively transferred 2 × 10^3 WT P14 T cells i.v. and subsequently infected recipient mice i.v. with 2 × 10^5 PFU LCMV Armstrong clone (LCMV Arm.) or 2 × 10^6 PFU LCMV Docile clone (LCMV Doc.). For *Tox*$^{-/-}$ P14 memory mice, we adoptively transferred 2 × 10^3 *Tox*$^{-/-}$ P14 memory mice and subsequently infected with 2 × 10^5 PFU LCMV Arm.; we allowed 28 days to pass after initial LCMV infection before assaying tissues.

3.5.3 Study approvals

Mouse protocols and experimentation conducted at the Fred Hutchinson Cancer Research Center were approved by and in compliance with the ethical regulations of the Fred Hutchinson Cancer Research Center's IACUC. Experiments performed at the Technical University of Munich were in compliance with institutional and governmental regulations in Germany and approved by the veterinarian authorities of the Regierung von Oberbayern in Germany.

Twenty-three healthy, HIV-uninfected adults were recruited by the Seattle HIV Vaccine Trials Unit (Seattle, Washington, USA) as part of the study "Establishing Immunologic Assays for Determining HIV-1 Prevention and Control." These samples are also known as the Seattle Area Control Cohort. All participants were provided and signed informed consent, and the Fred Hutchinson Cancer Research Center IRB approved the study protocol.

3.5.4 T cell isolation and in vitro stimulation

We harvested spleen and LN from memory mice and mechanically prepared single-cell suspensions. We thawed approximately 4×10^7 cryopreserved PBMC in human RP10 media (RPMI1640 supplemented with 10% FBS, 2 mM L-glutamine, 100 U/mL penicillin-streptomycin). To enrich bulk T cells from single-cell suspensions, we respectively used mouse-specific and human-specific T cell negative isolation MACS (STEMCELL Technologies). We plated 0.5 to 1×10^6 T cells per well in 96-well V-bottom tissue culture plates. We cultured cells in human RP10 or mouse RP10 media (RPMI 1640 supplemented with 10% FBS, 2 mM L-glutamine, 100 U/mL penicillin-streptomycin, 1 mM sodium pyruvate, 0.05 mM β-mercaptoethanol, and 1 mM HEPES). To stimulate cells, we cultured mouse T cells in mouse RP10 with rIL-12, rIL-15, and rIL-18 (each at 100 ng/mL; BioLegend), with Dynabeads mouse T-Activator (Thermo Fisher) anti-CD3/CD28 beads (at a 1:1 bead/cell ratio) or media alone. For human T cell stimulations, we used human RP10 media with combinations of rIL-6 (BioLegend), rIL-12, rIL-15, and/or rIL-18 (each at 100 ng/mL; Peprotech), with Dynabeads human T-Activator (Thermo Fisher) anti-CD3/CD28 beads (at a 1:1 bead/cell ratio) or RP10 alone. In calcineurin inhibition experiments, we conducted stimulations in the presence of cyclosporin A (CsA) (Sigma Aldrich; 0.1μg/mL) and FK506 (EMD Millipore; 1μg/mL). We cultured cells at 37ºC, 5% CO_2, sampling cells at 0, 24, and/or 48 hours for flow staining. For intracellular cytokine staining, we added GolgiPlug (BD Biosciences) at a 1:1000 dilution 6 hours prior to cell harvest.

3.5.5 Flow cytometric analysis

We conducted all flow staining for mouse and human T cells on ice and at room temperature, respectively. All mouse and human flow panel reagent information, stain conditions, and gating are included in Figure 3.19, Figure 3.20, Figure 3.21, Figure 3.22, Figure 3.23, Figure 3.24 and Table 3.1, Table 3.2, Table 3.3, Table 3.4, Table 3.5, Table 3.6, Table 3.7. We conducted LIVE/DEAD fixable aqua or blue viability dye (Thermo Fisher) (AViD or BViD, respectively) or Zombie Near-IR viability dye (NIRViD) (BioLegend) staining in 1 × PBS. For surface staining, we utilized FACS Wash (1 × PBS supplemented with 2% FBS and 0.2% sodium azide) as the stain diluent. For all TOX staining panels, we fixed cells with the FOXP3 Fixation/Permeabilization Buffer Kit (Thermo Fisher) and conducted intranuclear stains using the FOXP3 Permeabilization Buffer (Thermo Fisher) as diluent. To minimize day-to-day variation for TOX staining, we conducted all intracellular stains within a batch (0-, 24-, and 48-hour samples) at the same time. We resuspended cells in FACS Wash and acquired events on a FACSymphony A5 and LSRFortessa cell analyzers (BD Biosciences), which we analyzed using FlowJo v10 (BD Biosciences). We conducted statistical testing using Prism v8 (GraphPad).

Table 3.1 Mouse flow cytometry panel for SPF C57BL/6J mice, LCMV Armstrong P14 memory mice, and LCMV Docile memory mice

Reagent	Fluor	Clone	Vendor	Dilution
Viability stain (1x PBS diluent, 20 min, on ice)				
Zombie NIR fixable viability kit (NIRViD)	APC-Cy7	NA	BioLegend	1:500
Surface stain (FACSWash diluent, 30 min, on ice)				
Fc block (CD16/CD32)	Unconjugated	2.4G2	BD	1:200
CD4	PerCP-Cy5.5	RM4-4	BioLegend	1:200
CD8α	AF700	53-6.7	Thermo Fisher	1:200
CD45.1	PE-Cy7	A20	Thermo Fisher	1:200
CD44	BV421	IM7	BioLegend	1:200
PD-1	BV605	29F.1A12	BioLegend	1:100
CD62L	BV785	MEL-14	BioLegend	1:200
Fix (1x eBioscience FOXP3 fixation buffer, 20 min, on ice)				
Intracellular stain (1x eBioscience FOXP3 permeabilization buffer, 30 min, on ice)				
Fc block (CD16/32)	Unconjugated	2.4G2	BD	1:200
TOX	e660	TXRX10	Thermo Fisher	1:200
TCF1/7	PE	S33966	BD	1:200

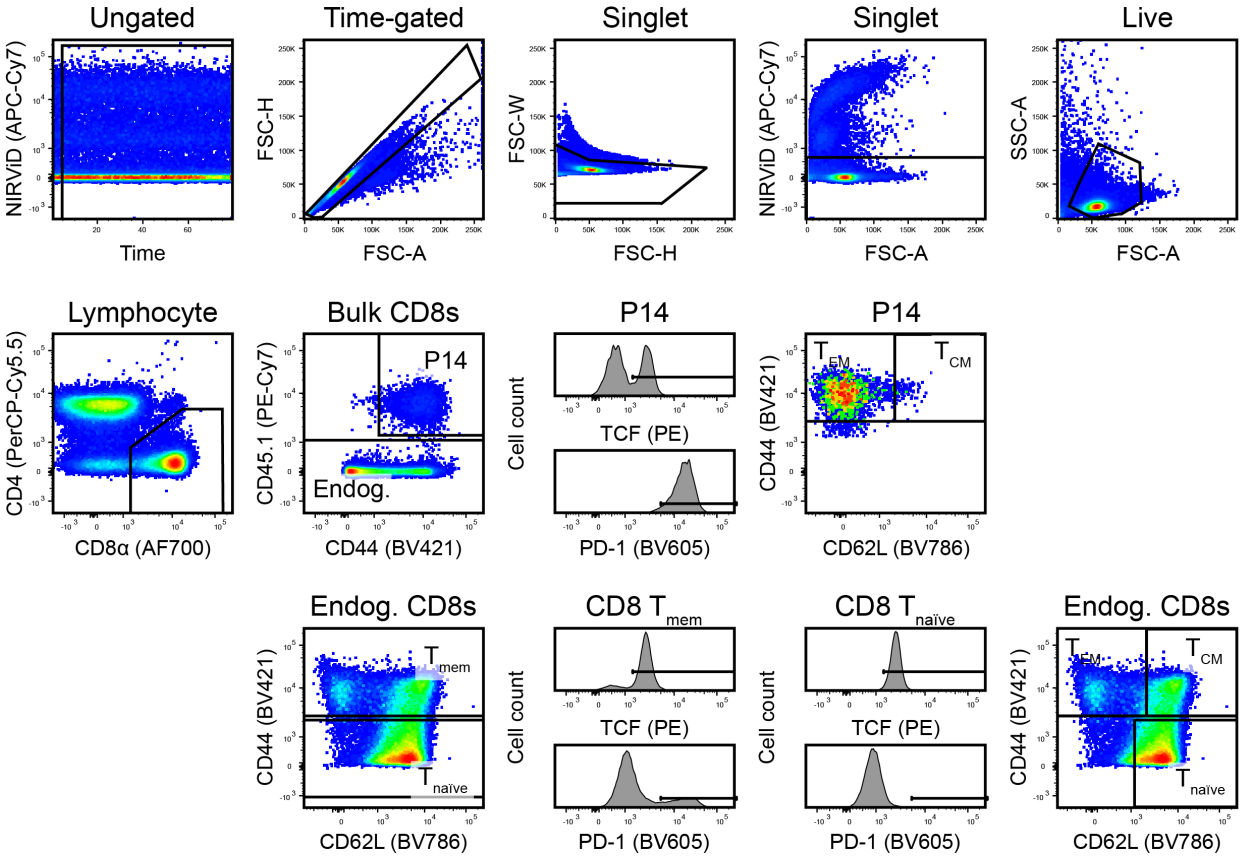

Figure 3.19 Flow cytometry gating strategy for SPF C57BL/6J mice, LCMV Armstrong P14 memory mice, and LCMV Docile memory mice

Table 3.2 Mouse flow cytometry panel for VSV-OVA OT-I memory mice, LM-OVA memory mice, and LM-gB gBT-I memory mice

Reagent	Fluor	Clone	Vendor	Dilution
Viability stain (1x PBS diluent, 20 min, on ice)				
LIVE/DEAD fixable blue viability dye (BViD)	UV450	NA	Thermo Fisher	1:500
Surface stain (FACSWash diluent, 30 min, on ice)				
Fc block (CD16/CD32)	Unconjugated	2.4G2	BD Biosciences	1:200
CD4	BV786	GK1.5	BD Biosciences	1:200
CD8α	PE-CF594	53-6.7	BD Biosciences	1:200
CD45.1	BUV395	A20	BD Biosciences	1:200
CD44	e450	IM7	Thermo Fisher	1:200
PD-1	BV605	29F.1A12	BioLegend	1:100
CD62L	FITC	MEL-14	Thermo Fisher	1:200
Fix (1x eBioscience FOXP3 fixation buffer, 20 min, on ice)				
Intracellular stain (1x eBioscience FOXP3 permeabilization buffer, 30 min, on ice)				
Fc block (CD16/32)	Unconjugated	2.4G2	BD Biosciences	1:200
TOX	APC	REA473	Miltenyi Biotec	1:100
TCF1/7	PE	C63D9	Cell Signaling	1:40

Table 3.3 Mouse flow cytometry panel for VSV-OVA OT-I memory mice

Reagent	Fluor	Clone	Vendor	Dilution
Viability stain (1x PBS diluent, 20 min, on ice)				
LIVE/DEAD fixable aqua viability dye (AViD)	V510	NA	Thermo Fisher	1:500
Surface stain (FACSWash diluent, 30 min, on ice)				
Fc block (CD16/CD32)	Unconjugated	2.4G2	BD Biosciences	1:200
CD4	BV786	GK1.5	BD Biosciences	1:200
CD8α	PE-CF594	53-6.7	BD Biosciences	1:200
CD45.1	BUV395	A20	BD Biosciences	1:200
CD45.2	FITC	104	Thermo Fisher	1:200
CD44	APC-e780	IM7	Thermo Fisher	1:200
PD-1	BV605	29F.1A12	BioLegend	1:100
Fix (1x eBioscience FOXP3 fixation buffer, 20 min, on ice)				
Intracellular stain (1x eBioscience FOXP3 permeabilization buffer, 30 min, on ice)				
Fc block (CD16/32)	Unconjugated	2.4G2	BD Biosciences	1:200
TOX	APC	REA473	Miltenyi Biotec	1:100

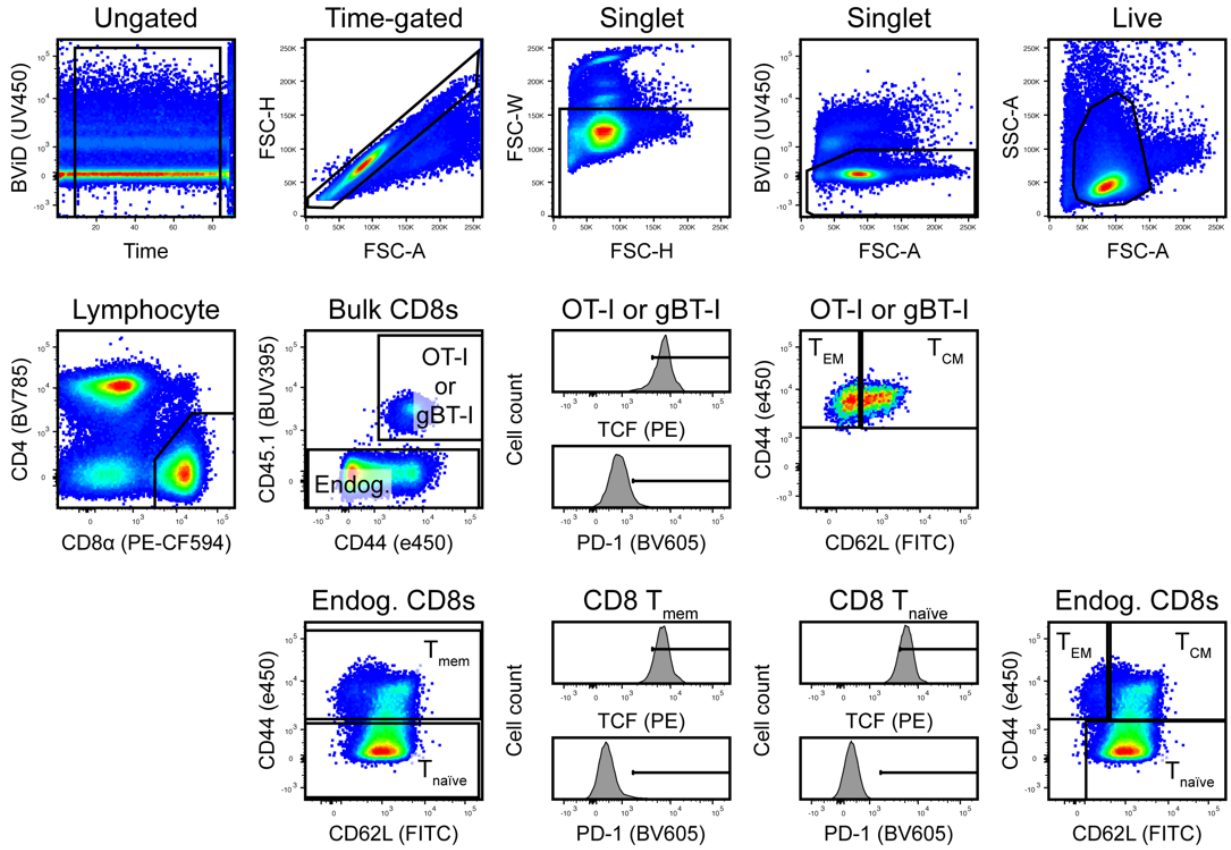

Figure 3.20 Flow cytometry gating strategy for VSV-OVA OT-I memory mice, LM-OVA memory mice, and LM-gB gBT-I memory mice

Table 3.4 Flow cytometry panel for intracellular cytokine staining in mouse T cells.

Reagent	Fluor	Clone	Vendor	Dilution
Viability stain (1x PBS diluent, 20 min, on ice)				
LIVE/DEAD fixable blue viability dye (BViD)	UV450	NA	Thermo Fisher	1:500
Surface stain (FACSWash diluent, 30 min, on ice)				
Fc block (CD16/CD32)	Unconjugated	2.4G2	BD Biosciences	1:200
CD4	PE-Cy7	RM4-5	BD Biosciences	1:200
CD8α	BV786	53-6.7	BD Biosciences	1:200
CD44	e450	IM7	Thermo Fisher	1:200
CD62L	FITC	MEL-14	Thermo Fisher	1:200
CD69	PE-Dz594	H1.2F3	BioLegend	1:100
NKG2D	BV711	CX5	BD Biosciences	1:200
PD-1	BV605	29F.1A12	BioLegend	1:100
Fix (1x eBioscience FOXP3 fixation buffer, 20 min, on ice)				
Intracellular stain (1x eBioscience FOXP3 permeabilization buffer, 30 min, on ice)				
Fc block (CD16/32)	Unconjugated	2.4G2	BD Biosciences	1:200
IFNγ	BUV737	XMG1.2	BD Biosciences	1:200
Granzyme B	PE	GB11	Thermo Fisher	1:100
TOX	APC	REA473	Miltenyi Biotec	1:100

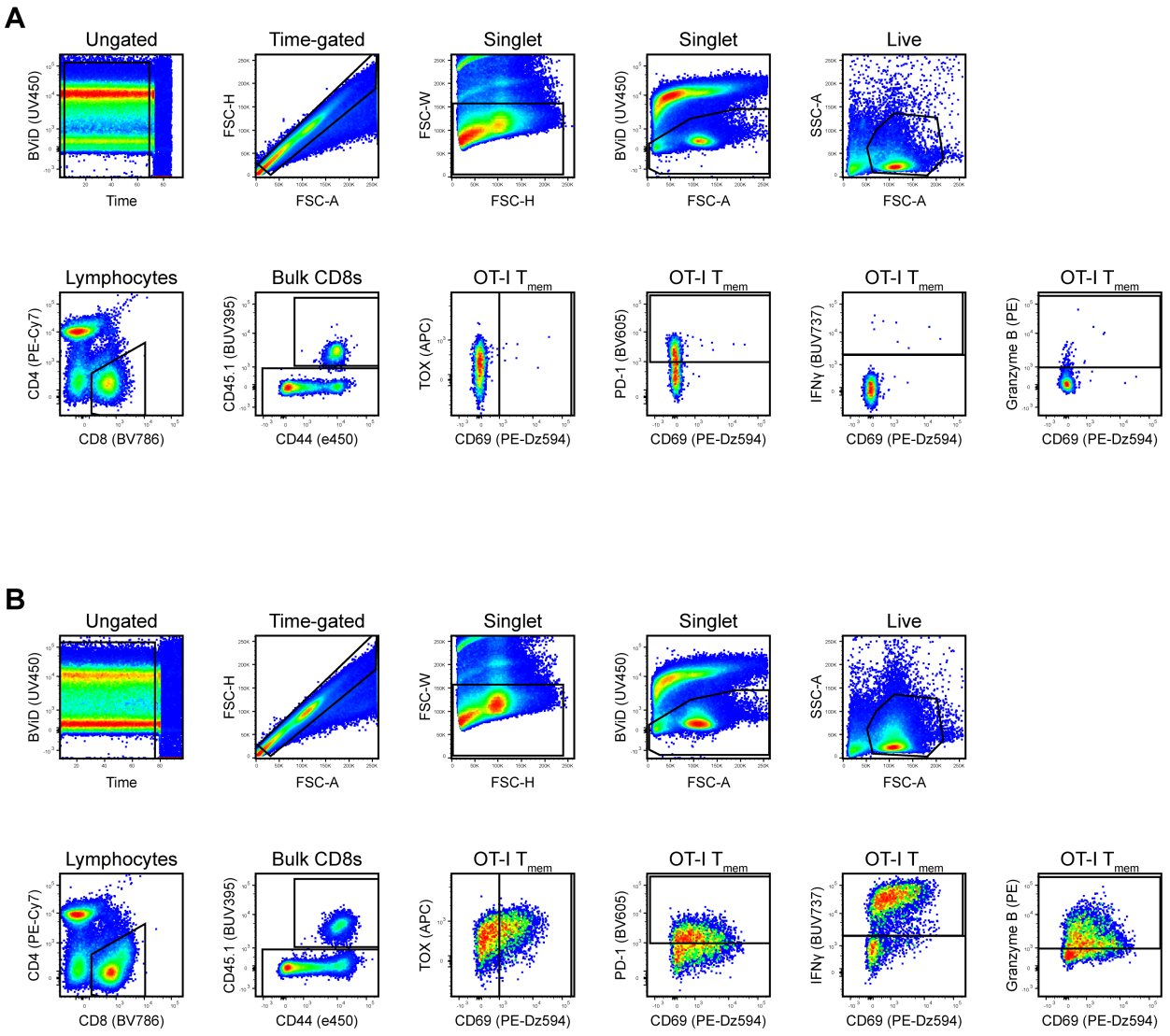

Figure 3.21 Flow cytometry gating for parallel cytokine, TOX, and PD-1 analysis in mouse T cells.

Representative flow gating in **A** mock-stimulated and **B** IL-12, IL-15, and IL-18 (100ng/mL, each) after 24 hours of culture.

Table 3.5 Flow cytometry panel for HLA-A*02 human PBMC samples.

Reagent	Fluor	Clone	Vendor	Dilution
Viability stain (1x PBS diluent, 20 min, room temperature)				
LIVE/DEAD fixable blue viability dye (BViD)	UV450	NA	Thermo Fisher	1:500
Tetramer stain (FACSWash diluent, 60 min, room temperature)				
MR1 OP-5-RU (MAIT cell) tetramer	BV421	NA	NIH Tetramer Core	1:500
HLA-A*02 influenza A virus (IAV) (GILGFVFTL) tetramer	PE	NA	Fred Hutch Immune Monitoring	1:150
TruStain FcX (Fc block)	NA	NA	BioLegend	1:20
Surface stain (FACSWash diluent, 20 min, room temperature)				
CD3	BUV496	UCHT1	BD Biosciences	1:40
CD4	APC-H7	RPA-T4	BD Biosciences	1:40
CD8	BUV395	RPA-T8	BD Biosciences	1:80
CD45RO	BB515	UCHL1	BD Biosciences	1:160
CD69	BUV737	FN50	BD Biosciences	1:40
CCR7	PE-Cy7	3D12	BD Biosciences	1:40
PD-1	BB700	EH12.1	BD Biosciences	1:20
Fix (1x eBioscience FOXP3 fixation buffer, 20 min, room temperature)				
Intracellular stain (1x eBioscience FOXP3 permeabilization buffer, 30 min, room temperature)				
TOX*	APC	REA473	Miltenyi Biotec	1:80
KLH-specific REA control antibody I*	APC	REA293	Miltenyi Biotec	1:80

*Reagents were not used in unison, but as stains in separate samples.

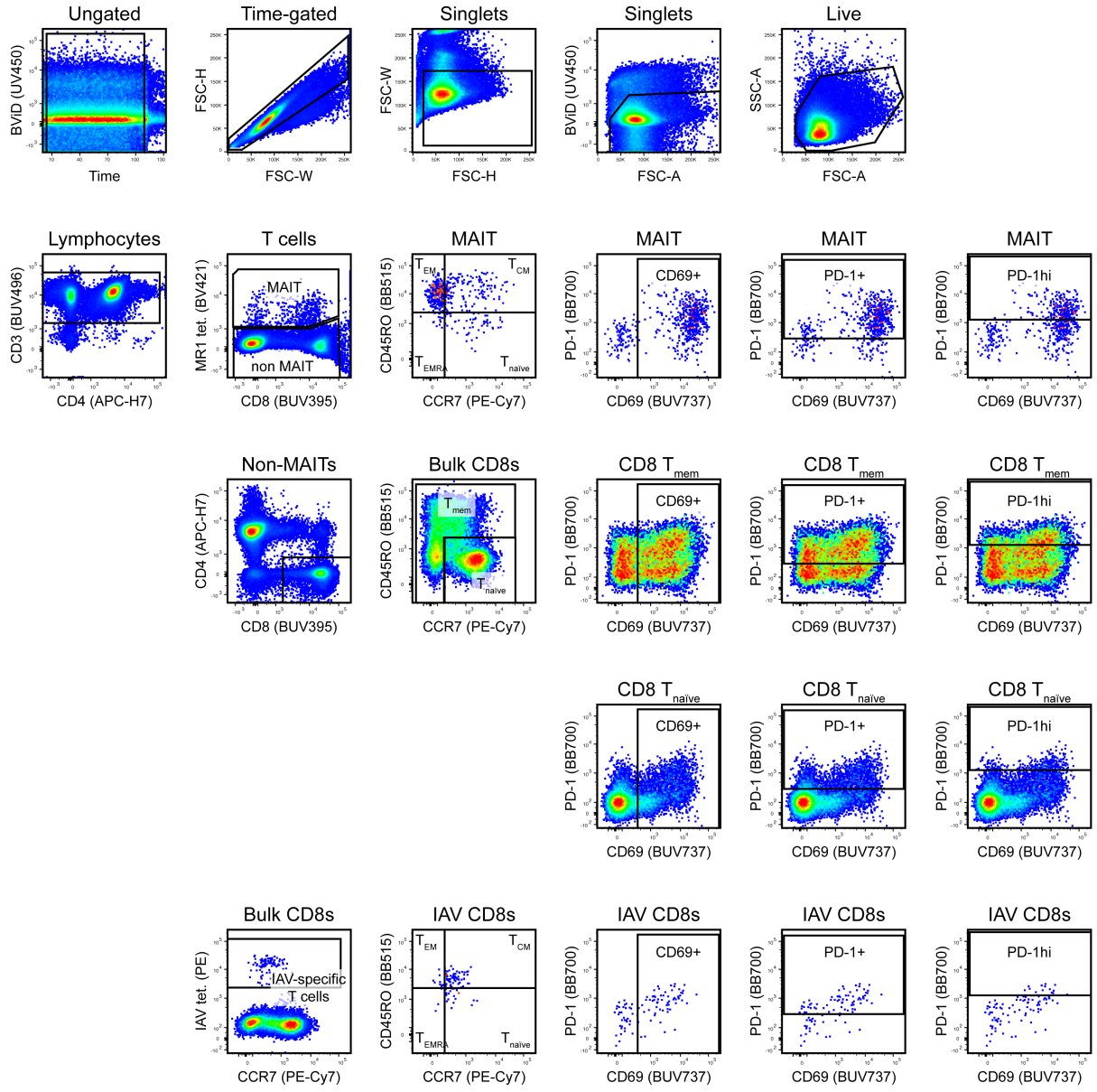

Figure 3.22 Flow cytometry gating strategy identifying tetramer-stained human T cells.

Representative flow gating for bulk CD8$^+$, IAV-specific, and MAIT cell subsets (IL-12, IL-15, IL-18–stimulated, 24 hours).

Table 3.6 Flow cytometry panel for general human PBMC samples

Reagent	Fluor	Clone	Vendor	Dilution
Viability stain (1x PBS diluent, 20 min, room temperature)				
LIVE/DEAD fixable blue viability dye (BViD)	UV450	NA	Thermo Fisher	1:500
Tetramer stain (FACSWash diluent, 60 min, room temperature)				
MR1 OP-5-RU (MAIT cell) tetramer	BV421	NA	NIH Tetramer Core	1:500
TruStain FcX (Fc block)	NA	NA	BioLegend	1:20
Surface stain (FACSWash diluent, 20 min, room temperature)				
CD3	BUV496	UCHT1	BD Biosciences	1:40
CD4	APC-H7	RPA-T4	BD Biosciences	1:40
CD8	BUV395	RPA-T8	BD Biosciences	1:80
CD45RO	BB515	UCHL1	BD Biosciences	1:160
CD69	BUV737	FN50	BD Biosciences	1:40
CCR7	PE-Cy7	3D12	BD Biosciences	1:40
PD-1	BB700	EH12.1	BD Biosciences	1:20
Fix (1x eBioscience FOXP3 fixation buffer, 20 min, room temperature)				
Intracellular stain (1x eBioscience FOXP3 permeabilization buffer, 30 min, room temperature)				
TOX	APC	REA473	Miltenyi Biotec	1:80
TCF-1/7	PE	C63D9	Cell Signaling	1:40

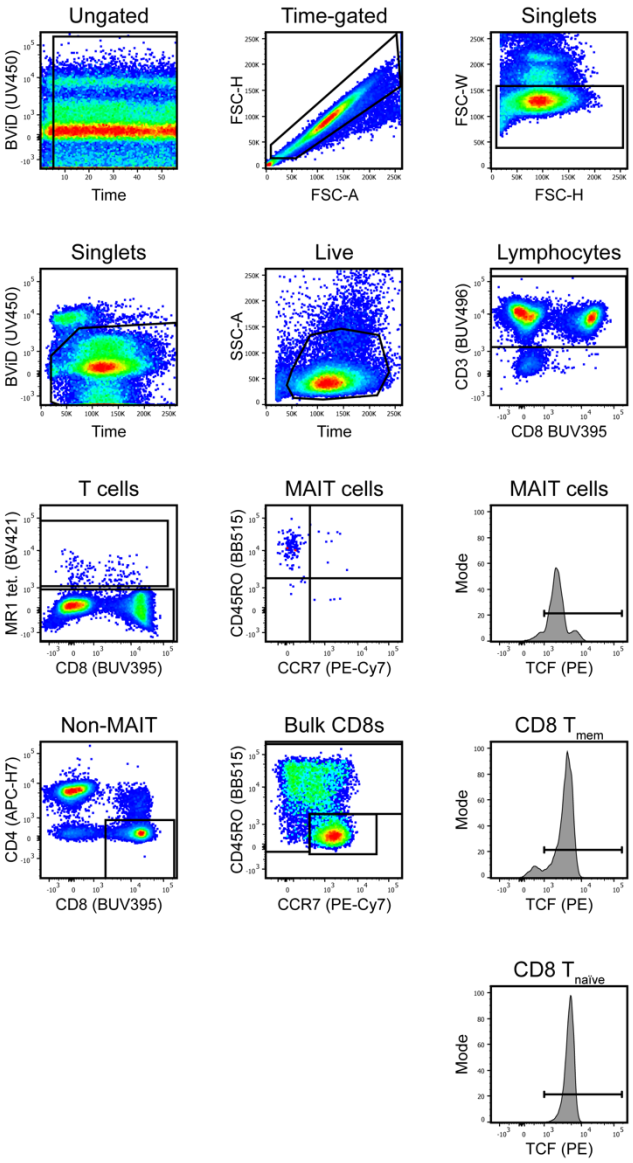

Figure 3.23 Flow cytometry gating for TCF1 expression in human T cell subsets

Table 3.7 Flow cytometry panel for CsA/FK506 ICS assay in human T cells

Reagent	Fluor	Clone	Vendor	Dilution
Viability stain (1x PBS diluent, 20 min, room temperature)				
LIVE/DEAD fixable blue viability dye (BViD)	UV450	NA	Thermo Fisher	1:500
Surface stain (FACSWash diluent, 20 min, room temperature)				
CD45RO	BB515	UCHL1	BD Biosciences	1:160
CCR7	PE-Cy7	3D12	BD Biosciences	1:40
Fix (1x BD Cytofix/Cytoperm fixation buffer, 20 min, room temperature)				
Intracellular stain (1x BD Perm/wash permeabilization buffer, 30 min, room temperature)				
CD3	BUV496	UCHT1	BD Biosciences	1:40
CD4	AF647	RPA-T4	BD Biosciences	1:40
CD8	BV786	RPA-T8	BD Biosciences	1:40
TCR Vα7.2	PE	3C10	BioLegend	1:20
IFNγ	BUV395	B27	BD Biosciences	1:50
IL-2	BV421	MQ1-17H12	BD Biosciences	1:20
Granzyme B	AF700	GB11	BD Biosciences	1:80
TNFα	FITC	MAb11	Thermo Fisher	1:100

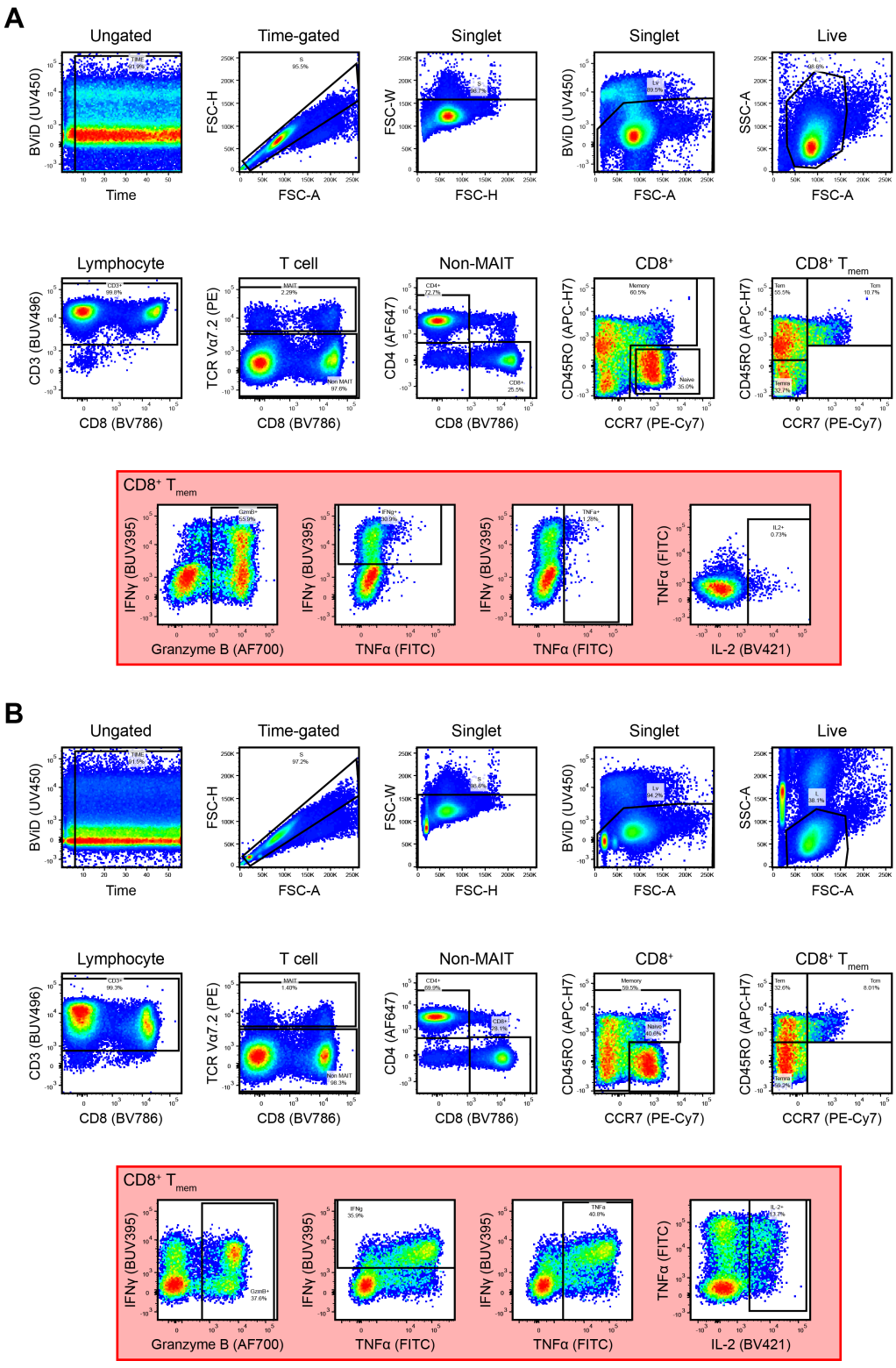

Figure 3.24 Flow gating strategy for CsA/FK506 ICS assay in human T cells

Gating strategy in T cells after 24h (**A**) IL-12/15/18 (100ng/mL, each) or (**B**) TCR stimulation.

3.5.6 Statistics

We used 2-tailed paired *t* tests, Mann-Whitney *U* tests, Wilcoxon's matched-pairs signed-rank tests, as well as Friedman's tests with Dunn's multiple comparisons tests.

3.6 Acknowledgements

We thank Andrea Schietinger for helpful discussions and critical review of the manuscript. We also thank the Prlic lab, especially Jami Erickson, Florian Mair, Marie Frutoso, and Veronica Davé, for critical review of the manuscript. This work was supported by NIH grant R01 AI123323 (to MP) and National Cancer Institute Grant F99 CA245735 (to NJM). NJM is a Leslie and Pete Higgins Achievement Rewards for College Scientists Fellow and Dr. Nancy Herrigel-Babienko Memorial Scholar. DZ and JB were supported by a European Research Council consolidator grant (ToCCaTa) and by the German Research Foundation (SFB1054 and SFB1371).

Chapter 4. Converging cytokine and metabolite networks shape asymmetric T cell residence at the term human maternal-fetal interface

Portions of the text and data from this dissertation are reproduced from the following work:

Maurice NJ, McCartney SA, Erickson JR, Frutoso M, DeJong CS, Islas LV, Vigil A, Lawler RL, Mair F, Taber AK, McElrath MJ, Newell EW, Sullivan LB, Shree R, Gammill HS, Prlic M "Converging cytokine and metabolite networks shape asymmetric T cell residence at the term human maternal-fetal interface"

Placentation presents immune conflict between mother and fetus, yet maternal immunity against infection is maintained without expense to fetal tolerance. This is generally believed to result from maternal-fetal interface (MFI) adaptations rendering it inaccessible to T cells. Despite this, we found that maternal T cells are broadly recruited to the MFI via chemokines and asymmetrically retained by pro-inflammatory cytokine networks in an antigen-independent manner. Co-receptors necessary for tissue residence and retention are elicited by IL-6, IL-15, and IL-18 and can be engaged by local macrophages. Although pro-inflammatory molecules elicit T cell effector functions, we show that additional cytokine (TGF-β1) and metabolite (kynurenine) networks converge to tune T cell function at the MFI to those of sentinels. Together, we demonstrate an additional facet of fetal tolerance, wherein T cells are broadly recruited and silenced in an antigen-independent, cytokine/metabolite-dependent manner. These mechanisms provide insight into antigen-nonspecific T cell regulation, especially in tissue microenvironments where they are enriched.

4.1 Introduction

Despite having evolved under the pressures of adaptive immunity, placentation is an immunologically paradoxical balancing act in which 1) maternal immunity tolerates a fetal allograft while 2) maintaining competency towards other pathogens (184, 185). Previous studies have illustrated that the placenta, the component of the fetal graft most exposed to maternal immunity, avoids detection by the maternal immune system. By virtue of thymic selection, maternal T cells are selected for reactivity to non-self peptide antigens (Ag) sourced from intracellular protein degradation (186, 187); but half of the fetal genome encodes paternal alleles that could potentially be seen as non self. In order to limit maternal T cell recognition and killing, placental trophoblast

downregulate the expression of major histocompatibility complex class I (MHC-I), the molecule required for surface presentation of Ags (188). Further studies have found additional evasive tactics which are used to restrict maternal T cells at the site of placentation (i.e., the maternal-fetal interface: MFI). Mouse models found that the decidua (the endometrial tissue which is remodeled by invading placental trophoblast), forbids maternal T cell entry by silencing the expression of chemokines encoded by *Cxcl9*, *Cxcl10*, and *Ccl5*, even during artificially high levels of systemic inflammation (189). Together, these models suggest that maternal immunocompetency and fetal tolerance is achieved by mechanisms that make the MFI as immunologically invisible as possible.

Despite these mechanisms, there is mounting evidence that the MFI, and even pregnancy itself, are not immunologically silent. Early in pregnancy, NK cells at the decidua contribute to effective placentation (190-194); and NK cells, as well as T cells, can be found at the first-trimester MFI using single-cell RNA sequencing (scRNAseq) (195). Pregnancy affects T cells, elevating regulatory T cell (T_{reg}) frequencies (196-198), and even expanding T cell clones with specificity to fetal Ag systemically (199). As pregnancy progresses, so does a signature of IL-2–STAT5 signaling, which ceases postpartum (200). At the end of gestation, signatures of immune cell activation can be detected in human choriodecidual tissues (201), suggesting immunity's role in both pregnancy and labor. Furthermore, inducing inflammation at the MFI with TCR or Toll-like receptor (TLR)-4 agonists, led to labor in mice (202). Given the immunologic nature of these phenomena, we hypothesize that maintaining homeostasis during maternal-fetal conflict is not addressed by evasion alone, but selective tuning of immune cell functions.

Though an invaluable research tool, mouse models present limitations in studying the MFI: 1) syngeneic mating limits the antigenic difference between mother and fetal graft, 2) rodent pregnancy fails to mirror human pregnancy in duration, number of conceptuses, and depth of placentation (203-205), and mice housed in specific pathogen-free (SPF) conditions fail to demonstrate the same level of immune cell differentiation and diversity as humans (161). Using samples from a cohort of patients undergoing uninduced, term cesarean section, we utilize 28-color flow cytometric and untargeted transcriptomic single-cell analyses to uncover maternal T cell adaptations unique to the MFI, in which a subset of $CD8^+$ T cells are tissue resident and highly activated. Despite activation signatures congruent with TCR activation, we leveraged mass cytometry metal-tagged tetramer screens and found this phenomenon is likely independent of TCR specificity or cognate Ag. Using a combination of single-cell transcriptomics and proteomics,

we instead discover pro-inflammatory chemokine and cytokine networks which recruit and activate maternal $CD8^+$ T cells at the MFI. Though these signals are sufficient to elicit $CD8^+$ T cell cytotoxicity in vitro, this is curbed in vivo by elevated levels of regulatory molecules in situ. Specifically, elevated levels of transforming growth factor-β1 (TGF-β1) and the tryptophan metabolite, kynurenine, are found at the placenta. During in vitro cytokine stimulation, these factors cooperate to limit inflammation-mediated cytotoxicity without restricting other programs resulting from inflammation-dependent activation. Together, our data suggests that mechanisms at the MFI symmetrically recruit, retain, and restrain maternal T cells at the maternal side of the MFI. Importantly, these factors at the placenta do not attenuate TCR-driven $CD8^+$ T cell effector programs in vitro, suggesting that Ag-specific immunity is not compromised by elevated TGF-β1 or kynurenine. We discuss the relevance of inflammation-dependent $CD8^+$ T cell programs for both fetal tolerance and maternal competence against pathogens.

4.2 Results

4.2.1 A tissue-resident phenotype is biased towards the maternal side of the MFI

The maternal-fetal interface (MFI) is the primary site of immune conflict, so we initially sought to comprehensively test changes in cellular immunity here versus the periphery of mother and fetus. Since our initial aim was to develop a dataset concerning immunity at the MFI during homeostasis at term, we selectively recruited women without pregnancy and/or immunologic complications undergoing routine, term, uninduced cesarean section at University of Washington Medical Center Labor and Delivery. We chose to exclude cases undergoing vaginal delivery or cesarean after induction to minimize immune modifications that have been associated with labor and parturition (206). Since the placenta is a circulatory interface, we isolated leukocytes from both maternal blood (MB) and fetal cord blood (CB), to determine if our observations resulted from peripheral cell contamination or tissue-dependent phenomena (Figure 4.1A). The fetal-derived placenta is disproportionately exposed to maternal immunity; therefore, we sampled biopsies from the maternal side of the placenta (including adherent decidual tissue) and the fetal side of the placenta (mPLAC and fPLAC, respectively) (Figure 4.1A). We interrogated these tissues using 28-color flow cytometry (207), including cryopreserved peripheral blood mononuclear cells (PBMC) from a single Seattle Area Cohort (SAC) donor to determine batch-to-batch variation (Figure 4.1A).

Though we found a decreased frequency of $CD3^+$ T cells in placental tissues, $CD8^+$ T cells constituted a greater proportion of the T cell pools at these sites than in circulation (Figure 4.1B). Given the stark change in $CD8^+$ T cell frequency, we surveyed for other tissue-based changes in phenotypes. Owing to the high complexity of 28-color flow data, we first utilized dimensionality reduction using uniform manifold approximation projections (UMAP) (208, 209) on pre-gated $CD8^+$ T cell events (Figure 4.1C). When we color-coded $CD8^+$ T cell events based on tissue source, we noted an island dominated by cells isolated from mPLAC biopsies (PLAC-enriched gate). This population, compared to all other events, was characterized by T cells with an effector memory (T_{EM}) phenotype ($CCR7^{lo}$, $CD45RA^{lo}$) and upregulation of markers associated with activation, exhaustion, and/or tissue residence (CD69, CD103, PD-1, and HLA-DR) (Figure 4.1C, Figure 4.2A, B).

Previous studies have described an enrichment of activated (i.e., CD69-expressing(210)) and/or T_{EM} at the MFI (211, 212), yet these studies predated the discovery of tissue resident memory (T_{RM}) cells and biomarkers which define them (213). T_{RM} share a T_{EM} phenotype ($CCR7^{lo}$ $CD45RA^{lo}$), yet near-constitutively express the activation marker CD69 and reside in tissues long-term (213, 214). Therefore, we asked if PLAC-enriched $CD8^+$ T cells were of a T_{RM} phenotype. We surveyed the expression of CD69 and CD103, which can be singly or doubly expressed by T_{RM} (159, 176, 213). Despite donor-to-donor variation, we found significant expression of CD69 in mPLAC $CD8^+$ T cells, and to a lesser degree, CD69 CD103 co-expression (Figure 4.1D). Further, nearly all $CD69^+$ events from mPLAC $CD8^+$ T cells maintained a T_{EM} phenotype (Figure 4.2C), in line with using CD69 as a biomarker of tissue residence rather than activation alone.

4.2.2 $CD8^+$ T_{RM} populations are maternally-derived and highly activated

To ensure appropriate use of CD69 as a biomarker of tissue residence, we leveraged single-cell RNA sequencing (scRNAseq) on $CD8^+$ T cells that we sorted fresh from tissues using fluorescence-activated cell sorting (FACS). Like our targeted cytometry-based proteomics data (Figure 4.1C), we could identify a placenta-enriched subpopulation of $CD8^+$ T cells using untargeted transcriptomics (Figure 4.3A). We identified this population with graph-based clustering (cluster 5) and found it had transcriptional profiles concurrent with mouse and human $CD8^+$ T_{RM} from other organs (low *CCR7*, *SELL*, *KLF2*, *KLF3*, *TCF7*, *S1PR4*; high *CD69*, *RGS1*) (Figure 4.3A, B) (149, 176, 215, 216). Since mother (XX) and fetus (XY) were sex mismatched, we were able to identify this T_{RM} population as maternal-derived, as it expressed higher levels of

the X-inactivating transcript, *XIST*, and negligible levels of the Y-associated transcript, *RPS4Y1* (Figure 4.3B). To further prove this phenotype was one of bona fide tissue residence, rather than transient activation of circulating $CD8^+$ T cells in the placenta, we isolated maternal intervillous blood (IVB) for flow analysis (Figure 4.3C). IVB $CD8^+$ T cell frequency and phenotype mirrored that of maternal circulation, indicating a non-circulating T_{RM} population. Indeed, we found $CD8^+$ T_{RM} to be associated with the decidua basalis, a thin layer of remodeled endometrial tissue that remains adhered to the placenta due to interdigitation with invading placental cytotrophoblasts (Figure 4.3D).

The decidua basalis is the site at which maternal immunity is most exposed to the fetal allograft. Having found $CD8^+$ T_{RM} here, we asked if these cells have additional modifications in comparison to memory T cells (T_{mem}) that circulate here (i.e., $CD69^-$ $CD103^-$ cells). We chose to omit naïve (i.e., $CCR7^+$ $CD45RA^+$) $CD8^+$ T cells from this comparison (Figure 4.1E) since 1) naïve T cells do not form tissue residence (217, 218) and 2) are unable to respond to the same breadth of stimuli as T_{mem} (be it resident or circulating) (156). In comparison to their circulating counterparts, $CD8^+$ T_{RM} were more frequently of an activated phenotype, expressing higher percentages of HLA-DR and CD38 or PD-1 (Figure 4.1F). Surprisingly, mPLAC $CD8^+$ T_{RM} expressed high levels of PD-1 (Figure 4.1G), which is often only seen after TCR-mediated activation or dysfunction (133, 219). We therefore sought to determine whether PD-1 expression levels in mPLAC $CD8^+$ T_{RM} correlated with other phenotypes reflecting TCR stimulation, including ICOS (220), 4-1BB (98), TIM-3 (221, 222), and CD39 (41, 78-80). Much to our surprise, a considerable fraction of PD-1^{hi} $CD8^+$ T_{RM} co-expressed these proteins (Figure 4.1G, Figure 4.2D). Further, we found altered levels of transcription factors TCF-1 and TOX (Figure 4.1G), paralleling patterns found in T cells rendered dysfunctional by chronic TCR stimulation (130, 136, 137, 140, 152). Given these profiles, we asked whether we could determine the TCR specificity of these cells.

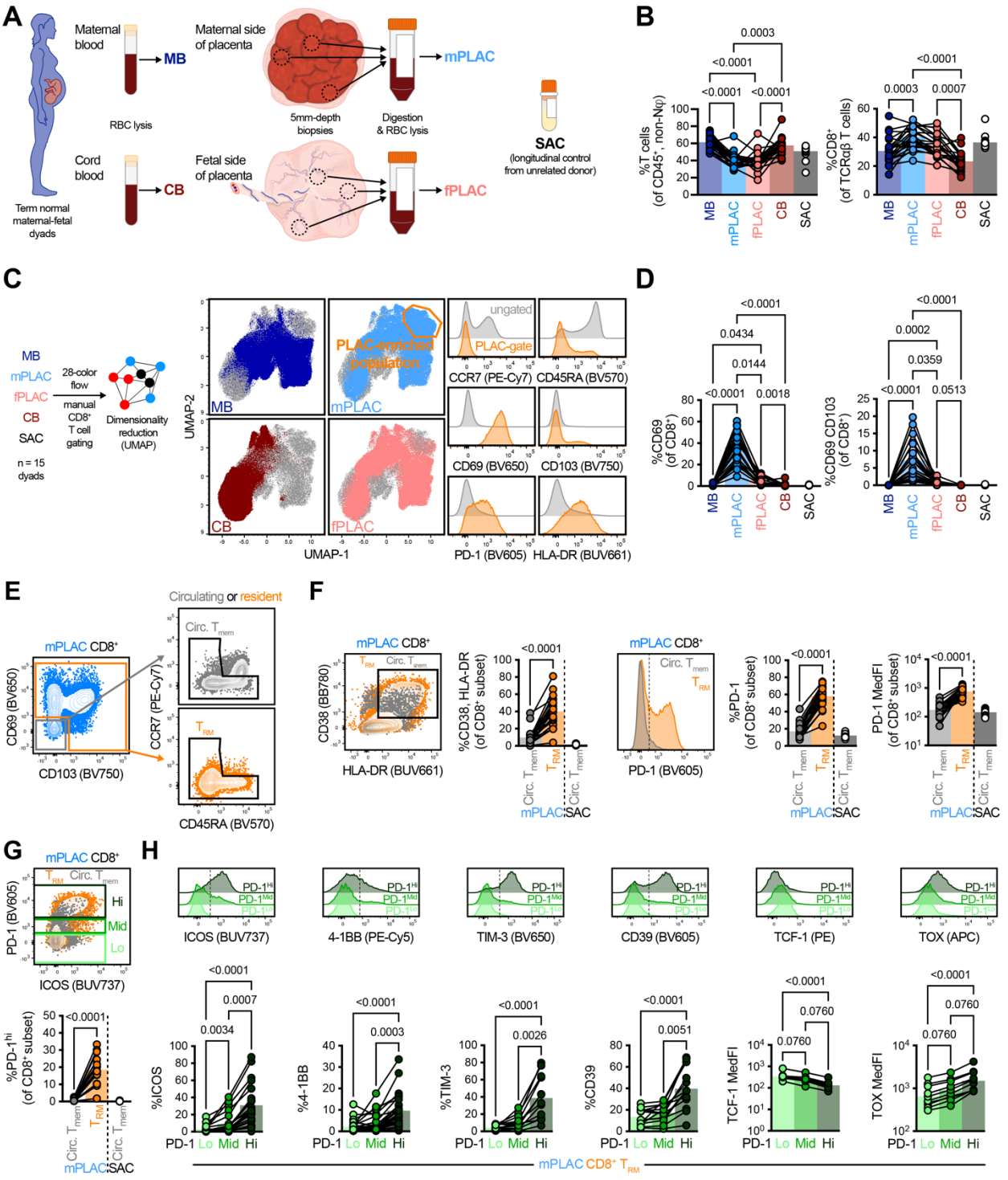

Figure 4.1 A T_{RM} population with an activated phenotype is asymmetrically distributed at the human MFI

A Overview of tissue sampling for cytometric analyses of leukocytes in maternal blood (MB), cord blood (CB), the maternal or fetal sides of the MFI (mPLAC and fPLAC, respectively), and a longitudinal PBMC donor from the Seattle Area Cohort (SAC). **B** Frequencies of bulk and $CD8^+$ T

cells across tissues. **C** 28-color T cell phenotyping flow data for $CD8^+$ T cells from 15 dyads visualized by UMAP and subsequent identification of a PLAC-enriched subpopulation. **D** Frequency of T_{RM}-phenotype (i.e. $CD69^+$ and $CD69^+CD103^+$) $CD8^+$ T cells across tissues. **E** Representative gating of $CD8^+$ T_{RM} and circulating T_{mem} from mPLAC samples. **F** Comparisons of activation markers in $CD8^+$ T_{RM} and circulating T_{mem}. **G** Frequency of PD-1^{hi} events within $CD8^+$ subsets and representative gating. **H** Activation phenotypes across mPLAC $CD8^+$ T_{RM} stratified by PD-1 intensity. **B** depicts 22-25 dyads, C depicts 10,000 $CD8^+$ T cells per tissue, per dyad from 15 dyads. **D** depicts 20-21 donors. **G** depicts 21 donors. **H** depicts 10–25 donors. All symbols represent a unique population which are connected across donor identity with bars depicting mean. All statistical significances where $p < 0.1$ are indicated as calculated by **B**, **D**, **H** Friedman tests and Dunn's multiple comparison tests or **F**, **G** Wilcoxon tests.

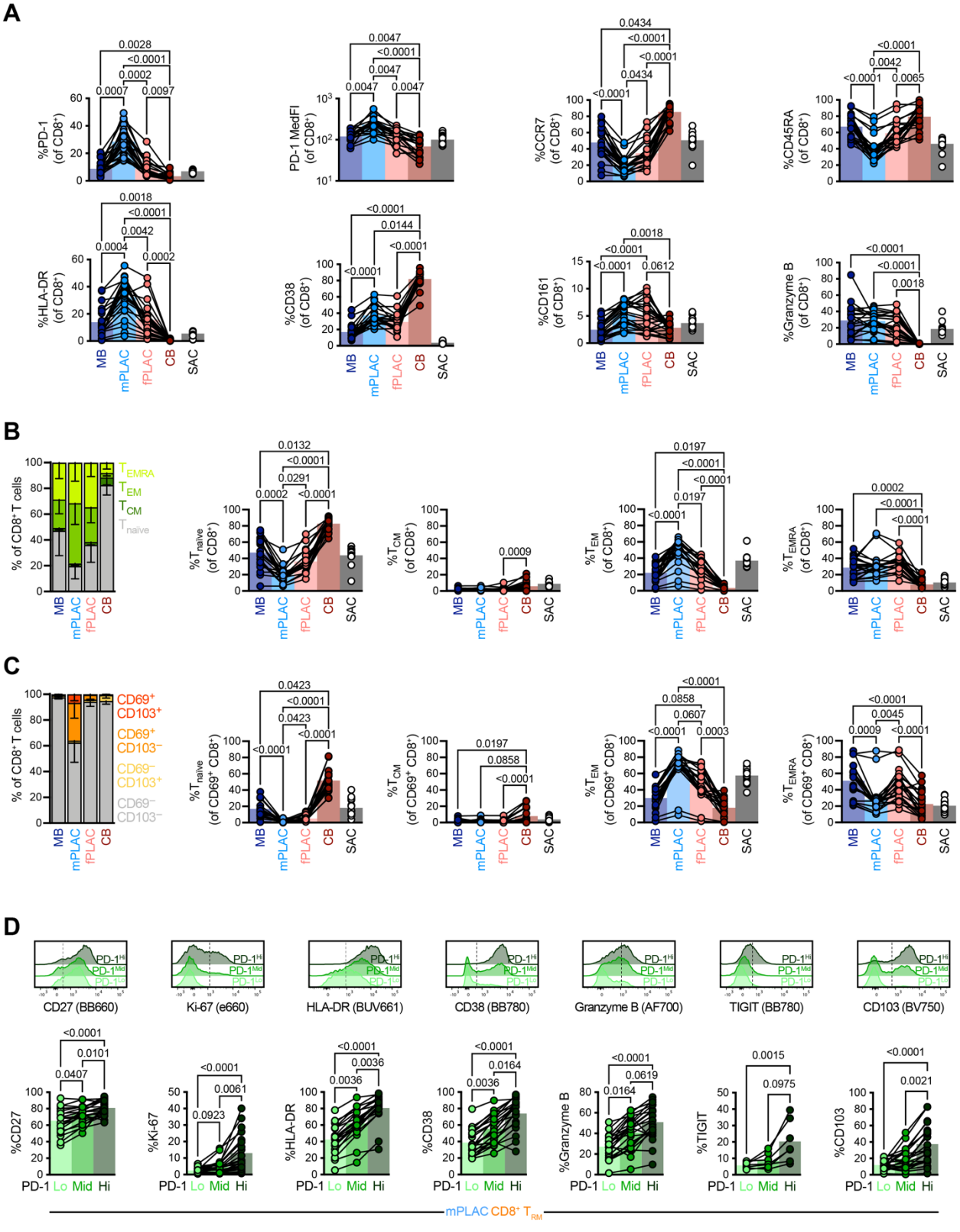

Figure 4.2 CD8$^+$ T_{RM} from the maternal side of the MFI are phenotypically distinct

A Phenotypes of bulk $CD8^+$ T cells across tissue compartments. **B** Memory subset distributions of $CD8^+$ T cells within tissue compartments. **C** Memory subset distributions of $CD69^+$ $CD8^+$ T cell events across tissues. **D** Phenotypic differences across PD-1^{Hi}, PD-1^{Mid}, and PD-1^{Lo} $CD8^+$ T_{RM} from mPLAC. **A** depicts 13-22 dyads. **B** and **C** depict 20 dyads. **D** depicts 7–21 donors. All points represent a unique population that are connected by donor identity, with bars signifying mean. In bar charts in **B** and **C**, bars depict mean with SD. All statistical significances where $p < 0.1$ are shown as calculated by Friedman tests with Dunn's multiple comparison test.

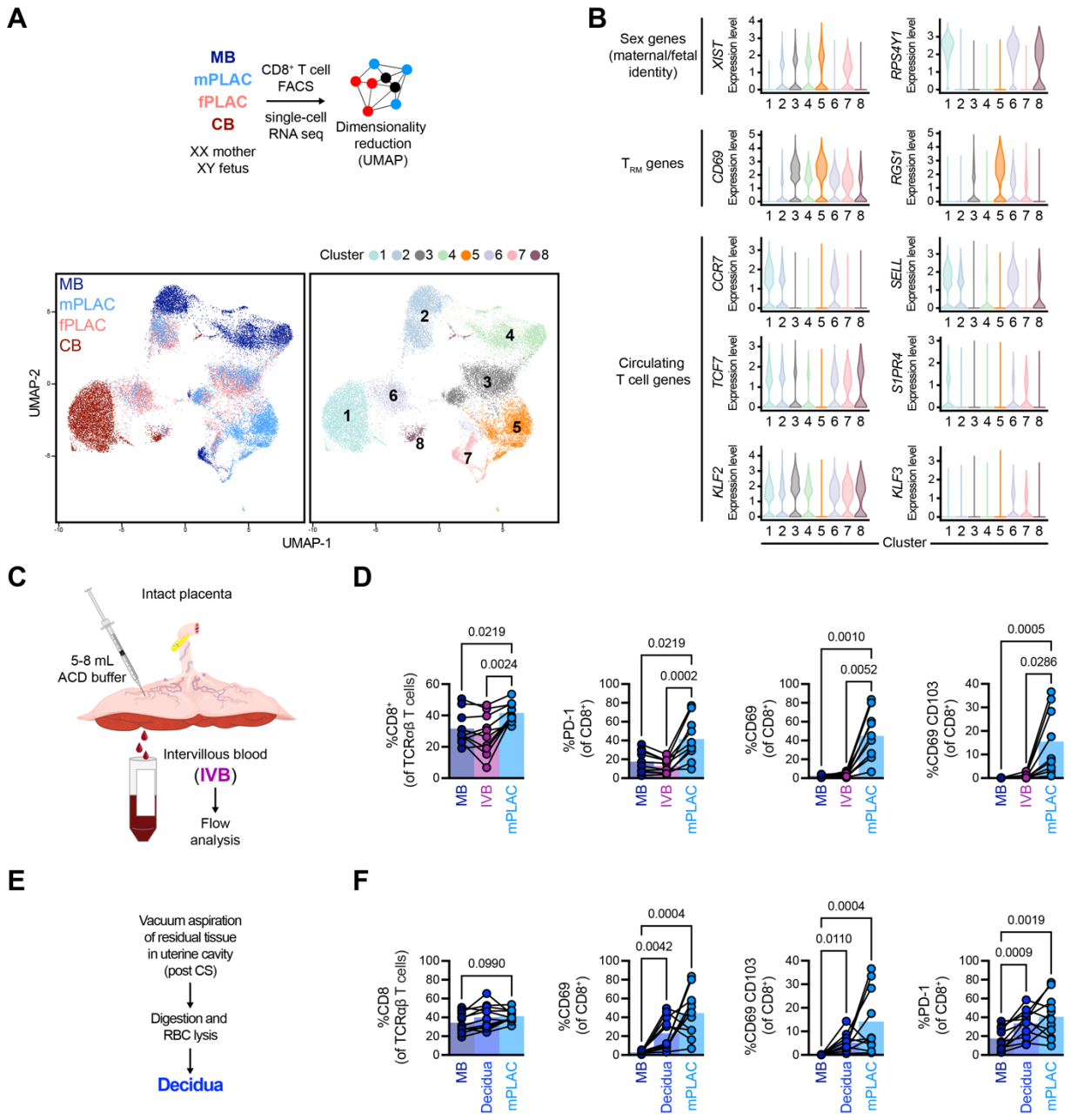

Figure 4.3 **CD8⁺ T_{RM} are maternally derived and absent from circulatory elements of the MFI**

A Overview of single-cell RNAseq approach, in which CD8⁺ T cells were isolated from tissues using FACS, and resulting data visualized by UMAP colored by tissue source (left) and graph-based clustering (right). **B** Violin plots of log-transformed normalized transcript counts across clusters for genes indicative of sex (*XIST*, female; *RPS4Y1*, male), tissue residence (*CD69*, *RGS1*), and capacity to circulate (*CCR7*, *SELL*, *TCF7*, *S1PR4*, *KLF2*, *KLF3*). **C** Overview of intervillous blood (IVB) isolation. **D** Frequency of CD8⁺ T cells and T_{RM}-associated proteins within CD8⁺ T cell events from MB, IVB, and mPLAC. **E** Overview of decidua collection and processing. **F** Frequency of CD8⁺ T cells and T_{RM}-associated proteins within CD8⁺ T cell events from MB,

decidua, and mPLAC. **A** and **B** depicts 1 dyad with an XY fetus. **D** depicts 9–10 donors. **F** depicts 10–11 donors. All points in **D** and **F** depict a unique population with points connected by donor identity, with bars indicating mean. Statistical significances by Friedman tests with Dunn's multiple comparison tests where $p < 0.1$ are indicated.

4.2.3 Virus-specific bystander T_{RM} at the MFI are found at frequencies reflecting those in circulation

Since we observed a subset of maternal-derived $CD8^+$ T_{RM} expressing markers indicative of TCR-mediated activation and/or exhaustion, we sought to test their TCR specificities. We identified four mothers for whom we had cryopreserved samples (paired MB and mPLAC) for combinatorial tetramer screening using cytometry by time of flight (CyTOF) (223) (Figure 4.4A). These donors specifically encoded HLA alleles compatible for screens via qPCR (HLA-A*01, -A*02, -A*03, -A*011, and/or B*07); our tetramers included Y-associated (199, 224), tumor-associated (41), and viral antigens (Ag) (Table 4.11, Table 4.12). We specifically gated resident ($CD69^+$ and/or $CD103^+$) and circulating ($CD69^-$ $CD103^-$) $CD8^+$ T cells with a memory phenotype (i.e., not $CCR7^+$ $CD45RA^+$) (162) for our analysis (Figure 4.4B). Although we failed to identify $CD8^+$ T cells with specificities for published Y or tumor Ags, we found $CD8^+$ T cells specific for both chronic (Epstein-Barr virus, EBV; cytomegalovirus, CMV; herpes simplex virus, HSV) and acute viruses (influenza A virus, IAV; adenovirus, AdV) (Figure 4.4C). Surprisingly, we observed the frequency of $CD8^+$ T_{RM} with defined TCR specificities was proportional to their abundance in the circulating memory pool (in both peripheral or placental blood) (Figure 4.4C). This notably contrasts with previous studies demonstrating elevated frequencies of virus-specific $CD8^+$ T cells at the MFI (225), which was likely inflated compared to blood due to the inclusion of naïve $CD8^+$ T cells in blood sample analyses, despite their inability to seed tissues.

Given the presence of virus-specific "bystander" $CD8^+$ T_{RM} at the MFI, we asked if they fail to upregulate markers of TCR engagement due to their lack of Ag specificity. We chose to interrogate CD39, a biomarker recently found to be elevated on cells receiving in situ TCR stimulation (41, 78-80). Surprisingly, virus-specific (i.e., tetramer-positive) $CD8^+$ T_{RM} expressed similar levels of CD39 to their bulk counterparts that we could not characterize by tetramer stains (Figure 4.4D). Though we cannot formally exclude alloreactivity of mPLAC $CD8^+$ T_{RM} (226), we believe this to be unlikely since TCR specificities in this population are not dramatically enriched over their frequency in circulating $CD8^+$ T_{mem}, as one may expect following TCR-mediated

expansion. Therefore, we hypothesized that generalized signals may influence T_{RM} fate and phenotypes at the MFI.

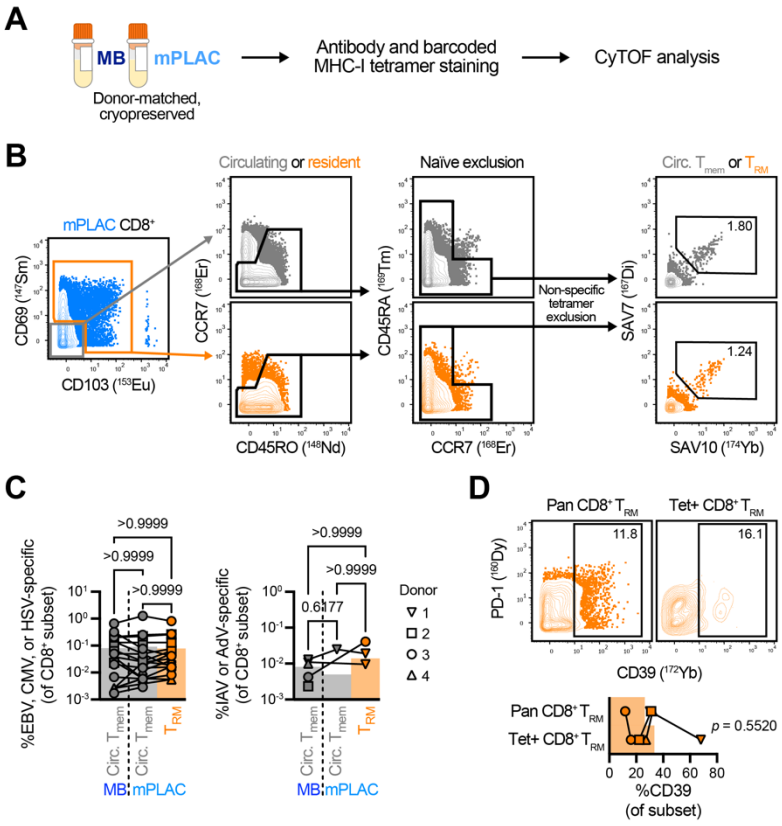

Figure 4.4 Ag-nonspecific CD8$^+$ T_{RM} frequencies at MFI mirror those of circulating CD8$^+$ T_{mem}

A Overview of barcoded tetramer screening of cryopreserved, donor-matched MB and mPLAC samples. **B** Representative gating of CD8$^+$ T_{RM} and circulating T_{mem} populations and downstream tetramer gating. **C** Frequency of CD8$^+$ T cells (circulating T_{mem} from MB, circulating T_{mem} and T_{RM} from mPLAC) that are specific for chronic/latent viral infections (left; EBV, CMV, VZV, HSV) or acute viral infections (right; IAV, AdV). **D** Frequency of CD39 expression within bulk, polyclonal (pan) and virus specific (tetramer+) CD8$^+$ T_{RM}. **C** depicts 7, 4, 7, and 3 T cell populations specific for EBV, CMV, or HSV Ag and 1, 1, 1, and 2 T cell populations specific for IAV and AdV Ag from n = 4 donors. **D** depicts n = 4 donors. Symbols are connected by (**C**) tetramer specificity and donor identity or (**D**) donor identity. Indicated statistical significances were calculated by **C** Friedman tests with Dunn's multiple comparisons or **D** paired t test.

4.2.4 Signaling networks at the placenta predispose for T cell recruitment and retention

We first analyzed untargeted scRNAseq data from donor-matched FACS-enriched CD8$^+$ T cells and non-B cell HLA-DR$^+$ Ag-presenting cells (APCs) with the NicheNet package (227). We

specifically used NicheNet to identify ligand-receptor interactions that were intact at the transcriptomic level between APC and $CD8^+$ T cells, querying for interactions that were elevated in mPLAC versus MB populations, as well as those elevated in mPLAC $CD8^+$ T_{RM} versus mPLAC circulating $CD8^+$ T_{mem} (Figure 4.5A, Figure 4.6A). We delineated mPLAC $CD8^+$ T_{RM} from mPLAC circulating $CD8^+$ T_{mem} as events with a T_{EM} phenotype and high *RGS1* levels. We found that chemokine and cytokine interactions were predicted to be elevated at the mPLAC versus MB (Figure 4.6A); but that this was not due to anatomic location alone, for these same signaling pathways were predicted to be elevated in mPLAC $CD8^+$ T_{RM} versus mPLAC circulating $CD8^+$ T_{mem} interacting with the same APCs (Figure 4.5B).

Since cytokine signaling is in line with our hypothesis of generalized signaling pathways, we next tested if these molecules are indeed expressed at the MFI. We interrogated cytokine and chemokines in MB, CB, and IVB plasma as well as mPLAC and fPLAC tissue lysate supernatants using multiplexed cytokine analysis. Much to our surprise, we found the chemokine, CXCL10, which can recruit Ag-specific and -nonspecific $CD8^+$ T_{mem} through CXCR3 (6, 110), was elevated in both IVB plasma and tissue lysates (Figure 4.5C, Figure 4.6B). This contrasts with mouse models demonstrating chemokine gene expression is silenced at the decidua as a means to restrict maternal T cell entry and ensure tolerance towards the fetal graft (189). Although TNF signaling was intact at the transcriptional level, we were unable to find it elevated at the MFI (Figure 4.5C), illustrating limitations of transcriptional analysis alone (228, 229). Despite this, NicheNet accurately predicted intact IL-15 signaling networks, which like CXCL10, were elevated in IVB plasma and mPLAC lysates (Figure 4.5C, Figure 4.6B). IL-15, amongst other cytokines (IL-2, IL-4, IL-7, IL-9, and IL-21) signal through receptor complexes involving the common γ chain (γ_c), leading to downstream STAT5 signaling (230). Though a previous study described an immunologic STAT5 signature of pregnancy, hypothesized to result from IL-2 signaling (200), we were unable to find elevated levels of other γ_c cytokines in IVB plasma or placental tissue lysates (Figure 4.6C–D). While NicheNet assisted in identifying CXCL10 and IL-15, we also found increased concentrations of IL-6 and IL-18 at the MFI that NicheNet had failed to predict (Figure 4.5C, Figure 4.6B). This could result from these signals originating from a different cell type (i.e., non APCs) at the MFI or to limitations in sensitivity with smaller, non-targeted scRNAseq datasets (228, 229, 231-233). Using flow cytometry, we found that $CD8^+$ T cells express factors underlying recruitment and cytokine mediated activation (Figure 4.5D) indicating these signaling pathways can indeed influence $CD8^+$ T_{mem} at the MFI.

We next sought to determine how pro-inflammatory cytokines at the MFI could augment T cells in vitro. We specifically cultured T cells with IL-6, IL-15, and IL-18 for up to 48h (Figure 4.5E) and then assessed cell phenotype. We specifically enriched T cells from cryopreserved PBMCs with negative selection magnet-activated cell sorting (MACS) to mitigate indirect activation that could arise from contaminating APCs (151). While pro-inflammatory cytokines sufficiently activated $CD8^+$ T_{mem} (vis-à-vis CD69 upregulation), we also saw induction of proteins observed in $CD8^+$ T_{RM} from mPLAC biopsies, including PD-1, ICOS, 4-1BB, TIM-3, CD39, and TOX (Figure 4.5E). Therefore, it is quite possible that pro-inflammatory networks at the MFI recruit and activate $CD8^+$ T_{mem} even in the absence of cognate Ag. But what is the consequence of this activation? Given the role of 4-1BB–4-1BBL signaling in the retention of T_{RM} (92, 234), we hypothesized that inflammation-induced 4-1BB expression could be a path to the residence of bystander $CD8^+$ T_{mem} at the MFI.

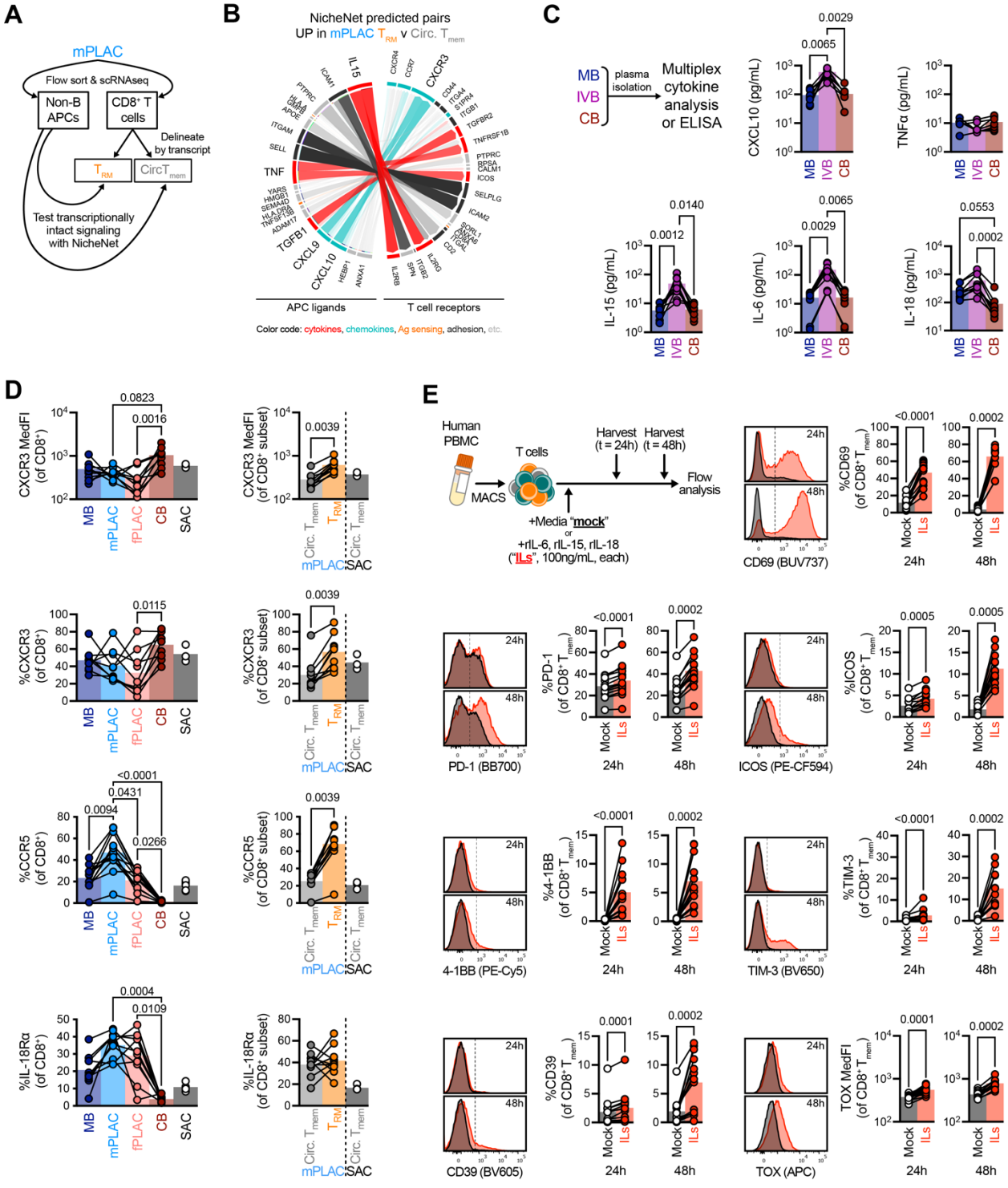

Figure 4.5 Intact signaling networks at the MFI induce T_{RM}-like phenotypes in vitro

A Experimental approach to identify cellular interactions in mPLAC. Specifically, we FACS-sorted APCs and CD8$^+$ T cells from mPLAC, conducted single-cell RNAseq, and tested potential ligand-receptor interactions using NicheNet. Non-B cell, HLA-DR$^+$ cells were used as the "sender" population and circulating memory and tissue resident CD8$^+$ T cell subsets were delineated by

transcript and used as the “receiver populations.” **B** Circos plot identifying potential ligand-receptor pairs up in mPLAC $CD8^+$ T_{RM} versus circulating $CD8^+$ T_{mem}. Interactions implicating cytokines, chemokines, Ag presentation/sensing, and adhesion molecules are respectively colored red, teal, orange, and dark grey. **C** Chemokine and cytokine concentrations determined by multiplex analysis of plasma from MB, IVB, and CB. **D** Expression on chemokine and cytokine receptors in $CD8^+$ T cells across tissues (left) and within circulating $CD8^+$ T_{mem} and T_{RM} subsets from mPLAC samples (right). **E** Induction of activation markers with cytokines. Specifically, we MACS-isolated T cells from PBMC samples and stimulated cells with media alone (“mock”) or IL-6, IL-15, and IL-18 in combination (“ILs, ”100ng/mL, each) and measured changes in $CD8^+$ T_{mem} phenotypes using flow. **B** depicts scRNAseq data from n = 1 dyad with an XY fetus. **C** depicts n = 7–9 dyads. **D** depicts n = 10–13 dyads. **E** depicts n = 12-15 donors across 6 technical replicates. Indicated are statistical significance where $p < 0.1$ by **C**, **D** Friedman tests with Dunn’s multiple comparisons and **C**, **D** Wilcoxon tests.

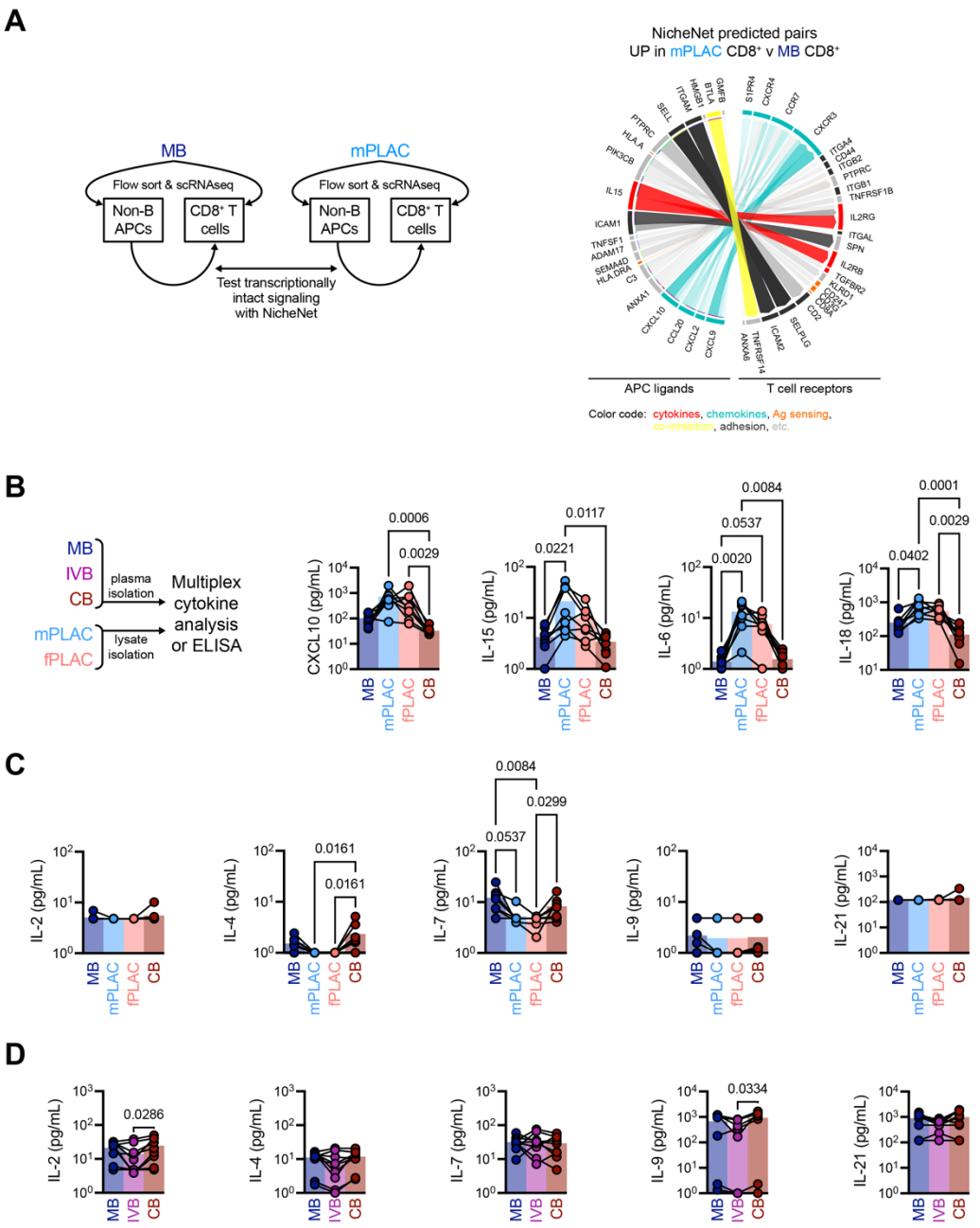

Figure 4.6 Other γ_c cytokines are not elevated at the MFI

A NicheNet analysis of potential ligand-receptor interactions that are enriched in mPLAC APCs and CD8$^+$ T cells versus MB APCs and CD8$^+$ T cells. CIRCOS plot interactions are colored to highlight cytokine (red), chemokine (teal), Ag presentation/sensing (orange), co-inhibitory (yellow), and adhesion (dark grey) interactions enriched in mPLAC APCs and CD8$^+$ T cells over blood. **B** Multiplex analysis of paired MB and CB plasmas, as well as lysates from mPLAC and fPLAC tissues. **C** and **D** Multiplex analysis for γ_c cytokines (IL-2, IL-4, IL-7, IL-9, and IL-21) in (**B**) MB and CB plasmas and mPLAC and fPLAC lysates or (**C**) MB, IVB, and CB plasmas. **A** depicts scRNAseq data from *n* = 1 dyad with an XY fetus. **B** and **C** depict *n* = 8 dyads. **D** depicts *n* = 7–9

dyads. Indicated are statistical significances where $p < 0.1$ by Friedman tests with Dunn's multiple comparison tests. Symbols in **B**–**D** are connected by donor identity.

4.2.5 Decidual macrophages express cognate ligands for inflammation-induced receptors and physically engage CD8$^+$ T cells in situ

We tested which APC subset was most likely influencing NicheNet predictions and found that CD14$^+$ macrophages/monocytes were the sole APC subset overrepresented within mPLAC versus MB (Figure 4.7A, Figure 4.8A). Given the increased frequency of CD14$^+$ events at the MFI, we asked if these cells express ligands for T cell co-receptors that we found on CD8$^+$ T_{RM} and cytokine-stimulated CD8$^+$ T_{mem}. We found that mPLAC CD14$^+$ macrophages/monocytes expressed cognate ligands for both 4-1BB (4-1BBL) and PD-1 (PD-L1) on CD8$^+$ T_{RM} (Figure 4.7B, C). Within mPLAC CD14$^+$ events, we observed a subpopulation which expresses high levels of CD206 (Figure 4.7D), phenotypically aligning with descriptions of maternal-derived decidual macrophages (235, 236). In agreement with this definition, CD206^{hi} CD14$^+$ cells were abundant in decidual aspirates but absent from IVB (Figure 4.8B); further, these CD206^{hi} cells phenocopied the low CD45, CD11b, and CD11c expression also reported in decidual macrophages (236-238) (Figure 4.7D, Figure 4.8C) and did not express fetal sex transcripts (data not shown). Of the CD14$^+$ subsets at the MFI, CD206^{hi} decidual macrophages were the primary producers of 4-1BBL and PD-L1 (Figure 4.7D). Given the high expression of 4-1BBL and PD-L1 on CD206^{hi} decidual macrophages, we asked if these macrophages could physically engage with CD8$^+$ T cells in situ, to provide 4-1BB co-stimulation for tissue residence. While we were unable to leverage CD206 staining in immunofluorescence assays, we used CD163 as a surrogate marker, owing to its high expression on CD206^{hi} decidual macrophages (Figure 4.7D). Unexpectedly, we found CD45$^+$ leukocytes in distinct aggregates in the decidua. Within these aggregates, we observed CD163$^+$ CD45^{lo} decidual macrophages forming contacts with CD8$^+$ and non CD8$^+$ infiltrates, indicating that 4-1BB–4-1BBL interactions can indeed occur at the MFI as a T_{RM} retention signal (Figure 4.7E).

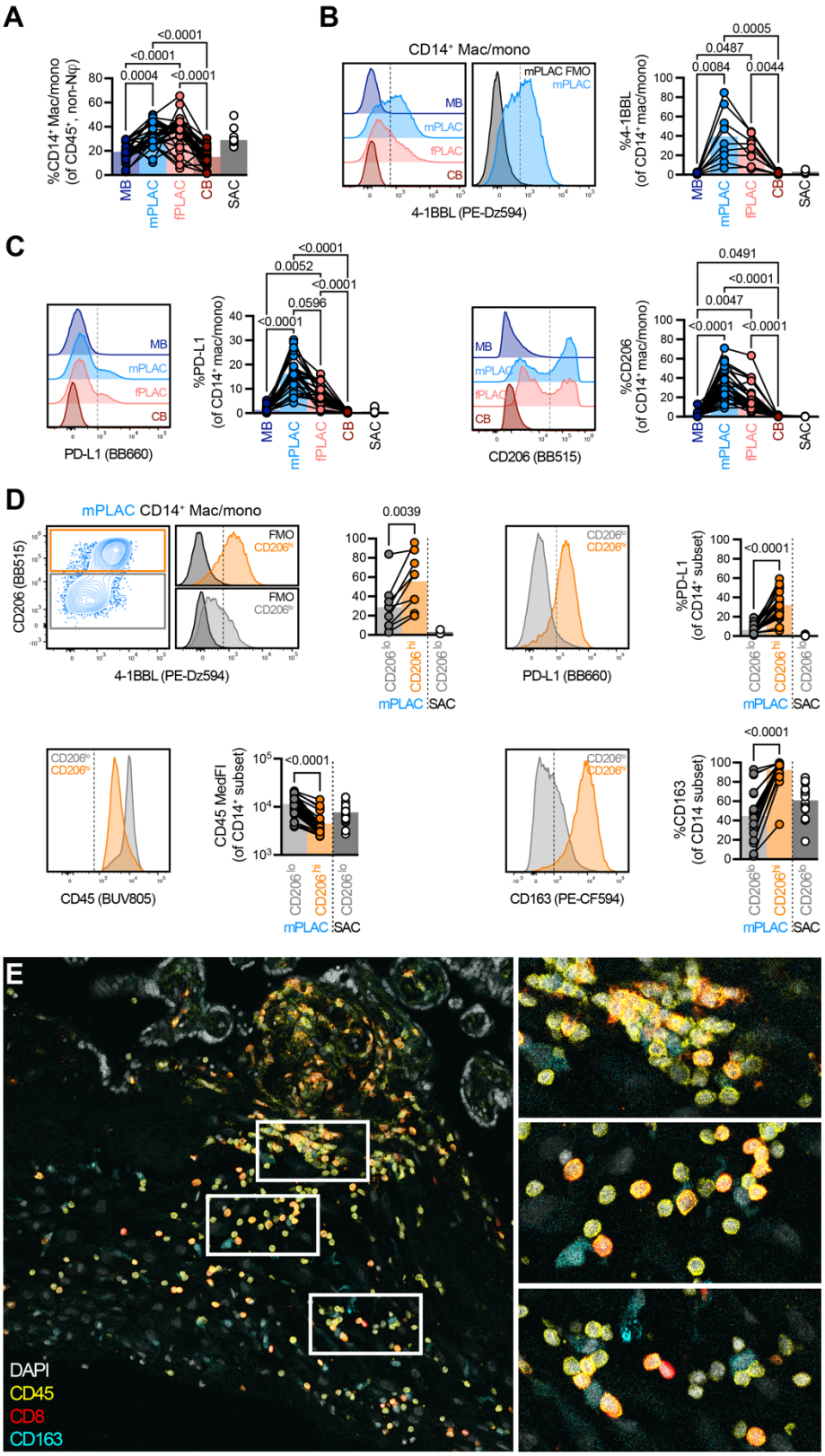

Figure 4.7 **Macrophages at the MFI can engage inflammation-induced receptors on tissue-infiltrating T cells.**

A Frequency of CD14^{+} macrophages and monocytes across tissues. **B** 4-1BBL expression within CD14^{+} events across tissues. **C** Expression of PD-L1 and CD206 in CD14^{+} events across tissues. **D** Phenotypic differences of CD206^{hi} and CD206^{lo} CD14^{+} macrophages and monocytes from mPLAC. **E** Immunofluorescence microscopy of CD8^{+} T cells and CD163^{+} cells at the maternal side of the MFI (decidua basalis). **A** depicts *n* = 29 dyads. **B** depicts *n* = 9 dyads. **C** depicts *n* = 26–33 dyads. **D** depicts *n* = 9–31 dyads. Indicated are statistical significances where $p < 0.1$ by **A**–**C** Friedman tests with Dunn's multiple comparisons tests or **D** Wilcoxon tests. Symbols in **A**–**D** are connected by donor identity.

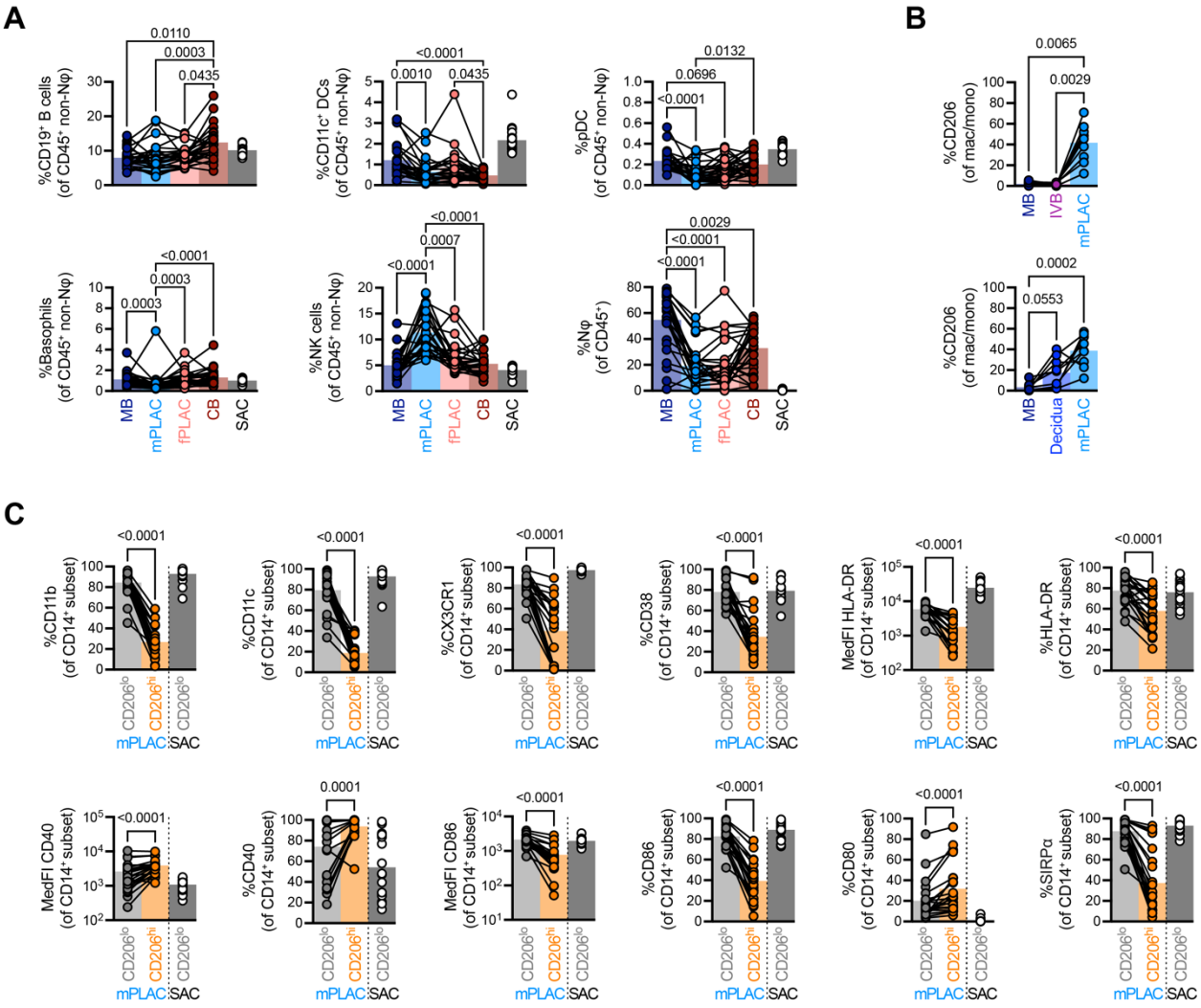

Figure 4.8 Phenotypically distinct macrophages occupy the stroma of the MFI

A Frequencies of major leukocyte subsets across MB, mPLAC, fPLAC, and CB. **B** CD206^{hi} CD14^{+} monocyte/macrophage frequencies across MB, IVB, mPLAC or MB, decidua, and mPLAC. **C** Phenotypic differences between CD206^{lo} and CD206^{hi} CD14^{+} macrophages/monocytes from mPLAC tissues. **A** depicts *n* = 26 dyads. **B** depicts *n* = 9 dyads. **C** depicts *n* = 22 dyads. Indicated are statistical significances where $p < 0.1$ by **A**, **B** Friedman tests with Dunn's multiple comparisons tests and **C** Wilcoxon tests. Symbols in **A**–**C** are connected by donor identity.

4.2.6 Cytokine and metabolite networks mitigate inflammation-mediated effector programs without compromising cellular activation

Although inflammation can potently upregulate $CD8^+$ T_{mem} expression co-receptors involved in tissue residence, it also elicits a cytotoxic effector program, termed bystander activation (25, 156). Indeed, our in vitro stimulations with IL-6, IL-15, and IL-18 in combination were able to elicit IFNγ and GzmB upregulation (Figure 4.10A); yet IFNγ levels at the MFI in plasma or tissue lysates remained undetectable (Figure 4.9A, Figure 4.10B). We therefore hypothesized that regulatory mechanisms may be present at the MFI to restrain cytotoxicity elicited by pro-inflammatory signals. We chose to test IL-10, given its role in T_{reg}-mediated control of T cell functions (239), and found limited levels across all plasma and tissue samples (Figure 4.9A, Figure 4.10B). We also surveyed TGF-β1 levels using ELISA, given its presence in NicheNet analysis (Figure 4.5), and found significantly higher levels in IVB plasma (Figure 4.9A). Although TGF-β1 levels were highest in IVB plasma (Figure 4.9A), detection was impaired in tissue lysate supernatants potentially reflecting limitations in directly comparing tissues and plasmas (Figure 4.10B). Given the role of L-tryptophan (Trp) metabolism in pregnancy (240) and immune cell fate (241-243), we screened its presence across the depth of the MFI using LC-MS. Complementing the bias of immunoregulatory cytokines, we found elevated levels of the Trp metabolite, L-kynurenine (KYN), at the maternal versus the fetal side of the MFI (Figure 4.9B). We excluded that MB perfusing the placenta drove this bias, as MB demonstrated significantly lower KYN levels in comparison to CB (Figure 4.10C). Since KYN must bind to cytosolic aryl hydrocarbon receptor (AhR) to induce AhR nuclear translocation and gene expression (244, 245), we asked if mPLAC $CD8^+$ T_{RM} could take up KYN. We stained for the large neutral amino acid transporter molecule, CD98, responsible for tryptophan and tryptophan metabolite uptake (246). We found mPLAC $CD8^+$ T_{RM} expressed higher amounts of CD98 than their circulating counterparts (Figure 4.9C). Since PD-1 intensity in $CD8^+$ T_{RM} correlated with higher CD98 staining (Figure 4.9C), we asked if cytokine-mediated activation could underlie this expression pattern. Using in vitro T cell stimulations, we found that durable exposure to IL-6, IL-15, and IL-18 could substantially raise CD98 expression (Figure 4.9D). Together, these data suggest TGF-β1 and KYN networks can be sensed by $CD8^+$ T_{RM} at the maternal side of the MFI.

We next tested whether TGF-β1 and KYN could augment $CD8^+$ T_{mem} effector functions caused by inflammation. We isolated T cells from PBMC with MACS and stimulated them with IL-6, IL-15, and IL-18 in combination (each at 100ng/mL) in the presence of TGF-β1 (at 0.2ng/mL) and/or

KYN (at 100μM). In order to interrogate cytokine expression on a per-cell basis, we added Golgi inhibitors 6 hours prior to harvesting cells and conducting stains for surface expression of activation markers and intracellular cytokine accumulation (Figure 4.9E). Though TGF-β1 or KYN alone could limit inflammation-mediated IFNγ expression in $CD8^+$ T_{mem}, combinations of both demonstrated cooperativity in attenuating this specific effector function (Figure 4.9F, G). We observed similar cooperativity between TGF-β1 and KYN in T cell culture supernatants in limiting the overall concentrations of IFNγ (Figure 4.9G). While TGF-β1 and KYN profoundly reduced IFNγ expression caused by pro-inflammatory signals, its effects were less pronounced on other effector molecules induced by inflammation, like GzmB (Figure 4.10D–E). Given the limited effects of TGF-β1 and KYN on the upregulation of GzmB, we hypothesized that TGF-β1 and KYN selectively limit IFNγ expression and secretion, rather than impair inflammation-mediated activation in its entirety. Therefore, we tested for markers of cellular activation, CD69 on $CD8^+$ T_{mem} (210) and soluble IL-2Rα (sIL-2Rα) in culture supernatants (247). While stimulation with IL-6, IL-15, and IL-18 was a potent inducer of CD69 and sIL-2Rα expression, TGF-β1 and/or KYN were unable to abrogate their expression (Figure 4.9G). Since TGF-β1 and/or KYN were unable to abrogate cytokine-mediated $CD8^+$ T_{mem} activation, we tested whether these cells also maintained expression of receptors associated with tissue residence. Though TGF-β1 and KYN were able to impair the overall expression of 4-1BB, ICOS, or TIM-3 caused by IL-6, IL-15, and IL-18 stimulation, $CD8^+$ T_{mem} still expressed these receptors at levels higher than baseline. Therefore, cellular activation that could beget tissue residence is not entirely forfeited by TGF-β1 and KYN networks.

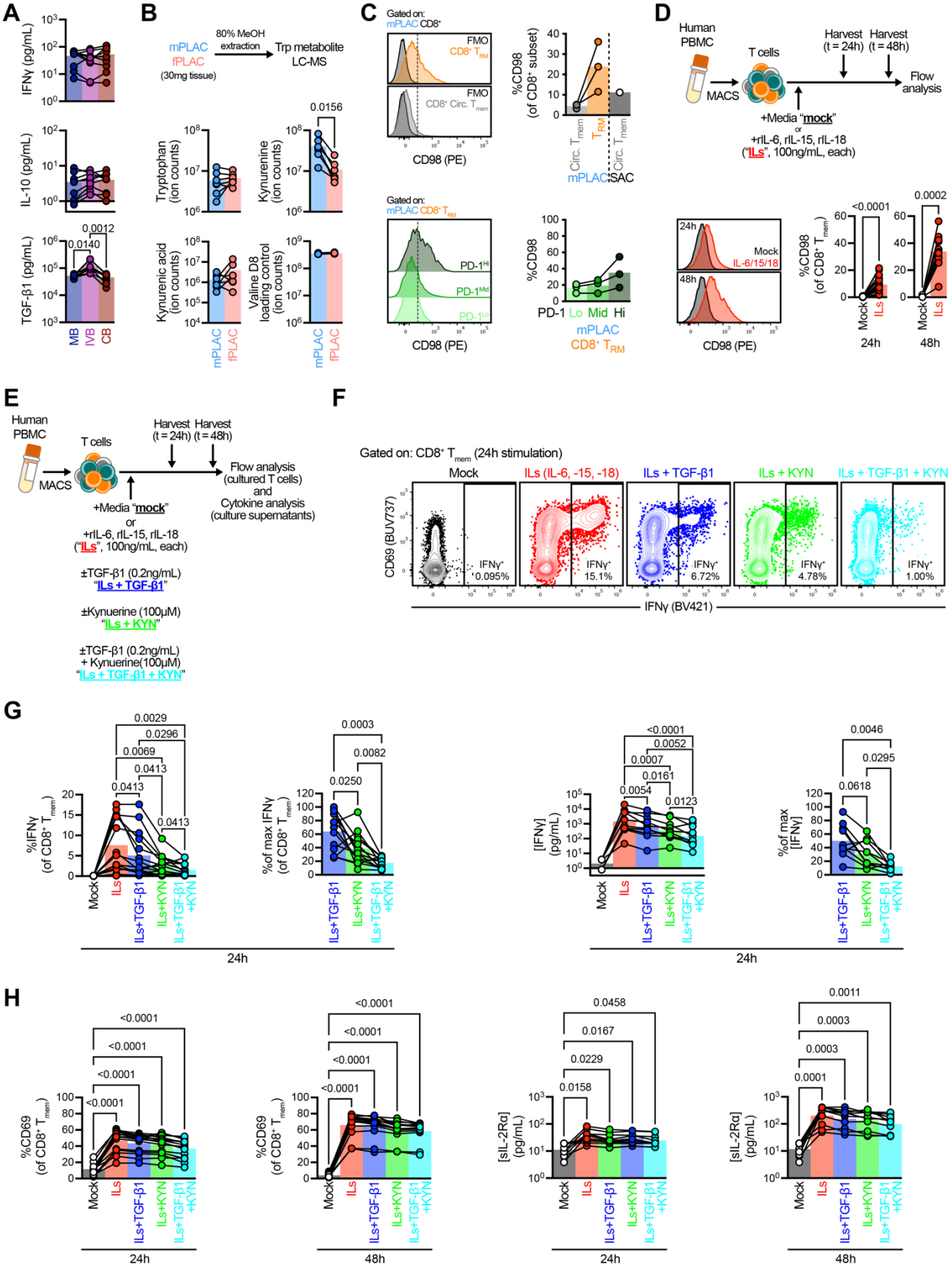
A
IFNγ (pg/mL)
IL-10 (pg/mL)
TGF-β1 (pg/mL)
0.0012
0.0140
MB
IVB
CB
B
mPLAC
fPLAC
(30mg tissue)
80% MeOH extraction
Trp metabolite LC-MS
Tryptophan (ion counts)
Kynurenine (ion counts)
0.0156
Kynurenic acid (ion counts)
Valine D8 loading control (ion counts)
C
Gated on: mPLAC CD8+
FMO CD8+ TRM
FMO CD8+ Circ. Tmem
CD98 (PE)
%CD98 (of CD8+ subset)
Circ. Tmem
TRM
mPLAC SAC
Gated on: mPLAC CD8+ TRM
PD-1Hi
PD-1Mid
PD-1Lo
PD-1 Lo Mid Hi
mPLAC CD8+ TRM
D
Human PBMC
MACS
T cells
Harvest (t = 24h)
Harvest (t = 48h)
Flow analysis
+Media "mock"
or
+rIL-6, rIL-15, rIL-18
("ILs", 100ng/mL, each)
24h
48h
Mock
IL-6/15/18
CD98 (PE)
%CD98 (of CD8+ Tmem)
<0.0001
0.0002
Mock
ILs
24h
48h
E
Human PBMC
MACS
T cells
Harvest (t = 24h)
Harvest (t = 48h)
Flow analysis (cultured T cells) and Cytokine analysis (culture supernatants)
+Media "mock"
or
+rIL-6, rIL-15, rIL-18
("ILs", 100ng/mL, each)
±TGF-β1 (0.2ng/mL)
"ILs + TGF-β1"
±Kynuerine (100μM)
"ILs + KYN"
±TGF-β1 (0.2ng/mL)
+ Kynuerine(100μM)
"ILs + TGF-β1 + KYN"
F
Gated on: CD8+ Tmem (24h stimulation)
Mock
ILs (IL-6, -15, -18)
ILs + TGF-β1
ILs + KYN
ILs + TGF-β1 + KYN
CD69 (BUV737)
IFNγ+ 0.095%
IFNγ+ 15.1%
IFNγ+ 6.72%
IFNγ+ 4.78%
IFNγ+ 1.00%
IFNγ (BV421)
G
%IFNγ (of CD8+ Tmem)
0.0029
0.0296
0.0069
0.0413
0.0413
0.0413
%of max IFNγ (of CD8+ Tmem)
0.0003
0.0082
0.0250
[IFNγ] (pg/mL)
<0.0001
0.0052
0.0007
0.0161
0.0054
0.0123
%of max [IFNγ]
0.0046
0.0295
0.0618
Mock
ILs
ILs+TGF-β1
ILs+KYN
ILs+TGF-β1 +KYN
24h
H
%CD69 (of CD8+ Tmem)
<0.0001
24h
48h
[sIL-2Rα] (pg/mL)
0.0458
0.0167
0.0229
0.0158
0.0011
0.0003
0.0003
0.0001
Mock
ILs
ILs+TGF-β1
ILs+KYN
ILs+TGF-β1 +KYN

Figure 4.9 Inhibitory cytokine and metabolite networks at the MFI cooperatively limit inflammation-dependent effector function in $CD8^+$ T_{mem}

A IFNγ, IL-10, and TGF-β1 concentrations across MB, IVB, and CB plasma. **B** LC-MS analysis of tryptophan metabolites and loading controls in mPLAC and fPLAC lysates. **C** Expression of tryptophan/kynurenine transporter, CD98, in $CD8^+$ T_{RM} and circulating T_{mem} from mPLAC (top) and across PD-1 intensities in mPLAC $CD8^+$ T_{RM}. **D** CD98 expression in $CD8^+$ T_{mem} after in vitro stimulation with IL-6, IL-15, and IL-18 (100ng/mL, each). **E** Kynurenine and TGF-β1 stimulation assay overview, in which T cells were MACS-isolated from PBMC, cultured with IL-6, IL-15, and IL-18 (100ng/mL, each) in the presence or absence of TGF-β1 (0.2ng/mL) and/or kynurenine (KYN, 100μM), and subsequently analyzed using flow cytometry and multiplex analysis. **F** Representative flow plots of IFNγ expression in $CD8^+$ T_{mem} across stimulation conditions after 24h. **G** IFNγ expression in $CD8^+$ T_{mem} (left) and IFNγ concentration in culture supernatant (right) across stimulation conditions after 24h. **H** Activation status via CD69 expression in $CD8^+$ T_{mem} (left) and sIL-2Rα concentration in culture supernatant (right) across stimulation conditions after 24 and 48h. **A** depicts $n = 9$ dyads. **B** depict $n = 7$ placentas. **C** depicts $n = 3$ placentas. **D** depicts $n = 13–15$ PBMC donors. **G** and **H** depict $n = 13–15$ and $n = 10$ PBMC donors analyzed via flow and multiplex cytokine analysis, respectively. Symbols are connected by donor identity. Indicated are statistical significance where $p < 0.1$ by **A** Friedman tests with Dunn's multiple comparisons tests, **D** Wilcoxon tests, **G** and **H** RM one-way ANOVA with Geisser-Greenhouse correction and Holm-Šídák multiple comparisons tests against **G** all experimental columns or **H** mock-treated columns.

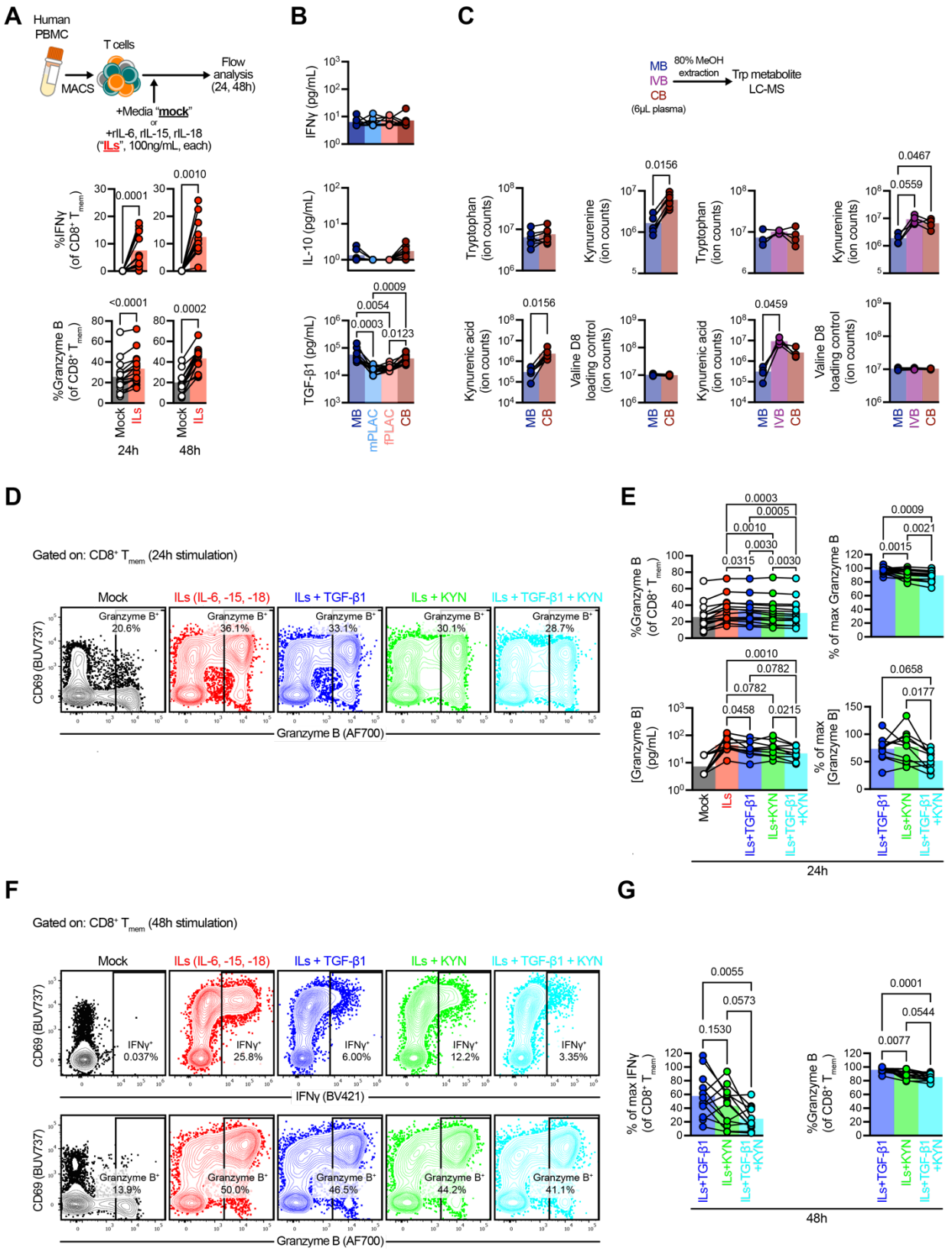

Figure 4.10 TGF-β1 and kynurenine impair inflammation-mediated IFNγ and GzmB upregulation.

A Expression of IFNγ and GzmB after in vitro cytokine stimulation with IL-6, IL-15, and IL-18 (100ng/mL, each). **B** Concentrations of IFNγ, IL-10, and TGF-β1 across MB and CB plasmas and mPLAC and fPLAC lysates. **C** LC-MS for tryptophan metabolites and loading control in MB, IVB, and CB plasma. **D** Representative flow plots of GzmB expression in $CD8^+$ T_{mem} across stimulation conditions after 24h. **E** Expression of GzmB in $CD8^+$ T_{mem} (top) and concentration of GzmB in culture supernatant (bottom) across stimulation conditions after 24h. **F** Representative flow plots of IFNγ and GzmB expression in $CD8^+$ T_{mem} across stimulation conditions after 48h. **G** Percent of maximal IFNγ (left) and GzmB (right) expression in $CD8^+$ T_{mem} after 48h. **A** depicts n = 15 PBMC donors. **B** Depicts n = 8–12 dyads. **C** depicts n = 4 dyads with IVB and n = 7 MB and CB dyads. **D** depicts n = 15 and n = 10 PBMC donors analyzed via flow and multiplex cytokine analysis, respectively. **G** depicts n = 12 PBMC donors. Symbols are connected by donor identity. Indicated are statistical significances where $p < 0.1$ by **A**–**C** Wilcoxon tests and Friedman tests with Dunn's multiple comparisons or **D**, **G** RM one-way ANOVA with Geisser-Greenhouse correction and Holm-Šídák multiple comparisons tests.

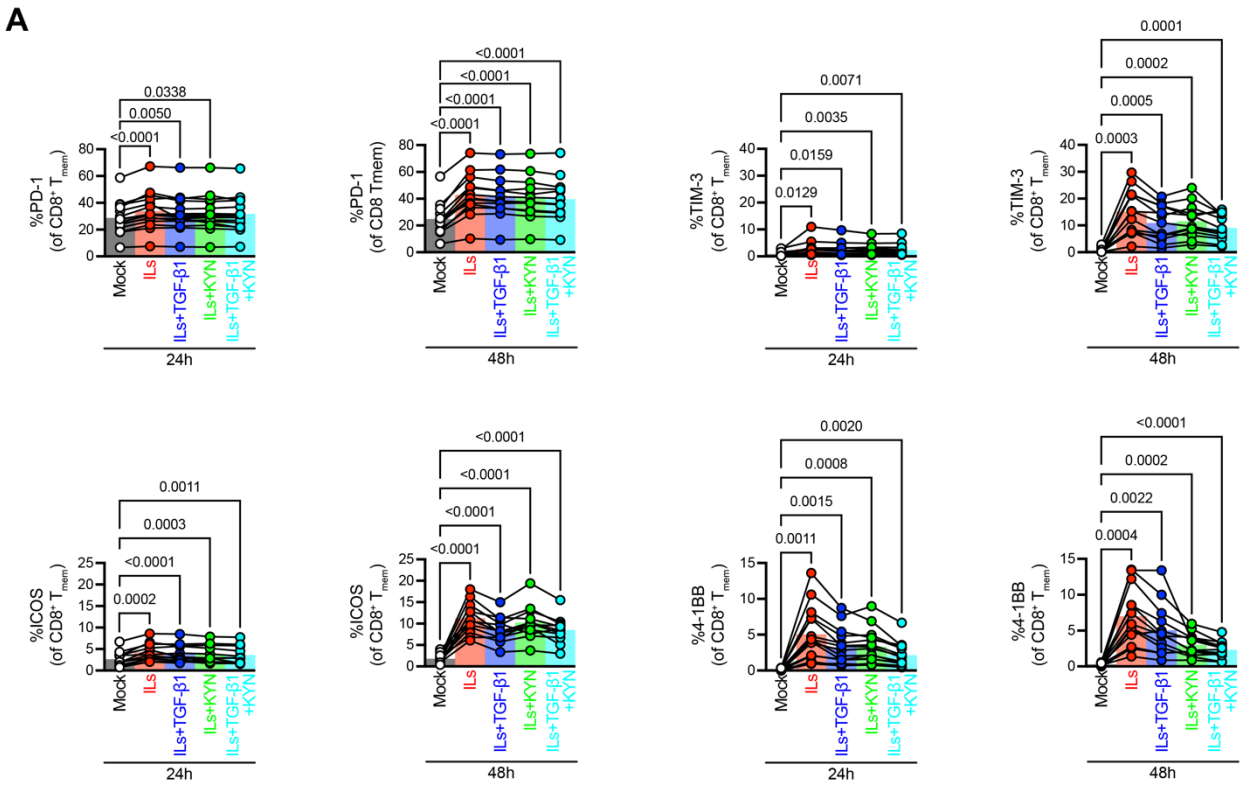

Figure 4.11 TGF-β1 and kynurenine do not abrogate inflammation-mediated receptor upregulation in $CD8^+$ T_{mem}

A PD-1, TIM-3, ICOS, and 4-1BB expression frequencies in $CD8^+$ T_{mem} across stimulation conditions at 24h and 48h timepoints. **A** depicts n = 12–15 PBMC donors with symbols connected by donor identity. Indicated are statistical significance where $p < 0.1$ by RM one-way ANOVA with Geisser-Greenhouse correction and Holm-Šídák multiple comparisons tests (all columns compared to mock).

4.2.7 Cytokine and metabolite networks selectively permit TCR-mediated effector functions

Since TGF-β1 and KYN inhibited IFNγ to a greater degree in unison, rather than alone, we sought mechanisms that could underlie this cooperativity. We previously found that IL-6, IL-15, and IL-18 could together induce the expression of the KYN transporter, CD98 (Figure 4.9D); however, it was unclear whether TGF-β1 could modify CD98 expression. Using in vitro stimulations of MACS-isolated T cells, we found that the addition of TGF-β1 (at 4ng/mL) to IL-6, IL-15, and IL-18 boosted CD98 expression in $CD8^+$ T_{mem} by both frequency and median fluorescence intensity (MedFI) (Figure 4.12). This phenomenon was most apparent at the 48h timepoint, suggesting that cells durably exposed to these signals (like those retained at the MFI) change transporter expression to properly adapt to their environment.

But TCR ligation can induce both the upregulation of CD98 and IFNγ in $CD8^+$ T_{mem}. Therefore, we asked if TGF-β1 and KYN cooperatively limits IFNγ expression across T cell activation mechanisms (i.e., both inflammation- and TCR-mediated) or if these molecules solely attenuate IFNγ levels during bystander activation. To test this, we stimulated T cells MACS isolated from PBMC samples with IL-6, IL-15, and IL-18 (each at 100ng/mL) or TCR-agonizing anti-CD3/CD28 microbeads (at a 1:1 bead:cell ratio) in the presence or absence of TGF-β1 (0.2ng/mL) and KYN (100μM) (Figure 4.12B). Afterwards, we determined IFNγ concentrations in culture supernatants and interrogated IFNγ expression in $CD8^+$ T_{mem} using flow. When we stimulated T cells with IL-6, IL-15, and IL-18 in the presence of TGF-β1and KYN, we observed secreted IFNγ levels decrease by a full order of magnitude; however, TGF-β1 and KYN had negligible effect on IFNγ induced by TCR ligation (Figure 4.12B). Despite TGF-β1 and KYN failing to augment IFNγ expression in TCR-mediated $CD8^+$ T_{mem}, we observed that TGF-β1 and KYN could still be sensed by these T cells. Specifically, bulk T cell responses (secreted IL-2 and TNFα) and outward signs of activation in $CD8^+$ T_{mem} elicited by TCR stimulation were slightly impaired by TGF-β1 and KYN (Figure 4.13A–C). Together, this suggests that while TGF-β1 and KYN can be sensed by $CD8^+$ T_{mem} across all activation states, that their inhibitory effect on IFNγ expression is constrained to $CD8^+$ T_{mem} activated by pro-inflammatory cytokines.

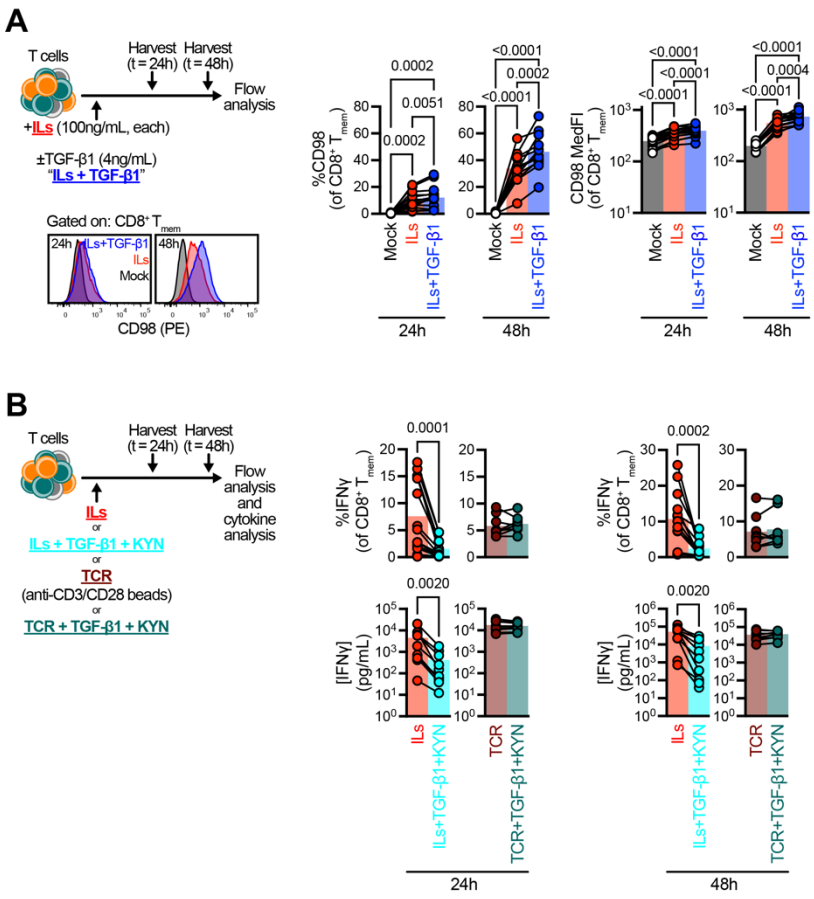

Figure 4.12 TGF-β1 and kynurenine cooperation selectively impairs cytokine-mediated, but not TCR-mediated, effector responses.

A CD98 expression after stimulation with IL-6, IL-15, and IL-18 ("ILs"; 100ng/mL, each) in the presence or absence of TGF-β1 (4ng/mL). **B** IFNγ expression in $CD8^+$ T_{mem} and culture supernatant after IL-6, IL-15, and IL-18 ("ILs"; 100ng/mL, each) or anti-CD3/CD28 microbead ("TCR"; 1:1 bead:cell ratio) stimulation in the presence or absence of TGF-β1 (0.2ng/mL) and kynurenine (100μM) after 24 and 48h of culture. Bar plots in **A** depict *n* = 13–15 PBMC donors. Bar plots in **B** depict *n* = 8–15 PBMC donors. Symbols in plots are connected by donor identity. Indicated are statistical significance where $p < 0.1$ by **A** RM one-way ANOVA with Geisser-Greenhouse correction and Holm-Šídák multiple comparisons tests or **B** Wilcoxon tests.

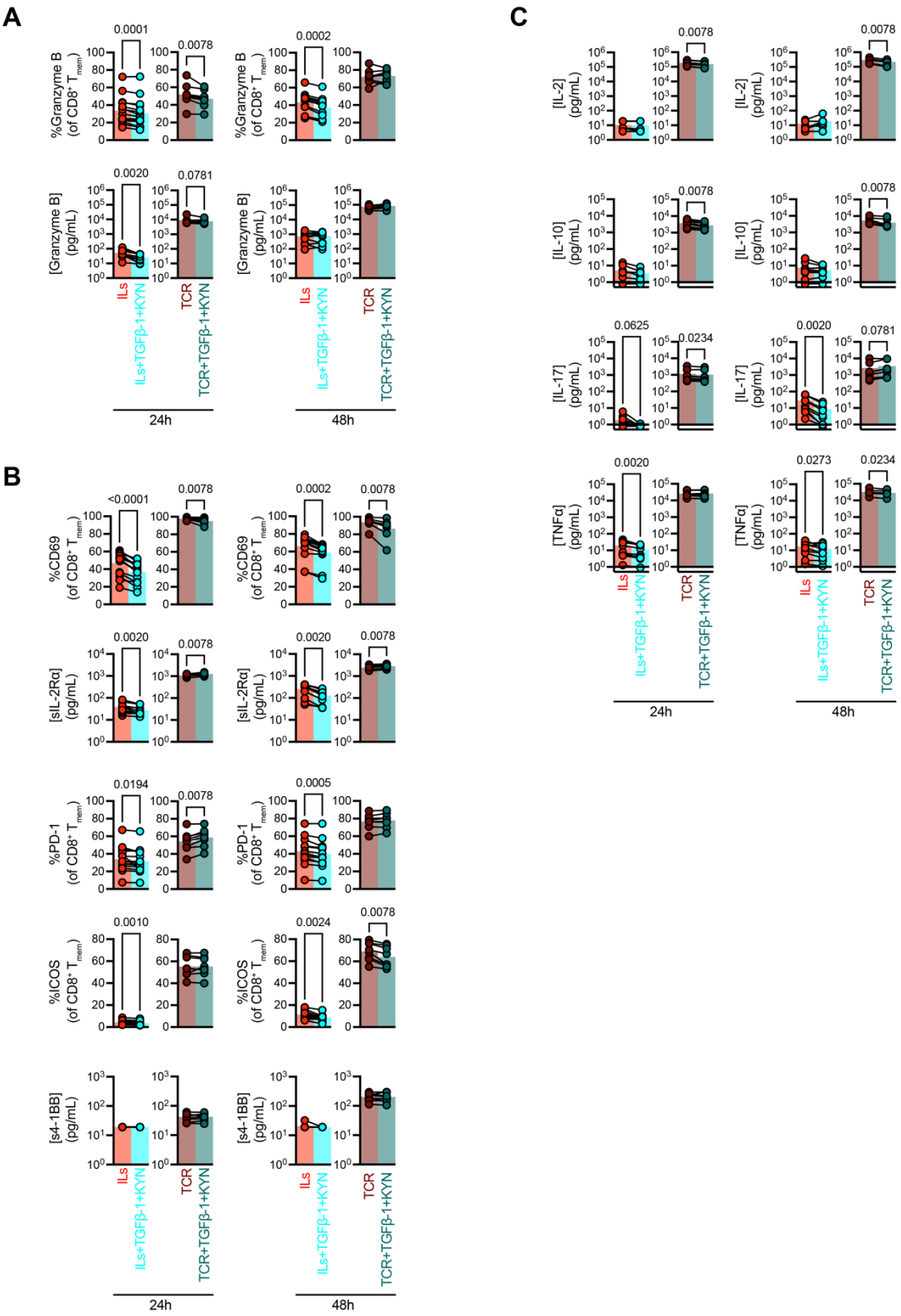

Figure 4.13 Differential effects of TGF-β1 and kynurenine on TCR- and cytokine-mediated activation.

Cells were stimulated as described in Figure 6B where MACS-isolated T cells were stimulated with IL-6, IL-15, IL-18 stimulation ("ILs"; 100ng/mL, each) or anti-CD3/CD28 microbead ("TCR"; 1:1 bead:cell ratio) in the presence or absence of TGF-β1 (0.2ng/mL) and kynurenine (100μM) for 24 and 48h. Afterwards, T cells were characterized via flow cytometry and culture supernatants were analyzed using multiplex cytokine analysis. **A** GzmB expression in $CD8^+$ T_{mem} and concentration in culture supernatants. **B** Expression of activations markers (CD69, PD-1, ICOS) in $CD8^+$ T_{mem} or concentrations of factors indicative of activation (sIL-2Rα, s4-1BB) across stimulation conditions. **C** Expression of effector molecules (IL-2, IL-10, IL-17, TNFα) in culture supernatants across stimulation conditions. **A**–**C** depict 8–15 PBMC donors, with symbols connected by donor identity. Indicated are statistical significance where $p < 0.1$ by Wilcoxon tests.

4.3 Discussion

Maternal-fetal immune conflict during pregnancy has been best understood as an act of avoidance. In these models, maternal immune cells fail to detect fetal elements because they are denied access to both the MFI (189) and the Ag presentation molecules necessary for TCR-mediated activation and target killing (188). We initially asked if T cells at the term, uninduced MFI mirror those in circulation, in line with the placenta as an "immunologically silent" organ. Contrasting with Nancy, *et al*., (189) we observed a sizable immune infiltrate largely in the decidua basalis. Using single-cell targeted proteomics and untargeted transcriptomics, we found that a subset of maternal $CD8^+$ T cells at the MFI exhibited a tissue resident phenotype, which was corroborated by their absence in intervillous circulation. Although Ag presentation is impaired at the MFI, we observed a paradoxical signature of TCR activation in these $CD8^+$ T_{RM}, including 4-1BB, PD-1, and TOX expression. Therefore, we conducted tetramer screens to identify previously defined Y-encoded antigens (PCDH11Y, USP9Y, DDX3Y, UTY, SMCY/JARID1D) (199, 224, 248). Though we were unable to identify Y Ag-specific $CD8^+$ T cells in MB or mPLAC, we found a wide array of T cells specific for viral Ags. Given the role of cognate Ag and TCR signals in animal models of tissue residence (91, 149, 150, 249-253), we asked if $CD8^+$ T_{RM} were purely specific for chronic viruses, which could reactivate and provide Ag (141). Instead, we also detected $CD8^+$ T_{RM} specific for Ag from acute viral infections, like influenza A virus (IAV) and adenovirus (AdV). These bystander $CD8^+$ T_{mem} also expressed markers of activation. Though we cannot formally exclude the possibility of an alloresponse leading to TCR agonism (226), TCR engagement should promote T cell proliferation and enhanced numbers in tissues. But we observed that virus-specific $CD8^+$ T_{mem} formed a similar percentage of the circulating and resident $CD8^+$ T_{mem} pool. Together, these data support a model where maternal T cells are retained at the MFI in an Ag-agnostic manner.

Using an untargeted transcriptomic approach, we extricated signatures of chemokine-mediated T cell recruitment (*CXCL10*–*CXCR3*) and inflammation-dependent T cell activation (*IL15*–*IL2RG*, *IL2RB*), which we validated with targeted cytokine analyses. The presence of factors capable of recruiting T cells to the MFI contrasts with a previous study describing T cell exclusion from the MFI by means of epigenetically silencing *Cxcl10* (189). Instead, this finding complements other mechanistic studies which found CXCR3-mediated recruitment to the skin (149) and vagina (251) antecedent to residence. As surface CXCR3 levels drop after ligand engagement (6, 113), the decreased CXCR3 frequency in circulating $CD8^+$ T_{mem} at the MFI may reflect CXCR3-CXCL10 signaling in action. But this recruitment to the MFI ultimately exposes $CD8^+$ T_{mem} to an entirely different environment, in which there is sustained exposure to pro-inflammatory cytokines, like IL-6, IL-15, and IL-18. Using in vitro stimulations, we found that these pro-inflammatory signals could recapitulate the phenotypes observed in mPLAC $CD8^+$ T_{RM}, including PD-1, 4-1BB, ICOS, TIM-3, TOX, and CD39 expression. This, to our knowledge, is the first study that identifies a TCR-independent mechanism to CD39 expression, adding to a growing number of studies elucidating parallels in the outcomes of inflammation- and TCR-mediated activation in $CD8^+$ T_{mem} (8, 25, 146, 254-256). These similarities likely explain why $CD8^+$ T_{RM} paradoxically upregulate transcripts associated with TCR engagement despite the probable lack of cognate Ag (144, 145, 176, 249): homeostatic pro-inflammatory cytokine networks within tissues promote these phenotypic adaptations.

Ag-nonspecific $CD8^+$ T_{RM} are not often described in mice, likely because of the limited $CD8^+$ T_{mem} pool in animals reared in SPF settings (161). Given this limitation, signals necessary for tissue residence have been most understood downstream of TCR activation (91, 149, 150, 249-253). 1) TCR ligation induces 4-1BB expression in $CD8^+$ T cells and 2) subsequent 4-1BB–4-1BBL signaling is required for subsequent $CD8^+$ T cell tissue residence (92, 234). Our broad analysis of the placenta demonstrates that inflammation may serve as a substitute for TCR-agonism, maintaining 4-1BB expression in $CD8^+$ T_{mem} despite lack of cognate Ag, which can be engaged in situ by 4-1BBL–expressing $CD206^{hi}$ macrophages. This phenomenon may also explain why both Ag-specific and -nonspecific T cells are maintained in tissue. IL-15 signaling, which is critical for $CD8^+$ T_{RM} maintenance in some tissues (150, 249, 257), could drive 4-1BB–4-1BBL signaling which is thought to drive $CD8^+$ T cell survival in other contexts (255). Given the importance of pro-inflammatory cytokines in tissue retention, but their paradoxical role in bystander activation (156), we sought mechanisms which could selectively impair inflammation-driven cytotoxicity in $CD8^+$ T_{mem}. Using comprehensive transcriptomics, proteomics, and metabolomics, we identified that the

pro-inflammatory cytokine milieu at the MFI exists in juxtaposition with anti-inflammatory cytokine (TGF-β1) and metabolite (KYN) networks. IL-6, IL-15, and IL-18 can activate $CD8^+$ T_{mem} and lead to the acquisition of effector functions, like IFNγ secretion, which could threaten immune homeostasis; however, TGF-β1 and KYN can cooperatively restrain inflammation-mediated IFNγ expression without abrogating cellular activation and coreceptor upregulation. Finally, we do not observe these effects on cytotoxicity with TCR-stimulated T cells, suggesting this regulatory mechanism serves two purposes: 1) to broadly sustain $CD8^+$ T_{RM} at the MFI in situ with inflammation without inducing potentially detrimental inflammation-mediated cytotoxicity and 2) to concurrently maintain maternal immunocompetence against pathogens by selectively permitting TCR-mediated cytotoxicity. Incorporating these regulatory signals appears essential for $CD8^+$ T_{RM}, given their biased expression of the KYN transporter, CD98, alongside reports demonstrating that TGF-β1 (149, 150), and AhR (258) are required for their persistence at other organs.

Despite existing at the MFI, these regulatory programs are likely involved in the maintenance of immune homeostasis at other tissues characterized by pro-inflammatory microenvironments. Given the role of dysregulated inflammation (often IL-15–related) and bystander activation in various autoimmune pathologies (11, 36, 37, 39, 40, 71, 72, 74), TGF-β1 and/or KYN-AhR signaling could be leveraged to restore homeostasis in multiple contexts. Conversely, leveraging these programs may have therapeutic relevance in cancer. Tumor Ag-nonspecific $CD8^+$ T_{RM} are often found in solid tumors (41), but leveraging these cells to clear tumor in mouse models has proved challenging (84). Tumor Ag-nonspecific $CD8^+$ T_{RM} could not be bystander-activated by TLR agonists; only the cognate viral Ag for these tumor-nonspecific $CD8^+$ T_{RM} could elicit sufficient cytotoxicity to have therapeutic effect (84). Given the polyclonal nature of $CD8^+$ T_{RM} in humans, this approach is likely not feasible, but highlights programs that regulate inflammation-mediated cytotoxicity. Indeed, tumors are often enriched for TGF-β1 (259, 260) and KYN (243, 261, 262). But it remains unclear these regulatory molecules could be targeted so that bulk tumor Ag-nonspecific $CD8^+$ T_{RM} could be activated into killers by inflammation alone. Future work will be necessary to dissect the roles of TGF-β1, KYN, and pro-inflammatory cytokines across tissue types and disease states to better control $CD8^+$ T_{mem} functions.

In summary, based on our data we propose that Ag-nonspecific $CD8^+$ T_{mem} recruitment and retention can occur via pro-inflammatory homeostatic cytokine networks in situ; but immune homeostasis is maintained because inflammation-mediated cytotoxicity programs are restrained by contemporaneous sensing of regulatory cytokines and metabolites.

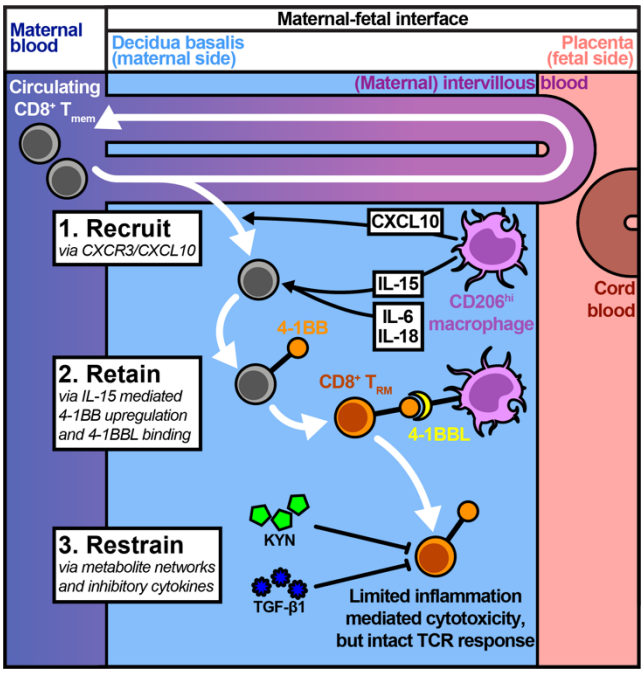

Figure 4.14 Inflammation poises cells for tissue residence, but bystander cytotoxicity is muted by regulatory cytokine and metabolite networks

Ag-nonspecific CD8$^+$ T_{mem} populations are **1**) recruited by chemokines to tissues and **2**) retained by inflammation-mediated 4-1BB upregulation and subsequent 4-1BB–4-1BBL signals. **3**) Tissue homeostasis is maintained despite homeostatic inflammatory signals due to TGF-β1 and KYN networks, which selectively inhibit inflammation-, but not TCR-mediated IFNγ expression.

4.4 Methods

4.4.1 Study population and approvals

Patients without underlying complications undergoing elective, term, non-induced cesarean section at the University of Washington (UW) Medical Center were recruited by the UW Department of Obstetrics and Gynecology (Seattle, Washington, USA) as part of the study "The Maternal-Fetal Immune Response to Complications of Pregnancy." Signed informed consent was obtained from all participants prior to sample collection. Institutional Review Boards of the University of Washington and Fred Hutchinson Cancer Research Center approved the study protocol.

HIV-uninfected adults were recruited by the Seattle HIV Vaccine Trials Unit (Seattle, Washington, USA) as part of the study "Establishing Immunologic Assays for Determining HIV-1 Prevention and Control." These samples are also known as the Seattle Area Control (SAC) cohort. All

participants were provided and signed informed consent, and the Fred Hutchinson Cancer Research Center Institutional Review Board approved the study protocol.

4.4.2 Blood collection for leukocyte and plasma isolation

We maintained all samples on ice after acquisition. Clinicians collected maternal peripheral blood (MB) antepartum and fetal cord blood (CB) postpartum by venipuncture. CB was obtained by double clamping the umbilical cord segment, washing residual blood on the umbilical cord, and drawing blood from the umbilical cord vein. MB and CB were collected in acid citrate dextrose solution A (ACD)-vacutainer tubes (BD Biosciences). To collect intervillous blood (IVB), we injected 6–10mL of ACD solution using a 28G½ syringe into the intervillous space of the placenta through the fetal membranes (Figure 4.3C). We obtained IVB which passively drained from the placenta and processed it alongside MB and CB samples. We centrifuged MB, CB, and IVB at 400g for 10 min, collected plasma and stored at -80ºC. We isolated leukocytes via ACK lysis (ThermoFisher) or density gradient centrifugation with Lymphoprep (STEMCELL Technologies) and resuspended in RP7.5 (RPMI 1640 supplemented with 7.5% FBS (Peak Serum), 2 mM L-glutamine, 100 U/mL penicillin–streptomycin (ThermoFisher)) before downstream use. To quantitate cells, we stained single-cell suspension aliquots (Table 4.1) and acquired events on a Guava easyCyte (EMD Millipore). We then stained cells immediately for flow analysis or cryopreserved cells in cryopreservation solution (CPS; 10% sterile DMSO (Sigma Aldrich), 90% FBS).

4.4.3 Tissue collection for leukocyte isolation

We maintained all tissues on ice after acquisition. Clinicians vacuum aspirated residual tissue in the uterine cavity to obtain decidual tissue. We rinsed intact placentas in 1x PBS and used sterile instruments to collect 0.5cm-depth biopsies from the maternal and fetal sides of the placenta (mPLAC and fPLAC, respectively). We minced decidual, mPLAC, and fPLAC tissues in digestion media: RP7.5 + 700U/mL Collagenase Type II (Sigma Aldrich), 200U/mL DNase (Sigma Aldrich), which were incubated in a shaking 37ºC incubator for 60 min at 225 RPM. Afterwards, we strained single-cell suspensions through a 70µm filter, centrifuged cells at 400g for 5 min, discarded supernatants, and washed cells with RP7.5 media. We removed contaminating RBCs using ACK lysis, and resuspended cell pellets in RP7.5 before downstream use. To quantitate cells, we

stained single-cell suspension aliquots (Table 4.1) and acquired events on a Guava easyCyte. We then stained cells immediately for flow analysis or cryopreserved cells in cryopreservation solution (CPS; 10% sterile DMSO (Sigma Aldrich), 90% FBS).

Table 4.1 Cell counting panel for Guava easyCyte

Reagent	Conjugate	Clone	Vendor	Dilution
Guava stain (FACSWash diluent, 20 min, room temperature)				
7-AAD	NA	NA	BD Biosciences	1:15
CD45	FITC	2D1	BD Biosciences	1:50
CD3	PE	UCHT1	BD Biosciences	1:30
Fix (1% PFA)				

4.4.4 In vitro stimulation assays

We thawed 2–4 × 10^7 cryopreserved PBMC in RP10 media (RPMI1640 supplemented with 10% FBS, 2 mM L-glutamine, 100 U/mL penicillin-streptomycin). To enrich bulk T cells from single-cell suspensions, we used human-specific T cell negative isolation MACS (STEMCELL Technologies). We plated 0.5–2 × 10^6 T cells per well in 96-well V-bottom tissue culture plates. We cultured cells in RP10 at 37ºC and 5% CO_2. We stimulated T cells with human recombinant IL-6 (BioLegend), IL-15, and IL-18 (Peprotech) in combination (each at 100ng/mL) or with Dynabeads human T-Activator (ThermoFisher) anti-CD3/CD28 beads (at a 1:1 bead/cell ratio). We added 100μM L-kynurenine (Sigma) dissolved in RP10 and/or human recombinant TGF-β1 (Peprotech) at the time of stimulation. Six hours prior to harvesting T cells (t = 18 or 42h), we added GolgiPlug (BD Biosciences) at 1:1000 dilution to allow intracellular accumulation of cytokines. At harvest timepoints (t = 24 or 48h), we centrifuged plates, collected and froze media supernatants at -80ºC, and conducted flow cytometric staining on cells.

4.4.5 Flow cytometry

When handling cryopreserved samples for ex vivo cytometric analysis, we thawed single-cell suspensions in warm RP10 (RPMI 1640 supplemented with 10% FBS, 2 mM L-glutamine, 100 U/mL penicillin–streptomycin). We aliquoted fresh or thawed single-cell suspension samples at 0.5–2 × 10^6 cells/well in a 96-well v-bottom plate. All flow panel reagent information, stain conditions, and gating strategies are included in Figure 4.15, Figure 4.16, Figure 4.17, Figure 4.18, Figure 4.19, Figure 4.20, Figure 4.21, Figure 4.22, Table 4.1, Table 4.2, Table 4.3, Table 4.4, Table 4.5, Table 4.6, Table 4.7, Table 4.8, Table 4.9. We conducted LIVE/DEAD fixable aqua

or blue viability dye (Thermo Fisher) (AViD or BViD, respectively) staining in 1x PBS. For FACS surface staining, we utilized FACSWash (1x PBS supplemented with 2% PBS) as the stain diluent; and for all other flow analysis, we utilized FACSWash + Azide (1 × PBS supplemented with 2% FBS and 0.2% sodium azide) as the stain diluent. For T cell panels (Table 4.2, Table 4.4, Table 4.5, Table 4.6, Table 4.7) we fixed cells with the FOXP3 Fixation/Permeabilization Buffer Kit (Thermo Fisher) and conducted intracellular/nuclear stains using the FOXP3 Permeabilization Buffer (Thermo Fisher) as diluent. For APC panels (Table 4.8, Table 4.9) we fixed cells with Cytofix/Cytoperm (BD Biosciences) and conducted intracellular stains using 1x Perm/Wash buffer (BD Biosciences) as diluent. We resuspended cells in FACS Wash and acquired events on a FACSymphony A5 and sorted cells on a FACSAria II (BD Biosciences), which we analyzed using FlowJo v10 (BD Biosciences). We conducted statistical testing using Prism v8 (GraphPad).

Table 4.2 T cell stimulation and intracellular cytokine staining panel

Reagent	Conjugate	Clone	Vendor	Dilution
Viability stain (1x PBS diluent, 20 min, room temperature)				
LIVE/DEAD fixable blue viability dye (BViD)	UV450	NA	Thermo Fisher	1:500
Surface stain (FACSWash + Azide diluent, 20 min, room temperature)				
Brilliant stain buffer plus	NA	NA	BD Biosciences	1:5
TruStain FcX (Fc block)	NA	NA	BioLegend	1:20
CD69	BUV737	FN50	BD Biosciences	1:40
CD39	BV605	A1	BioLegend	1:20
TIM-3	BV650	7D3	BD Biosciences	1:20
PD-1	BB700	EH12.1	BD Biosciences	1:20
CD98	PE	MEM-108	Thermo Fisher	1:100
CD278 (ICOS)	PE-CF594	C398.4A	BD Biosciences	1:1000
CD137 (4-1BB)	PE-Cy5	4B4-1	BD Biosciences	1:20
CD19	PE-Cy5.5	SJ25-C1	Thermo Fisher	1:160
CCR7	PE-Cy7	3D12	BD Biosciences	1:40
CD45RO	APC-H7	UCHL1	BD Biosciences	1:40
Fix (1x eBioscience FOXP3 fixation buffer, 20 min, room temperature)				
Intracellular stain (1x eBioscience FOXP3 permeabilization buffer, 30 min, room temperature)				
CD8	BUV395	RPA-T8	BD Biosciences	1:80
CD3	BUV496	UCHT1	BD Biosciences	1:40
CD4	BUV805	SK3	BD Biosciences	1:80
IFNγ	BV421	4S.B3	BioLegend	1:40
FoxP3	AF488	259D/C7	BD Biosciences	1:10
CTLA-4	BB630	BNI3	BD Biosciences	1:80
TOX	APC	REA473	Miltenyi Biotec	1:80
Granzyme B	AF700	GB11	BD Biosciences	1:80

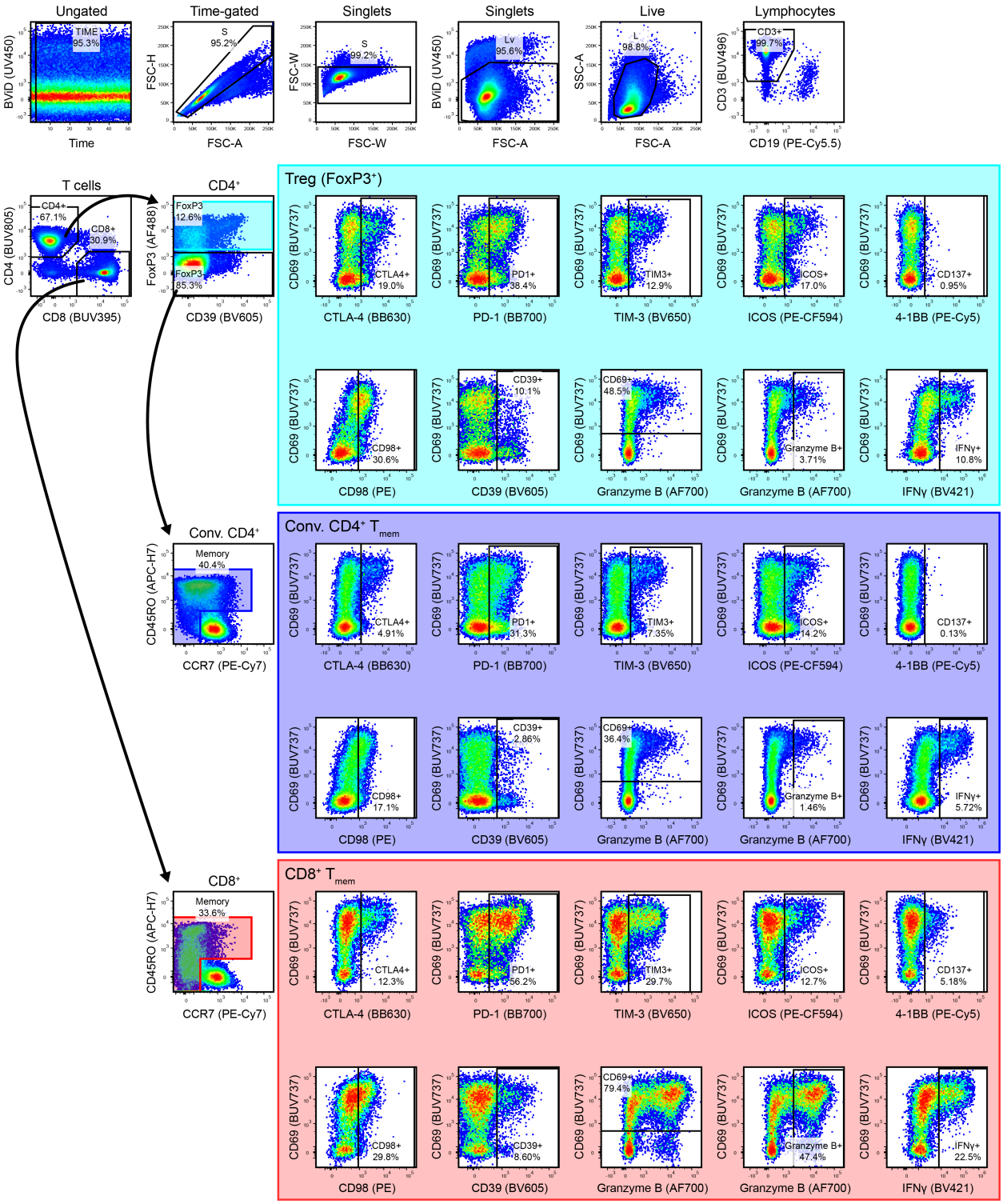

Figure 4.15 Gating strategy for T cell stimulation and intracellular cytokine staining panel

Gating strategy depicts T cells after stimulation with IL-6, IL-15, and IL-18 in combination (100ng/mL, each) for 48 h.

Table 4.3 FACS panel for scRNAseq

Reagent	Conjugate	Clone	Vendor	Dilution
Viability stain (1x PBS diluent, 20 min, room temperature)				
LIVE/DEAD fixable aqua viability dye (AViD)	V510	NA	Thermo Fisher	1:500
Tetramer stain (FACSWash diluent, 45 min, room temperature)				
TruStain FcX (Fc block)	NA	NA	BioLegend	1:20
MR1 OP-5-RU (MAIT cell) tetramer	PE	NA	NIH Tetramer core	1:400
Surface stain (FACSWash diluent, 20 min, room temperature)				
CD25	BV421	M-A251	BD Biosciences	1:40
CD14	BV711	MφP9	BD Biosciences	1:40
CD127	BV786	HIL-7R-M21	BD Biosciences	1:10
CD45	FITC	2D1	BD Biosciences	1:40
CD19	PE-Cy5.5	SJ25-C1	Thermo Fisher	1:160
CD8	PE-Cy7	RPA-T8	BD Biosciences	1:40
CD3	APC	SK7	BD Biosciences	1:50
CD4	AF700	RPA-T4	BD Biosciences	1:100
HLA-DR	APC-H7	G46-6	BD Biosciences	1:40

Table 4.4 T cell phenotyping panel 1

Reagent	Conjugate	Clone	Vendor	Dilution
Viability stain (1x PBS diluent, 20 min, room temperature)				
LIVE/DEAD fixable blue viability dye (BViD)	UV450	NA	Thermo Fisher	1:500
Tetramer stain (FACSWash + Azide diluent, 60 min, room temperature)				
MR1 OP-5-RU (MAIT cell) tetramer	BV421	NA	NIH Tetramer Core	1:500
TruStain FcX (Fc block)	NA	NA	BioLegend	1:20
Surface stain (FACSWash + Azide diluent, 20 min, room temperature)				
Brilliant stain buffer concentrate	NA	NA	BD Biosciences	1:5
CD8	BUV395	RPA-T8	BD Biosciences	1:80
CD3	BUV496	UCHT1	BD Biosciences	1:40
CD25	BUV563	2A3	BD Biosciences	1:40
HLA-DR	BUV661	G46-6	BD Biosciences	1:80
CD278 (ICOS)	BUV737	DX29	BD Biosciences	1:10
CD45	BUV805	HI30	BD Biosciences	1:80
CD28	BV480	CD28.2	BD Biosciences	1:40
CD45RA	BV570	HI100	BioLegend	1:160
PD-1	BV605	EH12.1	BD Biosciences	1:20
CD69	BV650	FN50	BD Biosciences	1:20-40*
OX40	BV711	Act35	BD Biosciences	1:40
CD103	BV750	Ber-ACT8	BD Biosciences	1:160
CD127	BV786	HIL-7R-M21	BD Biosciences	1:10
CD27	BB660	M-T271	BD Biosciences	1:160
CD161	BB700	DX12	BD Biosciences	1:20
CD38	BB790	HIT2	BD Biosciences	1:80
TCRγδ	PE-CF594	B1	BD Biosciences	1:20
CD137 (4-1BB)	PE-Cy5	4B4-1	BD Biosciences	1:20
CD19	PE-Cy5.5	SJ25-C1	Thermo Fisher	1:160
CCR7	PE-Cy7	3D12	BD Biosciences	1:40
CD4	APC-H7	RPA-T4	BD Biosciences	1:40
Fix (1x eBioscience FOXP3 fixation buffer, 20 min, room temperature)				
Intracellular stain (1x eBioscience FOXP3 permeabilization buffer, 30 min, room temperature)				
FoxP3	AF488	259D/C7	BD Biosciences	1:20
CTLA-4	BB630	BNI3	BD Biosciences	1:80
Helios	PE	22F6	BD Biosciences	1:500
Ki-67	e660	Sola15	Thermo Fisher	1:1000
Granzyme B	AF700	GB11	BD Biosciences	1:80

*Lot-dependent dilution variability

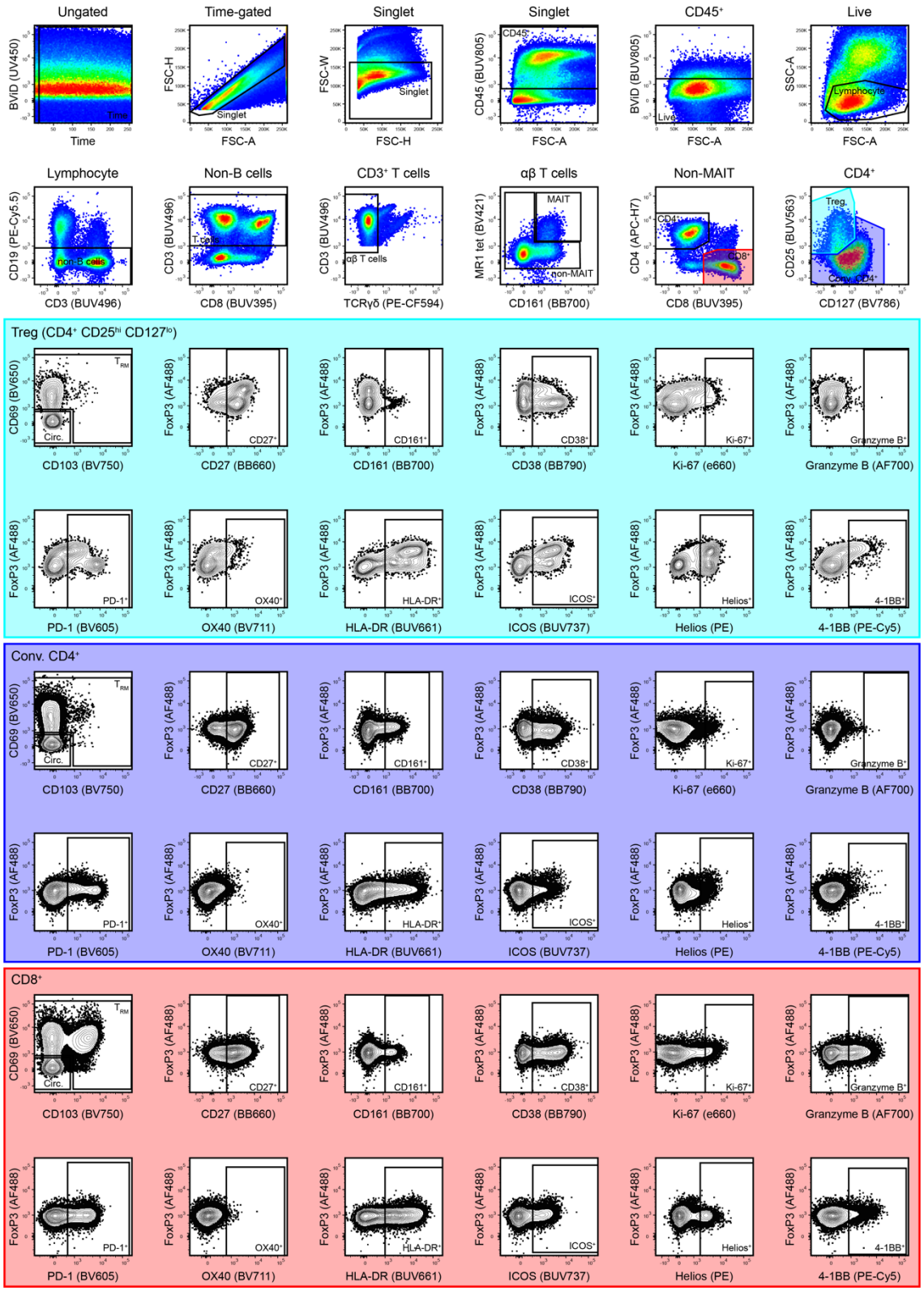

Figure 4.16 Gating strategy for T cell phenotyping panel 1

Representative gating example from cells freshly isolated from mPLAC

Table 4.5 T cell phenotyping panel 2

Reagent	Conjugate	Clone	Vendor	Dilution
Viability stain (1x PBS diluent, 20 min, room temperature)				
LIVE/DEAD fixable blue viability dye (BViD)	UV450	NA	Thermo Fisher	1:500
Tetramer stain (FACSWash + Azide diluent, 60 min, room temperature)				
MR1 OP-5-RU (MAIT cell) tetramer	BV421	NA	NIH Tetramer Core	1:500
TruStain FcX (Fc block)	NA	NA	BioLegend	1:20
1º Surface stain (FACSWash + Azide diluent, 20 min, room temperature)				
CD127	Biotin	A019D5	BioLegend	1:40
2º Surface stain (FACSWash + Azide diluent, 20 min, room temperature)				
Brilliant stain buffer plus	NA	NA	BD Biosciences	1:5
CD8	BUV395	RPA-T8	BD Biosciences	1:80
CD3	BUV496	UCHT1	BD Biosciences	1:40
CD25	BUV563	2A3	BD Biosciences	1:40
CD69	BUV737	FN50	BD Biosciences	1:80
CD45	BUV805	HI30	BD Biosciences	1:80
TCRγδ	BV480	B1	BD Biosciences	1:10
CD45RA	BV570	HI100	BioLegend	1:160
CD39	BV605	A1	BioLegend	1:20
TIM-3	BV650	7D3	BD Biosciences	1:20
CCR5	BV711	2D7/CCR5	BD Biosciences	1:20
CD103	BV750	Ber-ACT8	BD Biosciences	1:160
Ki-67	BV786	B56	BD Biosciences	1:320
Streptavidin	BB660	NA	BD Biosciences	1:400
PD-1	BB700	EH12.1	BD Biosciences	1:20
TIGIT	BB790	741182	BD Biosciences	1:80
CD137 (4-1BB)	PE-Cy5	4B4-1	BD Biosciences	1:20
CD19	PE-Cy5.5	SJ25-C1	Thermo Fisher	1:160
CD4	APC-H7	RPA-T4	BD Biosciences	1:40
Fix (1x eBioscience FOXP3 fixation buffer, 20 min, room temperature)				
Intracellular stain (1x eBioscience FOXP3 permeabilization buffer, 30 min, room temperature)				
FoxP3	AF488	259D/C7	BD Biosciences	1:20
CTLA-4	BB630	BNI3	BD Biosciences	1:80
TCF-1	PE	22F6	BD Biosciences	1:500
Eomes	PE-e610	WD1928	Thermo Fisher	1:20
Tbet	PE-Cy7	4B10	Thermo Fisher	1:40
TOX	APC	REA473	Miltenyi Biotec	1:80
Granzyme B	AF700	GB11	BD Biosciences	1:80

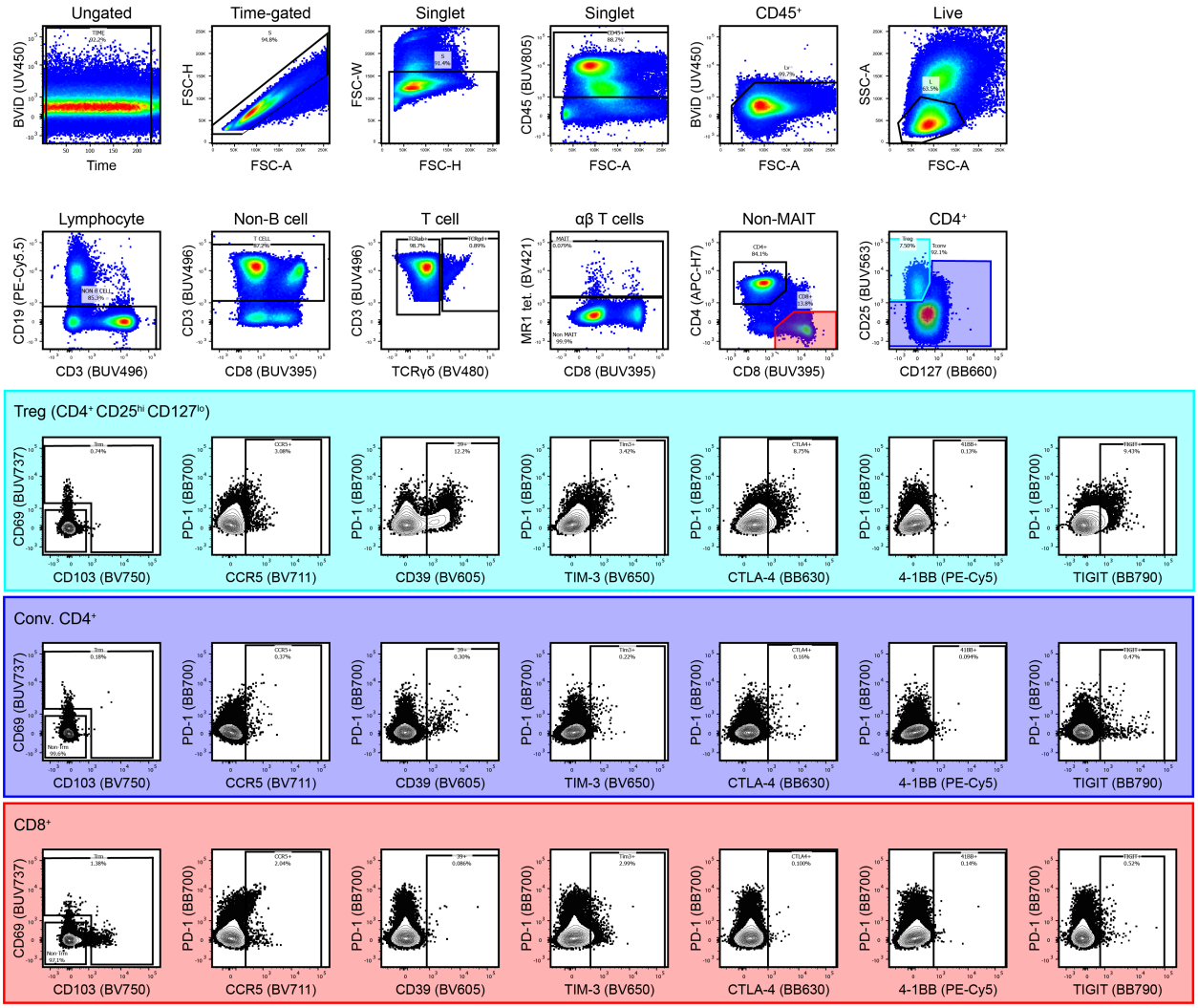

Figure 4.17 Gating strategy for T cell phenotyping panel 2 (CB)

Representative gating example from cell freshly isolated from CB

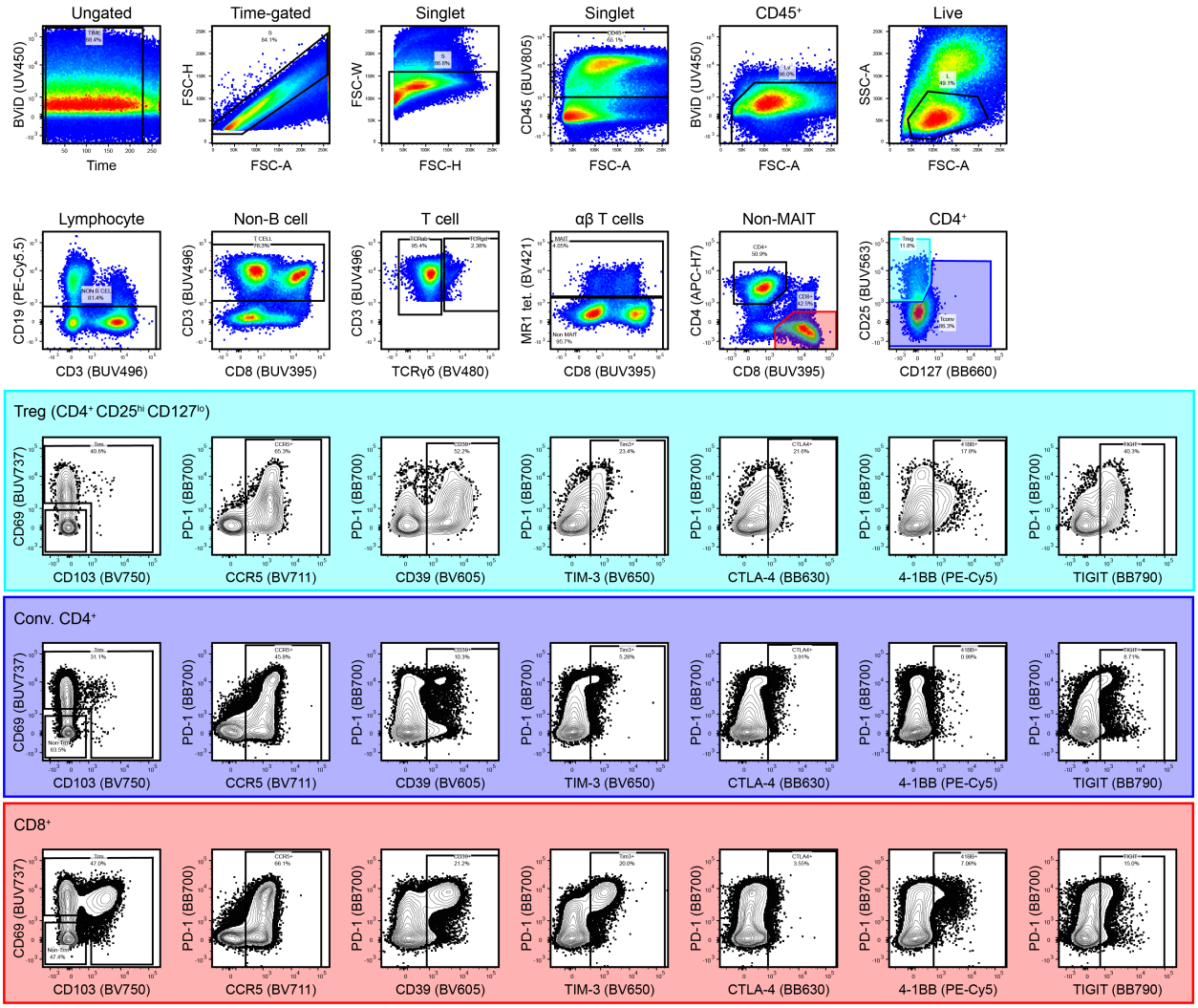

Figure 4.18 Gating strategy for T cell phenotyping panel 2 (mPLAC)

Representative gating example from cell freshly isolated from mPLAC

Table 4.6 T cell phenotyping panel 3

Reagent	Conjugate	Clone	Vendor	Dilution
Viability stain (1x PBS diluent, 20 min, room temperature)				
LIVE/DEAD fixable blue viability dye (BViD)	UV450	NA	Thermo Fisher	1:500
1º Surface stain (FACSWash + Azide diluent, 20 min, room temperature)				
CD127	Biotin	A019D5	BioLegend	1:40
TruStain FcX (Fc block)	NA	NA	BioLegend	1:20
2º Surface stain (FACSWash + Azide diluent, 20 min, room temperature)				
Brilliant stain buffer plus	NA	NA	BD Biosciences	1:5
CD8	BUV395	RPA-T8	BD Biosciences	1:80
CD3	BUV496	UCHT1	BD Biosciences	1:40
CCR7	BUV661	2-L1-A	BD Biosciences	1:80
ICOS	BUV737	DX29	BD Biosciences	1:20
CD45	BUV805	HI30	BD Biosciences	1:80
CD25	BV421	M-A251	BD Biosciences	1:40
CD28	BV480	CD28.2	BD Biosciences	1:40
CD45RA	BV570	HI100	BioLegend	1:160
CD39	BV605	A1	BioLegend	1:20
CD69	BV650	FN50	BD Biosciences	1:20-40*
OX40	BV711	ACT35	BD Biosciences	1:40
CD103	BV750	Ber-ACT8	BD Biosciences	1:160
CCR5	BV786	3A9	BD Biosciences	1:20
TIM-3	BB515	7D3	BD Biosciences	1:80
Streptavidin	BB660	NA	BD Biosciences	1:400
PD-1	BB700	EH12.1	BD Biosciences	1:20
TIGIT	BB790	741182	BD Biosciences	1:80
IL-1R1	PE	Goat polyclonal	R&D Systems	1:20
CXCR3	PE-CF594	1C6/CXCR3	BD Biosciences	1:20
CD137 (4-1BB)	PE-Cy5	4B4-1	BD Biosciences	1:20
CD19	PE-Cy5.5	SJ25-C1	Thermo Fisher	1:160
IL-18Rα	PE-Cy7	H44	BioLegend	1:40
IL-1R2	APC	34141	R&D Systems	1:20
HLA-DR	APC-R700	G46-6	BD Biosciences	1:160
CD4	APC-H7	RPA-T4	BD Biosciences	1:40
Fix (1x eBioscience FOXP3 fixation buffer, 20 min, room temperature)				
Intracellular stain (1x eBioscience FOXP3 permeabilization buffer, 30 min, room temperature)				
CTLA-4	BB630	BNI3	BD Biosciences	1:80

*Lot-dependent dilution variability

Table 4.7 T cell phenotyping panel 4

Reagent	Conjugate	Clone	Vendor	Dilution
Viability stain (1x PBS diluent, 20 min, room temperature)				
LIVE/DEAD fixable blue viability dye (BViD)	UV450	NA	Thermo Fisher	1:500
1º Surface stain (FACSWash + Azide diluent, 20 min, room temperature)				
CD127	Biotin	A019D5	BioLegend	1:40
TruStain FcX (Fc block)	NA	NA	BioLegend	1:20
2º Surface stain (FACSWash + Azide diluent, 20 min, room temperature)				
Brilliant stain buffer plus	NA	NA	BD Biosciences	1:5
CD8	BUV395	RPA-T8	BD Biosciences	1:80
CD3	BUV496	UCHT1	BD Biosciences	1:40
CCR7	BUV661	2-L1-A	BD Biosciences	1:80
ICOS	BUV737	DX29	BD Biosciences	1:20
CD45	BUV805	HI30	BD Biosciences	1:80
CD25	BV421	M-A251	BD Biosciences	1:40
CD28	BV480	CD28.2	BD Biosciences	1:40
CD45RA	BV570	HI100	BioLegend	1:160
CD39	BV605	A1	BioLegend	1:20
CD69	BV650	FN50	BD Biosciences	1:20-40*
OX40	BV711	ACT35	BD Biosciences	1:40
CD103	BV750	Ber-ACT8	BD Biosciences	1:160
CCR5	BV786	3A9	BD Biosciences	1:20
TIM-3	BB515	7D3	BD Biosciences	1:80
Streptavidin	BB660	NA	BD Biosciences	1:400
PD-1	BB700	EH12.1	BD Biosciences	1:20
CD98	PE	MEM-108	Thermo Fisher	1:100
CXCR3	PE-CF594	1C6/CXCR3	BD Biosciences	1:20
CD137 (4-1BB)	PE-Cy5	4B4-1	BD Biosciences	1:20
CD19	PE-Cy5.5	SJ25-C1	Thermo Fisher	1:160
IL-18Rα	PE-Cy7	H44	BioLegend	1:40
HLA-DR	APC-R700	G46-6	BD Biosciences	1:160
CD4	APC-H7	RPA-T4	BD Biosciences	1:40
Fix (1x eBioscience FOXP3 fixation buffer, 20 min, room temperature)				
Intracellular stain (1x eBioscience FOXP3 permeabilization buffer, 30 min, room temperature)				
CTLA-4	BB630	BNI3	BD Biosciences	1:80
AhR	e660	4MEJJ	Thermo Fisher	1:100

*Lot-dependent dilution variability

Table 4.8 APC phenotyping panel 1

Reagent	Conjugate	Clone	Vendor	Dilution
Viability stain (1x PBS diluent, 20 min, room temperature)				
LIVE/DEAD fixable blue viability dye (BViD)	UV450	NA	Thermo Fisher	1:500
1º Surface stain (FACSWash + Azide diluent, 20 min, room temperature)				
CX3CR1	PE-Cy7	2A9-1	BioLegend	1:160
TruStain FcX (Fc block)	NA	NA	BioLegend	1:20
2º Surface stain (FACSWash + Azide diluent, 20 min, room temperature)				
Brilliant stain buffer concentrate	NA	NA	BD Biosciences	1:5
CD40	BUV395	5C3	BD Biosciences	1:40
CD16	BUV496	3G8	BD Biosciences	1:320
CD56	BUV563	NCAM16.2	BD Biosciences	1:160
CD3	BUV661	UCHT1	BD Biosciences	1:80
CD86	BUV737	2331	BD Biosciences	1:40
CD45	BUV805	HI30	BD Biosciences	1:80
PD-L2	BV421	MIH18	BD Biosciences	1:20
CD85k	BV480	ZM3.8	BD Biosciences	1:40
CD14	BV570	M5E2	BioLegend	1:20
CD141	BV605	1A4	BD Biosciences	1:640
SIRPα	BV650	SE5A5	BD Biosciences	1:160
CD11b	BV750	ICRF44	BD Biosciences	1:160
CD123	BV786	7G3	BD Biosciences	1:40
CD206	BB515	19.2	BD Biosciences	1:20
BTLA	BB630	J168-540	BD Biosciences	1:80
PD-L1	BB660	MIH1	BD Biosciences	1:40
CD32	BB700	FLI8.26	BD Biosciences	1:160
CD38	BB790	HIT2	BD Biosciences	1:80
Axl	PE	108724	R&D Systems	1:20
CD163	PE-CF594	GHI/61	BD Biosciences	1:40
CD80	PE-Cy5	L37.4	BD Biosciences	1:10
CD19	PE-Cy5.5	SJ25-C1	Thermo Fisher	1:160
CD1c	AF647	F10/21A3	BD Biosciences	1:160
CD11c	AF700	B-ly6	BD Biosciences	1:320
HLA-DR	APC-H7	G46-6	BD Biosciences	1:40
Fix (1x eBioscience FOXP3 fixation buffer, 20 min, room temperature)				
Intracellular stain (1x eBioscience FOXP3 permeabilization buffer, 30 min, room temperature)				
CD68	BV711	Y1/82A	BD Biosciences	1:40

Table 4.9 APC phenotyping panel 2

Reagent	Conjugate	Clone	Vendor	Dilution
Viability stain (1x PBS diluent, 20 min, room temperature)				
LIVE/DEAD fixable blue viability dye (BViD)	UV450	NA	Thermo Fisher	1:500
1º Surface stain (FACSWash + Azide diluent, 20 min, room temperature)				
CX3CR1	PE-Cy7	2A9-1	BioLegend	1:160
TruStain FcX (Fc block)	NA	NA	BioLegend	1:20
2º Surface stain (FACSWash + Azide diluent, 20 min, room temperature)				
Brilliant stain buffer concentrate	NA	NA	BD Biosciences	1:5
CD40	BUV395	5C3	BD Biosciences	1:40
CD16	BUV496	3G8	BD Biosciences	1:320
CD56	BUV563	NCAM16.2	BD Biosciences	1:160
CD3	BUV661	UCHT1	BD Biosciences	1:80
CD86	BUV737	2331	BD Biosciences	1:40
CD45	BUV805	HI30	BD Biosciences	1:80
PD-L2	BV421	MIH18	BD Biosciences	1:20
CD85k	BV480	ZM3.8	BD Biosciences	1:40
CD14	BV570	M5E2	BioLegend	1:20
CD141	BV605	1A4	BD Biosciences	1:640
SIRPα	BV650	SE5A5	BD Biosciences	1:160
CD11b	BV750	ICRF44	BD Biosciences	1:160
CD123	BV786	7G3	BD Biosciences	1:40
CD206	BB515	19.2	BD Biosciences	1:20
BTLA	BB630	J168-540	BD Biosciences	1:80
PD-L1	BB660	MIH1	BD Biosciences	1:40
CD32	BB700	FLI8.26	BD Biosciences	1:160
CD38	BB790	HIT2	BD Biosciences	1:80
MR1	PE	26.5	BioLegend	1:10
CD137L (4-1BBL)	PE-Dz594	5F4	BioLegend	1:40
CD80	PE-Cy5	L37.4	BD Biosciences	1:10
CD19	PE-Cy5.5	SJ25-C1	Thermo Fisher	1:160
CD1c	AF647	F10/21A3	BD Biosciences	1:160
CD11c	AF700	B-ly6	BD Biosciences	1:320
HLA-DR	APC-H7	G46-6	BD Biosciences	1:40
Fix (1x eBioscience FOXP3 fixation buffer, 20 min, room temperature)				
Intracellular stain (1x eBioscience FOXP3 permeabilization buffer, 30 min, room temperature)				
CD68	BV711	Y1/82A	BD Biosciences	1:40

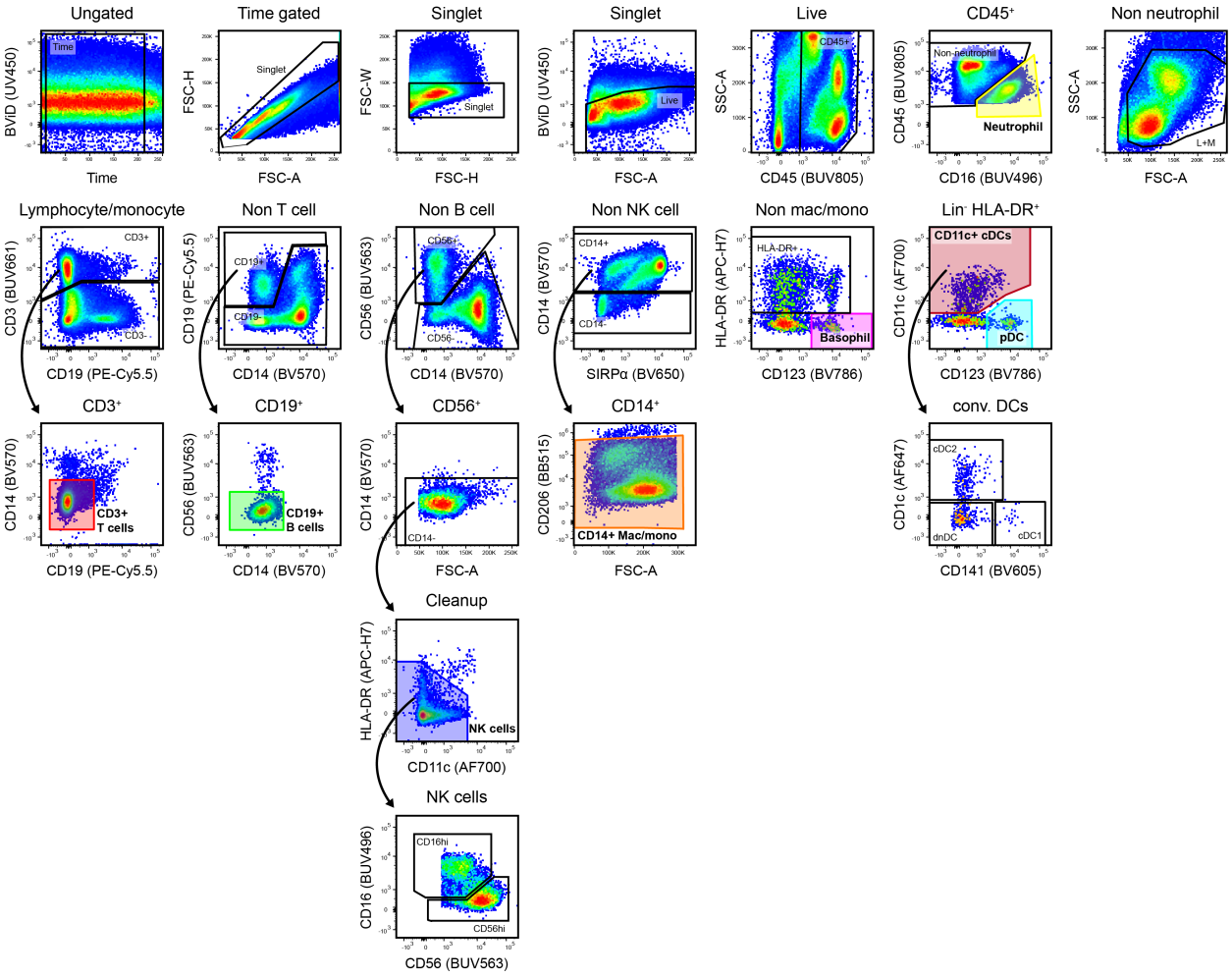

Figure 4.19 Gating strategy for major leukocyte populations for APC panels 1 and 2

Representative gating example for APC panels (shared backbone for major lineages) from cells freshly isolated from mPLAC

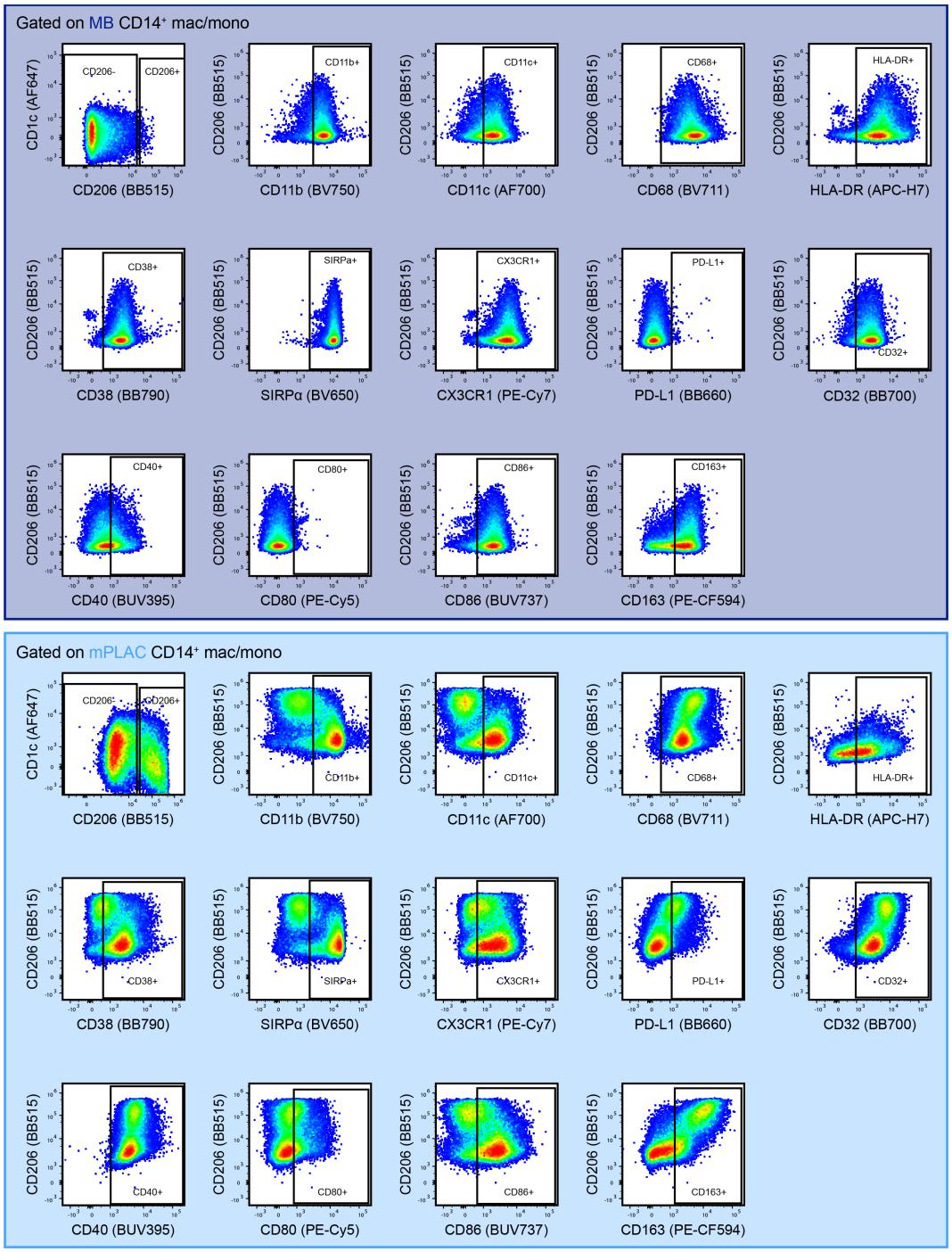

Figure 4.20 APC panel 1 gating strategy for CD14+ macrophage/monocyte phenotyping

Representative gating example for CD14+ macrophage/monocyte events from cells freshly isolated from MB (top) or mPLAC (bottom)

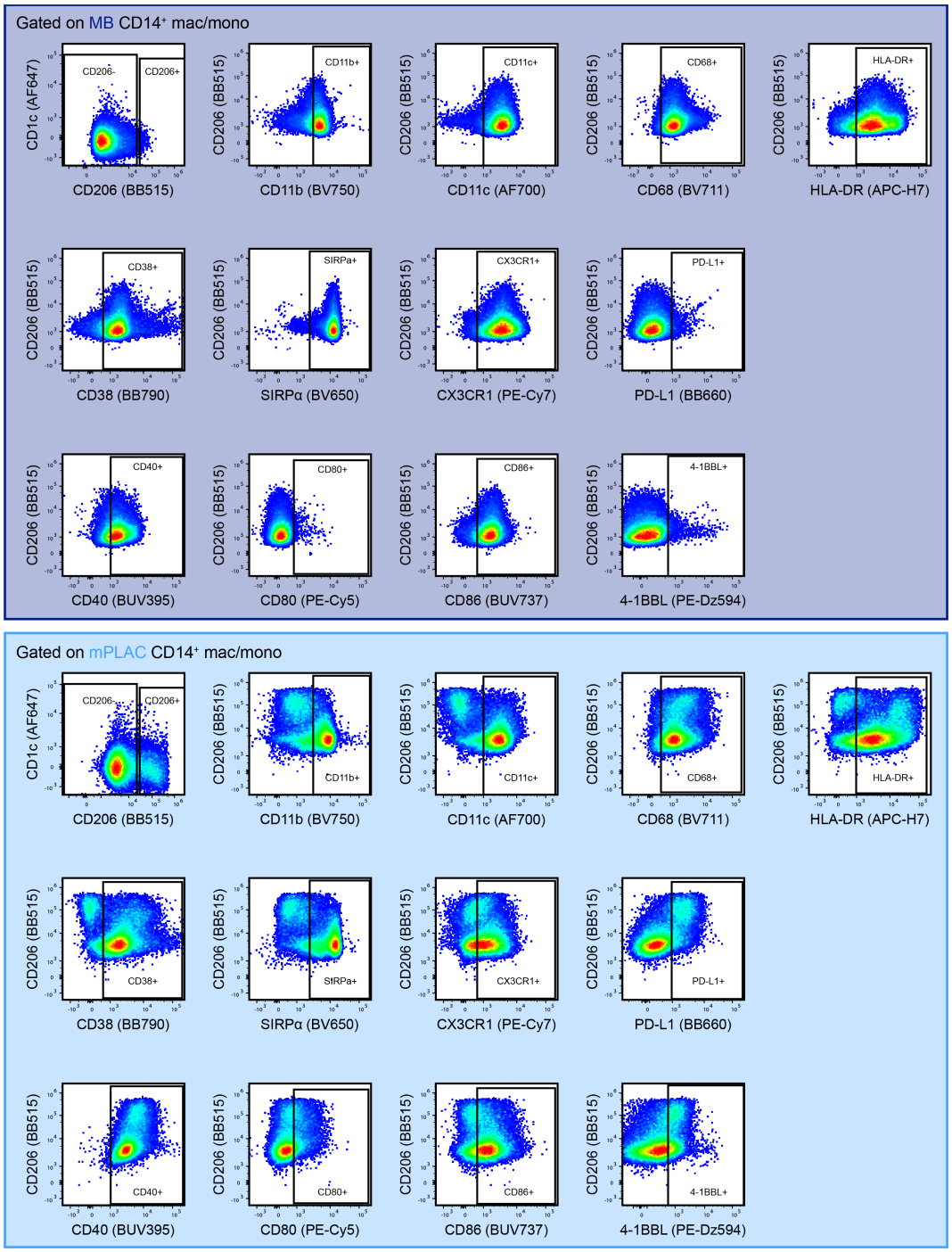

Figure 4.21 APC panel 2 gating strategy for CD14$^+$ macrophage/monocyte phenotyping

Representative gating example for CD14$^+$ macrophage/monocyte events from cells freshly isolated from MB (top) or mPLAC (bottom)

4.4.6 CyTOF tetramer screening

The Fred Hutchinson Cancer Research Center Immune Monitoring Core refolded HLA-A*01:01, HLA-A*02:01, HLA-A*03:01, HLA-A*11:01, and HLA-B*07:02 monomers with appropriate UV-cleavable peptides and biotinylated them (263). We labeled streptavidin (SA) with heavy metals as previously described (223). We purchased purified antibodies lacking carrier proteins, which we conjugated to heavy metals using DN3 polymers and according to protocols provided by Fluidigm.

We conducted multiplex tetramers staining in accordance with previously published protocols (264). Briefly, we labeled each tetramer with a combination of two different metal-labeled SAs. Using ten different SA conjugates (Table 4.10), we generated 45 possible combinations. We assigned each specific combination to a single peptide (Table 4.11, Table 4.12). We mixed SAs (50μg/mL, 30μL) in the assigned combination for each peptide in a 96-well plate. In another 96-well plate, we added 5μL of peptide (1mM) to 100μL of HLA monomer (0.1mg/mL, diluted in PBS), with a different peptide in each well. We exposed peptide-MHC plates to UV light for 10 min and then incubated at 4ºC overnight. After incubating, we tetramerized SAs (50μg/mL) to the assigned peptide-MHC complex by adding 3 additions of 10μL of each metal-labeled double-coded SA into peptide-MHC wells (3x 10μL) according to our coding scheme, with 10 min incubations between each addition. We then incubated tetramerized peptide-MHC complexes with 10μM free biotin (Avidity) for 10 min. We then combined all tetramers and concentrated in a 50-kDa Amicon filter (Millipore) to a final volume of 500μL. We added designated antibodies (1º surface stain, see Table 4.13), and adjusted the final cocktail volume to 1mL with PBS + 0.5% FBS and 0.02% sodium azide. Prior to use, we filtered the tetramer/antibody cocktail with a 0.1μm filter (Millipore).

We thawed cryopreserved MB and mPLAC samples where maternal HLA types were HLA-A*01:01, HLA-A*02:01, HLA-A*03:01, HLA-A*11:01, and/or HLA-B*07:02 in warm RP10 + 10μg/mL DNase. We stained samples in accordance with previously published protocols (264). Briefly, we stained cells with 1º surface stain cocktail (including tetramers) for 60 min at room temperature. We then conducted viability staining using 12.5μM cisplatin in 1x PBS for 10 min on ice. We prepared 2º surface stain antibody cocktails (Table 4.13) in advance, which we froze into multiple aliquots to minimize batch variance. We thawed and stained cells with this cocktail for 20 min on ice. Afterwards, we washed and fixed cells overnight in 2% PFA. We washed cells with 1x eBioscience FOXP3 permeabilization buffer, which we also used as a diluent for intracellular

antibody staining (30 min at room temperature). Prior to acquisition, we stained cells with Cell ID intercalator Ir (Fluidigm) for 10 min on ice and then washed 3x with Milli-Q H_2O. We then acquired samples using Helios (Fluidigm), analyzed using FlowJo v10, and conducted statistical testing with Prism v8.

Table 4.10 SA conjugates for HLA tetramerization and CyTOF screening

Reagent	Metal	Fluidigm metal kit
SA "1"	^{155}Gd	201155B
SA "2"	^{157}Gd	Trace Sciences*
SA "3"	^{159}Tb	201159B
SA "4"	^{161}Dy	201161B
SA "5"	^{163}Dy	201163B
SA "6"	^{164}Dy	201164B
SA "7"	^{167}Er	201167B
SA "8"	^{170}Er	201170B
SA "9"	^{173}Yb	201173B
SA "10"	^{174}Yb	201174B

*Isotope procured from Trace Sciences International

Table 4.11 SA tetramer combinations for HLA-A*01, -A*02, -A*03, and/or -B*07 donors

SA combo.	HLA	Antigen	Peptide
^{155}Gd, ^{157}Gd	A*01	CMV UL44	VTEHDTLLY
^{155}Gd, ^{159}Tb	A*01	CMV pp65	YSEHPTFTSQY
^{155}Gd, ^{161}Dy	A*01	HCV polyprotein	ATDALMTGY
^{155}Gd, ^{163}Dy	A*01	IAV NP	CTELKLSDY
^{155}Gd, ^{164}Dy	A*01	IAV PB1	VSDGGPNLY
^{155}Gd, ^{167}Er	A*01	AdV Hexon	TDLGQNLLY
^{155}Gd, ^{170}Yb	A*01	HSV1 UL46 (354–362)	ATDSLNNEY
^{155}Gd, ^{173}Yb	A*01	HSV1 UL48 (90–99)	SALPTNADLY
^{155}Gd, ^{174}Yb	A*01	HSV1 UL48 (479–488)	FTDALGIDEY
^{157}Gd, ^{159}Tb	A*02	CMV IE1	VLEETSVML
^{157}Gd, ^{161}Dy	A*02	CMV pp65	NLVPMVATV
^{157}Gd, ^{163}Dy	A*02	EBV LMP2A	CLGGLLTMV
^{157}Gd, ^{164}Dy	A*02	EBV BRLF1	YVLDHLIVV
^{157}Gd, ^{167}Er	A*02	EBV BLMF1	GLCTLVAML
^{157}Gd, ^{170}Yb	A*02	IAV M1	GILGFVFTL
^{157}Gd, ^{173}Yb	A*02	EBV LMP1-2	YLQQNWWTL
^{157}Gd, ^{174}Yb	A*02	EBV LMP1-1	YLLEMLWRL
^{159}Tb, ^{161}Dy	A*02	CMV pp65-2	QMWQARLTV
^{159}Tb, ^{163}Dy	A*02	Proinsulin precursor (15–24)	ALWGPDPAAA
^{159}Tb, ^{164}Dy	A*02	VZV IE62 (593–601)	ALWALPHAA
^{159}Tb, ^{167}Er	A*02	EBV BALF-4	FLDKGTYTL
^{159}Tb, ^{170}Yb	A*02	EBV BMRF-1	TLDYKPLSV
^{159}Tb, ^{173}Yb	A*02	MelanA/MART (26–35)	ELAGIGILTV
^{159}Tb, ^{174}Yb	A*02	MAGEA3 (271–279)	FLWGPRALV
^{161}Dy, ^{163}Dy	A*02	HSV1/2 UL25 (367–375)	FLWEDQTLL
^{161}Dy, ^{164}Dy	A*02	HSV1 UL47 (286-294)	FLADAVVRL
^{161}Dy, ^{167}Er	A*02	HSV1 UL47 (545–553)	RLLGFADTV
^{161}Dy, ^{170}Yb	A*03	EBV EMNA 3A	RLRAEAQVK
^{161}Dy, ^{173}Yb	A*03	HPV E6	IVYRDGNPY
^{161}Dy, ^{174}Yb	A*03	CMV IE-1	KLGGALQAK
^{163}Dy, ^{164}Dy	A*03	IAV PR8	ILRGSVAHK
^{163}Dy, ^{167}Er	A*03	HSV RS1 (1096–1105)	RLYPDAPPLR
^{163}Dy, ^{170}Yb	B*07	CMV pp65	RPHERNGFTVL
^{163}Dy, ^{173}Yb	B*07	CMV pp65	TPRVTGGGAM
^{163}Dy, ^{174}Yb	B*07	EBV BMRF1	RPQGGSRPEFVKL
^{164}Dy, ^{167}Er	B*07	EBV EBNA 3A	RPPIFIRRL
^{164}Dy, ^{170}Yb	B*07	EBV EBNA 6	QPRAPIRPI
^{164}Dy, ^{173}Yb	B*07	IAV NP	SPIVPSFDM
^{164}Dy, ^{174}Yb	B*07	IAV PB1	QPEWFRNVL
^{167}Er, ^{170}Yb	B*07	HSV ICP0 (698–706)	VPGWSRRTL
^{167}Er, ^{173}Yb	B*07	HSV1 UL21 (382–390)	VPRPDDPVL
^{167}Er, ^{174}Yb	B*07	HAV1 UL49 (281–290)	RPTERPRAPA
^{170}Yb, ^{173}Yb	A*02	SMCY/JARID1D	FIDSYICQV
^{170}Yb, ^{174}Yb	B*07	SMCY/JARID1D	SPSVDKARAEL
^{173}Yb, ^{174}Yb	A*02	CMV pp65	NLVPTVAML

Table 4.12 SA tetramer combinations for HLA-A*02 and/or -A*11 donors

SA combo.	HLA	Antigen	Peptide
^{155}Gd, ^{157}Gd	A*02	PCDH11Y	FLLENAAYLD
^{155}Gd, ^{159}Tb	A*02	USP9Y	LLMPAGVPLT
^{155}Gd, ^{161}Dy	A*02	DDX3Y	FLLDILGAT
^{155}Gd, ^{163}Dy	A*02	UTY	LLIADNPQL
^{155}Gd, ^{164}Dy	A*02	UTY	YLQQNTHTL
^{155}Gd, ^{167}Er	A*02	UTY	ALIDCNPCTL
^{155}Gd, ^{170}Yb	A*02	UTY	KLLSSGAFSA
^{155}Gd, ^{173}Yb	A*02	UTY	LLSSGAFSA
^{155}Gd, ^{174}Yb	A*02	SMCY/JARID1D	FIDSYICQV
^{157}Gd, ^{159}Tb	A*02	SMCY/JARID1D	KMAAFPETL
^{157}Gd, ^{161}Dy	A*02	SMCY/JARID1D	SLMASSPTSI
^{157}Gd, ^{163}Dy	A*02	SMCY/JARID1D	HLLTSPKPSL
^{157}Gd, ^{164}Dy	A*02	SMCY/JARID1D	NVMPVLDQSV
^{157}Gd, ^{167}Er	A*02	SMCY/JARID1D	LMASSPTSI
^{157}Gd, ^{170}Yb	NA	NA	NA
^{157}Gd, ^{173}Yb	NA	NA	NA
^{157}Gd, ^{174}Yb	NA	NA	NA
^{159}Tb, ^{161}Dy	A*02	CMV IE1	VLEETSVML
^{159}Tb, ^{163}Dy	A*02	CMV pp65	NLVPMVATV
^{159}Tb, ^{164}Dy	A*02	EBV LMP2A	CLGGLLTMV
^{159}Tb, ^{167}Er	A*02	EBV BRLF1	YVLDHLIVV
^{159}Tb, ^{170}Yb	A*02	EBV BLMF1	GLCTLVAML
^{159}Tb, ^{173}Yb	A*02	IAV M1	GILGFVFTL
^{159}Tb, ^{174}Yb	A*02	EBV LMP1-2	YLQQNWWTL
^{161}Dy, ^{163}Dy	A*02	EBV LMP1-1	YLLEMLWRL
^{161}Dy, ^{164}Dy	A*02	CMV pp65-2	QMWQARLTV
^{161}Dy, ^{167}Er	A*02	Proinsulin precursor (15–24)	ALWGPDPAAA
^{161}Dy, ^{170}Yb	A*02	VZV IE62 (593–601)	ALWALPHAA
^{161}Dy, ^{173}Yb	A*02	EBV BALF-4	FLDKGTYTL
^{161}Dy, ^{174}Yb	A*02	EBV BMRF-1	TLDYKPLSV
^{163}Dy, ^{164}Dy	A*02	MelanA/MART (26–35)	ELAGIGILTV
^{163}Dy, ^{167}Er	A*02	MAGEA3 (271–279)	FLWGPRALV
^{163}Dy, ^{170}Yb	A*02	HSV1/2 UL25 (367–375)	FLWEDQTLL
^{163}Dy, ^{173}Yb	A*02	HSV1 UL47 (286–294)	FLADAVVRL
^{163}Dy, ^{174}Yb	A*02	HSV UL47 (545–553)	RLLGFADTV
^{164}Dy, ^{167}Er	A*02	RCC c-MET (654–662)	YVDPVITSI
^{164}Dy, ^{170}Yb	A*02	RCC MUC1 (950–958)	STAPPVHNV
^{164}Dy, ^{173}Yb	A*02	RCC (146–154) (A02)	ALCNTDSPL
^{164}Dy, ^{174}Yb	A*02	RCC Survivin (96–104)	LTLGEFLKL
^{167}Er, ^{170}Yb	A*02	RCC EphA2 (58)	IMNDMPIYM
^{167}Er, ^{173}Yb	A*11	EBV EBNA 3B	AVFDRKSDAK
^{167}Er, ^{174}Yb	A*11	EBV EBNA 4	IVTDFSVIK
^{170}Yb, ^{173}Yb	A*11	EBV BRFL1	ATIGTAMYK
^{170}Yb, ^{174}Yb	A*11	EBV LMP2	SSCSSCPLSK
^{173}Yb, ^{174}Yb	A*11	IAV H1N2 PB2	KVYKTYFEK

Table 4.13 CyTOF tetramer screen staining panel

Reagent	Conjugate	Clone	Vendor	Metal	Fluidigm metal kit	Reagent dilution
Tetramer and 1º Surface stain (1x PBS + 0.5% FBS, 0.02% sodium azide; 60 min, room temperature)						
TCRγδ	PE	5A6.E9	ThermoFisher	NA	NA	1:200
CD8	Pure	RPA-T8	BioLegend	^{111}Cd	201111A	1:100
CXCR3	Pure	G025H7	BioLegend	^{158}Gd	201158B	1:200
PD-1	Pure	eBioJ105	ThermoFisher	^{160}Gd	201160B	1:200
CXCR5	Pure	RF8B2	BD Biosciences	^{165}Ho	201165B	1:100
CCR7	Pure	150503	R&D Systems	^{168}Er	201168B	1:100
CCR5	^{171}Yb	NP-6G4	Fluidigm	^{171}Yb	NA	1:100
Viability stain (1x PBS diluent, 10 min, on ice)						
Cisplatin	NA	NA	Fluidigm	$^{194/195}$Pt	NA	1:8000
2º Surface stain (1x PBS + 0.5% FBS, 0.02% sodium azide; 20 min, on ice)						
CD4	Pure	RPA-T4	BioLegend	^{110}Cd	201110A	1:100
CD14	Pure	M5E2	BioLegend	^{112}Cd	201112A	1:50
CD19	Pure	HIB19	BioLegend	^{113}Cd	201113A	1:50
CD56	Pure	NCAM16.2	BD Biosciences	^{114}Cd	201114A	1:50
CD45	^{89}Y	HI30	Fluidigm	^{89}Y	NA	1:100
CD57	Pure	HNK-1	BioLegend	^{115}In	Trace Sciences*	1:200
CLA	Pure	HECA-452	BioLegend	^{141}Pr	201141B	1:200
HLA-DR	Pure	L243	BioLegend	^{142}Nd	201142B	1:100
ITB7	Pure	FIB504	BioLegend	^{143}Nd	201143B	1:200
TIGIT	Pure	741182	R&D Systems	^{144}Nd	201144B	1:50
PE	Pure	PE001	BioLegend	^{146}Nd	201146B	1:200
CD69	Pure	FN50	BioLegend	^{147}Sm	201147B	1:100
CD45RO	Pure	UCHL1	BioLegend	^{148}Nd	201148B	1:200
CD161	Pure	HP-3G10	BioLegend	^{149}Sm	201149B	1:100
KLRG1	Pure	13F12F2	ThermoFisher	^{150}Nd	201150B	1:200
CD27	Pure	LG.7F9	ThermoFisher	^{151}Eu	201151B	1:200
CD137	Pure	4B4-1	BioLegend	^{152}Sm	201152B	1:100
CD103	Pure	B-Ly7	ThermoFisher	^{153}Eu	201153B	1:200
CD3	Pure	UCHT1	BioLegend	^{154}Sm	201154B	1:200
TIM-3	Pure	F38-2E2	BioLegend	^{162}Dy	201162B	1:200
CD71	Pure	CY1G4	BioLegend	^{166}Er	201166B	1:200
CD45RA	Pure	HI100	BioLegend	^{169}Tm	201169B	1:200
CD39	Pure	A1	BioLegend	^{172}Yb	201172B	1:100
CD38	Pure	HIT2	BioLegend	^{176}Yb	201176B	1:100
CD16	^{209}Bi	3G8	Fluidigm	^{209}Bi	NA	1:100
Fix (2% PFA, overnight, 4ºC)						
Intracellular stain (1x eBioscience FOXP3 permeabilization buffer, 30 min, room temperature)						
Granzyme K	Pure	GM6C3	Santa Cruz	^{145}Nd	201145B	1:100
CTLA-4	Pure	BNI3	BD Biosciences	^{156}Gd	201156B	1:200
Perforin	Pure	B-D48	Abcam	^{175}Lu	201175B	1:200
DNA intercalator stain (1x PBS, 10 minutes, on ice)						
Cell ID Ir	NA	NA	Fluidigm	$^{191/193}$Ir	NA	1:4000

*Isotope procured from Trace Sciences International

Donor 3 MB

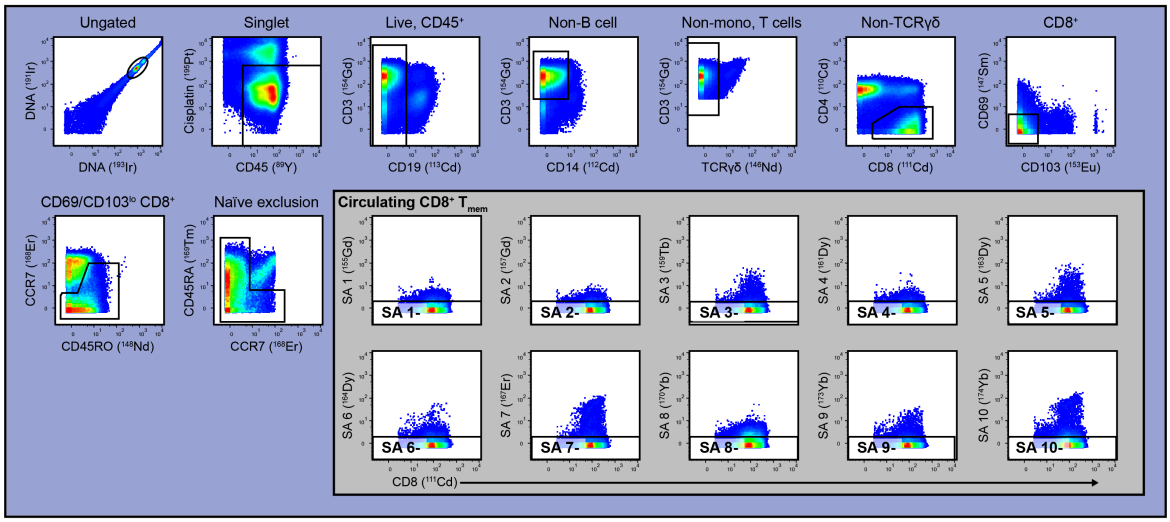

Donor 3 mPLAC

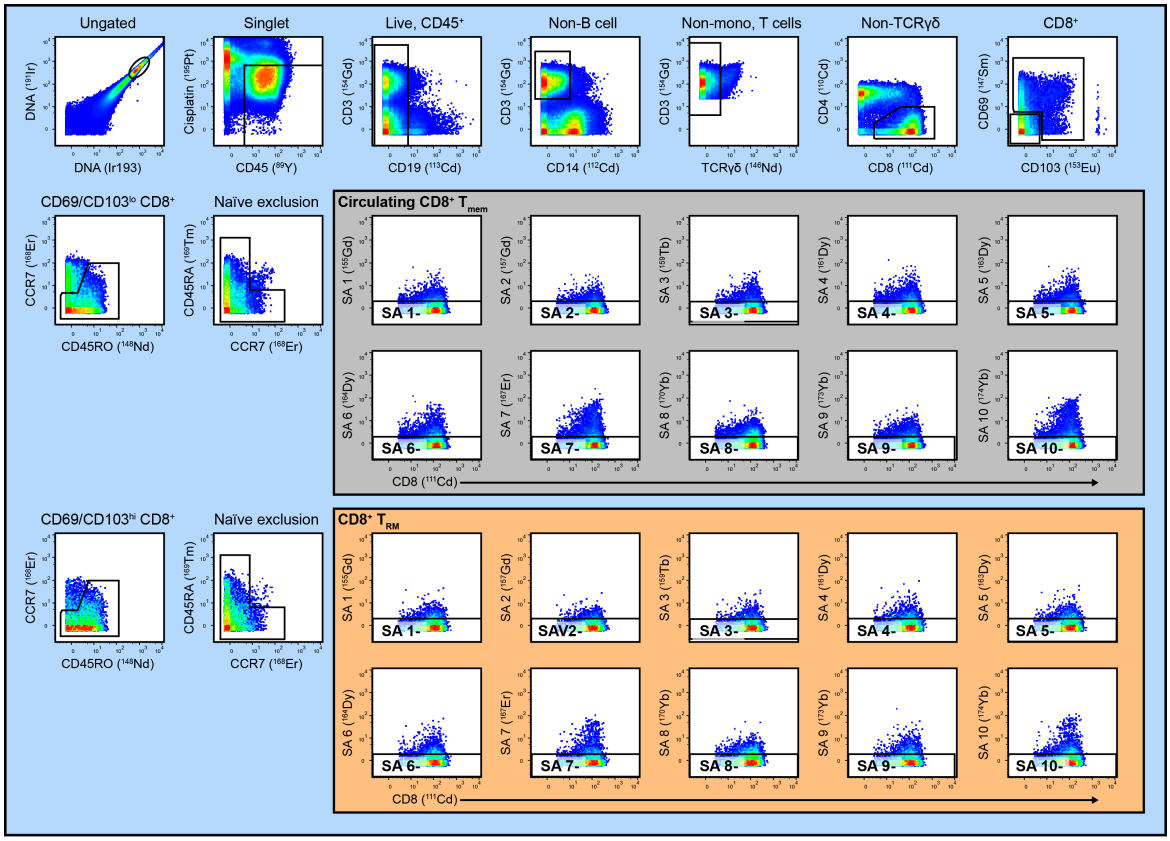

Ag-specific population identificaiton

Boolean gating combining all subset-specific events negative for all but two of surveyed SAs

Gated on:
SA 1-, SA 2-, SA 3-, SA 4-, SA 5-, SA 6-, SA 8-, SA 9-

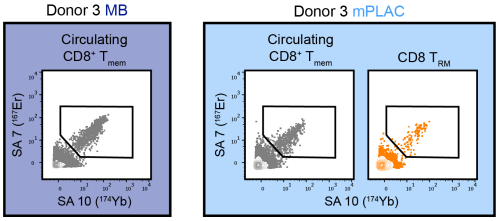

Gated on:
SA 1-, SA 2-, SA 3-, SA 4-, SA 5-, SA 6-, SA 8-, SA 10-

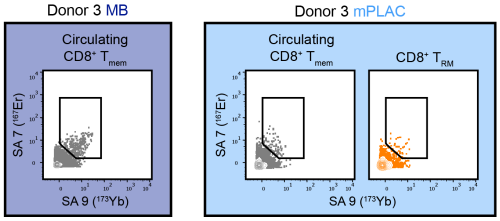

Figure 4.22 Gating strategy for CyTOF tetramer screen staining panel

We identified circulating memory (grey) and resident memory (orange) $CD8^+$ T cells in cryopreserved MB (dark blue) and mPLAC (light blue) samples. Within these subpopulations, we gated tetramer-negative populations, which we combined all but two (in all possible combinations) using Boolean gating. Within these Booleans, we measured tetramer-SA staining for the two excluded SAs to identify Ag-specific $CD8^+$ T cells within each tissue and memory subset

4.4.7 Single-cell library preparation and sequencing

We generated cDNA libraries from sorted cell populations ($CD8^+$ T cell and $CD45^+$ $CD3^-$ $CD19^-$ HLA-DR^+ APCs) using the Chromium Single Cell 3' Reagent Kits (v2 protocol) or the Single Cell 5' Reagent Kit (v1 protocol) (10x Genomics). We used the Chromium Controller (10x Genomics) to generate oil emulsion droplets of single cells with barcoded gel beads and reverse transcriptase mix. We generated barcoded cDNA within these droplets, and purified cDNA using DynaBeads MyOne Silane magnetic beads (ThermoFisher). We amplified cDNA by PCR (10 cycles) using reagents from the Chromium Single Cell 3' Reagent Kit (v2) or the GEX Reagent kit (v1). We purified amplified cDNA with SPRIselect magnetic beads (Beckman Coulter) according to their protocol. We enzymatically fragmented and size-selected cDNA prior to library construction, which we conducted by performing end repair, A-tailing, adaptor ligation, and PCR (12 cycles). In order to assess library quality, we used Agilent 2200 TapeStation with High Sensitivity D5000 ScreenTape (Agilent). We assessed library quantities using digital droplet PCR (ddPCR) with the Library Quantification Kit for Illumina TruSeq (BioRad). We diluted libraries to 2nM and performed paired-end sequencing using a HiSeq 2500 (Illumina).

4.4.8 Single-cell RNA sequencing analysis

We utilized the R package, Seurat (265), for all downstream analysis, following general guidelines for analyzing scRNAseq data. For our analyses, we only included cells that had ≥ 200 genes, and depending on sample distribution, ≤ 10% mitochondrial genes. We merged all acquired samples into a single Seurat object. We then used a natural log normalization with a scale factor of 10,000, determined variable genes using the vst method, and z-score scaled. We used principal component analysis (PCA) to generate 50 PCs which were used to calculate UMAPs (208), for which we created graph-based clusters using a resolution between 0.2 and 0.6. For non-biased cell annotation, we applied SingleR (266) and used the expression of typical lineage transcripts to verify the cell label annotation. For all differential gene expression analyses, we utilized the

Seurat implementation of MAST (model-based analysis of single-cell transcriptomes) (267) with the number of unique molecular indexes (UMIs) included as a covariate (proxy for cellular detection rate (CDR)) in the model. NicheNet (227) analysis was adapted from the vignette described at https://github.com/saeyslab/nichenetr containing T cells and APCs (described above). We subset these populations to contain only immune sorted from mPLAC biopsies. We set different $CD8^+$ T cell subsets as "receiver" (i.e., resident or circulating memory $CD8^+$ T cell clusters) and all myeloid cell cluster (except the mast cell cluster) as "sender" populations. We conducted a DE gene test to find genes enriched in mPLAC over MB samples. We performed NicheNet analysis based on the vignette to infer receptors, filtered for documented links, and generated a circos plot of the ligand-receptor interactions for the top 20 ligands within the respective cellular populations. Main scripts used for data processing are available at https://github.com/Jami-Erickson.

4.4.9 Tissue collection for protein isolation

We collected 0.5cm-depth mPLAC and fPLAC biopsies and homogenized tissues in lysing buffer (1x PBS + 0.05% Tween 20 (ThermoFisher)) at 1g tissue/5mL buffer. We centrifuged samples at 10,000g for 5 min at 4ºC, collected lysate supernatants, and stored at -80ºC.

4.4.10 Cytokine analysis

We provided plasma, tissue lysate supernatants, and cell culture supernatants to the Fred Hutchinson Cancer Research Center Immune Monitoring Core for ELISA (TGF-β1) or multiplex cytokine analysis (all other factors). Multiplex measurements were analyzed on a Luminex 200 (Luminex Corporation).

4.4.11 Immunofluorescence

We collected full-depth (i.e., spanning the maternal and fetal surfaces) biopsies from the placenta and fixed overnight in Cytofix buffer (BD Biosciences) diluted 1:4 in 1x PBS. We dehydrated fixed tissues in sterile-filtered 20% w/v sucrose (Sigma Aldrich), embedded in Tissue-Tek OCT media (Sakura Finetek), froze in the vapor phase of LN_2, and stored at -80ºC. We cut 8–10 µm sections of tissues using a CM1950 cryostat (Leica), dried slides at room temperature overnight, and then

stored at -80ºC. On the day of staining, we incubated slides in -20ºC acetone for 5 min, dried slides, and outlined tissues with a hydrophobic pap pen. We rehydrated slides in 1x PBS for 5 min, and then incubated slides in blocking buffer (1x TBS + 5% normal human serum) for 30 minutes. We conducted stains as described in Table 4.14 and washed slides with TBS-T (1x TBS + 0.05% Tween-20). We mounted slides in ProLong Gold (ThermoFisher), cured slides overnight, and imaged on a SP8 confocal microscope (Leica) at 20x magnification.

Table 4.14 Placental immune infiltrate immunofluorescence panel

Tissue: placenta fixed in 1:4 BD Cytofix:1xPBS overnight				
Reagent	**Conjugate**	**Clone**	**Vendor**	**Dilution**
1º stain (1x TBS + 5% normal human serum diluent) 60 min, room temperature				
Mouse anti-human CD8	AF647	RPA-T8	BD Biosciences	1:100
Mouse anti-human CD163	PE-CF594	GHI/61	BD Biosciences	1:100
Rabbit anti-human CD45	Pure	EP322Y	Abcam	1:100
2º stain (1x TBS + 5% normal human serum diluent) 60 min, room temperature				
Donkey anti-rabbit IgG	Dy488	Poly4064	BioLegend	1:200
Nuclear intercalator stain (1x PBS diluent) 5 min, room temperature				
DAPI	NA	NA	ThermoFisher	1ng/mL

4.4.12 Metabolomics sample preparation

We prepared a reference library of tryptophan (Trp) metabolites for our liquid chromatography mass spectrometry (LC-MS) analyses by dissolving select metabolites in HPLC grade H_2O at ~0.5mM (cinnabarinic acid) or ~5mM (all other metabolites) (Table 4.15).

We prepared plasma samples for LC-MS by adding 6µL plasma to a microcentrifuge tube with 200µL ice cold HPLC-grade 80% MeOH with 250µM valine D8 standard as a loading control. We vortexed samples for 10 minutes at 4ºC, then centrifuged at 17,000g for 10 min at 4ºC. We transferred 100µL of supernatant to a new microfuge tube, with 50µL moved to an LC-MS vial for metabolomics analysis.

We prepared flash-frozen mPLAC and fPLAC biopsies by weighing out 30mg of frozen tissue, which were transferred to a microcentrifuge tube and maintained in LN_2. We homogenized tissues within microtubes with a miniature LN_2-cooled mortar and pestle. To extract metabolites, we added 900µL ice-cold HPLC-grade 80% MeOH with 250µM valine D8 loading control and

vortexed samples for 10 min at 4ºC. We removed debris by centrifuging tubes at 17,000g for 10 minutes at 4ºC, and transferred 700µL of supernatant to a new microcentrifuge tube, with 50µL moved to a LC-MS vial for metabolomics analysis.

Table 4.15 Trp metabolite LC-MS standards

Metabolite name	Vendor	Molecular weight	Mass weighed (mg)	Molarity (mM)
Pool 1, dissolved in 15mL H_2O				
Indole	Sigma	117.15	8.92	5.07611325
Anthranilic acid	Sigma	137.14	10.25	4.9827427
Indoleacetic acid	Sigma	175.18	13.08	4.97773718
5-Hydroxyindoleacetic acid	Sigma	191.18	14.32	4.99354884
L-Kynurenine	Sigma	208.21	15.5	4.96293806
Cinnabarinic acid	Sigma	300.22	1.99	0.44189816
Pool 2, dissolved in 9.08mL H_2O				
Nicotinic acid	Sigma	123.11	5.54	4.95599187
3-Hydroxyanthranilic acid	Sigma	153.14	6.96	5.00535343
Serotonin (HCl salt)	Sigma	212.68	9.66	5.00224117
Indolepyruvate	Sigma	203.19	9.16	4.96486329
5-Hydroxytryptophan	Sigma	220.22	9.99	4.9960052
Pool 3, dissolved in 15mL H_2O				
Picolinic acid	Sigma	123.11	9.3	5.03614654
Tryptamine	Sigma	160.22	12.15	5.05554862
Kynurenic acid	Sigma	189.17	14.26	5.02546211
L-Tryptophan	Sigma	204.23	15.33	5.00416197
3-Hydroxykynurenine	Sigma	224.2133	16.6	4.93577619
Pool 4, dissolved in 9.08mL H_2O				
Trigonelline (HCl salt)	Sigma	173.6	7.86	4.98639842
Quinolinic acid	Sigma	167.12	7.6	5.00840357
Indole-3-propionic acid	Sigma	189.21	8.59	4.999922
Xanthurenic acid	Fisher	205.17	9.28	4.9813639
Melatonin	Sigma	232.28	10.56	5.00686927

4.4.13 LC-MS metabolomics

We transferred samples into LC-MS vials for measurement by LC-MS. We performed metabolite quantitation using a Q Exactive HF-X Hybrid Quadrupole-Orbitrap Mass Spectrometer equipped with an Ion Max API source and H-ESI II probe, coupled to a Vanquish Flex Binary UHPLC system (ThermoFisher). We completed mass calibrations at a minimum of every 5 days in both the positive and negative polarity modes using LTQ Velos ESI Calibration Solution (Pierce). We

chromatographically separated samples by injecting a sample volume of 1µL into a SeQuant ZIC-pHILIC Polymeric column (150 x 2.1mm 5µM, EMD Millipore). We set flow rates to 150µL, autosampler temperature to 10ºC, and column temperature to 30ºC. Our Mobile Phase A consisted of 20mM ammonium carbonate an 0.1% (v/v) ammonium hydroxide, while Mobile Phase B consisted of 100% acetonitrile. Our samples were gradient eluted (%B) from the column as follows: 0–20 min: linear gradient from 80% to 20% B; 20–24 min: hold at 20% B; 24–24.5 min: linear gradient from 20% to 85% B; 24.5 min–end: hold at 85% B until equilibrated with ten column volumes. Mobile We directed Mobile Phase into the ion source with the following parameters: sheath gas = 45, auxiliary gas = 15, sweep gas = 2, spray voltage = 2.9 kV in the negative mode or 3.5 kV in the positive mode, capillary temperature = 300ºC, RF level = 40%, auxiliary gas heater temperature = 325ºC. We conducted mass detection with a resolution of 240,000 in full scan mode, with an AGC target of 3,000,000 and maximum injection time 250 msec. We detected metabolites over a mass range of 70-1050 *m*/*z* in full scan mode with polarity switching. We quantitated all metabolites using Tracefinder 4.1 (ThermoFisher) referencing our in-house kynurenine pathway metabolite standards libraries using ≤ 5 ppm mass error.

4.5 Acknowledgements

We thank the UWMC Labor and Delivery staff and study participants for their generosity. We thank our study coordinators, Caitlin Laughney and Chenee Holcomb, and the Northwest BioSpecimen, specifically Cody Avalos, Marlie Reinmuth, and Piper Driskell. We also thank Fred Hutch Shared Resources for technical assistance and Alec Wilkens, Antje Heit, and Kimberly Smythe for helpful discussions. This work was supported by NIH grants R21 AI144677 (to M.P. and R.S.), F31 HD098769 (to N.J.M.), TL1 TR002318 (to N.J.M.), and National Cancer Institute grant F99 CA245735 (to N.J.M.). N.J.M. is a Leslie and Pete Higgins Achievement Rewards for College Scientists Fellow and Dr. Nancy Herrigel-Babienko Memorial Scholar, C.S.D. is a Hartwell Fellow.

Chapter 5. Concluding remarks

Despite the intrinsic differences between the languages of TCR and inflammation, we show that both means of communication can beget a number of overlapping $CD8^+$ T_{mem} fates.

5.1 Inflammation-mediated bystander activation as a conserved component of the innate-like immune response

TCR ligation is the primary method to induce cytotoxicity in $CD8^+$ T_{mem}, ensuring specificity in downstream T cell-mediated killing (268). But inflammation can also beget a cytotoxic phenotype in $CD8^+$ T_{mem} (vis-à-vis IFNγ secretion and GzmB upregulation). But some have suggested that inflammation-mediated cytotoxicity is of little significance (17), for it has been understood best during rare instances of profound and/or prolonged inflammation (11-13, 34, 39, 40). On the contrary, we demonstrate that bystander activation is oft leveraged by the immune system, including during acute, localized inflammation. Specifically, fast-acting CXCR3-dependent mechanisms which recruit Ag-specific $CD8^+$ T_{mem} (110) also draw bystander $CD8^+$ T_{mem} towards the early immune response(6). While this positions Ag-specific $CD8^+$ T_{mem}, should they exist, to rapidly sense and kill infected targets via their TCRs, it also pulls bystander $CD8^+$ T_{mem} towards elevated levels of bystander-activating cytokines (like IL-12, IL-15, and IL-18). As a result, bystander $CD8^+$ T_{mem} sense the generalized “danger” signal of inflammation and become cytotoxic at the site of insult. This is particularly important to consider during a primary infection (i.e., when Ag-specific CD8 T cell memory does not yet exist). In the absence of memory, this localized, inflammation-dependent bystander-mediated killing program buys time for the Ag-specific T cell response (which takes days to mount) by limiting pathogen burden during the first days of infection (likely via GzmB degranulation) (3). At the same time, IFNγ secreted by activated bystander $CD8^+$ T_{mem} revs up the subsequent Ag-specific T cell response by enhancing APC functions (e.g., phagocytosis, Ag presentation, and co-stimulation) (9). Thus, the language of inflammation could be used as a “fall back” when Ag-specific signals cannot be rapidly integrated.

5.2 Inflammation as a different call to arms

While communication via TCR or inflammation has a functional parallel (i.e., $CD8^+$ T_{mem} cytotoxicity), we show they do not wholly overlap. NFAT inhibitors abrogate the expression of IFNγ in both mouse and human $CD8^+$ T_{mem} (and in mice, GzmB) after TCR ligation, but fail to impair IFNγ and GzmB induced by inflammation (specifically IL-12, IL-15, and IL-18 in combination). These mechanistic differences in integrating signals likely explain the truncated functionality of $CD8^+$ T_{mem} activated by inflammation: unlike TCR signals, inflammatory cues (specifically, combinations of IL-12, IL-15, and IL-18 or IL-6, IL-15, and IL-18) fail to induce TNFα, IL-2, or IL-17. Can these molecules be elicited by other cytokines, or are they restricted to TCR-mediated responses due to their reliance on NFAT? Further work will be necessary to determine how other non-TCR signals could control effector molecule expression in bystander activated $CD8^+$ T_{mem}. Despite their limited functional repertoire, we show here that bystander activated $CD8^+$ T_{mem} are still potent effectors. In vitro stimulation of $CD8^+$ T_{mem} with IL-6, IL-15, and IL-18 in combination leads to IFNγ secretion that rapidly rises to levels seen after TCR stimulation. Further, we observe kinetics that suggest inflammation-mediated IFNγ secretion could surpass that of TCR-stimulated $CD8^+$ T_{mem}. This potency warrants concern, as $CD8^+$ T_{mem} effector functions are often controlled by a myriad of regulatory programs to prevent autoimmunity.

Though TCR-mediated activation is potent, cell-intrinsic and -extrinsic signals can curb TCR-dependent effector programs (182, 239). But how is bystander activation terminated? Particularly since bystander activation is controlled by both different inputs (inflammation) and downstream signaling molecules and transcription factors. While inflammation may be the lynchpin to bystander activation, leading to uniform upregulation of IFNγ and GzmB in vitro, this is not the case in vivo. We show that during *L. monocytogenes* infection, IFNγ expression is limited to the first 24 hours of infection, while GzmB increases in the following days (6). While one could argue that this may reflect a changing milieu of pro-inflammatory cytokines, we observe other phenotypic changes that accompany bystander activation that suggest regulation. Specifically, we observe the expression of PD-1 and TOX, molecules involved in curtailing TCR-mediated functions, upregulated in bystander-activated $CD8^+$ T_{mem} (254); however, more work is necessary to discern the importance of these proteins in vivo.

5.3 Regional dialects of inflammation and bystander activation

Ag-nonspecific $CD8^+$ T cells either within or emigrating from the periphery have been the center of most studies on bystander activation. This has been shaped, to some degree, by scientific tools at hand. For instance, many mouse models use animals housed in specific pathogen-free conditions, leading to T cell distributions more like those of human neonates, rather than adults (161). A consequence of this is the absence of conventional memory populations, including tissue resident memory T cells (T_{RM}), which occupy and survey tissue barriers without recirculating in blood (159, 213, 217, 269). Further, many studies have focused on bystander activation caused by systemically-delivered (i.e., intravenously) pathogens (5, 6, 8-10, 32). Lastly, procuring solid tissues (either healthy or diseased) from human volunteers is logistically challenging compared to peripheral blood draws. Though these limitations exist, a select number of studies have found bystander $CD8^+$ T_{RM} in healthy and infected tissues (56) as well as solid tumors (41). Here, we show that bystander $CD8^+$ T_{RM} also exist at the term maternal-fetal interface (MFI).

The existence of bystander $CD8^+$ T_{RM} at the MFI is surprising, as T_{RM} retention is thought to rely on TCR stimulation with cognate Ag (91, 149, 150, 249-253)—yet Ag presentation is impaired at the MFI (188). We chose to test whether generalized signals could position bystander $CD8^+$ T_{mem} to become tissue resident, as we observed that specific bystander $CD8^+$ populations (i.e., those with defined TCR specificity) were at similar frequencies within T_{RM} and circulating memory pools. We found that pro-inflammatory cytokines are elevated in tissues like the MFI at homeostasis that T cells can ultimately sense. Though these cytokines can bystander activate $CD8^+$ T_{mem} (i.e., lead to the acquisition of cytotoxicity), we also demonstrate that they induce the expression of a suite of co-receptors including 4-1BB, which is often positioned as a marker of recent TCR stimulation (98). When engaged to its ligand (4-1BBL), 4-1BB is thought to promote memory T cells to adopt a tissue-resident fate (92, 234). At the MFI, macrophages expressing high levels of 4-1BBL can engage cytokine-induced 4-1BB on $CD8^+$ T cells and are often found in contact with various lymphocytes.

But why does homeostatic inflammation necessary for maintaining T_{RM} (150, 257) fail to lead to pathologies or aberrant bystander activation? After all, the cytokines we find elevated at placental tissues lead to IFNγ secretion by bystander $CD8^+$ T_{mem} when used in vitro. But we show here that other signals can regulate bystander $CD8^+$ T_{mem} cytotoxicity without forfeiting cellular activation. Specifically, levels of the cytokine, TGF-β1, and the tryptophan metabolite, kynurenine, are

elevated at the MFI and can selectively limit the effector functions of bystander-activated $CD8^+$ T_{mem} but spare activation (i.e., CD69 upregulation) and co-receptor expression (4-1BB, etc.). Thus, while inflammation is a common language for $CD8^+$ T_{mem}, how these T cells respond to inflammation varies on a regional basis. These "regional dialects" result from other signals within the tissue microenvironment, including, but not limited to, other cytokines and metabolites. This may explain the dichotomous outcomes of inflammation at various sites in the body. For instance, lung $CD8^+$ T_{RM} can limit disease when activated by inflammation (56), while exogeneous inflammation has limited effect on $CD8^+$ T_{RM} in tumors (84). Further work will be necessary to parse the full gamut of generalized signals that bystander $CD8^+$ T_{mem} can integrate.

5.4 A path to better command bystander T cells

There is significant therapeutic potential in harnessing the cytotoxic abilities of bystander $CD8^+$ T cells once they have been activated. But effectively commanding these cells has remained elusive. For instance, leveraging bystander $CD8^+$ T_{mem} as an anti-tumor therapeutic has yet been actualized. A study from the Masopust lab showed that bystander $CD8^+$ T_{mem} could promote tumor clearance. However, inflammation-mediated activation alone had little effect on tumor growth—substantial bystander-mediated tumor clearance was only seen when bystander $CD8^+$ T_{mem} were activated via their TCR with non-tumor cognate Ag (84). This is hard to therapeutically translate to humans due to the challenge of "talking" to these bystander T cells via their TCRs. The TCR repertoire (and subsequent antigenic specificity) in humans is highly diverse, shaped by the host's infection history and genetics. But we show that regulatory networks of cytokines and metabolites selectively limit inflammation-mediated, but not TCR-mediated effector responses in bystander-activated $CD8^+$ T_{mem}. Could these, too, be responsible for the Masopust lab's observations of poor bystander-mediated tumor clearance after administration of inflammation? If so, we could broadly activated bystander $CD8^+$ T_{mem} to kill (without the limitations of personalized, TCR-directed therapies) by blocking the sensing of these regulatory molecules.

While enhancing the cytotoxity of intratumoral bystander $CD8^+$ T_{mem} may prove beneficial to host, one must note that that bystander-mediated cytotoxicity is a double-edged sword (36). The regulatory "brakes" that may be released to enhance tumor clearance could potentially be leveraged in other contexts. For instance, we may be able to limit bystander-mediated immunopathology during inflammatory diseases by "applying the brakes" by enhancing TGF-β1

and/or kynurenine signaling. Further work will be necessary to test how widely TGF-β1 and kynurenine are used to restrain bystander-mediated cytotoxicity across tissue types and disease states to determine if this could be broadly implemented across multiple disease types and/or clinically viable.

5.5 Towards a more complete immunologic lexicon

As most T_{mem} express receptors for pro-inflammatory cytokines, inflammation is a widely understandable alarm, forgoing esoteric TCR-Ag interactions that can only alert a select few T cell clones during insult. But inflammation is not a simple command to activate killing programs—it is but a part of a complex language of generalized signals that serve as a common tongue for T cells. This work demonstrates that chemokines (which recruit T cells to sites of inflammation) and anti-inflammatory cytokines and metabolites (which dampen effector functions without affecting activation) are, too, part of this collective language. While these represent new and exciting ways in which we can interact with and ultimately command immune cells, it also suggests we have only scratched the surface when it comes to understanding the complete vernacular of immune cells.

BIBLIOGRAPHY

1. Prlic M, Williams MA, Bevan MJ. Requirements for CD8 T-cell priming, memory generation and maintenance. Curr Opin Immunol. 2007;19(3):315-9. Epub 2007/04/17. doi: 10.1016/j.coi.2007.04.010. PubMed PMID: 17433873.

2. Moran AE, Holzapfel KL, Xing Y, Cunningham NR, Maltzman JS, Punt J, Hogquist KA. T cell receptor signal strength in Treg and iNKT cell development demonstrated by a novel fluorescent reporter mouse. J Exp Med. 2011;208(6):1279-89. Epub 2011/05/25. doi: 10.1084/jem.20110308. PubMed PMID: 21606508; PMCID: PMC3173240.

3. Chu T, Tyznik AJ, Roepke S, Berkley AM, Woodward-Davis A, Pattacini L, Bevan MJ, Zehn D, Prlic M. Bystander-activated memory CD8 T cells control early pathogen load in an innate-like, NKG2D-dependent manner. Cell Rep. 2013;3(3):701-8. Epub 2013/03/26. doi: 10.1016/j.celrep.2013.02.020. PubMed PMID: 23523350; PMCID: PMC3628815.

4. Selin LK, Nahill SR, Welsh RM. Cross-reactivities in memory cytotoxic T lymphocyte recognition of heterologous viruses. J Exp Med. 1994;179(6):1933-43. Epub 1994/06/01. doi: 10.1084/jem.179.6.1933. PubMed PMID: 8195718; PMCID: PMC2191532.

5. Tough DF, Borrow P, Sprent J. Induction of bystander T cell proliferation by viruses and type I interferon in vivo. Science. 1996;272(5270):1947-50. Epub 1996/06/28. doi: 10.1126/science.272.5270.1947. PubMed PMID: 8658169.

6. Maurice NJ, McElrath MJ, Andersen-Nissen E, Frahm N, Prlic M. CXCR3 enables recruitment and site-specific bystander activation of memory CD8(+) T cells. Nat Commun. 2019;10(1):4987. Epub 2019/11/05. doi: 10.1038/s41467-019-12980-2. PubMed PMID: 31676770; PMCID: PMC6825240.

7. Berg RE, Crossley E, Murray S, Forman J. Memory CD8+ T cells provide innate immune protection against Listeria monocytogenes in the absence of cognate antigen. J Exp Med. 2003;198(10):1583-93. Epub 2003/11/19. doi: 10.1084/jem.20031051. PubMed PMID: 14623912; PMCID: PMC1592647.

8. Lertmemongkolchai G, Cai G, Hunter CA, Bancroft GJ. Bystander activation of CD8+ T cells contributes to the rapid production of IFN-gamma in response to bacterial pathogens. J Immunol. 2001;166(2):1097-105. Epub 2001/01/06. doi: 10.4049/jimmunol.166.2.1097. PubMed PMID: 11145690.

9. Soudja SM, Chandrabos C, Yakob E, Veenstra M, Palliser D, Lauvau G. Memory-T-cell-derived interferon-gamma instructs potent innate cell activation for protective immunity. Immunity. 2014;40(6):974-88. Epub 2014/06/17. doi: 10.1016/j.immuni.2014.05.005. PubMed PMID: 24931122; PMCID: PMC4105986.

10. Soudja SM, Ruiz AL, Marie JC, Lauvau G. Inflammatory monocytes activate memory CD8(+) T and innate NK lymphocytes independent of cognate antigen during microbial pathogen invasion. Immunity. 2012;37(3):549-62. Epub 2012/09/04. doi: 10.1016/j.immuni.2012.05.029. PubMed PMID: 22940097; PMCID: PMC3456987.

11. Kim J, Chang DY, Lee HW, Lee H, Kim JH, Sung PS, Kim KH, Hong SH, Kang W, Lee J, Shin SY, Yu HT, You S, Choi YS, Oh I, Lee DH, Lee DH, Jung MK, Suh KS, Hwang S, Kim W, Park SH, Kim HJ, Shin EC. Innate-like Cytotoxic Function of Bystander-Activated CD8(+) T Cells Is Associated with Liver Injury in Acute Hepatitis A. Immunity. 2018;48(1):161-73 e5. Epub 2018/01/07. doi: 10.1016/j.immuni.2017.11.025. PubMed PMID: 29305140.

12. Crosby EJ, Clark M, Novais FO, Wherry EJ, Scott P. Lymphocytic Choriomeningitis Virus Expands a Population of NKG2D+CD8+ T Cells That Exacerbates Disease in Mice Coinfected with Leishmania major. J Immunol. 2015;195(7):3301-10. Epub 2015/08/21. doi: 10.4049/jimmunol.1500855. PubMed PMID: 26290604; PMCID: PMC4575880.

13. Crosby EJ, Goldschmidt MH, Wherry EJ, Scott P. Engagement of NKG2D on bystander memory CD8 T cells promotes increased immunopathology following Leishmania major infection. PLoS Pathog. 2014;10(2):e1003970. Epub 2014/03/04. doi: 10.1371/journal.ppat.1003970. PubMed PMID: 24586170; PMCID: PMC3937277.

14. Curtsinger JM, Schmidt CS, Mondino A, Lins DC, Kedl RM, Jenkins MK, Mescher MF. Inflammatory cytokines provide a third signal for activation of naive CD4+ and CD8+ T cells. J Immunol. 1999;162(6):3256-62. Epub 1999/03/27. PubMed PMID: 10092777.

15. Greenwald RJ, Freeman GJ, Sharpe AH. The B7 family revisited. Annu Rev Immunol. 2005;23:515-48. Epub 2005/03/18. doi: 10.1146/annurev.immunol.23.021704.115611. PubMed PMID: 15771580.

16. Blank CU, Haining WN, Held W, Hogan PG, Kallies A, Lugli E, Lynn RC, Philip M, Rao A, Restifo NP, Schietinger A, Schumacher TN, Schwartzberg PL, Sharpe AH, Speiser DE, Wherry EJ, Youngblood BA, Zehn D. Defining 'T cell exhaustion'. Nat Rev Immunol. 2019;19(11):665-74. Epub 2019/10/02. doi: 10.1038/s41577-019-0221-9. PubMed PMID: 31570879; PMCID: PMC7286441.

17. Ehl S, Hombach J, Aichele P, Hengartner H, Zinkernagel RM. Bystander activation of cytotoxic T cells: studies on the mechanism and evaluation of in vivo significance in a transgenic mouse model. J Exp Med. 1997;185(7):1241-51. Epub 1997/04/07. doi: 10.1084/jem.185.7.1241. PubMed PMID: 9104811; PMCID: PMC2196250.

18. Cooper MD, Alder MN. The evolution of adaptive immune systems. Cell. 2006;124(4):815-22. Epub 2006/02/25. doi: 10.1016/j.cell.2006.02.001. PubMed PMID: 16497590.

19. Ahmed R. Tickling memory T cells. Science. 1996;272(5270):1904. Epub 1996/06/28. doi: 10.1126/science.272.5270.1904. PubMed PMID: 8658161.

20. Kim SK, Welsh RM. Comprehensive early and lasting loss of memory CD8 T cells and functional memory during acute and persistent viral infections. J Immunol. 2004;172(5):3139-50. Epub 2004/02/24. doi: 10.4049/jimmunol.172.5.3139. PubMed PMID: 14978120.

21. McNally JM, Zarozinski CC, Lin MY, Brehm MA, Chen HD, Welsh RM. Attrition of bystander CD8 T cells during virus-induced T-cell and interferon responses. J Virol. 2001;75(13):5965-76. Epub 2001/06/08. doi: 10.1128/JVI.75.13.5965-5976.2001. PubMed PMID: 11390598; PMCID: PMC114312.

22. Kohlmeier JE, Cookenham T, Roberts AD, Miller SC, Woodland DL. Type I interferons regulate cytolytic activity of memory CD8(+) T cells in the lung airways during respiratory virus challenge. Immunity. 2010;33(1):96-105. Epub 2010/07/20. doi: 10.1016/j.immuni.2010.06.016. PubMed PMID: 20637658; PMCID: PMC2908370.

23. Doisne JM, Urrutia A, Lacabaratz-Porret C, Goujard C, Meyer L, Chaix ML, Sinet M, Venet A. CD8+ T cells specific for EBV, cytomegalovirus, and influenza virus are activated during primary HIV infection. J Immunol. 2004;173(4):2410-8. Epub 2004/08/06. doi: 10.4049/jimmunol.173.4.2410. PubMed PMID: 15294954.

24. Younes SA, Freeman ML, Mudd JC, Shive CL, Reynaldi A, Panigrahi S, Estes JD, Deleage C, Lucero C, Anderson J, Schacker TW, Davenport MP, McCune JM, Hunt PW, Lee SA, Serrano-Villar S, Debernardo RL, Jacobson JM, Canaday DH, Sekaly RP, Rodriguez B, Sieg SF, Lederman MM. IL-15 promotes activation and expansion of CD8+ T cells in HIV-1 infection. J Clin Invest. 2016;126(7):2745-56. Epub 2016/06/21. doi: 10.1172/JCI85996. PubMed PMID: 27322062; PMCID: PMC4922693.

25. Odumade OA, Knight JA, Schmeling DO, Masopust D, Balfour HH, Jr., Hogquist KA. Primary Epstein-Barr virus infection does not erode preexisting CD8(+) T cell memory in humans. J Exp Med. 2012;209(3):471-8. Epub 2012/03/07. doi: 10.1084/jem.20112401. PubMed PMID: 22393125; PMCID: PMC3302231.

26. Chng MHY, Lim MQ, Rouers A, Becht E, Lee B, MacAry PA, Lye DC, Leo YS, Chen J, Fink K, Rivino L, Newell EW. Large-Scale HLA Tetramer Tracking of T Cells during Dengue Infection Reveals Broad Acute Activation and Differentiation into Two Memory Cell Fates. Immunity. 2019;51(6):1119-35 e5. Epub 2019/11/24. doi: 10.1016/j.immuni.2019.10.007. PubMed PMID: 31757672.

27. Rivino L, Kumaran EA, Thein TL, Too CT, Gan VC, Hanson BJ, Wilder-Smith A, Bertoletti A, Gascoigne NR, Lye DC, Leo YS, Akbar AN, Kemeny DM, MacAry PA. Virus-specific T lymphocytes home to the skin during natural dengue infection. Sci Transl Med. 2015;7(278):278ra35. Epub 2015/03/13. doi: 10.1126/scitranslmed.aaa0526. PubMed PMID: 25761891.

28. Sandalova E, Laccabue D, Boni C, Tan AT, Fink K, Ooi EE, Chua R, Shafaeddin Schreve B, Ferrari C, Bertoletti A. Contribution of herpesvirus specific CD8 T cells to anti-viral T cell response in humans. PLoS Pathog. 2010;6(8):e1001051. Epub 2010/09/03. doi: 10.1371/journal.ppat.1001051. PubMed PMID: 20808900; PMCID: PMC2924358.

29. Tough DF, Sun S, Sprent J. T cell stimulation in vivo by lipopolysaccharide (LPS). J Exp Med. 1997;185(12):2089-94. Epub 1997/06/16. doi: 10.1084/jem.185.12.2089. PubMed PMID: 9182680; PMCID: PMC2196347.

30. Mattei F, Schiavoni G, Belardelli F, Tough DF. IL-15 is expressed by dendritic cells in response to type I IFN, double-stranded RNA, or lipopolysaccharide and promotes dendritic cell activation. J Immunol. 2001;167(3):1179-87. Epub 2001/07/24. doi: 10.4049/jimmunol.167.3.1179. PubMed PMID: 11466332.

31. Raue HP, Brien JD, Hammarlund E, Slifka MK. Activation of virus-specific CD8+ T cells by lipopolysaccharide-induced IL-12 and IL-18. J Immunol. 2004;173(11):6873-81. Epub 2004/11/24. doi: 10.4049/jimmunol.173.11.6873. PubMed PMID: 15557182.

32. White JT, Cross EW, Burchill MA, Danhorn T, McCarter MD, Rosen HR, O'Connor B, Kedl RM. Virtual memory T cells develop and mediate bystander protective immunity in an IL-15-dependent manner. Nat Commun. 2016;7:11291. Epub 2016/04/22. doi: 10.1038/ncomms11291. PubMed PMID: 27097762; PMCID: PMC4844673.

33. Lin JS, Mohrs K, Szaba FM, Kummer LW, Leadbetter EA, Mohrs M. Virtual memory CD8 T cells expanded by helminth infection confer broad protection against bacterial infection. Mucosal Immunol. 2019;12(1):258-64. Epub 2018/10/27. doi: 10.1038/s41385-018-0100-x. PubMed PMID: 30361537; PMCID: PMC6301144.

34. Whiteside SK, Snook JP, Ma Y, Sonderegger FL, Fisher C, Petersen C, Zachary JF, Round JL, Williams MA, Weis JJ. IL-10 Deficiency Reveals a Role for TLR2-Dependent Bystander Activation of T Cells in Lyme Arthritis. J Immunol. 2018;200(4):1457-70. Epub 2018/01/14. doi: 10.4049/jimmunol.1701248. PubMed PMID: 29330323; PMCID: PMC5809275.

35. Maini MK, Boni C, Lee CK, Larrubia JR, Reignat S, Ogg GS, King AS, Herberg J, Gilson R, Alisa A, Williams R, Vergani D, Naoumov NV, Ferrari C, Bertoletti A. The role of virus-specific CD8(+) cells in liver damage and viral control during persistent hepatitis B virus infection. J Exp Med. 2000;191(8):1269-80. Epub 2000/04/19. doi: 10.1084/jem.191.8.1269. PubMed PMID: 10770795; PMCID: PMC2193131.

36. Whiteside SK, Snook JP, Williams MA, Weis JJ. Bystander T Cells: A Balancing Act of Friends and Foes. Trends Immunol. 2018;39(12):1021-35. Epub 2018/11/11. doi: 10.1016/j.it.2018.10.003. PubMed PMID: 30413351; PMCID: PMC6269193.

37. Kim TS, Shin EC. The activation of bystander CD8(+) T cells and their roles in viral infection. Exp Mol Med. 2019;51(12):1-9. Epub 2019/12/13. doi: 10.1038/s12276-019-0316-1. PubMed PMID: 31827070; PMCID: PMC6906361.

38. Barnstorf I, Borsa M, Baumann N, Pallmer K, Yermanos A, Joller N, Sporri R, Welten SPM, Krautler NJ, Oxenius A. Chronic virus infection compromises memory bystander T cell function in an IL-6/STAT1-dependent manner. J Exp Med. 2019;216(3):571-86. Epub 2019/02/13. doi: 10.1084/jem.20181589. PubMed PMID: 30745322; PMCID: PMC6400541.

39. Groh V, Bruhl A, El-Gabalawy H, Nelson JL, Spies T. Stimulation of T cell autoreactivity by anomalous expression of NKG2D and its MIC ligands in rheumatoid arthritis. Proc Natl Acad Sci U S A. 2003;100(16):9452-7. Epub 2003/07/25. doi: 10.1073/pnas.1632807100. PubMed PMID: 12878725; PMCID: PMC170939.

40. Meresse B, Chen Z, Ciszewski C, Tretiakova M, Bhagat G, Krausz TN, Raulet DH, Lanier LL, Groh V, Spies T, Ebert EC, Green PH, Jabri B. Coordinated induction by IL15 of a TCR-independent NKG2D signaling pathway converts CTL into lymphokine-activated killer cells in celiac disease. Immunity. 2004;21(3):357-66. Epub 2004/09/11. doi: 10.1016/j.immuni.2004.06.020. PubMed PMID: 15357947.

41. Simoni Y, Becht E, Fehlings M, Loh CY, Koo SL, Teng KWW, Yeong JPS, Nahar R, Zhang T, Kared H, Duan K, Ang N, Poidinger M, Lee YY, Larbi A, Khng AJ, Tan E, Fu C, Mathew R, Teo M, Lim WT, Toh CK, Ong BH, Koh T, Hillmer AM, Takano A, Lim TKH, Tan EH, Zhai W, Tan DSW, Tan IB, Newell EW. Bystander CD8(+) T cells are abundant and phenotypically distinct in human tumour infiltrates. Nature. 2018;557(7706):575-9. Epub 2018/05/18. doi: 10.1038/s41586-018-0130-2. PubMed PMID: 29769722.

42. Jiang J, Lau LL, Shen H. Selective depletion of nonspecific T cells during the early stage of immune responses to infection. J Immunol. 2003;171(8):4352-8. Epub 2003/10/08. doi: 10.4049/jimmunol.171.8.4352. PubMed PMID: 14530360.

43. Freeman BE, Hammarlund E, Raue HP, Slifka MK. Regulation of innate CD8+ T-cell activation mediated by cytokines. Proc Natl Acad Sci U S A. 2012;109(25):9971-6. Epub 2012/06/06. doi: 10.1073/pnas.1203543109. PubMed PMID: 22665806; PMCID: PMC3382521.

44. Smeltz RB. Profound enhancement of the IL-12/IL-18 pathway of IFN-gamma secretion in human CD8+ memory T cell subsets via IL-15. J Immunol. 2007;178(8):4786-92. Epub 2007/04/04. doi: 10.4049/jimmunol.178.8.4786. PubMed PMID: 17404259.

45. Slichter CK, McDavid A, Miller HW, Finak G, Seymour BJ, McNevin JP, Diaz G, Czartoski JL, McElrath MJ, Gottardo R, Prlic M. Distinct activation thresholds of human conventional and innate-like memory T cells. JCI Insight. 2016;1(8). Epub 2016/06/23. doi: 10.1172/jci.insight.86292. PubMed PMID: 27331143; PMCID: PMC4912124.

46. Guo L, Wei G, Zhu J, Liao W, Leonard WJ, Zhao K, Paul W. IL-1 family members and STAT activators induce cytokine production by Th2, Th17, and Th1 cells. Proc Natl Acad Sci U S A. 2009;106(32):13463-8. Epub 2009/08/12. doi: 10.1073/pnas.0906988106. PubMed PMID: 19666510; PMCID: PMC2726336.

47. Ussher JE, Willberg CB, Klenerman P. MAIT cells and viruses. Immunol Cell Biol. 2018;96(6):630-41. Epub 2018/01/20. doi: 10.1111/imcb.12008. PubMed PMID: 29350807; PMCID: PMC6055725.

48. Berkson JD, Prlic M. The MAIT conundrum - how human MAIT cells distinguish bacterial colonization from infection in mucosal barrier tissues. Immunol Lett. 2017;192:7-11. Epub 2017/10/11. doi: 10.1016/j.imlet.2017.09.013. PubMed PMID: 28987476; PMCID: PMC5685889.

49. Holzapfel KL, Tyznik AJ, Kronenberg M, Hogquist KA. Antigen-dependent versus -independent activation of invariant NKT cells during infection. J Immunol. 2014;192(12):5490-8. Epub 2014/05/13. doi: 10.4049/jimmunol.1400722. PubMed PMID: 24813205; PMCID: PMC4053538.

50. Tyznik AJ, Verma S, Wang Q, Kronenberg M, Benedict CA. Distinct requirements for activation of NKT and NK cells during viral infection. J Immunol. 2014;192(8):3676-85. Epub 2014/03/19. doi: 10.4049/jimmunol.1300837. PubMed PMID: 24634489; PMCID: PMC3981072.

51. Ribeiro ST, Ribot JC, Silva-Santos B. Five Layers of Receptor Signaling in gammadelta T-Cell Differentiation and Activation. Front Immunol. 2015;6:15. Epub 2015/02/13. doi: 10.3389/fimmu.2015.00015. PubMed PMID: 25674089; PMCID: PMC4306313.

52. Prlic M, Sacks JA, Bevan MJ. Dissociating markers of senescence and protective ability in memory T cells. PLoS One. 2012;7(3):e32576. Epub 2012/03/08. doi: 10.1371/journal.pone.0032576. PubMed PMID: 22396780; PMCID: PMC3292574.

53. Martin MD, Shan Q, Xue HH, Badovinac VP. Time and Antigen-Stimulation History Influence Memory CD8 T Cell Bystander Responses. Front Immunol. 2017;8:634. Epub 2017/06/24. doi: 10.3389/fimmu.2017.00634. PubMed PMID: 28642758; PMCID: PMC5462920.

54. Yee Mon KJ, Goldsmith E, Watson NB, Wang J, Smith NL, Rudd BD. Differential Sensitivity to IL-12 Drives Sex-Specific Differences in the CD8+ T Cell Response to Infection. Immunohorizons. 2019;3(4):121-32. Epub 2019/07/19. doi: 10.4049/immunohorizons.1800066. PubMed PMID: 31317126; PMCID: PMC6636834.

55. White JT, Cross EW, Kedl RM. Antigen-inexperienced memory CD8(+) T cells: where they come from and why we need them. Nat Rev Immunol. 2017;17(6):391-400. Epub 2017/05/10. doi: 10.1038/nri.2017.34. PubMed PMID: 28480897; PMCID: PMC5569888.

56. Ge C, Monk IR, Pizzolla A, Wang N, Bedford JG, Stinear TP, Westall GP, Wakim LM. Bystander Activation of Pulmonary Trm Cells Attenuates the Severity of Bacterial Pneumonia by Enhancing Neutrophil Recruitment. Cell Rep. 2019;29(13):4236-44 e3. Epub 2019/12/26. doi: 10.1016/j.celrep.2019.11.103. PubMed PMID: 31875535.

57. Schroder K, Hertzog PJ, Ravasi T, Hume DA. Interferon-gamma: an overview of signals, mechanisms and functions. J Leukoc Biol. 2004;75(2):163-89. Epub 2003/10/04. doi: 10.1189/jlb.0603252. PubMed PMID: 14525967.

58. Pamer EG. Immune responses to Listeria monocytogenes. Nat Rev Immunol. 2004;4(10):812-23. Epub 2004/10/02. doi: 10.1038/nri1461. PubMed PMID: 15459672.

59. Beckerman KP, Rogers HW, Corbett JA, Schreiber RD, McDaniel ML, Unanue ER. Release of nitric oxide during the T cell-independent pathway of macrophage activation. Its role in resistance to Listeria monocytogenes. J Immunol. 1993;150(3):888-95. Epub 1993/02/01. PubMed PMID: 7678626.

60. Dinauer MC, Deck MB, Unanue ER. Mice lacking reduced nicotinamide adenine dinucleotide phosphate oxidase activity show increased susceptibility to early infection with Listeria monocytogenes. J Immunol. 1997;158(12):5581-3. Epub 1997/06/15. PubMed PMID: 9190903.

61. Witter AR, Okunnu BM, Berg RE. The Essential Role of Neutrophils during Infection with the Intracellular Bacterial Pathogen Listeria monocytogenes. J Immunol. 2016;197(5):1557-65. Epub 2016/08/21. doi: 10.4049/jimmunol.1600599. PubMed PMID: 27543669; PMCID: PMC4995063.

62. Krummel MF, Mahale JN, Uhl LFK, Hardison EA, Mujal AM, Mazet JM, Weber RJ, Gartner ZJ, Gerard A. Paracrine costimulation of IFN-gamma signaling by integrins modulates CD8 T cell differentiation. Proc Natl Acad Sci U S A. 2018;115(45):11585-90. Epub 2018/10/24. doi: 10.1073/pnas.1804556115. PubMed PMID: 30348790; PMCID: PMC6233119.

63. Lettau M, Schmidt H, Kabelitz D, Janssen O. Secretory lysosomes and their cargo in T and NK cells. Immunol Lett. 2007;108(1):10-9. Epub 2006/11/14. doi: 10.1016/j.imlet.2006.10.001. PubMed PMID: 17097742.

64. Blott EJ, Griffiths GM. Secretory lysosomes. Nat Rev Mol Cell Biol. 2002;3(2):122-31. Epub 2002/02/12. doi: 10.1038/nrm732. PubMed PMID: 11836514.

65. Bauer S, Groh V, Wu J, Steinle A, Phillips JH, Lanier LL, Spies T. Activation of NK cells and T cells by NKG2D, a receptor for stress-inducible MICA. Science. 1999;285(5428):727-9. Epub 1999/07/31. doi: 10.1126/science.285.5428.727. PubMed PMID: 10426993.

66. Diefenbach A, Jensen ER, Jamieson AM, Raulet DH. Rae1 and H60 ligands of the NKG2D receptor stimulate tumour immunity. Nature. 2001;413(6852):165-71. Epub 2001/09/15. doi: 10.1038/35093109. PubMed PMID: 11557981; PMCID: PMC3900321.

67. Hamerman JA, Ogasawara K, Lanier LL. Cutting edge: Toll-like receptor signaling in macrophages induces ligands for the NKG2D receptor. J Immunol. 2004;172(4):2001-5. Epub 2004/02/07. doi: 10.4049/jimmunol.172.4.2001. PubMed PMID: 14764662.

68. Rolot M, Dougall AM, Chetty A, Javaux J, Chen T, Xiao X, Machiels B, Selkirk ME, Maizels RM, Hokke C, Denis O, Brombacher F, Vanderplasschen A, Gillet L, Horsnell WGC, Dewals BG. Helminth-induced IL-4 expands bystander memory CD8(+) T cells for early control of viral infection. Nat Commun. 2018;9(1):4516. Epub 2018/10/31. doi: 10.1038/s41467-018-06978-5. PubMed PMID: 30375396; PMCID: PMC6207712.

69. Sckisel GD, Tietze JK, Zamora AE, Hsiao HH, Priest SO, Wilkins DE, Lanier LL, Blazar BR, Baumgarth N, Murphy WJ. Influenza infection results in local expansion of memory CD8(+) T cells with antigen non-specific phenotype and function. Clin Exp Immunol. 2014;175(1):79-91. Epub 2013/08/14. doi: 10.1111/cei.12186. PubMed PMID: 23937663; PMCID: PMC3898557.

70. Loh L, Wang Z, Sant S, Koutsakos M, Jegaskanda S, Corbett AJ, Liu L, Fairlie DP, Crowe J, Rossjohn J, Xu J, Doherty PC, McCluskey J, Kedzierska K. Human mucosal-associated invariant T cells contribute to antiviral influenza immunity via IL-18-dependent activation. Proc Natl Acad Sci U S A. 2016;113(36):10133-8. Epub 2016/08/21. doi: 10.1073/pnas.1610750113. PubMed PMID: 27543331; PMCID: PMC5018778.

71. Abadie V, Jabri B. IL-15: a central regulator of celiac disease immunopathology. Immunol Rev. 2014;260(1):221-34. Epub 2014/06/20. doi: 10.1111/imr.12191. PubMed PMID: 24942692; PMCID: PMC4066219.

72. Harada S, Yamamura M, Okamoto H, Morita Y, Kawashima M, Aita T, Makino H. Production of interleukin-7 and interleukin-15 by fibroblast-like synoviocytes from patients with rheumatoid arthritis. Arthritis Rheum. 1999;42(7):1508-16. Epub 1999/07/14. doi: 10.1002/1529-0131(199907)42:7<1508::AID-ANR26>3.0.CO;2-L. PubMed PMID: 10403280.

73. McInnes IB, al-Mughales J, Field M, Leung BP, Huang FP, Dixon R, Sturrock RD, Wilkinson PC, Liew FY. The role of interleukin-15 in T-cell migration and activation in rheumatoid arthritis. Nat Med. 1996;2(2):175-82. Epub 1996/02/01. doi: 10.1038/nm0296-175. PubMed PMID: 8574962.

74. Jabri B, Abadie V. IL-15 functions as a danger signal to regulate tissue-resident T cells and tissue destruction. Nat Rev Immunol. 2015;15(12):771-83. Epub 2015/11/17. doi: 10.1038/nri3919. PubMed PMID: 26567920; PMCID: PMC5079184.

75. Liu K, Catalfamo M, Li Y, Henkart PA, Weng NP. IL-15 mimics T cell receptor crosslinking in the induction of cellular proliferation, gene expression, and cytotoxicity in CD8+ memory T cells. Proc Natl Acad Sci U S A. 2002;99(9):6192-7. Epub 2002/04/25. doi: 10.1073/pnas.092675799. PubMed PMID: 11972069; PMCID: PMC122925.

76. Roberts AI, Lee L, Schwarz E, Groh V, Spies T, Ebert EC, Jabri B. NKG2D receptors induced by IL-15 costimulate CD28-negative effector CTL in the tissue microenvironment. J Immunol. 2001;167(10):5527-30. Epub 2001/11/08. doi: 10.4049/jimmunol.167.10.5527. PubMed PMID: 11698420.

77. Tamang DL, Redelman D, Alves BN, Vollger L, Bethley C, Hudig D. Induction of granzyme B and T cell cytotoxic capacity by IL-2 or IL-15 without antigens: multiclonal responses that are extremely lytic if triggered and short-lived after cytokine withdrawal. Cytokine. 2006;36(3-4):148-59. Epub 2006/12/26. doi: 10.1016/j.cyto.2006.11.008. PubMed PMID: 17188506; PMCID: PMC1850105.

78. Canale FP, Ramello MC, Nunez N, Araujo Furlan CL, Bossio SN, Gorosito Serran M, Tosello Boari J, Del Castillo A, Ledesma M, Sedlik C, Piaggio E, Gruppi A, Acosta Rodriguez EA, Montes CL. CD39 Expression Defines Cell Exhaustion in Tumor-Infiltrating CD8(+) T Cells. Cancer Res. 2018;78(1):115-28. Epub 2017/10/27. doi: 10.1158/0008-5472.CAN-16-2684. PubMed PMID: 29066514.

79. Thelen M, Lechner A, Wennhold K, von Bergwelt-Baildon M, Schlosser HA. CD39 Expression Defines Cell Exhaustion in Tumor-Infiltrating CD8(+) T Cells-Letter. Cancer Res. 2018;78(17):5173-4. Epub 2018/08/18. doi: 10.1158/0008-5472.CAN-18-0873. PubMed PMID: 30115699.

80. Duhen T, Duhen R, Montler R, Moses J, Moudgil T, de Miranda NF, Goodall CP, Blair TC, Fox BA, McDermott JE, Chang SC, Grunkemeier G, Leidner R, Bell RB, Weinberg AD. Co-expression of CD39 and CD103 identifies tumor-reactive CD8 T cells in human solid tumors. Nat Commun. 2018;9(1):2724. Epub 2018/07/15. doi: 10.1038/s41467-018-05072-0. PubMed PMID: 30006565; PMCID: PMC6045647.

81. Schietinger A, Philip M, Krisnawan VE, Chiu EY, Delrow JJ, Basom RS, Lauer P, Brockstedt DG, Knoblaugh SE, Hammerling GJ, Schell TD, Garbi N, Greenberg PD. Tumor-Specific T Cell Dysfunction Is a Dynamic Antigen-Driven Differentiation Program Initiated Early during Tumorigenesis. Immunity. 2016;45(2):389-401. Epub 2016/08/16. doi: 10.1016/j.immuni.2016.07.011. PubMed PMID: 27521269; PMCID: PMC5119632.

82. O'Sullivan T, Saddawi-Konefka R, Vermi W, Koebel CM, Arthur C, White JM, Uppaluri R, Andrews DM, Ngiow SF, Teng MW, Smyth MJ, Schreiber RD, Bui JD. Cancer immunoediting by the innate immune system in the absence of adaptive immunity. J Exp Med. 2012;209(10):1869-82. Epub 2012/08/29. doi: 10.1084/jem.20112738. PubMed PMID: 22927549; PMCID: PMC3457735.

83. Guerra N, Tan YX, Joncker NT, Choy A, Gallardo F, Xiong N, Knoblaugh S, Cado D, Greenberg NM, Raulet DH. NKG2D-deficient mice are defective in tumor surveillance in models of spontaneous malignancy. Immunity. 2008;28(4):571-80. Epub 2008/04/09. doi: 10.1016/j.immuni.2008.02.016. PubMed PMID: 18394936; PMCID: PMC3528789.

84. Rosato PC, Wijeyesinghe S, Stolley JM, Nelson CE, Davis RL, Manlove LS, Pennell CA, Blazar BR, Chen CC, Geller MA, Vezys V, Masopust D. Virus-specific memory T cells populate tumors and can be repurposed for tumor immunotherapy. Nat Commun. 2019;10(1):567. Epub 2019/02/06. doi: 10.1038/s41467-019-08534-1. PubMed PMID: 30718505; PMCID: PMC6362136.

85. Tietze JK, Wilkins DE, Sckisel GD, Bouchlaka MN, Alderson KL, Weiss JM, Ames E, Bruhn KW, Craft N, Wiltrout RH, Longo DL, Lanier LL, Blazar BR, Redelman D, Murphy WJ. Delineation of antigen-specific and antigen-nonspecific CD8(+) memory T-cell responses after cytokine-based cancer immunotherapy. Blood. 2012;119(13):3073-83. Epub 2012/01/19. doi: 10.1182/blood-2011-07-369736. PubMed PMID: 22251483; PMCID: PMC3321869.

86. Braun M, Ress ML, Yoo YE, Scholz CJ, Eyrich M, Schlegel PG, Wolfl M. IL12-mediated sensitizing of T-cell receptor-dependent and -independent tumor cell killing. Oncoimmunology. 2016;5(7):e1188245. Epub 2016/09/14. doi: 10.1080/2162402X.2016.1188245. PubMed PMID: 27622043; PMCID: PMC5006926.

87. Monjazeb AM, Tietze JK, Grossenbacher SK, Hsiao HH, Zamora AE, Mirsoian A, Koehn B, Blazar BR, Weiss JM, Wiltrout RH, Sckisel GD, Murphy WJ. Bystander activation and anti-tumor effects of CD8+ T cells following Interleukin-2 based immunotherapy is independent of CD4+ T cell help. PLoS One. 2014;9(8):e102709. Epub 2014/08/15. doi: 10.1371/journal.pone.0102709. PubMed PMID: 25119341; PMCID: PMC4131875.

88. Wang X, Waschke BC, Woolaver RA, Chen SMY, Chen Z, Wang JH. MHC class I-independent activation of virtual memory CD8 T cells induced by chemotherapeutic agent-treated cancer cells. Cell Mol Immunol. 2021;18(3):723-34. Epub 2020/05/20. doi: 10.1038/s41423-020-0463-2. PubMed PMID: 32427883; PMCID: PMC8027191.

89. Goplen NP, Saxena V, Knudson KM, Schrum AG, Gil D, Daniels MA, Zamoyska R, Teixeiro E. IL-12 Signals through the TCR To Support CD8 Innate Immune Responses. J Immunol. 2016;197(6):2434-43. Epub 2016/08/16. doi: 10.4049/jimmunol.1600037. PubMed PMID: 27521342; PMCID: PMC5010952.

90. Danahy DB, Berton RR, Badovinac VP. Cutting Edge: Antitumor Immunity by Pathogen-Specific CD8 T Cells in the Absence of Cognate Antigen Recognition. J Immunol. 2020;204(6):1431-5. Epub 2020/02/14. doi: 10.4049/jimmunol.1901172. PubMed PMID: 32051220; PMCID: PMC7310247.

91. Muschaweckh A, Buchholz VR, Fellenzer A, Hessel C, Konig PA, Tao S, Tao R, Heikenwalder M, Busch DH, Korn T, Kastenmuller W, Drexler I, Gasteiger G. Antigen-dependent competition shapes the local repertoire of tissue-resident memory CD8+ T cells. J Exp Med. 2016;213(13):3075-86. Epub 2016/12/03. doi: 10.1084/jem.20160888. PubMed PMID: 27899444; PMCID: PMC5154944.

92. Zhou AC, Batista NV, Watts TH. 4-1BB Regulates Effector CD8 T Cell Accumulation in the Lung Tissue through a TRAF1-, mTOR-, and Antigen-Dependent Mechanism to Enhance Tissue-Resident Memory T Cell Formation during Respiratory Influenza Infection. J Immunol. 2019;202(8):2482-92. Epub 2019/03/15. doi: 10.4049/jimmunol.1800795. PubMed PMID: 30867239.

93. Alanio C, Nicoli F, Sultanik P, Flecken T, Perot B, Duffy D, Bianchi E, Lim A, Clave E, van Buuren MM, Schnuriger A, Johnsson K, Boussier J, Garbarg-Chenon A, Bousquet L, Mottez E, Schumacher TN, Toubert A, Appay V, Heshmati F, Thimme R, Pol S, Mallet V, Albert ML. Bystander hyperactivation of preimmune CD8+ T cells in chronic HCV patients. Elife. 2015;4. Epub 2015/11/17. doi: 10.7554/eLife.07916. PubMed PMID: 26568315; PMCID: PMC4752008.

94. Biancotto A, Grivel JC, Iglehart SJ, Vanpouille C, Lisco A, Sieg SF, Debernardo R, Garate K, Rodriguez B, Margolis LB, Lederman MM. Abnormal activation and cytokine spectra in lymph nodes of people chronically infected with HIV-1. Blood. 2007;109(10):4272-9. Epub 2007/02/10. doi: 10.1182/blood-2006-11-055764. PubMed PMID: 17289812; PMCID: PMC1885500.

95. Thompson LJ, Lai JF, Valladao AC, Thelen TD, Urry ZL, Ziegler SF. Conditioning of naive CD4(+) T cells for enhanced peripheral Foxp3 induction by nonspecific bystander inflammation. Nat Immunol. 2016;17(3):297-303. Epub 2016/01/12. doi: 10.1038/ni.3329. PubMed PMID: 26752376; PMCID: PMC4757503.

96. Goepfert PA, Elizaga ML, Seaton K, Tomaras GD, Montefiori DC, Sato A, Hural J, DeRosa SC, Kalams SA, McElrath MJ, Keefer MC, Baden LR, Lama JR, Sanchez J, Mulligan MJ, Buchbinder SP, Hammer SM, Koblin BA, Pensiero M, Butler C, Moss B, Robinson HL, Group HS, National Institutes of A, Infectious Diseases HIVVTN. Specificity and 6-month durability of immune responses induced by DNA and recombinant modified vaccinia Ankara vaccines expressing HIV-1 virus-like particles. J Infect Dis. 2014;210(1):99-110. Epub 2014/01/10. doi: 10.1093/infdis/jiu003. PubMed PMID: 24403557; PMCID: PMC4072895.

97. Wyatt LS, Earl PL, Vogt J, Eller LA, Chandran D, Liu J, Robinson HL, Moss B. Correlation of immunogenicities and in vitro expression levels of recombinant modified vaccinia virus Ankara HIV vaccines. Vaccine. 2008;26(4):486-93. Epub 2007/12/25. doi: 10.1016/j.vaccine.2007.11.036. PubMed PMID: 18155813; PMCID: PMC2262837.

98. Wolfl M, Kuball J, Eyrich M, Schlegel PG, Greenberg PD. Use of CD137 to study the full repertoire of CD8+ T cells without the need to know epitope specificities. Cytometry A. 2008;73(11):1043-9. Epub 2008/06/19. doi: 10.1002/cyto.a.20594. PubMed PMID: 18561198; PMCID: PMC2784669.

99. Youngblood B, Oestreich KJ, Ha SJ, Duraiswamy J, Akondy RS, West EE, Wei Z, Lu P, Austin JW, Riley JL, Boss JM, Ahmed R. Chronic virus infection enforces demethylation of the locus that encodes PD-1 in antigen-specific CD8(+) T cells. Immunity. 2011;35(3):400-12. Epub 2011/09/29. doi: 10.1016/j.immuni.2011.06.015. PubMed PMID: 21943489; PMCID: PMC3183460.

100. Ussher JE, Bilton M, Attwod E, Shadwell J, Richardson R, de Lara C, Mettke E, Kurioka A, Hansen TH, Klenerman P, Willberg CB. CD161++ CD8+ T cells, including the MAIT cell subset, are specifically activated by IL-12+IL-18 in a TCR-independent manner. Eur J Immunol. 2014;44(1):195-203. Epub 2013/09/11. doi: 10.1002/eji.201343509. PubMed PMID: 24019201; PMCID: PMC3947164.

101. van Wilgenburg B, Scherwitzl I, Hutchinson EC, Leng T, Kurioka A, Kulicke C, de Lara C, Cole S, Vasanawathana S, Limpitikul W, Malasit P, Young D, Denney L, consortium S-H, Moore MD, Fabris P, Giordani MT, Oo YH, Laidlaw SM, Dustin LB, Ho LP, Thompson FM, Ramamurthy N, Mongkolsapaya J, Willberg CB, Screaton GR, Klenerman P. MAIT cells are activated during human viral infections. Nat Commun. 2016;7:11653. Epub 2016/06/24. doi: 10.1038/ncomms11653. PubMed PMID: 27337592; PMCID: PMC4931007.

102. Turner DL, Cauley LS, Khanna KM, Lefrancois L. Persistent antigen presentation after acute vesicular stomatitis virus infection. J Virol. 2007;81(4):2039-46. Epub 2006/12/08. doi: 10.1128/JVI.02167-06. PubMed PMID: 17151119; PMCID: PMC1797569.

103. Neuenhahn M, Kerksiek KM, Nauerth M, Suhre MH, Schiemann M, Gebhardt FE, Stemberger C, Panthel K, Schroder S, Chakraborty T, Jung S, Hochrein H, Russmann H, Brocker T, Busch DH. CD8alpha+ dendritic cells are required for efficient entry of Listeria monocytogenes into the spleen. Immunity. 2006;25(4):619-30. Epub 2006/10/10. doi: 10.1016/j.immuni.2006.07.017. PubMed PMID: 17027298.

104. Aoshi T, Carrero JA, Konjufca V, Koide Y, Unanue ER, Miller MJ. The cellular niche of Listeria monocytogenes infection changes rapidly in the spleen. Eur J Immunol. 2009;39(2):417-25. Epub 2009/01/09. doi: 10.1002/eji.200838718. PubMed PMID: 19130474; PMCID: PMC2749683.

105. Edelson BT, Bradstreet TR, Hildner K, Carrero JA, Frederick KE, Kc W, Belizaire R, Aoshi T, Schreiber RD, Miller MJ, Murphy TL, Unanue ER, Murphy KM. CD8alpha(+) dendritic cells are an obligate cellular entry point for productive infection by Listeria monocytogenes. Immunity. 2011;35(2):236-48. Epub 2011/08/27. doi: 10.1016/j.immuni.2011.06.012. PubMed PMID: 21867927; PMCID: PMC3172670.

106. den Haan JM, Kraal G. Innate immune functions of macrophage subpopulations in the spleen. J Innate Immun. 2012;4(5-6):437-45. Epub 2012/02/14. doi: 10.1159/000335216. PubMed PMID: 22327291; PMCID: PMC6741446.

107. Galkina E, Thatte J, Dabak V, Williams MB, Ley K, Braciale TJ. Preferential migration of effector CD8+ T cells into the interstitium of the normal lung. J Clin Invest. 2005;115(12):3473-83. Epub 2005/11/26. doi: 10.1172/JCI24482. PubMed PMID: 16308575; PMCID: PMC1288831.

108. Anderson KG, Mayer-Barber K, Sung H, Beura L, James BR, Taylor JJ, Qunaj L, Griffith TS, Vezys V, Barber DL, Masopust D. Intravascular staining for discrimination of vascular and tissue leukocytes. Nat Protoc. 2014;9(1):209-22. Epub 2014/01/05. doi: 10.1038/nprot.2014.005. PubMed PMID: 24385150; PMCID: PMC4428344.

109. Jamieson AM, Diefenbach A, McMahon CW, Xiong N, Carlyle JR, Raulet DH. The role of the NKG2D immunoreceptor in immune cell activation and natural killing. Immunity. 2002;17(1):19-29. Epub 2002/08/02. doi: 10.1016/s1074-7613(02)00333-3. PubMed PMID: 12150888.

110. Hickman HD, Reynoso GV, Ngudiankama BF, Cush SS, Gibbs J, Bennink JR, Yewdell JW. CXCR3 chemokine receptor enables local CD8(+) T cell migration for the destruction of virus-infected cells. Immunity. 2015;42(3):524-37. Epub 2015/03/15. doi: 10.1016/j.immuni.2015.02.009. PubMed PMID: 25769612; PMCID: PMC4365427.

111. Cole AM, Ganz T, Liese AM, Burdick MD, Liu L, Strieter RM. Cutting edge: IFN-inducible ELR- CXC chemokines display defensin-like antimicrobial activity. J Immunol. 2001;167(2):623-7. Epub 2001/07/07. doi: 10.4049/jimmunol.167.2.623. PubMed PMID: 11441062.

112. Colvin RA, Campanella GS, Sun J, Luster AD. Intracellular domains of CXCR3 that mediate CXCL9, CXCL10, and CXCL11 function. J Biol Chem. 2004;279(29):30219-27. Epub 2004/05/20. doi: 10.1074/jbc.M403595200. PubMed PMID: 15150261.

113. Meiser A, Mueller A, Wise EL, McDonagh EM, Petit SJ, Saran N, Clark PC, Williams TJ, Pease JE. The chemokine receptor CXCR3 is degraded following internalization and is replenished at the cell surface by de novo synthesis of receptor. J Immunol. 2008;180(10):6713-24. Epub 2008/05/06. doi: 10.4049/jimmunol.180.10.6713. PubMed PMID: 18453591; PMCID: PMC2556381.

114. Kurachi M, Kurachi J, Suenaga F, Tsukui T, Abe J, Ueha S, Tomura M, Sugihara K, Takamura S, Kakimi K, Matsushima K. Chemokine receptor CXCR3 facilitates CD8(+) T cell differentiation into short-lived effector cells leading to memory degeneration. J Exp Med. 2011;208(8):1605-20. Epub 2011/07/27. doi: 10.1084/jem.20102101. PubMed PMID: 21788406; PMCID: PMC3149224.

115. Kang SJ, Liang HE, Reizis B, Locksley RM. Regulation of hierarchical clustering and activation of innate immune cells by dendritic cells. Immunity. 2008;29(5):819-33. Epub 2008/11/14. doi: 10.1016/j.immuni.2008.09.017. PubMed PMID: 19006696; PMCID: PMC2858430.

116. Zak DE, Andersen-Nissen E, Peterson ER, Sato A, Hamilton MK, Borgerding J, Krishnamurty AT, Chang JT, Adams DJ, Hensley TR, Salter AI, Morgan CA, Duerr AC, De Rosa SC, Aderem A, McElrath MJ. Merck Ad5/HIV induces broad innate immune activation that predicts CD8(+) T-cell responses but is attenuated by preexisting Ad5 immunity. Proc Natl Acad Sci U S A. 2012;109(50):E3503-12. Epub 2012/11/16. doi: 10.1073/pnas.1208972109. PubMed PMID: 23151505; PMCID: PMC3528489.

117. Kastenmuller W, Torabi-Parizi P, Subramanian N, Lammermann T, Germain RN. A spatially-organized multicellular innate immune response in lymph nodes limits systemic pathogen spread. Cell. 2012;150(6):1235-48. Epub 2012/09/18. doi: 10.1016/j.cell.2012.07.021. PubMed PMID: 22980983; PMCID: PMC3514884.

118. Schenkel JM, Fraser KA, Vezys V, Masopust D. Sensing and alarm function of resident memory CD8(+) T cells. Nat Immunol. 2013;14(5):509-13. Epub 2013/04/02. doi: 10.1038/ni.2568. PubMed PMID: 23542740; PMCID: PMC3631432.

119. Wherry EJ, Blattman JN, Murali-Krishna K, van der Most R, Ahmed R. Viral persistence alters CD8 T-cell immunodominance and tissue distribution and results in distinct stages of functional impairment. J Virol. 2003;77(8):4911-27. Epub 2003/03/29. doi: 10.1128/jvi.77.8.4911-4927.2003. PubMed PMID: 12663797; PMCID: PMC152117.

120. Johnson LR, Weizman OE, Rapp M, Way SS, Sun JC. Epitope-Specific Vaccination Limits Clonal Expansion of Heterologous Naive T Cells during Viral Challenge. Cell Rep. 2016;17(3):636-44. Epub 2016/10/13. doi: 10.1016/j.celrep.2016.09.019. PubMed PMID: 27732841; PMCID: PMC5503750.

121. Oberle SG, Hanna-El-Daher L, Chennupati V, Enouz S, Scherer S, Prlic M, Zehn D. A Minimum Epitope Overlap between Infections Strongly Narrows the Emerging T Cell Repertoire. Cell Rep. 2016;17(3):627-35. Epub 2016/10/13. doi: 10.1016/j.celrep.2016.09.072. PubMed PMID: 27732840; PMCID: PMC5081394.

122. Zehn D, Roepke S, Weakly K, Bevan MJ, Prlic M. Inflammation and TCR signal strength determine the breadth of the T cell response in a bim-dependent manner. J Immunol. 2014;192(1):200-5. Epub 2013/11/26. doi: 10.4049/jimmunol.1302289. PubMed PMID: 24273000; PMCID: PMC3903384.

123. Robinson TO, Schluns KS. The potential and promise of IL-15 in immuno-oncogenic therapies. Immunol Lett. 2017;190:159-68. Epub 2017/08/22. doi: 10.1016/j.imlet.2017.08.010. PubMed PMID: 28823521; PMCID: PMC5774016.

124. Miller JD, van der Most RG, Akondy RS, Glidewell JT, Albott S, Masopust D, Murali-Krishna K, Mahar PL, Edupuganti S, Lalor S, Germon S, Del Rio C, Mulligan MJ, Staprans SI, Altman JD, Feinberg MB, Ahmed R. Human effector and memory CD8+ T cell responses to smallpox and yellow fever vaccines. Immunity. 2008;28(5):710-22. Epub 2008/05/13. doi: 10.1016/j.immuni.2008.02.020. PubMed PMID: 18468462.

125. Zajac AJ, Blattman JN, Murali-Krishna K, Sourdive DJ, Suresh M, Altman JD, Ahmed R. Viral immune evasion due to persistence of activated T cells without effector function. J Exp Med. 1998;188(12):2205-13. Epub 1998/12/22. doi: 10.1084/jem.188.12.2205. PubMed PMID: 9858507; PMCID: PMC2212420.

126. Pauken KE, Wherry EJ. Overcoming T cell exhaustion in infection and cancer. Trends Immunol. 2015;36(4):265-76. Epub 2015/03/24. doi: 10.1016/j.it.2015.02.008. PubMed PMID: 25797516; PMCID: PMC4393798.

127. Schietinger A, Greenberg PD. Tolerance and exhaustion: defining mechanisms of T cell dysfunction. Trends Immunol. 2014;35(2):51-60. Epub 2013/11/12. doi: 10.1016/j.it.2013.10.001. PubMed PMID: 24210163; PMCID: PMC3946600.

128. Goepfert PA, Bansal A, Edwards BH, Ritter GD, Jr., Tellez I, McPherson SA, Sabbaj S, Mulligan MJ. A significant number of human immunodeficiency virus epitope-specific cytotoxic T lymphocytes detected by tetramer binding do not produce gamma interferon. J Virol. 2000;74(21):10249-55. Epub 2000/10/12. doi: 10.1128/jvi.74.21.10249-10255.2000. PubMed PMID: 11024158; PMCID: PMC102068.

129. Zehn D, Utzschneider DT, Thimme R. Immune-surveillance through exhausted effector T-cells. Curr Opin Virol. 2016;16:49-54. Epub 2016/02/02. doi: 10.1016/j.coviro.2016.01.002. PubMed PMID: 26826950.

130. Alfei F, Kanev K, Hofmann M, Wu M, Ghoneim HE, Roelli P, Utzschneider DT, von Hoesslin M, Cullen JG, Fan Y, Eisenberg V, Wohlleber D, Steiger K, Merkler D, Delorenzi M, Knolle PA, Cohen CJ, Thimme R, Youngblood B, Zehn D. TOX reinforces the phenotype and longevity of exhausted T cells in chronic viral infection. Nature. 2019;571(7764):265-9. Epub 2019/06/18. doi: 10.1038/s41586-019-1326-9. PubMed PMID: 31207605.

131. Lee PP, Yee C, Savage PA, Fong L, Brockstedt D, Weber JS, Johnson D, Swetter S, Thompson J, Greenberg PD, Roederer M, Davis MM. Characterization of circulating T cells specific for tumor-associated antigens in melanoma patients. Nat Med. 1999;5(6):677-85. Epub 1999/06/17. doi: 10.1038/9525. PubMed PMID: 10371507.

132. Utzschneider DT, Legat A, Fuertes Marraco SA, Carrie L, Luescher I, Speiser DE, Zehn D. T cells maintain an exhausted phenotype after antigen withdrawal and population reexpansion. Nat Immunol. 2013;14(6):603-10. Epub 2013/05/07. doi: 10.1038/ni.2606. PubMed PMID: 23644506.

133. Speiser DE, Utzschneider DT, Oberle SG, Munz C, Romero P, Zehn D. T cell differentiation in chronic infection and cancer: functional adaptation or exhaustion? Nat Rev Immunol. 2014;14(11):768-74. Epub 2014/09/27. doi: 10.1038/nri3740. PubMed PMID: 25257362.

134. Barber DL, Wherry EJ, Masopust D, Zhu B, Allison JP, Sharpe AH, Freeman GJ, Ahmed R. Restoring function in exhausted CD8 T cells during chronic viral infection. Nature. 2006;439(7077):682-7. Epub 2005/12/31. doi: 10.1038/nature04444. PubMed PMID: 16382236.

135. Blackburn SD, Shin H, Freeman GJ, Wherry EJ. Selective expansion of a subset of exhausted CD8 T cells by alphaPD-L1 blockade. Proc Natl Acad Sci U S A. 2008;105(39):15016-21. Epub 2008/09/24. doi: 10.1073/pnas.0801497105. PubMed PMID: 18809920; PMCID: PMC2567485.

136. Scott AC, Dundar F, Zumbo P, Chandran SS, Klebanoff CA, Shakiba M, Trivedi P, Menocal L, Appleby H, Camara S, Zamarin D, Walther T, Snyder A, Femia MR, Comen EA, Wen HY, Hellmann MD, Anandasabapathy N, Liu Y, Altorki NK, Lauer P, Levy O, Glickman MS, Kaye J, Betel D, Philip M, Schietinger A. TOX is a critical regulator of tumour-specific T cell differentiation. Nature. 2019;571(7764):270-4. Epub 2019/06/18. doi: 10.1038/s41586-019-1324-y. PubMed PMID: 31207604; PMCID: PMC7698992.

137. Khan O, Giles JR, McDonald S, Manne S, Ngiow SF, Patel KP, Werner MT, Huang AC, Alexander KA, Wu JE, Attanasio J, Yan P, George SM, Bengsch B, Staupe RP, Donahue G, Xu W, Amaravadi RK, Xu X, Karakousis GC, Mitchell TC, Schuchter LM, Kaye J, Berger SL, Wherry EJ. TOX transcriptionally and epigenetically programs CD8(+) T cell exhaustion. Nature. 2019;571(7764):211-8. Epub 2019/06/18. doi: 10.1038/s41586-019-1325-x. PubMed PMID: 31207603; PMCID: PMC6713202.

138. Seo H, Chen J, Gonzalez-Avalos E, Samaniego-Castruita D, Das A, Wang YH, Lopez-Moyado IF, Georges RO, Zhang W, Onodera A, Wu CJ, Lu LF, Hogan PG, Bhandoola A, Rao A. TOX and TOX2 transcription factors cooperate with NR4A transcription factors to impose CD8(+) T cell exhaustion. Proc Natl Acad Sci U S A. 2019;116(25):12410-5. Epub 2019/06/04. doi: 10.1073/pnas.1905675116. PubMed PMID: 31152140; PMCID: PMC6589758.

139. Correction for Seo et al., TOX and TOX2 transcription factors cooperate with NR4A transcription factors to impose CD8(+) T cell exhaustion. Proc Natl Acad Sci U S A. 2019;116(39):19761. Epub 2019/09/19. doi: 10.1073/pnas.1914896116. PubMed PMID: 31527257; PMCID: PMC6765256.

140. Yao C, Sun HW, Lacey NE, Ji Y, Moseman EA, Shih HY, Heuston EF, Kirby M, Anderson S, Cheng J, Khan O, Handon R, Reilley J, Fioravanti J, Hu J, Gossa S, Wherry EJ, Gattinoni L, McGavern DB, O'Shea JJ, Schwartzberg PL, Wu T. Single-cell RNA-seq reveals TOX as a key regulator of CD8(+) T cell persistence in chronic infection. Nat Immunol. 2019;20(7):890-901. Epub 2019/06/19. doi: 10.1038/s41590-019-0403-4. PubMed PMID: 31209400; PMCID: PMC6588409.

141. Sekine T, Perez-Potti A, Nguyen S, Gorin JB, Wu VH, Gostick E, Llewellyn-Lacey S, Hammer Q, Falck-Jones S, Vangeti S, Yu M, Smed-Sorensen A, Gaballa A, Uhlin M, Sandberg JK, Brander C, Nowak P, Goepfert PA, Price DA, Betts MR, Buggert M. TOX is expressed by exhausted and polyfunctional human effector memory CD8(+) T cells. Sci Immunol. 2020;5(49). Epub 2020/07/06. doi: 10.1126/sciimmunol.aba7918. PubMed PMID: 32620560.

142. Galletti G, De Simone G, Mazza EMC, Puccio S, Mezzanotte C, Bi TM, Davydov AN, Metsger M, Scamardella E, Alvisi G, De Paoli F, Zanon V, Scarpa A, Camisa B, Colombo FS, Anselmo A, Peano C, Polletti S, Mavilio D, Gattinoni L, Boi SK, Youngblood BA, Jones RE, Baird DM, Gostick E, Llewellyn-Lacey S, Ladell K, Price DA, Chudakov DM, Newell EW, Casucci M, Lugli E. Two subsets of stem-like CD8(+) memory T cell progenitors with distinct fate commitments in humans. Nat Immunol. 2020;21(12):1552-62. Epub 2020/10/14. doi: 10.1038/s41590-020-0791-5. PubMed PMID: 33046887; PMCID: PMC7610790.

143. Utzschneider DT, Kallies A. Human effector T cells express TOX-Not so "TOX"ic after all. Sci Immunol. 2020;5(49). Epub 2020/07/06. doi: 10.1126/sciimmunol.abc8272. PubMed PMID: 32620561.

144. Kurd NS, He Z, Louis TL, Milner JJ, Omilusik KD, Jin W, Tsai MS, Widjaja CE, Kanbar JN, Olvera JG, Tysl T, Quezada LK, Boland BS, Huang WJ, Murre C, Goldrath AW, Yeo GW, Chang JT. Early precursors and molecular determinants of tissue-resident memory CD8(+) T lymphocytes revealed by single-cell RNA sequencing. Sci Immunol. 2020;5(47). Epub 2020/05/18. doi: 10.1126/sciimmunol.aaz6894. PubMed PMID: 32414833; PMCID: PMC7341730.

145. Wang Z, Wang S, Goplen NP, Li C, Cheon IS, Dai Q, Huang S, Shan J, Ma C, Ye Z, Xiang M, Limper AH, Porquera EC, Kohlmeier JE, Kaplan MH, Zhang N, Johnson AJ, Vassallo R, Sun J. PD-1(hi) CD8(+) resident memory T cells balance immunity and fibrotic sequelae. Sci Immunol. 2019;4(36). Epub 2019/06/16. doi: 10.1126/sciimmunol.aaw1217. PubMed PMID: 31201259; PMCID: PMC7458867.

146. Kinter AL, Godbout EJ, McNally JP, Sereti I, Roby GA, O'Shea MA, Fauci AS. The common gamma-chain cytokines IL-2, IL-7, IL-15, and IL-21 induce the expression of programmed death-1 and its ligands. J Immunol. 2008;181(10):6738-46. Epub 2008/11/05. doi: 10.4049/jimmunol.181.10.6738. PubMed PMID: 18981091.

147. Hombrink P, Helbig C, Backer RA, Piet B, Oja AE, Stark R, Brasser G, Jongejan A, Jonkers RE, Nota B, Basak O, Clevers HC, Moerland PD, Amsen D, van Lier RA. Programs for the persistence, vigilance and control of human CD8(+) lung-resident memory T cells. Nat Immunol. 2016;17(12):1467-78. Epub 2016/11/01. doi: 10.1038/ni.3589. PubMed PMID: 27776108.

148. Hombrink P, Helbig C, Backer RA, Piet B, Oja AE, Stark R, Brasser G, Jongejan A, Jonkers RE, Nota B, Basak O, Clevers HC, Moerland PD, Amsen D, van Lier RA. Erratum: Programs for the persistence, vigilance and control of human CD8(+) lung-resident memory T cells. Nat Immunol. 2017;18(2):246. Epub 2017/01/20. doi: 10.1038/ni0217-246d. PubMed PMID: 28102212.

149. Mackay LK, Rahimpour A, Ma JZ, Collins N, Stock AT, Hafon ML, Vega-Ramos J, Lauzurica P, Mueller SN, Stefanovic T, Tscharke DC, Heath WR, Inouye M, Carbone FR, Gebhardt T. The developmental pathway for CD103(+)CD8+ tissue-resident memory T cells of skin. Nat Immunol. 2013;14(12):1294-301. Epub 2013/10/29. doi: 10.1038/ni.2744. PubMed PMID: 24162776.

150. Mackay LK, Wynne-Jones E, Freestone D, Pellicci DG, Mielke LA, Newman DM, Braun A, Masson F, Kallies A, Belz GT, Carbone FR. T-box Transcription Factors Combine with the Cytokines TGF-beta and IL-15 to Control Tissue-Resident Memory T Cell Fate. Immunity. 2015;43(6):1101-11. Epub 2015/12/20. doi: 10.1016/j.immuni.2015.11.008. PubMed PMID: 26682984.

151. Martin MD, Jensen IJ, Ishizuka AS, Lefebvre M, Shan Q, Xue HH, Harty JT, Seder RA, Badovinac VP. Bystander responses impact accurate detection of murine and human antigen-specific CD8 T cells. J Clin Invest. 2019;129(9):3894-908. Epub 2019/06/21. doi: 10.1172/JCI124443. PubMed PMID: 31219804; PMCID: PMC6715387.

152. Utzschneider DT, Charmoy M, Chennupati V, Pousse L, Ferreira DP, Calderon-Copete S, Danilo M, Alfei F, Hofmann M, Wieland D, Pradervand S, Thimme R, Zehn D, Held W. T Cell Factor 1-Expressing Memory-like CD8(+) T Cells Sustain the Immune Response to Chronic Viral Infections. Immunity. 2016;45(2):415-27. Epub 2016/08/18. doi: 10.1016/j.immuni.2016.07.021. PubMed PMID: 27533016.

153. Hudson WH, Gensheimer J, Hashimoto M, Wieland A, Valanparambil RM, Li P, Lin JX, Konieczny BT, Im SJ, Freeman GJ, Leonard WJ, Kissick HT, Ahmed R. Proliferating Transitory T Cells with an Effector-like Transcriptional Signature Emerge from PD-1(+) Stem-like CD8(+) T Cells during Chronic Infection. Immunity. 2019;51(6):1043-58 e4. Epub 2019/12/08. doi: 10.1016/j.immuni.2019.11.002. PubMed PMID: 31810882; PMCID: PMC6920571.

154. Yu S, Zhou X, Steinke FC, Liu C, Chen SC, Zagorodna O, Jing X, Yokota Y, Meyerholz DK, Mullighan CG, Knudson CM, Zhao DM, Xue HH. The TCF-1 and LEF-1 transcription factors have cooperative and opposing roles in T cell development and malignancy. Immunity. 2012;37(5):813-26. Epub 2012/10/30. doi: 10.1016/j.immuni.2012.08.009. PubMed PMID: 23103132; PMCID: PMC3501598.

155. Zhou X, Yu S, Zhao DM, Harty JT, Badovinac VP, Xue HH. Differentiation and persistence of memory CD8(+) T cells depend on T cell factor 1. Immunity. 2010;33(2):229-40. Epub 2010/08/24. doi: 10.1016/j.immuni.2010.08.002. PubMed PMID: 20727791; PMCID: PMC2928475.

156. Maurice NJ, Taber AK, Prlic M. The Ugly Duckling Turned to Swan: A Change in Perception of Bystander-Activated Memory CD8 T Cells. J Immunol. 2021;206(3):455-62. Epub 2021/01/21. doi: 10.4049/jimmunol.2000937. PubMed PMID: 33468558; PMCID: PMC7839146.

157. Valenzuela J, Schmidt C, Mescher M. The roles of IL-12 in providing a third signal for clonal expansion of naive CD8 T cells. J Immunol. 2002;169(12):6842-9. Epub 2002/12/10. doi: 10.4049/jimmunol.169.12.6842. PubMed PMID: 12471116.

158. Kieper WC, Prlic M, Schmidt CS, Mescher MF, Jameson SC. Il-12 enhances CD8 T cell homeostatic expansion. J Immunol. 2001;166(9):5515-21. Epub 2001/04/21. doi: 10.4049/jimmunol.166.9.5515. PubMed PMID: 11313390.

159. Jameson SC, Masopust D. Understanding Subset Diversity in T Cell Memory. Immunity. 2018;48(2):214-26. Epub 2018/02/22. doi: 10.1016/j.immuni.2018.02.010. PubMed PMID: 29466754; PMCID: PMC5863745.

160. Duraiswamy J, Ibegbu CC, Masopust D, Miller JD, Araki K, Doho GH, Tata P, Gupta S, Zilliox MJ, Nakaya HI, Pulendran B, Haining WN, Freeman GJ, Ahmed R. Phenotype, function, and gene expression profiles of programmed death-1(hi) CD8 T cells in healthy human adults. J Immunol. 2011;186(7):4200-12. Epub 2011/03/09. doi: 10.4049/jimmunol.1001783. PubMed PMID: 21383243; PMCID: PMC3723805.

161. Beura LK, Hamilton SE, Bi K, Schenkel JM, Odumade OA, Casey KA, Thompson EA, Fraser KA, Rosato PC, Filali-Mouhim A, Sekaly RP, Jenkins MK, Vezys V, Haining WN, Jameson SC, Masopust D. Normalizing the environment recapitulates adult human immune traits in laboratory mice. Nature. 2016;532(7600):512-6. Epub 2016/04/21. doi: 10.1038/nature17655. PubMed PMID: 27096360; PMCID: PMC4871315.

162. Sallusto F, Lenig D, Forster R, Lipp M, Lanzavecchia A. Two subsets of memory T lymphocytes with distinct homing potentials and effector functions. Nature. 1999;401(6754):708-12. Epub 1999/10/28. doi: 10.1038/44385. PubMed PMID: 10537110.

163. Kjer-Nielsen L, Patel O, Corbett AJ, Le Nours J, Meehan B, Liu L, Bhati M, Chen Z, Kostenko L, Reantragoon R, Williamson NA, Purcell AW, Dudek NL, McConville MJ, O'Hair RA, Khairallah GN, Godfrey DI, Fairlie DP, Rossjohn J, McCluskey J. MR1 presents microbial vitamin B metabolites to MAIT cells. Nature. 2012;491(7426):717-23. Epub 2012/10/12. doi: 10.1038/nature11605. PubMed PMID: 23051753.

164. Voillet V, Buggert M, Slichter CK, Berkson JD, Mair F, Addison MM, Dori Y, Nadolski G, Itkin MG, Gottardo R, Betts MR, Prlic M. Human MAIT cells exit peripheral tissues and recirculate via lymph in steady state conditions. JCI Insight. 2018;3(7). Epub 2018/04/06. doi: 10.1172/jci.insight.98487. PubMed PMID: 29618662; PMCID: PMC5928862.

165. Reantragoon R, Corbett AJ, Sakala IG, Gherardin NA, Furness JB, Chen Z, Eckle SB, Uldrich AP, Birkinshaw RW, Patel O, Kostenko L, Meehan B, Kedzierska K, Liu L, Fairlie DP, Hansen TH, Godfrey DI, Rossjohn J, McCluskey J, Kjer-Nielsen L. Antigen-loaded MR1 tetramers define T cell receptor heterogeneity in mucosal-associated invariant T cells. J Exp Med. 2013;210(11):2305-20. Epub 2013/10/09. doi: 10.1084/jem.20130958. PubMed PMID: 24101382; PMCID: PMC3804952.

166. Macian F. NFAT proteins: key regulators of T-cell development and function. Nat Rev Immunol. 2005;5(6):472-84. Epub 2005/06/02. doi: 10.1038/nri1632. PubMed PMID: 15928679.

167. Oestreich KJ, Yoon H, Ahmed R, Boss JM. NFATc1 regulates PD-1 expression upon T cell activation. J Immunol. 2008;181(7):4832-9. Epub 2008/09/20. doi: 10.4049/jimmunol.181.7.4832. PubMed PMID: 18802087; PMCID: PMC2645436.

168. Ahn E, Araki K, Hashimoto M, Li W, Riley JL, Cheung J, Sharpe AH, Freeman GJ, Irving BA, Ahmed R. Role of PD-1 during effector CD8 T cell differentiation. Proc Natl Acad Sci U S A. 2018;115(18):4749-54. Epub 2018/04/15. doi: 10.1073/pnas.1718217115. PubMed PMID: 29654146; PMCID: PMC5939075.

169. Flanagan WM, Corthesy B, Bram RJ, Crabtree GR. Nuclear association of a T-cell transcription factor blocked by FK-506 and cyclosporin A. Nature. 1991;352(6338):803-7. Epub 1991/08/29. doi: 10.1038/352803a0. PubMed PMID: 1715516.

170. Vaeth M, Feske S. NFAT control of immune function: New Frontiers for an Abiding Trooper. F1000Res. 2018;7:260. Epub 2018/03/24. doi: 10.12688/f1000research.13426.1. PubMed PMID: 29568499; PMCID: PMC5840618.

171. Willinger T, Freeman T, Hasegawa H, McMichael AJ, Callan MF. Molecular signatures distinguish human central memory from effector memory CD8 T cell subsets. J Immunol. 2005;175(9):5895-903. Epub 2005/10/21. doi: 10.4049/jimmunol.175.9.5895. PubMed PMID: 16237082.

172. Martin MD, Badovinac VP. Defining Memory CD8 T Cell. Front Immunol. 2018;9:2692. Epub 2018/12/06. doi: 10.3389/fimmu.2018.02692. PubMed PMID: 30515169; PMCID: PMC6255921.

173. Kim CG, Jang M, Kim Y, Leem G, Kim KH, Lee H, Kim TS, Choi SJ, Kim HD, Han JW, Kwon M, Kim JH, Lee AJ, Nam SK, Bae SJ, Lee SB, Shin SJ, Park SH, Ahn JB, Jung I, Lee KY, Park SH, Kim H, Min BS, Shin EC. VEGF-A drives TOX-dependent T cell exhaustion in anti-PD-1-resistant microsatellite stable colorectal cancers. Sci Immunol. 2019;4(41). Epub 2019/11/11. doi: 10.1126/sciimmunol.aay0555. PubMed PMID: 31704735.

174. Heim K, Binder B, Sagar, Wieland D, Hensel N, Llewellyn-Lacey S, Gostick E, Price DA, Emmerich F, Vingerhoet H, Kraft ARM, Cornberg M, Boettler T, Neumann-Haefelin C, Zehn D, Bengsch B, Hofmann M, Thimme R. TOX defines the degree of CD8+ T cell dysfunction in distinct phases of chronic HBV infection. Gut. 2020. Epub 2020/10/25. doi: 10.1136/gutjnl-2020-322404. PubMed PMID: 33097558; PMCID: PMC8292571.

175. Guo L, Li X, Liu R, Chen Y, Ren C, Du S. TOX correlates with prognosis, immune infiltration, and T cells exhaustion in lung adenocarcinoma. Cancer Med. 2020;9(18):6694-709. Epub 2020/07/24. doi: 10.1002/cam4.3324. PubMed PMID: 32700817; PMCID: PMC7520261.

176. Kumar BV, Ma W, Miron M, Granot T, Guyer RS, Carpenter DJ, Senda T, Sun X, Ho SH, Lerner H, Friedman AL, Shen Y, Farber DL. Human Tissue-Resident Memory T Cells Are Defined by Core Transcriptional and Functional Signatures in Lymphoid and Mucosal Sites. Cell Rep. 2017;20(12):2921-34. Epub 2017/09/21. doi: 10.1016/j.celrep.2017.08.078. PubMed PMID: 28930685; PMCID: PMC5646692.

177. Wang X, He Q, Shen H, Xia A, Tian W, Yu W, Sun B. TOX promotes the exhaustion of antitumor CD8(+) T cells by preventing PD1 degradation in hepatocellular carcinoma. J Hepatol. 2019;71(4):731-41. Epub 2019/06/08. doi: 10.1016/j.jhep.2019.05.015. PubMed PMID: 31173813.

178. Arora M, Kumari S, Singh J, Chopra A, Chauhan SS. Expression pattern, regulation, and clinical significance of TOX in breast cancer. Cancer Immunol Immunother. 2021;70(2):349-63. Epub 2020/08/07. doi: 10.1007/s00262-020-02689-3. PubMed PMID: 32757053.

179. Tucker CG, Mitchell JS, Martinov T, Burbach BJ, Beura LK, Wilson JC, Dwyer AJ, Singh LM, Mescher MF, Fife BT. Adoptive T Cell Therapy with IL-12-Preconditioned Low-Avidity T Cells Prevents Exhaustion and Results in Enhanced T Cell Activation, Enhanced Tumor Clearance, and Decreased Risk for Autoimmunity. J Immunol. 2020;205(5):1449-60. Epub 2020/08/02. doi: 10.4049/jimmunol.2000007. PubMed PMID: 32737148; PMCID: PMC8293279.

180. Page N, Klimek B, De Roo M, Steinbach K, Soldati H, Lemeille S, Wagner I, Kreutzfeldt M, Di Liberto G, Vincenti I, Lingner T, Salinas G, Bruck W, Simons M, Murr R, Kaye J, Zehn D, Pinschewer DD, Merkler D. Expression of the DNA-Binding Factor TOX Promotes the Encephalitogenic Potential of Microbe-Induced Autoreactive CD8(+) T Cells. Immunity. 2018;48(5):937-50 e8. Epub 2018/05/17. doi: 10.1016/j.immuni.2018.04.005. PubMed PMID: 29768177; PMCID: PMC6040915.

181. Page N, Klimek B, De Roo M, Steinbach K, Soldati H, Lemeille S, Wagner I, Kreutzfeldt M, Di Liberto G, Vincenti I, Lingner T, Salinas G, Bruck W, Simons M, Murr R, Kaye J, Zehn D, Pinschewer DD, Merkler D. Expression of the DNA-Binding Factor TOX Promotes the Encephalitogenic Potential of Microbe-Induced Autoreactive CD8(+) T Cells. Immunity. 2019;50(3):763. Epub 2019/03/21. doi: 10.1016/j.immuni.2019.02.011. PubMed PMID: 30893589.

182. Brown KE, Freeman GJ, Wherry EJ, Sharpe AH. Role of PD-1 in regulating acute infections. Curr Opin Immunol. 2010;22(3):397-401. Epub 2010/04/30. doi: 10.1016/j.coi.2010.03.007. PubMed PMID: 20427170; PMCID: PMC2905659.

183. Jubel JM, Barbati ZR, Burger C, Wirtz DC, Schildberg FA. The Role of PD-1 in Acute and Chronic Infection. Front Immunol. 2020;11:487. Epub 2020/04/09. doi: 10.3389/fimmu.2020.00487. PubMed PMID: 32265932; PMCID: PMC7105608.

184. Erlebacher A. Immunology of the maternal-fetal interface. Annu Rev Immunol. 2013;31:387-411. Epub 2013/01/10. doi: 10.1146/annurev-immunol-032712-100003. PubMed PMID: 23298207.

185. Medawar PB, Medawar PB. Some immunological and endocrinological problems raised by the evolution of viviparity in verte- brates. Symposia of the Society for Experimental Biology. 1953.

186. Starr TK, Jameson SC, Hogquist KA. Positive and negative selection of T cells. Annu Rev Immunol. 2003;21:139-76. Epub 2002/11/05. doi: 10.1146/annurev.immunol.21.120601.141107. PubMed PMID: 12414722.

187. Palmer E. Negative selection--clearing out the bad apples from the T-cell repertoire. Nat Rev Immunol. 2003;3(5):383-91. Epub 2003/05/27. doi: 10.1038/nri1085. PubMed PMID: 12766760.

188. Apps R, Murphy SP, Fernando R, Gardner L, Ahad T, Moffett A. Human leucocyte antigen (HLA) expression of primary trophoblast cells and placental cell lines, determined using single antigen beads to characterize allotype specificities of anti-HLA antibodies. Immunology. 2009;127(1):26-39. Epub 2009/04/17. doi: 10.1111/j.1365-2567.2008.03019.x. PubMed PMID: 19368562; PMCID: PMC2678179.

189. Nancy P, Tagliani E, Tay CS, Asp P, Levy DE, Erlebacher A. Chemokine gene silencing in decidual stromal cells limits T cell access to the maternal-fetal interface. Science. 2012;336(6086):1317-21. Epub 2012/06/09. doi: 10.1126/science.1220030. PubMed PMID: 22679098; PMCID: PMC3727649.

190. Hanna J, Goldman-Wohl D, Hamani Y, Avraham I, Greenfield C, Natanson-Yaron S, Prus D, Cohen-Daniel L, Arnon TI, Manaster I, Gazit R, Yutkin V, Benharroch D, Porgador A, Keshet E, Yagel S, Mandelboim O. Decidual NK cells regulate key developmental processes at the human fetal-maternal interface. Nat Med. 2006;12(9):1065-74. Epub 2006/08/08. doi: 10.1038/nm1452. PubMed PMID: 16892062.

191. Lash GE, Schiessl B, Kirkley M, Innes BA, Cooper A, Searle RF, Robson SC, Bulmer JN. Expression of angiogenic growth factors by uterine natural killer cells during early pregnancy. J Leukoc Biol. 2006;80(3):572-80. Epub 2006/07/04. doi: 10.1189/jlb.0406250. PubMed PMID: 16816146.

192. Vacca P, Cantoni C, Prato C, Fulcheri E, Moretta A, Moretta L, Mingari MC. Regulatory role of NKp44, NKp46, DNAM-1 and NKG2D receptors in the interaction between NK cells and trophoblast cells. Evidence for divergent functional profiles of decidual versus peripheral NK cells. Int Immunol. 2008;20(11):1395-405. Epub 2008/09/26. doi: 10.1093/intimm/dxn105. PubMed PMID: 18815119.

193. Wu X, Jin LP, Yuan MM, Zhu Y, Wang MY, Li DJ. Human first-trimester trophoblast cells recruit CD56brightCD16- NK cells into decidua by way of expressing and secreting of CXCL12/stromal cell-derived factor 1. J Immunol. 2005;175(1):61-8. Epub 2005/06/24. doi: 10.4049/jimmunol.175.1.61. PubMed PMID: 15972632.

194. Xiong S, Sharkey AM, Kennedy PR, Gardner L, Farrell LE, Chazara O, Bauer J, Hiby SE, Colucci F, Moffett A. Maternal uterine NK cell-activating receptor KIR2DS1 enhances placentation. J Clin Invest. 2013;123(10):4264-72. Epub 2013/10/05. doi: 10.1172/JCI68991. PubMed PMID: 24091323; PMCID: PMC4382274.

195. Vento-Tormo R, Efremova M, Botting RA, Turco MY, Vento-Tormo M, Meyer KB, Park JE, Stephenson E, Polanski K, Goncalves A, Gardner L, Holmqvist S, Henriksson J, Zou A, Sharkey AM, Millar B, Innes B, Wood L, Wilbrey-Clark A, Payne RP, Ivarsson MA, Lisgo S, Filby A, Rowitch DH, Bulmer JN, Wright GJ, Stubbington MJT, Haniffa M, Moffett A, Teichmann SA. Single-cell reconstruction of the early maternal-fetal interface in humans. Nature. 2018;563(7731):347-53. Epub 2018/11/16. doi: 10.1038/s41586-018-0698-6. PubMed PMID: 30429548.

196. Santner-Nanan B, Peek MJ, Khanam R, Richarts L, Zhu E, Fazekas de St Groth B, Nanan R. Systemic increase in the ratio between Foxp3+ and IL-17-producing CD4+ T cells in healthy pregnancy but not in preeclampsia. J Immunol. 2009;183(11):7023-30. Epub 2009/11/17. doi: 10.4049/jimmunol.0901154. PubMed PMID: 19915051.

197. Somerset DA, Zheng Y, Kilby MD, Sansom DM, Drayson MT. Normal human pregnancy is associated with an elevation in the immune suppressive CD25+ CD4+ regulatory T-cell subset. Immunology. 2004;112(1):38-43. Epub 2004/04/21. doi: 10.1111/j.1365-2567.2004.01869.x. PubMed PMID: 15096182; PMCID: PMC1782465.

198. Tilburgs T, Scherjon SA, van der Mast BJ, Haasnoot GW, Versteeg VDV-MM, Roelen DL, van Rood JJ, Claas FH. Fetal-maternal HLA-C mismatch is associated with decidual T cell activation and induction of functional T regulatory cells. J Reprod Immunol. 2009;82(2):148-57. Epub 2009/07/28. doi: 10.1016/j.jri.2009.05.003. PubMed PMID: 19631389.

199. Piper KP, McLarnon A, Arrazi J, Horlock C, Ainsworth J, Kilby MD, Martin WL, Moss PA. Functional HY-specific CD8+ T cells are found in a high proportion of women following pregnancy with a male fetus. Biol Reprod. 2007;76(1):96-101. Epub 2006/09/22. doi: 10.1095/biolreprod.106.055426. PubMed PMID: 16988213.

200. Aghaeepour N, Ganio EA, McIlwain D, Tsai AS, Tingle M, Van Gassen S, Gaudilliere DK, Baca Q, McNeil L, Okada R, Ghaemi MS, Furman D, Wong RJ, Winn VD, Druzin ML, El-Sayed YY, Quaintance C, Gibbs R, Darmstadt GL, Shaw GM, Stevenson DK, Tibshirani R, Nolan GP, Lewis DB, Angst MS, Gaudilliere B. An immune clock of human pregnancy. Sci Immunol. 2017;2(15). Epub 2017/09/03. doi: 10.1126/sciimmunol.aan2946. PubMed PMID: 28864494; PMCID: PMC5701281.

201. Gomez-Lopez N, Vega-Sanchez R, Castillo-Castrejon M, Romero R, Cubeiro-Arreola K, Vadillo-Ortega F. Evidence for a role for the adaptive immune response in human term parturition. Am J Reprod Immunol. 2013;69(3):212-30. Epub 2013/01/26. doi: 10.1111/aji.12074. PubMed PMID: 23347265; PMCID: PMC3600361.

202. Arenas-Hernandez M, Romero R, Xu Y, Panaitescu B, Garcia-Flores V, Miller D, Ahn H, Done B, Hassan SS, Hsu CD, Tarca AL, Sanchez-Torres C, Gomez-Lopez N. Effector and Activated T Cells Induce Preterm Labor and Birth That Is Prevented by Treatment with Progesterone. J Immunol. 2019;202(9):2585-608. Epub 2019/03/29. doi: 10.4049/jimmunol.1801350. PubMed PMID: 30918041; PMCID: PMC6570421.

203. Carter AM. Animal models of human placentation--a review. Placenta. 2007;28 Suppl A:S41-7. Epub 2007/01/02. doi: 10.1016/j.placenta.2006.11.002. PubMed PMID: 17196252.

204. Carter AM. Unique Aspects of Human Placentation. Int J Mol Sci. 2021;22(15). Epub 2021/08/08. doi: 10.3390/ijms22158099. PubMed PMID: 34360862; PMCID: PMC8347521.

205. Red-Horse K, Rivera J, Schanz A, Zhou Y, Winn V, Kapidzic M, Maltepe E, Okazaki K, Kochman R, Vo KC, Giudice L, Erlebacher A, McCune JM, Stoddart CA, Fisher SJ. Cytotrophoblast induction of arterial apoptosis and lymphangiogenesis in an in vivo model of human placentation. J Clin Invest. 2006;116(10):2643-52. Epub 2006/09/26. doi: 10.1172/JCI27306. PubMed PMID: 16998586; PMCID: PMC1570373.

206. Gomez-Lopez N, StLouis D, Lehr MA, Sanchez-Rodriguez EN, Arenas-Hernandez M. Immune cells in term and preterm labor. Cell Mol Immunol. 2014;11(6):571-81. Epub 2014/06/24. doi: 10.1038/cmi.2014.46. PubMed PMID: 24954221; PMCID: PMC4220837.

207. Mair F, Prlic M. OMIP-044: 28-color immunophenotyping of the human dendritic cell compartment. Cytometry A. 2018;93(4):402-5. Epub 2018/01/23. doi: 10.1002/cyto.a.23331. PubMed PMID: 29356334; PMCID: PMC6785241.

208. McInnes L, Healy J, Saul N, Großberger L. UMAP: Uniform Manifold Approximation and Projection. Journal Name: Journal of Open Source Software; Journal Volume: 3; Journal Issue: 29. 2018:Medium: X; Size: 861. PubMed PMID: OSTI ID: 10104557.

209. Becht E, McInnes L, Healy J, Dutertre CA, Kwok IWH, Ng LG, Ginhoux F, Newell EW. Dimensionality reduction for visualizing single-cell data using UMAP. Nat Biotechnol. 2018. Epub 2018/12/12. doi: 10.1038/nbt.4314. PubMed PMID: 30531897.

210. Ziegler SF, Ramsdell F, Alderson MR. The activation antigen CD69. STEM CELLS. 1994;12(5):456-65. doi: https://doi.org/10.1002/stem.5530120502.

211. Saito S, Nishikawa K, Morii T, Narita N, Enomoto M, Ichijo M. Expression of activation antigens CD69, HLA-DR, interleukin-2 receptor-alpha (IL-2R alpha) and IL-2R beta on T cells of human decidua at an early stage of pregnancy. Immunology. 1992;75(4):710-2. Epub 1992/04/01. PubMed PMID: 1592443; PMCID: PMC1384855.

212. Sindram-Trujillo A, Scherjon S, Kanhai H, Roelen D, Claas F. Increased T-cell activation in decidua parietalis compared to decidua basalis in uncomplicated human term pregnancy. Am J Reprod Immunol. 2003;49(5):261-8. Epub 2003/07/12. doi: 10.1034/j.1600-0897.2003.00041.x. PubMed PMID: 12854730.

213. Clark RA, Watanabe R, Teague JE, Schlapbach C, Tawa MC, Adams N, Dorosario AA, Chaney KS, Cutler CS, Leboeuf NR, Carter JB, Fisher DC, Kupper TS. Skin effector memory T cells do not recirculate and provide immune protection in alemtuzumab-treated CTCL patients. Sci Transl Med. 2012;4(117):117ra7. Epub 2012/01/21. doi: 10.1126/scitranslmed.3003008. PubMed PMID: 22261031; PMCID: PMC3373186.

214. Masopust D, Vezys V, Marzo AL, Lefrancois L. Preferential localization of effector memory cells in nonlymphoid tissue. Science. 2001;291(5512):2413-7. Epub 2001/03/27. doi: 10.1126/science.1058867. PubMed PMID: 11264538.

215. Skon CN, Lee JY, Anderson KG, Masopust D, Hogquist KA, Jameson SC. Transcriptional downregulation of S1pr1 is required for the establishment of resident memory CD8+ T cells. Nat Immunol. 2013;14(12):1285-93. Epub 2013/10/29. doi: 10.1038/ni.2745. PubMed PMID: 24162775; PMCID: PMC3844557.

216. Szabo PA, Miron M, Farber DL. Location, location, location: Tissue resident memory T cells in mice and humans. Sci Immunol. 2019;4(34). Epub 2019/04/07. doi: 10.1126/sciimmunol.aas9673. PubMed PMID: 30952804; PMCID: PMC6778482.

217. Masopust D, Soerens AG. Tissue-Resident T Cells and Other Resident Leukocytes. Annu Rev Immunol. 2019;37:521-46. Epub 2019/02/07. doi: 10.1146/annurev-immunol-042617-053214. PubMed PMID: 30726153; PMCID: PMC7175802.

218. Schenkel JM, Masopust D. Tissue-resident memory T cells. Immunity. 2014;41(6):886-97. Epub 2014/12/20. doi: 10.1016/j.immuni.2014.12.007. PubMed PMID: 25526304; PMCID: PMC4276131.

219. Day CL, Kaufmann DE, Kiepiela P, Brown JA, Moodley ES, Reddy S, Mackey EW, Miller JD, Leslie AJ, DePierres C, Mncube Z, Duraiswamy J, Zhu B, Eichbaum Q, Altfeld M, Wherry EJ, Coovadia HM, Goulder PJ, Klenerman P, Ahmed R, Freeman GJ, Walker BD. PD-1 expression on HIV-specific T cells is associated with T-cell exhaustion and disease progression. Nature. 2006;443(7109):350-4. Epub 2006/08/22. doi: 10.1038/nature05115. PubMed PMID: 16921384.

220. Hutloff A, Dittrich AM, Beier KC, Eljaschewitsch B, Kraft R, Anagnostopoulos I, Kroczek RA. ICOS is an inducible T-cell co-stimulator structurally and functionally related to CD28. Nature. 1999;397(6716):263-6. Epub 1999/02/04. doi: 10.1038/16717. PubMed PMID: 9930702.

221. Jin HT, Anderson AC, Tan WG, West EE, Ha SJ, Araki K, Freeman GJ, Kuchroo VK, Ahmed R. Cooperation of Tim-3 and PD-1 in CD8 T-cell exhaustion during chronic viral infection. Proc Natl Acad Sci U S A. 2010;107(33):14733-8. Epub 2010/08/04. doi: 10.1073/pnas.1009731107. PubMed PMID: 20679213; PMCID: PMC2930455.

222. Sakuishi K, Apetoh L, Sullivan JM, Blazar BR, Kuchroo VK, Anderson AC. Targeting Tim-3 and PD-1 pathways to reverse T cell exhaustion and restore anti-tumor immunity. J Exp Med. 2010;207(10):2187-94. Epub 2010/09/08. doi: 10.1084/jem.20100643. PubMed PMID: 20819927; PMCID: PMC2947065.

223. Newell EW, Sigal N, Nair N, Kidd BA, Greenberg HB, Davis MM. Combinatorial tetramer staining and mass cytometry analysis facilitate T-cell epitope mapping and characterization. Nat Biotechnol. 2013;31(7):623-9. Epub 2013/06/12. doi: 10.1038/nbt.2593. PubMed PMID: 23748502; PMCID: PMC3796952.

224. Wang W, Meadows LR, den Haan JM, Sherman NE, Chen Y, Blokland E, Shabanowitz J, Agulnik AI, Hendrickson RC, Bishop CE, et al. Human H-Y: a male-specific histocompatibility antigen derived from the SMCY protein. Science. 1995;269(5230):1588-90. Epub 1995/09/15. doi: 10.1126/science.7667640. PubMed PMID: 7667640.

225. van Egmond A, van der Keur C, Swings GM, Scherjon SA, Claas FH. The possible role of virus-specific CD8(+) memory T cells in decidual tissue. J Reprod Immunol. 2016;113:1-8. Epub 2015/10/27. doi: 10.1016/j.jri.2015.09.073. PubMed PMID: 26496155.

226. van der Zwan A, van der Meer-Prins EMW, van Miert P, van den Heuvel H, Anholts JDH, Roelen DL, Claas FHJ, Heidt S. Cross-Reactivity of Virus-Specific CD8+ T Cells Against Allogeneic HLA-C: Possible Implications for Pregnancy Outcome. Front Immunol. 2018;9:2880. Epub 2018/12/24. doi: 10.3389/fimmu.2018.02880. PubMed PMID: 30574149; PMCID: PMC6291497.

227. Browaeys R, Saelens W, Saeys Y. NicheNet: modeling intercellular communication by linking ligands to target genes. Nat Methods. 2020;17(2):159-62. Epub 2019/12/11. doi: 10.1038/s41592-019-0667-5. PubMed PMID: 31819264.

228. Schwanhausser B, Busse D, Li N, Dittmar G, Schuchhardt J, Wolf J, Chen W, Selbach M. Global quantification of mammalian gene expression control. Nature. 2011;473(7347):337-42. Epub 2011/05/20. doi: 10.1038/nature10098. PubMed PMID: 21593866.

229. Schwanhausser B, Busse D, Li N, Dittmar G, Schuchhardt J, Wolf J, Chen W, Selbach M. Corrigendum: Global quantification of mammalian gene expression control. Nature. 2013;495(7439):126-7. Epub 2013/02/15. doi: 10.1038/nature11848. PubMed PMID: 23407496.

230. Lin J-X, Leonard WJ. The role of Stat5a and Stat5b in signaling by IL-2 family cytokines. Oncogene. 2000;19(21):2566-76. doi: 10.1038/sj.onc.1203523.

231. Zheng GX, Terry JM, Belgrader P, Ryvkin P, Bent ZW, Wilson R, Ziraldo SB, Wheeler TD, McDermott GP, Zhu J, Gregory MT, Shuga J, Montesclaros L, Underwood JG, Masquelier DA, Nishimura SY, Schnall-Levin M, Wyatt PW, Hindson CM, Bharadwaj R, Wong A, Ness KD, Beppu LW, Deeg HJ, McFarland C, Loeb KR, Valente WJ, Ericson NG, Stevens EA, Radich JP, Mikkelsen TS, Hindson BJ, Bielas JH. Massively parallel digital transcriptional profiling of single cells. Nat Commun. 2017;8:14049. Epub 2017/01/17. doi: 10.1038/ncomms14049. PubMed PMID: 28091601; PMCID: PMC5241818 L.M., D.A.M., S.Y.N., M.S.L., P.W.W., C.M.H., R.B., A.W., K.D.N., T.S.M. and B.J.H. are employees of 10x Genomics.

232. Azimifar SB, Nagaraj N, Cox J, Mann M. Cell-type-resolved quantitative proteomics of murine liver. Cell Metab. 2014;20(6):1076-87. Epub 2014/12/04. doi: 10.1016/j.cmet.2014.11.002. PubMed PMID: 25470552.

233. Mair F, Erickson JR, Voillet V, Simoni Y, Bi T, Tyznik AJ, Martin J, Gottardo R, Newell EW, Prlic M. A Targeted Multi-omic Analysis Approach Measures Protein Expression and Low-Abundance Transcripts on the Single-Cell Level. Cell Rep. 2020;31(1):107499. Epub 2020/04/09. doi: 10.1016/j.celrep.2020.03.063. PubMed PMID: 32268080; PMCID: PMC7224638.

234. Zhou AC, Wagar LE, Wortzman ME, Watts TH. Intrinsic 4-1BB signals are indispensable for the establishment of an influenza-specific tissue-resident memory CD8 T-cell population in the lung. Mucosal Immunol. 2017;10(5):1294-309. Epub 2017/01/05. doi: 10.1038/mi.2016.124. PubMed PMID: 28051085.

235. Gustafsson C, Mjosberg J, Matussek A, Geffers R, Matthiesen L, Berg G, Sharma S, Buer J, Ernerudh J. Gene expression profiling of human decidual macrophages: evidence for immunosuppressive phenotype. PLoS One. 2008;3(4):e2078. Epub 2008/05/01. doi: 10.1371/journal.pone.0002078. PubMed PMID: 18446208; PMCID: PMC2323105.

236. Svensson J, Jenmalm MC, Matussek A, Geffers R, Berg G, Ernerudh J. Macrophages at the fetal-maternal interface express markers of alternative activation and are induced by M-CSF and IL-10. J Immunol. 2011;187(7):3671-82. Epub 2011/09/06. doi: 10.4049/jimmunol.1100130. PubMed PMID: 21890660.

237. Houser BL, Tilburgs T, Hill J, Nicotra ML, Strominger JL. Two unique human decidual macrophage populations. J Immunol. 2011;186(4):2633-42. Epub 2011/01/25. doi: 10.4049/jimmunol.1003153. PubMed PMID: 21257965; PMCID: PMC3712354.

238. Jiang X, Wang H. Macrophage subsets at the maternal-fetal interface. Cell Mol Immunol. 2020;17(8):889-91. Epub 2020/05/10. doi: 10.1038/s41423-020-0435-6. PubMed PMID: 32382125; PMCID: PMC7203721.

239. Couper KN, Blount DG, Riley EM. IL-10: the master regulator of immunity to infection. J Immunol. 2008;180(9):5771-7. Epub 2008/04/22. doi: 10.4049/jimmunol.180.9.5771. PubMed PMID: 18424693.

240. Munn DH, Zhou M, Attwood JT, Bondarev I, Conway SJ, Marshall B, Brown C, Mellor AL. Prevention of allogeneic fetal rejection by tryptophan catabolism. Science. 1998;281(5380):1191-3. Epub 1998/08/26. doi: 10.1126/science.281.5380.1191. PubMed PMID: 9712583.

241. Frumento G, Rotondo R, Tonetti M, Damonte G, Benatti U, Ferrara GB. Tryptophan-derived catabolites are responsible for inhibition of T and natural killer cell proliferation induced by indoleamine 2,3-dioxygenase. J Exp Med. 2002;196(4):459-68. Epub 2002/08/21. doi: 10.1084/jem.20020121. PubMed PMID: 12186838; PMCID: PMC2196046.

242. Munn DH, Shafizadeh E, Attwood JT, Bondarev I, Pashine A, Mellor AL. Inhibition of T cell proliferation by macrophage tryptophan catabolism. J Exp Med. 1999;189(9):1363-72. Epub 1999/05/04. doi: 10.1084/jem.189.9.1363. PubMed PMID: 10224276; PMCID: PMC2193062.

243. Opitz CA, Litzenburger UM, Sahm F, Ott M, Tritschler I, Trump S, Schumacher T, Jestaedt L, Schrenk D, Weller M, Jugold M, Guillemin GJ, Miller CL, Lutz C, Radlwimmer B, Lehmann I, von Deimling A, Wick W, Platten M. An endogenous tumour-promoting ligand of the human aryl hydrocarbon receptor. Nature. 2011;478(7368):197-203. Epub 2011/10/07. doi: 10.1038/nature10491. PubMed PMID: 21976023.

244. Murray IA, Patterson AD, Perdew GH. Aryl hydrocarbon receptor ligands in cancer: friend and foe. Nat Rev Cancer. 2014;14(12):801-14. Epub 2015/01/09. doi: 10.1038/nrc3846. PubMed PMID: 25568920; PMCID: PMC4401080.

245. Gutierrez-Vazquez C, Quintana FJ. Regulation of the Immune Response by the Aryl Hydrocarbon Receptor. Immunity. 2018;48(1):19-33. Epub 2018/01/19. doi: 10.1016/j.immuni.2017.12.012. PubMed PMID: 29343438; PMCID: PMC5777317.

246. Sinclair LV, Neyens D, Ramsay G, Taylor PM, Cantrell DA. Single cell analysis of kynurenine and System L amino acid transport in T cells. Nature communications. 2018;9(1):1-11.

247. Damoiseaux J. The IL-2 - IL-2 receptor pathway in health and disease: The role of the soluble IL-2 receptor. Clin Immunol. 2020;218:108515. Epub 2020/07/04. doi: 10.1016/j.clim.2020.108515. PubMed PMID: 32619646.

248. Ofran Y, Kim HT, Brusic V, Blake L, Mandrell M, Wu CJ, Sarantopoulos S, Bellucci R, Keskin DB, Soiffer RJ, Antin JH, Ritz J. Diverse patterns of T-cell response against multiple newly identified human Y chromosome-encoded minor histocompatibility epitopes. Clin Cancer Res. 2010;16(5):1642-51. Epub 2010/02/18. doi: 10.1158/1078-0432.CCR-09-2701. PubMed PMID: 20160060; PMCID: PMC2834217.

249. Holz LE, Prier JE, Freestone D, Steiner TM, English K, Johnson DN, Mollard V, Cozijnsen A, Davey GM, Godfrey DI, Yui K, Mackay LK, Lahoud MH, Caminschi I, McFadden GI, Bertolino P, Fernandez-Ruiz D, Heath WR. CD8(+) T Cell Activation Leads to Constitutive Formation of Liver Tissue-Resident Memory T Cells that Seed a Large and Flexible Niche in the Liver. Cell Rep. 2018;25(1):68-79 e4. Epub 2018/10/04. doi: 10.1016/j.celrep.2018.08.094. PubMed PMID: 30282039.

250. Mackay LK, Stock AT, Ma JZ, Jones CM, Kent SJ, Mueller SN, Heath WR, Carbone FR, Gebhardt T. Long-lived epithelial immunity by tissue-resident memory T (TRM) cells in the absence of persisting local antigen presentation. Proc Natl Acad Sci U S A. 2012;109(18):7037-42. Epub 2012/04/18. doi: 10.1073/pnas.1202288109. PubMed PMID: 22509047; PMCID: PMC3344960.

251. Shin H, Iwasaki A. A vaccine strategy that protects against genital herpes by establishing local memory T cells. Nature. 2012;491(7424):463-7. Epub 2012/10/19. doi: 10.1038/nature11522. PubMed PMID: 23075848; PMCID: PMC3499630.

252. Wakim LM, Woodward-Davis A, Bevan MJ. Memory T cells persisting within the brain after local infection show functional adaptations to their tissue of residence. Proc Natl Acad Sci U S A. 2010;107(42):17872-9. Epub 2010/10/07. doi: 10.1073/pnas.1010201107. PubMed PMID: 20923878; PMCID: PMC2964240.

253. Lee YT, Suarez-Ramirez JE, Wu T, Redman JM, Bouchard K, Hadley GA, Cauley LS. Environmental and antigen receptor-derived signals support sustained surveillance of the lungs by pathogen-specific cytotoxic T lymphocytes. J Virol. 2011;85(9):4085-94. Epub 2011/02/25. doi: 10.1128/JVI.02493-10. PubMed PMID: 21345961; PMCID: PMC3126261.

254. Maurice NJ, Berner J, Taber AK, Zehn D, Prlic M. Inflammatory signals are sufficient to elicit TOX expression in mouse and human CD8+ T cells. JCI Insight. 2021;6(13). Epub 2021/05/26. doi: 10.1172/jci.insight.150744. PubMed PMID: 34032638; PMCID: PMC8410038.

255. Pulle G, Vidric M, Watts TH. IL-15-dependent induction of 4-1BB promotes antigen-independent CD8 memory T cell survival. J Immunol. 2006;176(5):2739-48. Epub 2006/02/24. doi: 10.4049/jimmunol.176.5.2739. PubMed PMID: 16493029.

256. Mujib S, Jones RB, Lo C, Aidarus N, Clayton K, Sakhdari A, Benko E, Kovacs C, Ostrowski MA. Antigen-independent induction of Tim-3 expression on human T cells by the common gamma-chain cytokines IL-2, IL-7, IL-15, and IL-21 is associated with proliferation and is dependent on the phosphoinositide 3-kinase pathway. J Immunol. 2012;188(8):3745-56. Epub 2012/03/17. doi: 10.4049/jimmunol.1102609. PubMed PMID: 22422881.

257. Schenkel JM, Fraser KA, Casey KA, Beura LK, Pauken KE, Vezys V, Masopust D. IL-15-Independent Maintenance of Tissue-Resident and Boosted Effector Memory CD8 T Cells. J Immunol. 2016;196(9):3920-6. Epub 2016/03/24. doi: 10.4049/jimmunol.1502337. PubMed PMID: 27001957; PMCID: PMC5145194.

258. Zaid A, Mackay LK, Rahimpour A, Braun A, Veldhoen M, Carbone FR, Manton JH, Heath WR, Mueller SN. Persistence of skin-resident memory T cells within an epidermal niche. Proc Natl Acad Sci U S A. 2014;111(14):5307-12. Epub 2014/04/08. doi: 10.1073/pnas.1322292111. PubMed PMID: 24706879; PMCID: PMC3986170.

259. Colak S, Ten Dijke P. Targeting TGF-beta Signaling in Cancer. Trends Cancer. 2017;3(1):56-71. Epub 2017/07/19. doi: 10.1016/j.trecan.2016.11.008. PubMed PMID: 28718426.

260. Seoane J, Gomis RR. TGF-beta Family Signaling in Tumor Suppression and Cancer Progression. Cold Spring Harb Perspect Biol. 2017;9(12). Epub 2017/03/02. doi: 10.1101/cshperspect.a022277. PubMed PMID: 28246180; PMCID: PMC5710110.

261. Li H, Ning S, Ghandi M, Kryukov GV, Gopal S, Deik A, Souza A, Pierce K, Keskula P, Hernandez D, Ann J, Shkoza D, Apfel V, Zou Y, Vazquez F, Barretina J, Pagliarini RA, Galli GG, Root DE, Hahn WC, Tsherniak A, Giannakis M, Schreiber SL, Clish CB, Garraway LA, Sellers WR. The landscape of cancer cell line metabolism. Nat Med. 2019;25(5):850-60. Epub 2019/05/10. doi: 10.1038/s41591-019-0404-8. PubMed PMID: 31068703; PMCID: PMC6629041.

262. Venkateswaran N, Conacci-Sorrell M. Kynurenine: an oncometabolite in colon cancer. Cell Stress. 2020;4(1):24-6. Epub 2020/01/11. doi: 10.15698/cst2020.01.210. PubMed PMID: 31922097; PMCID: PMC6946015.

263. Toebes M, Coccoris M, Bins A, Rodenko B, Gomez R, Nieuwkoop NJ, van de Kasteele W, Rimmelzwaan GF, Haanen JB, Ovaa H, Schumacher TN. Design and use of conditional MHC class I ligands. Nat Med. 2006;12(2):246-51. Epub 2006/02/08. doi: 10.1038/nm1360. PubMed PMID: 16462803.

264. Simoni Y, Fehlings M, Newell EW. Multiplex MHC Class I Tetramer Combined with Intranuclear Staining by Mass Cytometry. Methods Mol Biol. 2019;1989:147-58. Epub 2019/05/12. doi: 10.1007/978-1-4939-9454-0_11. PubMed PMID: 31077105.

265. Hao Y, Hao S, Andersen-Nissen E, Mauck WM, 3rd, Zheng S, Butler A, Lee MJ, Wilk AJ, Darby C, Zager M, Hoffman P, Stoeckius M, Papalexi E, Mimitou EP, Jain J, Srivastava A, Stuart T, Fleming LM, Yeung B, Rogers AJ, McElrath JM, Blish CA, Gottardo R, Smibert P, Satija R. Integrated analysis of multimodal single-cell data. Cell. 2021;184(13):3573-87 e29. Epub 2021/06/02. doi: 10.1016/j.cell.2021.04.048. PubMed PMID: 34062119; PMCID: PMC8238499.

266. Aran D, Looney AP, Liu L, Wu E, Fong V, Hsu A, Chak S, Naikawadi RP, Wolters PJ, Abate AR, Butte AJ, Bhattacharya M. Reference-based analysis of lung single-cell sequencing reveals a transitional profibrotic macrophage. Nat Immunol. 2019;20(2):163-72. Epub 2019/01/16. doi: 10.1038/s41590-018-0276-y. PubMed PMID: 30643263; PMCID: PMC6340744.

267. Finak G, McDavid A, Yajima M, Deng J, Gersuk V, Shalek AK, Slichter CK, Miller HW, McElrath MJ, Prlic M, Linsley PS, Gottardo R. MAST: a flexible statistical framework for assessing transcriptional changes and characterizing heterogeneity in single-cell RNA sequencing data. Genome Biol. 2015;16:278. Epub 2015/12/15. doi: 10.1186/s13059-015-0844-5. PubMed PMID: 26653891; PMCID: PMC4676162.

268. Barber DL, Wherry EJ, Ahmed R. Cutting edge: rapid in vivo killing by memory CD8 T cells. J Immunol. 2003;171(1):27-31. Epub 2003/06/21. doi: 10.4049/jimmunol.171.1.27. PubMed PMID: 12816979.

269. Schenkel JM, Fraser KA, Beura LK, Pauken KE, Vezys V, Masopust D. T cell memory. Resident memory CD8 T cells trigger protective innate and adaptive immune responses. Science. 2014;346(6205):98-101. Epub 2014/08/30. doi: 10.1126/science.1254536. PubMed PMID: 25170049; PMCID: PMC4449618.

VITA

Prior to conducting his Ph.D. studies in Dr. Martin Prlic's laboratory, Nicholas Joseph Maurice attended Seattle Pacific University, graduating *magna cum laude* with a Bachelor of Science in Physiology and a Bachelor of Art in Chemistry. Here, he conducted research under the mentorship of Dr. Benjamin McFarland. Afterwards, he conducted post-baccalaureate training at the HIV Vaccine Trials Network, the *Rheinische Friedrich-Wilhelms-Universität Bonn*, and the Fred Hutchinson Cancer Research Center. Nicholas' Ph.D. culminated with being awarded the University of Washington's highest student honor, the 2021 Graduate School Medal. Nicholas will be joining the labs of Dr. Kristin Hogquist and Dr. Stephen Jameson at the University of Minnesota's Center for Immunology. Here, he will conduct his post-doctoral training with the support of the NCI-funded F99/K00 Pre-doctoral to Post-doctoral Transition Award.